Research Topics

Applications of date-driven artificial intelligence in integrated energy systems

Edited by
Qiuye Sun, Qihe Shan, Xiangnan Zhong and Renke Han

Published in
Frontiers in Energy Research

ISSN 1664-8714
ISBN 978-2-83251-025-4
DOI 10.3389/978-2-83251-025-4

About Frontiers

Frontiers is more than just an open access publisher of scholarly articles: it is a pioneering approach to the world of academia, radically improving the way scholarly research is managed. The grand vision of Frontiers is a world where all people have an equal opportunity to seek, share and generate knowledge. Frontiers provides immediate and permanent online open access to all its publications, but this alone is not enough to realize our grand goals.

Frontiers journal series

The Frontiers journal series is a multi-tier and interdisciplinary set of open-access, online journals, promising a paradigm shift from the current review, selection and dissemination processes in academic publishing. All Frontiers journals are driven by researchers for researchers; therefore, they constitute a service to the scholarly community. At the same time, the *Frontiers journal series* operates on a revolutionary invention, the tiered publishing system, initially addressing specific communities of scholars, and gradually climbing up to broader public understanding, thus serving the interests of the lay society, too.

Dedication to quality

Each Frontiers article is a landmark of the highest quality, thanks to genuinely collaborative interactions between authors and review editors, who include some of the world's best academicians. Research must be certified by peers before entering a stream of knowledge that may eventually reach the public - and shape society; therefore, Frontiers only applies the most rigorous and unbiased reviews. Frontiers revolutionizes research publishing by freely delivering the most outstanding research, evaluated with no bias from both the academic and social point of view. By applying the most advanced information technologies, Frontiers is catapulting scholarly publishing into a new generation.

What are Frontiers Research Topics?

Frontiers Research Topics are very popular trademarks of the *Frontiers journals series*: they are collections of at least ten articles, all centered on a particular subject. With their unique mix of varied contributions from Original Research to Review Articles, Frontiers Research Topics unify the most influential researchers, the latest key findings and historical advances in a hot research area.

Find out more on how to host your own Frontiers Research Topic or contribute to one as an author by contacting the Frontiers editorial office: frontiersin.org/about/contact

Applications of date-driven artificial intelligence in integrated energy systems

Topic editors
Qiuye Sun — Northeastern University, China
Qihe Shan — Dalian Maritime University, China
Xiangnan Zhong — Florida Atlantic University, United States
Renke Han — University of Oxford, United Kingdom

Citation
Sun, Q., Shan, Q., Zhong, X., Han, R., eds. (2023). *Applications of date-driven artificial intelligence in integrated energy systems*. Lausanne: Frontiers Media SA. doi: 10.3389/978-2-83251-025-4

Table of contents

frontiers | Frontiers in Energy Research

ORIGINAL RESEARCH
published: 06 June 2022
doi: 10.3389/fenrg.2022.915023

An IPAVSG Control Strategy for Microgrid With Multi-Parallel VSG System

Xinqing Song[1], **Fanglin Zhu**[1], **Xingchen Cao**[1]*, **Jiawei Liu**[1], **Rui Wang**[1], **Yi Zhang**[2] and **Yao Liu**[3]

[1]College of Information Science and Engineering, Northeastern University, Shenyang, China, [2]State Key Laboratory of Alternate Electrical Power System with Renewable Energy Sources, North China Electric Power University, Beijing, China, [3]Computer Science and Engineering, University of New South Wales, Sydney, NSW, Australia

Virtual synchronous generator (VSG) is widely used in various distributed power generation systems due to great simulated inertia and damping support performance. However, when the microgrid (MG) composed of multi-parallel VSG is in both grid-connected and islanded modes with various large disturbances, the control strategy with fixed parameters cannot guarantee the stable operation of the MG under all disturbances. To this end, an improved parameter-adaptive virtual synchronous generator (IPAVSG) control strategy is proposed in this paper to ensure that the virtual inertia and damping are adaptively optimized with the system operating state during the disturbance process. Therefore, the dynamic performance of the power frequency regulation and transient stability are significantly improved. Meanwhile, in order to realize the output active power of each VSG is distributed among the loads according to the ratio of its rated capacity, the active power decoupling control is designed to eliminate the influence of the virtual damping on the output active power of the VSG in islanded MG. The effectiveness and practicability of the proposed control strategy are verified through several experiments.

Keywords: virtual synchronous generator, simulated inertia and damping, large disturbances, rated capacity, active power decoupling control

OPEN ACCESS

Edited by:
Qihe Shan,
Dalian Maritime University, China

Reviewed by:
Zhiqiang Tian,
Xi'an Jiaotong University, China
Chao Huang,
Hong Kong Polytechnic University, Hong Kong SAR, China

***Correspondence:**
Xingchen Cao
cao13623481290@163.com

Specialty section:
This article was submitted to Smart Grids, a section of the journal Frontiers in Energy Research

Received: *07 April 2022*
Accepted: *03 May 2022*
Published: *06 June 2022*

Citation:
Song X, Zhu F, Cao X, Liu J, Wang R, Zhang Y and Liu Y (2022) An IPAVSG Control Strategy for Microgrid With Multi-Parallel VSG System. Front. Energy Res. 10:915023. doi: 10.3389/fenrg.2022.915023

1 INTRODUCTION

In recent years, distributed generation (DG) devices with clean energy such as solar energy and wind energy are widely used in many fields of production and life. The microgrid, which is composed of various distributed generation units with power converter, can be integrated into the power grid or operated in islanded mode (Liserre et al., 2010; Mojica-Nava et al., 2014; Zhao et al., 2016; Meng et al., 2019). Because of the rapid penetration of distributed generation units in power systems, a variety of serious challenges such as poor transient response performance, insufficient inertia and damping have emerged (Weng S. et al., 2019; Tian and Peng, 2020). In order to effectively solve these problems, many reasonable control strategies by Ma et al. (2021c), Hu et al. (2021a) and Wang et al. (2021) have been introduced into interface power converters of DG units.

The droop control is a classical control strategy for distributed generation units. Through simulating the static droop characteristics of synchronous generator, the control of voltage and frequency of the MG system are realized. The DG with droop control can maintain the load voltage and frequency stability according to the droop curve. In addition, power can be reasonably distributed among parallel DG units according to their respective droop curves without external communication (Li et al., 2021). However, the droop control strategy cannot provide inertia and damping similar to synchronous generator (SG) to inverter-interfaced distributed generation (IIDG) units (Li, 2019). Thus, when a large disturbance occurs, if additional power cannot be provided in time to balance the disturbance, the stability of the MG with the droop control strategy is extremely poor (Fang et al., 2019). Although the low-pass filter droop control strategy with equivalent virtual inertia is introduced by Eskandari et al. (2019). the adjustment range of the parameters is small, and the performance of dynamic adjustment needs to be further improved.

Compared with the droop control, the virtual synchronous generator (VSG) control strategy effectively solves the lack of inertia and damping in the MG (Liu et al., 2014; D'Arco and Suul, 2014; Ma et al., 2021a). The basic principle of VSG is to introduce an equivalent rotation equation to emulate the inertia and damping characteristics of synchronous generator (SG). And the concept of VSG is originally proposed by Beck and Hesse (2007) and Driesen and Visscher (2008). Then, the equivalent mathematical model and specific implementation method of VSG based on three-phase inverter are preliminarily studied by Zhong and Weiss (2011) and Zhong et al. (2014). Afterwards, the VSG control is applied in the control of voltage, frequency, power flow and so on (Yang et al., 2011). With further in-depth research, VSG control strategy or improved control strategy based on it are used in various types of equipment or occasions such as energy storage (Rene et al., 2009; Kong et al., 2019), doubly-fed induction generators (Hwang et al., 2017), high voltage direct current transmission (Aouini et al., 2016) and direct current MG (Wu et al., 2017).

VSG can effectively simulate the inertia and damping performance of SG well. Thus, when MG fluctuates violently, the system can alleviate the fluctuation of active power and frequency of DG units. Improving the dynamic characteristics of the MG by designing appropriate virtual inertia and damping coefficients has been demonstrated by Zhong et al. (2014) and Yang et al. (2011). At present, the research on parameter selection based on VSG control is mainly divided into two categories: one is the fixed virtual inertia and damping value represented by Kerdphol et al. (2018), Fang et al. (2018) and Soni et al. (2013), while the (Simpson-Porco et al., 2013; Hou et al., 2016; Meng et al., 2016; Li et al., 2017; Alipoor et al., 2018; Andalib et al., 2018; Wang et al., 2018) focus on the study of adaptive parameters. Obviously, compared with fixed parameter control, adaptive parameter control has a wider adjustment range, which can better cope with various disturbances in the MG. In the parameter adaptive control strategy mentioned above, the damping coefficient is not considered or fixed at zero by Andalib et al. (2018) Hou et al. (2016), Alipoor et al. (2018) and Simpson-Porco et al. (2013). Therefore, the areas and scenarios are easily limited. Theoretical analysis of virtual inertia and damping coefficients is not mentioned by Li et al. (2017), and the realization of the control process is complicated. The design principles of virtual inertia and damping are given by Wang et al. (2018). Therein, the two key parameters change in opposite directions. However, the parameter extremums and optimal damping ratios that satisfy the stability of the system are not explained in any way. A control strategy called Bang-Bang is proposed by Meng et al. (2016). This strategy systematically analyzes the specific effects of virtual inertia and damping on power frequency, and designs the principle of parameter value accordingly. Unfortunately, the Bang-Bang control contains only two virtual inertia values, and the performance of the controller cannot be greatly improved. It is noteworthy that the vast majority of adaptive VSG strategies consider MG in grid-connected mode. However, the MG also needs to operate in islanded mode. In islanded mode, MG is impossible to establish an electrical connection with the power grid. So, the energy supply of the load and the voltage amplitude and frequency adjustment are independently completed by each DG unit (Lin et al., 2017). Once a disturbance occurs, the MG needs better inertia and damping support. Therefore, in order to effectively suppress the power-frequency oscillation of the perturbation process, the parameter-adaptive VSG control strategy needs to be considered for application to the islanded MG. In addition, another core control requirement is that the DG units connected in parallel should distribute the output active power proportionally according to their rated capacity (Huang et al., 2019; Jiang et al., 2020). Therefore, it is necessary to introduce both adaptive VSG and power equalization control in the islanded MG.

In summary, this paper proposes an improved parameter-adaptive VSG control strategy for MG that is suitable for grid-connected and islanded mode. In addition, power decoupling control strategy used in islanded MG is also taken into account. The outstanding features of the IPAVSG control strategy can be summarized as follows.

1) The IPAVSG control strategy proposed in this paper is suitable for grid-connected and islanded MG. In the two modes, the virtual inertia and damping can be optimally selected according to changes in the state of the MG transient adjustment process to improve the power frequency adjustment performance of the system. Especially at the initial moment of disturbance, the virtual inertia and damping quickly respond to larger values to suppress oscillation and fluctuation.
2) An active power proportional distribution control strategy is introduced into the islanded MG to eliminate the influence of damping on the output power of the DG units at steady state. Therefore, the output active power of each DG unit is proportional to its rated capacity.

The structure of this article is arranged as follows. Section The Basic Principle and Mathematical Model of VSG introduces the mathematical model and power controller of the VSG. Section The Transient Response Analysis of Parameter Perturbation analyzes the specific effects of virtual inertia and damping on the power and frequency transient adjustment process. Section The IPAVSG Control Strategy for MPVS presents the virtual inertia adaptive expression and power sharing control block diagram of two parallel VSGs suitable for both grid-connected and islanded mode. Section The Experimental Results analyzes the experimental results and proves the superiority and feasibility of the control strategy proposed in this paper. Section The Conclusion summarizes the advantages and feasibility of the control strategy proposed in this paper.

2 BASIC PRINCIPLE AND MATHEMATICAL MODEL OF VSG

To facilitate the interpretation, the IIDG unit controlled by VSG strategy is referred to as a VSG in this paper. A classic control topology of VSG is shown in **Figure 1**. It is composed of an inverter triggered by PWM generator and an LC filter set to reduce the current and voltage ripple. Utilizing the current and voltage measurement signals from VSG terminals, the power calculation and frequency measurement could be expediently realized. In order to better investigate the control strategy of the inverter, the dynamic characteristics of DG and energy storages are omitted in this paper. Moreover, the state-of-charge of energy storages is supposed to well satisfy the system requirements. In order to better investigate the control strategy of the inverter, the dynamic characteristics of DG and energy storages are omitted in this paper. Hence, the IIDG containing energy storages can be substituted for a DC voltage source (Simpson-Porco et al., 2013). Moreover, the state-of-charge of energy storages is supposed to well satisfy the system requirements.

As shown in **Figure 1**, the core of VSG can be separated into two parts: the active power control module and the reactive power control module. The active power control module is composed of the equivalent governor and mechanical model. The former simulates the prime mover of SG with the feature of primary frequency modulation whereas the latter takes charge of imitating mechanical rotor motion, which is considered as the most essential part of VSG. The reactive power control module is responsible for reactive power regulation. In operation, the active power control module export phase angle and the reactive power control module produce voltage magnitude respectively, then the generated reference sine waves are conveyed to the PWM generator to emit trigger signals. The details of these two parts are shown in **Figures 2**, **3**. The control system depicted in **Figure 2** is suitable for both the grid-connected mode and islanded mode. Because the active power control module of the VSG should include the swing equation and the equivalent governor in both modes. The reactive power control module in **Figure 3** includes voltage regulator and integrator, which can obtain the amplitude of reference voltage. The total mathematical model can be concluded as

$$\begin{cases} P_m - P_e - D\omega_n\left(\omega - \omega_n\right) = J\omega_n \dfrac{d\omega}{dt} \\ Q_{ref} - K_p\left(U - U_n\right) - Q_e = K\dfrac{dU}{dt} \\ \delta = \int\left(\omega - \omega_p\right)dt \end{cases} \tag{1}$$

where P_m, P_e, Q_{ref}, Q_e are the virtual mechanical power, actual output active power, the reactive power reference and actual output reactive power, respectively. J and D represent the virtual inertia and the damping coefficient, respectively. U and U_n represent the voltage of the VSG and the reference voltage, and δ is the phase angle of the voltage. In actual control, the output power angle δ should be connected to the power angle balance compensator, which is shown in **Figure 4**, where $\overline{\delta}_i$, δ_i, δ_i^* respectively represent the average output power angle of all VSGs in the system, the actual power angle of the ith VSG, and the power angle of the ith VSG after compensation. This method has been proposed well by Jiang et al. (2020) and Ma et al. (2021b). ω and ω_n indicate the virtual angular frequency and the reference angular frequency, respectively, and $\Delta\omega = (\omega - \omega_n)$

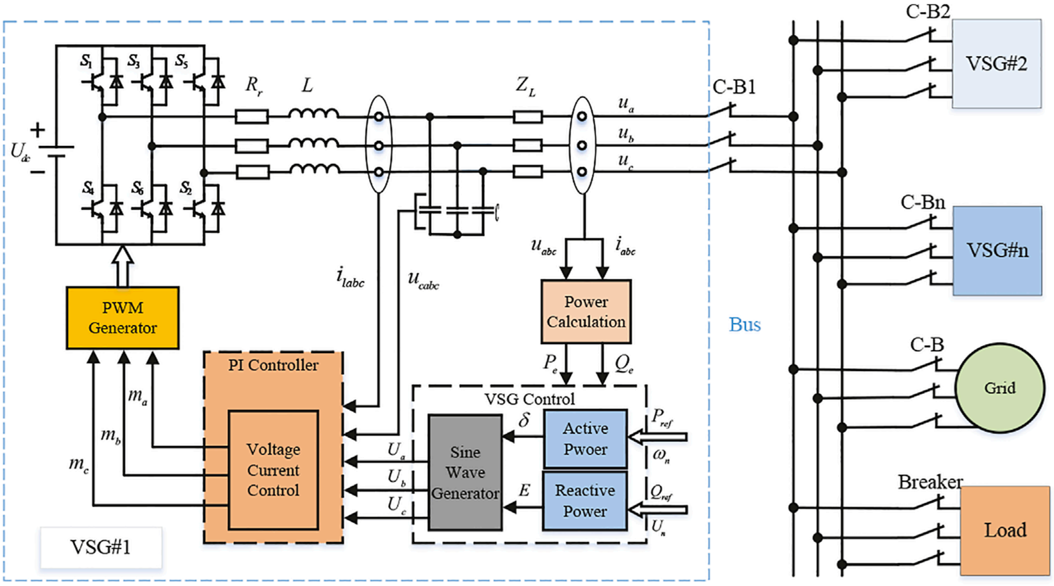

FIGURE 1 | Classic topology and control block of MPVS.

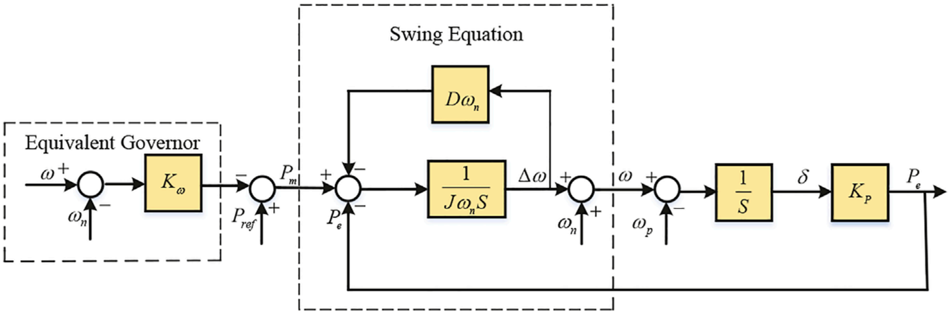

FIGURE 2 | Control modules of active power control module.

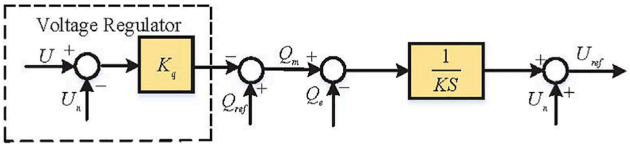

FIGURE 3 | Control modules of reactive power control module.

is the frequency deviation. In both grid-connected state and islanded state, ω_p represents the reference angular frequency of the PCC, and it is directly collected by the phase-locked loop. Under this operation, the smooth switching between islanded mode and connected-grid mode can be achieved (Wang et al., 2019). In order to avoid the complex iterative computation of **Eq. (1)**, the controller is designed in the frequency domain.

Observations obtained from **Figure 2** depict that P_m is composed of the active power reference P_{ref} and the output power regulated by the equivalent governor according to the frequency deviation. It could be expressed as

$$P_m = P_{ref} - K_\omega\left(\omega - \omega_n\right) \tag{2}$$

Then, the whole process of the active power control module is calculated as

$$P_{ref} - K_\omega\left(\omega - \omega_n\right) - P_e - D\omega_n\Delta\omega = J\omega_n\frac{d\omega}{dt} \tag{3}$$

where K_ω is the droop coefficient of the equivalent governor.

Eqs. (1)–(3) indicate that the VSG control strategy plays a significant role in imitating the operating characteristics of SG through introducing the rotor motion equation.

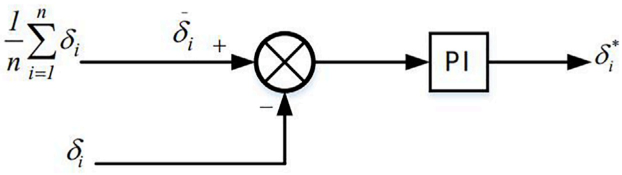

FIGURE 4 | Block diagram of power angle balance compensator.

3 TRANSIENT RESPONSE ANALYSIS OF PARAMETER PERTURBATION

Theoretically, VSG can be operated alone or in parallel. This paper aims to investigate the impact of some key parameters (virtual inertia and damping coefficient) on the frequency and active power outputs of the MG with multiple VSGs connected in parallel, and we called this system as the multi-parallel VSG system (MPVS). The structure of MPVS is depicted in **Figure 1**, where the VSGs are attached to a point of common coupling (PCC) through a distribution line, then the PCC is connected to the utility grid via circuit breaker (CB). Notice that the capacitor of the output LC filter can be neglected in consequence of the susceptance is inappreciable around the fundamental frequency. Thus, the VSG can be substituted with an ideal DC voltage source with a series output impedance.

For the purpose of deeper analyzing the output characteristics of the MPVS, networked power system, a universally applicable model, is selected for instance. **Figure 5** depicts the equivalent model of networked power system, which contains multi-paralleled virtual synchronous generators. To simplify the model, the reactive power output is not considered in this system and these simplifications have no impact on the precision of the model (Zhong et al., 2014).

According to **Eq. (1)** and **(3)**, the mathematical model of VSGi can be expressed as

$$\begin{cases} P_{refi} - K_{\omega i}\left(\omega_i - \omega_n\right) - P_{ei} - D_i\omega_n\left(\omega_i - \omega_n\right) = J_i\omega_n\dfrac{d\omega_i}{dt} \\ \delta_i = \int\left(\omega_i - \omega_p\right)dt \end{cases} \tag{4}$$

where P_{ei} means the active power of VSGi flowing into PCC. The relationship between the P_{ei} and the variables at PCC can be expressed as

$$P_{ei} = \frac{3E_iU_p}{Z_i}\sin\delta_i = K_{pi}\sin\delta_i \tag{5}$$

where $K_{pi} = 3E_iU_p/Z_i$, E_i and U_p represent the output voltages of the VSG i and the PCC separately. P_{e_i} denotes the output active power. Z_i represents the equivalent line impedance and the output impedance. $\sin\delta_i$ represents power angle. Z_L is the load impedance.

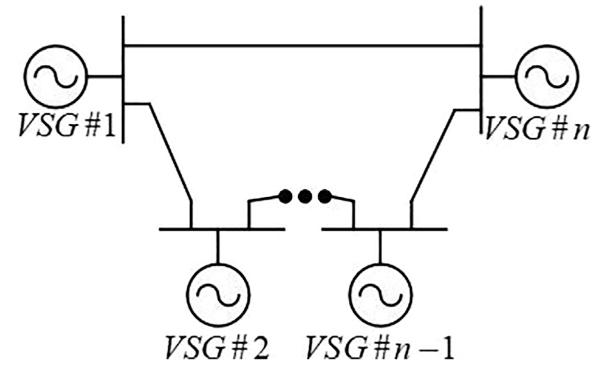

FIGURE 5 | Equivalent circuit model of networked power system.

The small signal model of the two-parallel VSG system is derived as follows. Let

$$\begin{cases} \omega_i = \omega_s + \Delta\omega_i \\ \omega_p = \omega_{ps} + \Delta\omega_p \\ \delta_i = \delta_{is} + \Delta\delta_i \\ P_{ei} = P_{eis} + \Delta P_{ei} \end{cases} \tag{6}$$

Notice that the state variables in **Eq. (6)** are equivalent to the value of steady state plus a perturbation value. Since $\Delta\delta_i$ is very small, the following equations $\sin(\Delta\delta_i) \approx \Delta\delta_i$ and $\cos(\Delta\delta_i) \approx 1$ are satisfied. Furthermore, the second-order perturbation terms could be omitted due to the frequency deviation is comparatively small. Therefore, the small signal model of **Figure 2** can be obtained as **Figure 6**. Then the closed loop transfer function from ΔP_{refi} to ΔP_{ei} is obtained as

$$\frac{\Delta P_{ei}}{\Delta P_{refi}} = \frac{E_i U_p}{J_i \omega_n Z_i s^2 + D_{pi} Z_i s + E_i U_p} \tag{7}$$

where $D_{pi} = K_{\omega i} + D_i \omega_n$.

In line with **Eq. (7)**, the peak time t_{p-p}, settling time t_{s-p} and overshoot M_{p-p} of the step response of the active power can be expressed as follows:

$$t_{p-p} = \frac{2\pi J_i \omega_n Z_i}{\sqrt{4 J_i \omega_n Z_i E_i U_p - D_{pi}^2 Z_i^2}} \tag{8}$$

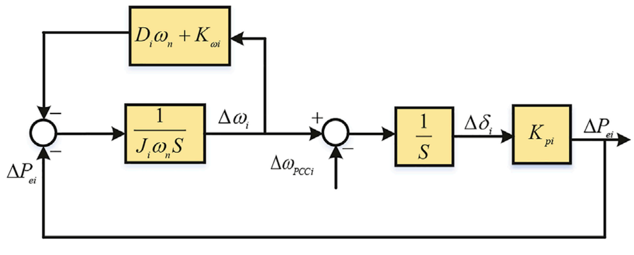

FIGURE 6 | Small signal model of active power control module.

$$M_{p-p} = e^{-\pi \sqrt{\frac{D_{pi}^2 Z_i^2}{4 J_i \omega_n Z_i E_i U_p - D_{pi}^2 Z_i^2}}} \tag{9}$$

$$t_{s-p} = \frac{D_{pi}}{2} \sqrt{\frac{Z_i}{J_i \omega_n E_i U_p}} \tag{10}$$

The closed loop transfer function from ΔP_{refi} to $\Delta\omega_i$ can be obtained as

$$\frac{\Delta\omega_i}{\Delta P_{refi}} = \frac{Z_i s}{J_i \omega_n Z_i s^2 + D_{pi} Z_i s + E_i U_p} \tag{11}$$

According to **Eq. (11)**, the influences on the step response of frequency caused by D_{pi} can be indicated as.

$$t_{p-\omega} = \frac{\arctan \sqrt{\frac{4 J_i \omega_n E_i U_p - D_{pi}^2 Z_i}{D_{pi}^2 Z_i}}}{\sqrt{\frac{E_i U_p}{J_i \omega_n Z_i} - \frac{D_{pi}^2}{4 J_i^2 \omega_n^2}}} \tag{12}$$

$$M_{p-\omega} = \sqrt{\frac{4 E_i U_p}{J_i \omega_n Z_i}} e^{-\sqrt{\frac{D_{pi}^2 Z_i}{4 J_i \omega_n E_i U_p - D_{pi}^2 Z_i}} \arctan \sqrt{\frac{4 J_i \omega_n E_i U_p - D_{pi}^2 Z_i}{D_{pi}^2 Z_i}}} \tag{13}$$

$$t_{s-w} = \frac{8 J_i w_n}{D_{pi}} \tag{14}$$

In line with **Eq. (7)** and **(11)**, the poles, the natural oscillation angular frequency and damping ratio of the characteristic equation can be calculated as

$$s_{1,2} = \frac{-D_{pi} Z_i \pm \sqrt{D_{pi}^2 Z_i^2 - 4 J_i \omega_n Z_i E_i U_p}}{2 J_i \omega_n Z_i} \tag{15}$$

$$\begin{cases} \omega_{ni} = \sqrt{\frac{K_{pi}}{J_i \omega_n}} \\ \zeta_{ni} = \frac{D_{pi}}{2} \sqrt{\frac{1}{J_i \omega_n K_{pi}}} \end{cases} \tag{16}$$

Eqs. (7)–(16) clearly shows that the natural oscillation angular frequency and damping ratio are determined by virtual inertia and damping coefficient. The typical indexes for the dynamic response the peak time (t_p), overshoot (M_s) and settling time (t_s) are directly associated with natural oscillation angular frequency and damping ratio, so that the dynamic responses of frequency and active power of VSG have relation to J_i and D_{pi}. The specific reflect is summarized in **Table 1**. Furthermore, the transit stability is affected by the two parameters as well since the poles would be to close to the imaginary axis to arouse oscillations. In other words, when the disturbances occur, not only deteriorated

TABLE 1 | Influence of parameter perturbation on dynamic responses.

Indexes	Frequency		Active power	
	J_i⇑	D_{pi}⇑	J_i⇑	D_{pi}⇑
t_{pi}	⇑	⇓	⇑	⇑
t_{si}	⇑	⇓	⇑	⇓
M_{si}	⇓	⇓	⇑	⇓

dynamic responses with long settling time, large overshoot and short peak time, but unstable oscillations will be caused if J_i and D_{pi} are chosen improperly. Therefore, it is of great significance to select appropriate J_i and D_{pi} to get better dynamic responses and improved transit stability of the MPVS.

Additionally, **Eq. (7)** also indicates that the active power outputs of VSG*i* during the steady state are bound up with $D_i\omega_n + K_{\omega i}$ when the MG is operated in islanded mode. In other words, the coupled effect between the primary frequency modulation and the damping characteristic results in the coupled effect of $K_{\omega i}$ and D_i on the active power output during steady operation. Whether active power can be shared proportionally by each VSG depends on whether the value of $D_i\omega_n + K_{\omega i}$ is proportional to its rated capacity. Power sharing error is prone to emerge once the parameters are chosen improperly. Consequently, it is essential to take measures to achieve proportional power sharing during steady state.

4 THE IPAVSG CONTROL STRATEGY FOR MPVS

In this section, a IPAVSG control strategy appropriate for both grid-connected and islanded MG is proposed, with which the ameliorative dynamic responses of the MPVS can be achieved through adaptively adjusting the virtual inertia and damping coefficient. Furthermore, proportional power sharing during steady operation in islanded mode is accomplished based on decoupling the coupled effect between the damping coefficient and equivalent governor droop coefficient on active power outputs.

4.1 Parameter-Adaptive VSG Control Strategy

In view of above analysis, if the virtual inertia and damping coefficient are selected improperly, deteriorated oscillations with long settling time and large overshoot will be aroused. Therefore, an adaptive virtual inertia and damping control strategy is designed to adaptively adjust inertia and damping to ameliorate the dynamic responses. This strategy is suitable for both grid-connected and islanded MG.

From **Table 1**, the influences of virtual inertia and damping coefficient on frequency and active power dynamic responses are roughly similar when it changes dynamically, so the dynamic responses of the active power will also be improved if those of frequency is modified. With respect to virtual inertia, in the case of large disturbances and sudden changes, within a limited value range, the smaller the virtual inertia is, the shorter the settling time becomes. In contrast, the larger the virtual inertia is, the smaller the overshoot and the longer the peak time stay, which means the firmer system holds. In order to combine these advantages, the virtual inertia should show a large value when the frequency deviates and a small one when frequency recovers (Andalib et al., 2018). Moreover, **Eq. (16)** shows that the damping coefficient changes accordantly with the virtual inertia.

For quantitative selection of virtual inertia, the step responses of the output frequency are plotted, and shown as **Figure 7**.

The two dashed lines represent the step responses of the output frequencies with two fixed rotational inertias *J*. Furthermore, as indicated by the expected curve (the solid one) in the picture above, if a big *J* is selected in the rising area and a small *J* is given in the descending area, the response time of the output frequency is decreased and the overshoot is also reduced. According to the same analysis method, the rules of the selection of virtual inertia and damping coefficient during transient process can be summarized as **Table 2**.

Notice that the large or small virtual inertia value mentioned here is relative to the steady-state virtual inertia. Besides, considering the stability of the system, the upper and lower limits ($J_{i\max}$ and $J_{i\min}$) of the virtual inertia need to be taken into consideration, because low frequency oscillations of active power may be caused if inertia exceeds the limits. Based on the aforementioned analysis, the arc-tangent function is employed for adaptive calculation of virtual inertia. The adaptive control strategy with adjustable virtual inertia is designed as follows

$$J_i = \begin{cases} J_{i0} + \dfrac{J_{i\max} - J_{i0}}{\pi/2}\arctan\left(\dfrac{\Delta\omega_i}{2M_i} \times sign\left(\dfrac{d\omega_i}{dt}\right)\right), \\ \qquad |\Delta\omega_i| > M_i \cap \Delta\omega_i \times sign\left(\dfrac{d\omega_i}{dt}\right) > 0 \\ J_{i0} + \dfrac{J_{i0} - J_{i\min}}{\pi/2}\arctan\left(\dfrac{\Delta\omega_i}{2M_i} \times sign\left(\dfrac{d\omega_i}{dt}\right)\right), \\ \qquad |\Delta\omega_i| > M_i \cap \Delta\omega_i \times sign\left(\dfrac{d\omega_i}{dt}\right) \le 0 \\ J_{i0}, \quad |\Delta\omega_i| \le M_i \end{cases} \tag{17}$$

where J_{i0} is the steady-state virtual inertia, which is associated with the rated capacity. M_i is the frequency deviation threshold set to avoid the chattering of J_i during steady state. In theory,

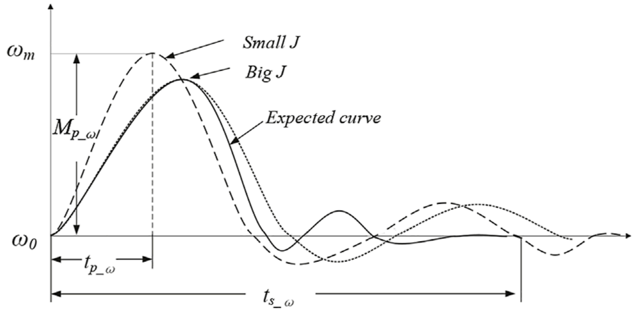

FIGURE 7 | Step response of frequency when *J* changes.

TABLE 2 | Rules of J_i and D_{pi}.

Parameters	J_i	D_{pi}
$\Delta\omega_i \times sign(d\omega_i/dt) > 0$	large	large
$\Delta\omega_i \times sign(d\omega_i/dt) \le 0$	small	small

there should also be a threshold M_{di} set for $d\omega_i/dt$, and the adaptive control for J_i will be triggered only if both $|\Delta\omega_i| > M_i$ and $d\omega_i/dt > M_{di}$ are satisfied. However, whether the frequency keeps stable or not is mainly determined by $\Delta\omega_i$ while the sign of $d\omega_i/dt$ only represents the trend of frequency changing, and the value of $\Delta\omega_i$ is normally smaller than $d\omega_i/dt$ especially at the initial stage when disturbances occur. Therefore, to facilitate analysis, only the threshold for $\Delta\omega_i$ is set in this paper. In actual situations, the change of $\Delta\omega_i$ may be small, $\Delta\omega_i/2M_i$ is introduced in this paper to amplify the frequency fluctuation value. With the proper threshold setting, the system can effectively filter out small disturbances while keeping sensitive to large disturbances. If the trigger condition $|\Delta\omega_i| > M_i$ is satisfied, the virtual inertia will be adaptively changed.

The curve of the virtual inertia is depicted in **Figure 8**. The right half part represents the period of frequency deviating whereas the left means the period of frequency recovering. As can be seen in **Figure 8**, different from the bang-bang control, the adaptive control strategy designed here contributes to a continuous and broader range of virtual inertia. When the frequency deviates with the feature of $\Delta\omega_i \times sign(d\omega_i/dt) > 0$, the larger $\Delta\omega_i$ is, the larger virtual inertia correspondingly becomes, which helps to suppress the overshoot and delay the peak time of the frequency oscillation. In reverse, smaller virtual inertia is conducive to shorten the settling time and accelerate the response speed when frequency recovers. In the whole process, the application of the arc-tangent function enables the virtual inertia to be more sensitive to frequency deviation, even for the initial small $\Delta\omega_i$, the J_i obtained from **Eq. (17)** is capable to be comparatively large to suppress the oscillation effectively at the initial stage of disturbances. With the further increase of the $\Delta\omega_i$, the J_i transits to the limits smoothly without beyond it, which is favorable for ensuring the system transient stability.

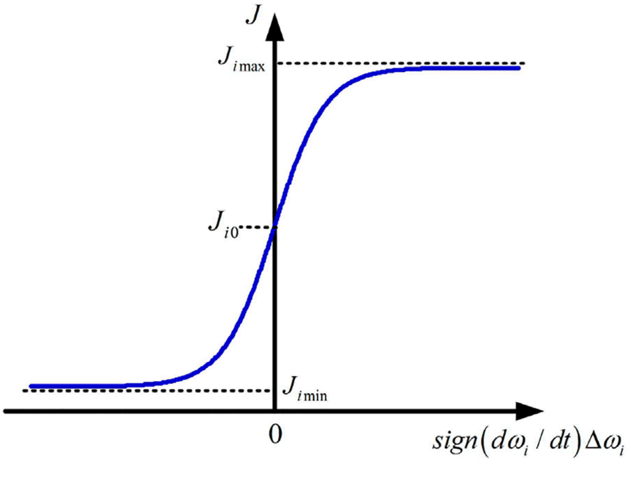

FIGURE 8 | Changing curve of virtual inertia.

In terms of the damping coefficient, according to **Table 1**, the adjustment of D_i influences frequency and active power dynamic responses in a similar tendency (Hu et al., 2021b). The adaptive control strategy of D_i is designed as

$$\zeta_{ni} = \frac{D_i\omega_n + K_{\omega i}}{2}\sqrt{\frac{1}{J_i\omega_n K_{pi}}} = \text{constant} \tag{18}$$

Equation (18) means that during the transit process, the J_i and D_i are adaptively adjusted in a similar tendency and at the same time with a constant damping ratio. The upper or lower limits of virtual inertia and damping coefficient are obtained when the damping ratio is 0.7 or 1. In practice, the optimal damping ratio ($\zeta_{ni} = 0.707$) is usually adopted for the best situation of the system. Hence, the damping ratio is kept at 0.707 in this paper to better ameliorate the dynamic responses and improve transient stability.

4.2 Active Power Proportional Distribution Control Strategy

In accordance with the above analysis, the active power outputs P_{ei} are associated with the coupled effect of primary frequency ω_p modulation and the damping characteristic in steady-state of islanded MG with MPVS. In general, the governor droop coefficient is set as $K_{\omega i} = S_{ratei}/(0.1\%\omega_n)$, S_{ratei} represents the rated capacity of the ith virtual synchronous generator (Zhang et al., 2017), and the value of D_i is supposed to prioritize the requirements of the best dynamic response. As can be seen in **Figure 9**, to fulfill these requirements, an active power proportional distribution control strategy is proposed to decouple the interaction between the equivalent governor droop coefficient and the damping coefficient in the conventional VSG control and eliminate the effect of D_i on the active power output during steady operation in islanded MG.

When the system is running in an islanded state and remains stable, the output angular frequency of the inverter ω no longer changes. According to equation **Eq. 3** and **Figure 9**, the active power output by VSGi and VSGj is shared in proportion to formula **Eq. (19)**.

$$\frac{P_{ei}}{P_{ej}} = \frac{P_{refi} - K_{\omega i}(\omega_i - \omega_n)}{P_{refj} - K_{\omega j}(\omega_j - \omega_n)} = C \tag{19}$$

Therefore, whether the line impedance is resistive, inductive or capacitive, the active power ratio sharing is determined by P_{ref}, K_ω and $(\omega - \omega_n)$.

Compared to the conventional VSG control strategy, the principal modification is the introduction of a first-order lead-lag unit in the damping feedback loops. Then, the closed loop transfer function of ΔP_{ei} is obtained as follows

$$\frac{\Delta P_{ei}}{\Delta\omega_p} = \frac{K_{pi} \times [J_i\omega_n T_{ci}s^2 + (J_i\omega_n + D_iT_{ci} + K_{\omega i}T_{ci})s + K_{\omega i}]}{J_i\omega_n T_{ci}s^3 + (J_i\omega_n + D_iT_{ci} + K_{\omega i}T_{ci})s^2 + (K_{\omega i} + K_{pi}T_{ci})s + K_{pi}} \tag{20}$$

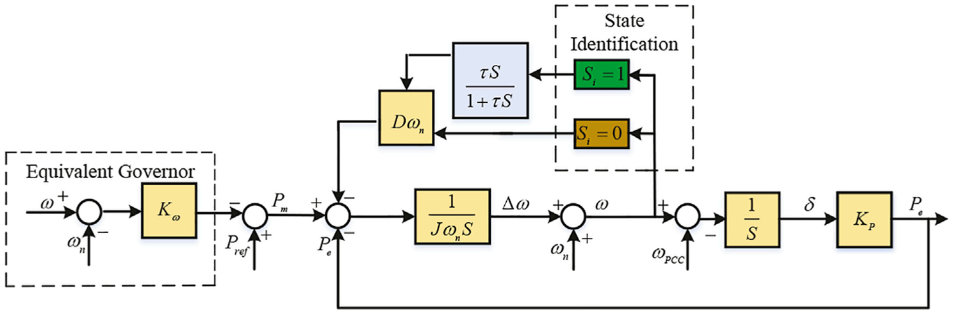

FIGURE 9 | Active power proportional distribution control strategy.

Equation (20) illustrates that the active power output is only up bounded by $K_{\omega i}$ and the effect of D_i has been eliminated during steady state. The specific implementation process of the whole control strategy is as follows.

$$S_i = \begin{cases} 1, |\Delta\omega_i| \le M_i \\ 0, |\Delta\omega_i| > M_i \end{cases} \tag{21}$$

During steady operation, the switching state value S_i remains at one and the branch included the first-order lead-lag unit is chosen to decouple the effect of D_i on active power output. Subsequent to disturbances, S_i changes to 0 so that the adaptive control of J_i and D_i will be activated. Consequently, the proportional power sharing of the MPVS during steady operation can be ensured while the dynamic responses of the system in transient process is ameliorated.

5 EXPERIMENT RESULTS

In this section, verifications of the IPAVSG control strategy are conducted through experiment results. As can be seen from **Figure 10**, the experimental platform contains two IIDG units operated in parallel. The corresponding experimental parameters are shown in **Table 3**. The parallel hard-switched PWM converters are digitally controlled by TMS28335 fixed-point DSP to implement the power and voltage control algorithm where switching frequency is 20 kHz. In practice, in order to save resource, a discrete table is created in advance. The value of arctan(x) can be directly taken from the table.

Firstly, an experiment is executed in grid-connected MG to verify the IPAVSG control strategy. The performances of the controllers to follow the power reference and maintain frequency stability are evaluated during a sudden load variation. The

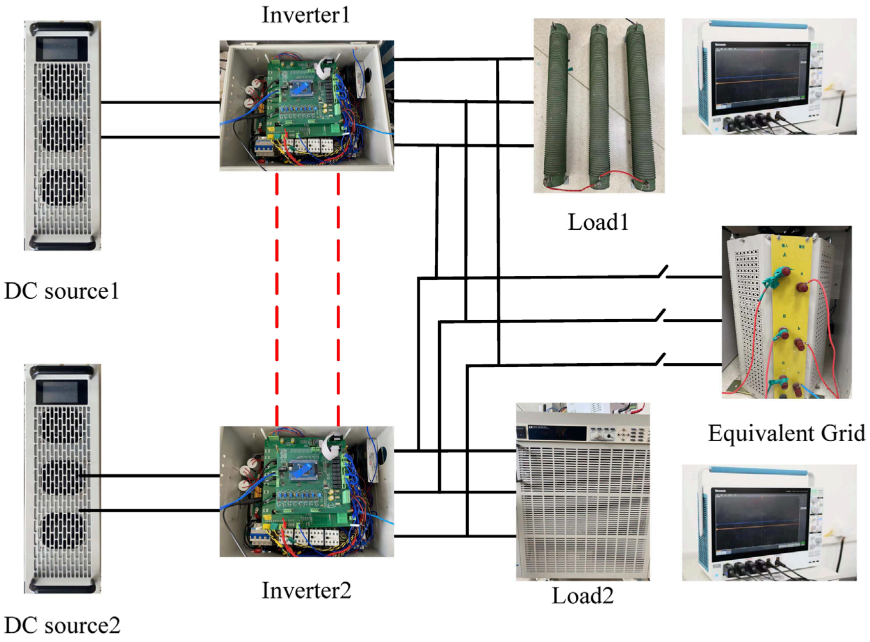

FIGURE 10 | Experimental testbed.

TABLE 3 | Parameters of the TEST system.

Parameters	Symbol	Values
Reference DC-bus voltage	U_{dc}	700V
Reference AC-bus voltage	U_n	380V
Reference frequency	f_n	50Hz
Reference or grid angular frequency	ω_n/ω_g	50Hz
Line impedance	R_L	0.032Ω
	X_L	0.0198Ω
LC filter	R_f	0.2Ω
	L_f	$3 \times 10^{-3}H$
	C_f	$15 \times 10^{-6}F$
Current controller	Proportional gain	0.1
Voltage controller	Proportional gain	280.8
	Integral gain	0.2
IPAVSG		
the rated inertia	J_0	3
maximum inertia	$J_{\max}$	8
minimum inertia	$J_{\min}$	0.3
the rated damping coefficient	D_0	25
maximum damping coefficient	$D_{\max}$	40
minimum damping coefficient	$D_{\min}$	8
droop coefficient	K_ω	1×10^4
Stator resistance	R_s	0.01Ω
Stator inductance	L_s	$3.56 \times 10^{-3}H$
Bang-Bang		
big inertia	J_{big}	5
small inertia	J_{small}	1
big damping	D_{big}	30
small damping	D_{small}	25
droop coefficient	K_ω	1×10^4
VSG		
inertia	J	3
damping	D	25
droop coefficient	K_ω	1×10^4

references of active and reactive power for each IIDG unit are assigned as 6 kW and 1 kVar. Then a 2 kW, 400 Var PCC load reduction happens at 6.4s.

The frequency and active power dynamic responses controlled by the conventional VSG and the Bang-Bang and the IPAVSG control strategies are displayed in **Figures 11, 12**. Similar to the previous statement, only the results of IIDG1 are displayed here because the parameters of the two IIDG units are identical. When the load decreases suddenly, the frequency deviations of the three control strategies are 0.027, 0.014 and 0.006 Hz, respectively. Besides, the active power overshoot of the three control strategies are 1120, 510 and 250 W, respectively. Obviously, the experiment results have verified that the frequency and active power deviations can be suppressed with the virtual inertia and the damping coefficient in three VSG control strategies, in which the suppression is more effective in the IPAVSG control strategy since the parameters can be adaptively adjusted.

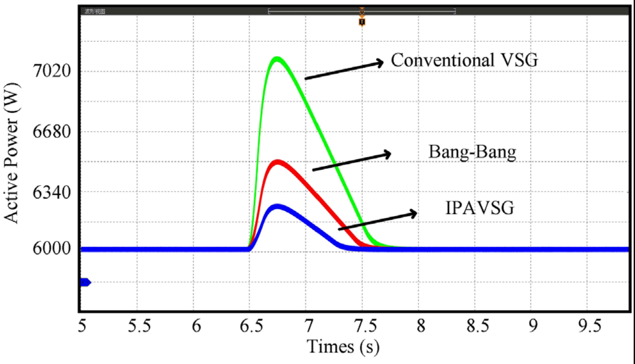

FIGURE 12 | Active power outputs of IIDG1.

Another experiment is executed in islanded MG. The rated capacities of the two IIDG units are 10kW and 5kW, respectively. The MG is operated steadily with PCC loads rated at 12 kW at frist. A 1.2 kW load step decrease happens at 0.5s, then reconnects to the MG at 1.3 s.

The IPAVSG control strategy in the islanded MG is supposed to not only realize the adaptive tuning of virtual inertia and damping coefficient, but also proportional active power sharing. The former experiment results have illustrated the buffer and suppression effect of virtual inertia and the damping coefficient,

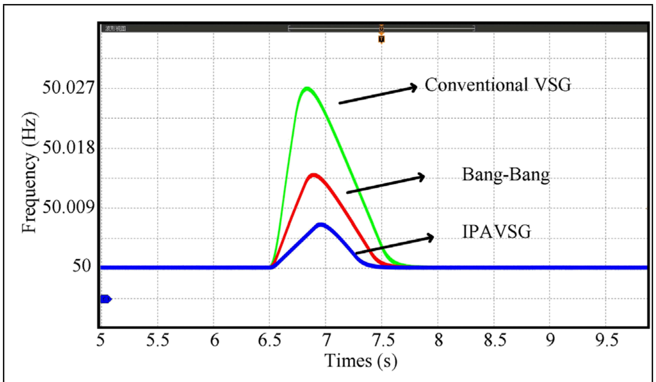

FIGURE 11 | Frequency outputs of IIDG1.

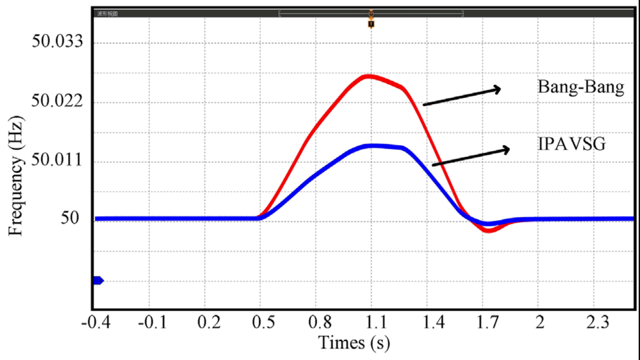

FIGURE 13 | Frequency outputs from IIDG1 and IIDG2.

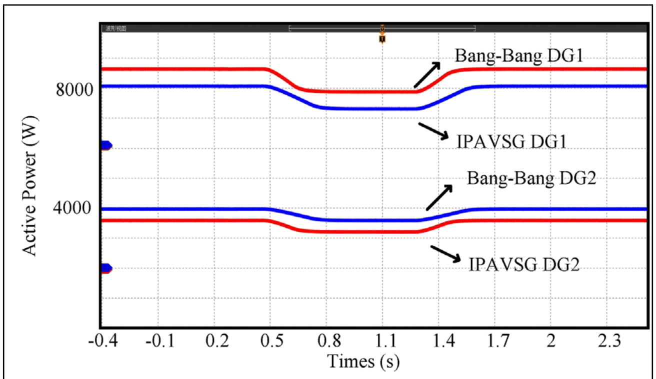

FIGURE 14 | Active power outputs from IIDG1 and IIDG2.

and the conventional VSG control strategy has less superiority than the Bang-Bang and IPAVSG control strategies in oscillation suppression. Hence, in this experiment, we focus on the performance comparison of Bang-Bang and IPAVSG control strategies.

The frequency and active power of the system are displayed in **Figures 13**, **14**. To get a clearer illustration, only the frequency responses of IIDG1 are displayed. **Figure 13** depictes that the frequency overshoot controlled by IPAVSG is 0.015 Hz, which is much smaller than 0.028 Hz of Bang-Bang control. And the frequency rising trendency controlled by IPAVSG is much slower than that of Bang-Bang. Therefore, the better performances in suppressing frequency dynamic response can be found in the IPAVSG control strategy. Furthermore, during steady operation, the loads connected to IIDG1 and IIDG2 of IPAVSG are 8000 and 4000 W, respectively. During load transition, the loads decrease by 800 W and 400 W, respectively. The active power decrease is even slower. By contract, the loads supported by IIDG1 and IIDG2 of Bang-Bang are 8400 and 3600 W during steady state, then the loads reduction are 840 W and 360 W after 0.5 s. Besides, the active power decrease is slight faster. These experiment results could validate that the IPAVSG control strategy containing adaptive virtual inertia and damping control and decoupling control in islanded MG, has effective impact on ameliorating frequency and active power dynamic responses and has decoupling effect of damping coefficient on power sharing, with which the outputs could transit to a new steady state smoothly and the loads can be shared proportionally no matter before or after the load transition.

6 CONCLUSION

An IPAVSG control strategy consists of adaptive virtual inertia and damping coefficient control along with decoupling control is proposed in this paper. The IPAVSG strategy can be adopted for MG with multiple IIDG units connected in parallel. The adaptive virtual inertia and damping control of IPAVSG has significantly ameliorated the dynamic responses of the MG in both grid-connected and islanded modes. Additionally, the active power outputs during steady state in islanded MG can be shared proportionally to rated capacities of IIDGs. The virtual inertia and damping coefficient of the IPAVSG control strategy can be adaptively adjusted based on the frequency responses, their proper selections are of great essentiality to the system dynamic resonances. In conclusion, the IPAVSG control strategy is of great benefit to the stability of the system.

Several experiment results in both grid-connected and islanded MG with different contingencies are conducted to validate the advantages and effectiveness of the IPAVSG control strategy. Comparisons between the conventional VSG control and Bang-Bang control are also provided in this paper, which facilitates a thorough acknowledge of these two promising control strategies for the utilization and development of renewable energy.

DATA AVAILABILITY STATEMENT

The original contributions presented in the study are included in the article/supplementary material, further inquiries can be directed to the corresponding author.

AUTHOR CONTRIBUTIONS

XS has done the main theory research work. FZ, XC, and JL conceived the project and wrote the manuscript. RW, YZ and YL designed and participated in the experiment. All authors discussed the results, read, and commented on the manuscript.

FUNDING

This study is supported by the State Key Laboratory of Alternate Electrical Power System with Renewable Energy Sources(Grant No.LAPS22002).

REFERENCES

Alipoor, J., Miura, Y., and Ise, T. (2018). Stability Assessment and Optimization Methods for Microgrid with Multiple VSG Units. *IEEE Trans. Smart Grid* 9 (2), 1462–1471. doi:10.1109/TSG.2016.2592508

Andalib-Bin-Karim, C., Liang, X., and Zhang, H. (2018). Fuzzy-Secondary-Controller-Based Virtual Synchronous Generator Control Scheme for Interfacing Inverters of Renewable Distributed Generation in Microgrids. *IEEE Trans. Ind. Appl.* 54 (2), 1047–1061. doi:10.1109/TIA.2017.2773432

Aouini, R., Marinescu, B., Ben Kilani, K., and Elleuch, M. (2016). Synchronverter-Based Emulation and Control of HVDC Transmission. *IEEE Trans. Power Syst.* 31 (1), 278–286. doi:10.1109/tpwrs.2015.2389822

Beck, H., and Hesse, R. (2007). "Virtual Synchronous Machine," in 2007 9th International Conference on Electrical Power Quality and Utilisation (Barcelona, Spain: IEEE), 1–6. doi:10.1109/epqu.2007.4424220

D'Arco, S., and Suul, J. A. (2014). Equivalence of Virtual Synchronous Machines and Frequency-Droops for Converter-Based MicroGrids. *IEEE Trans. Smart Grid* 5 (1), 394–395. doi:10.1109/tsg.2013.2288000

Driesen, J., and Visscher, K. (2008). "Virtual Synchronous Generators," in Proc. IEEE Power Energy Soc. Gen. Meeting-Conversion and Delivery of Electrical Energy in the 21st Century (IEEE), 1–3. doi:10.1109/pes.2008.4596800

Eskandari, M., Li, L., Moradi, M. H., Siano, P., and Blaabjerg, F. (2019). Active Power Sharing and Frequency Restoration in an Autonomous Networked Microgrid. *IEEE Trans. Power Syst.* 34 (6), 4706–4717. doi:10.1109/tpwrs.2019.2923797

Fang, J., Li, H., Tang, Y., and Blaabjerg, F. (2018). Distributed Power System Virtual Inertia Implemented by Grid-Connected Power Converters. *IEEE Trans. Power Electron.* 33 (10), 8488–8499. doi:10.1109/tpel.2017.2785218

Fang, J., Li, H., Tang, Y., and Blaabjerg, F. (2019). On the Inertia of Future More-Electronics Power Systems. *IEEE J. Emerg. Sel. Top. Power Electron.* 7 (4), 2130–2146. doi:10.1109/jestpe.2018.2877766

Hou, X., Zhong, C., Yuan, W., Yi, M., and Chen, Y. (2016). "Improvement of Transient Stability in Inverter-Based AC Microgrid via Adaptive Virtual Inertia," in 2016 IEEE Energy Conversion Congress and Exposition (IEEE), 1–6. doi:10.1109/ecce.2016.7855195

Hu, X., Zhang, H., Ma, D., and Wang, R. (2021a). "Hierarchical Pressure Data Recovery for Pipeline Network via Generative Adversarial Networks," in IEEE Transactions on Automation Science and Engineering (Early Access) (IEEE), 1–11. doi:10.1109/tase.2021.3069003

Hu, X., Zhang, H., Ma, D., Wang, R., and Tu, P. (2021b). "Small Leak Location for Intelligent Pipeline System via Action-dependent Heuristic Dynamic Programming," in IEEE Transactions on Industrial Electronics (Early Access) (IEEE), 1. doi:10.1109/tie.2021.3127016

Huang, B., Liu, L., Zhang, H., Li, y., and Sun, Q. (2019). Distributed Optimal Economic Dispatch for Microgrids Considering Communication Delays. *IEEE Trans. Syst. Man. Cybern. Syst.* 49 (8), 1634–1642. doi:10.1109/tsmc.2019.2900722

Hwang, M., Muljadi, E., Jang, G., and Kang, Y. C. (2017). Disturbance-Adaptive Short-Term Frequency Support of a DFIG Associated with the Variable Gain Based on the ROCOF and Rotor Speed. *IEEE Trans. Power Syst.* 32 (3), 1873–1881. doi:10.1109/tpwrs.2016.2592535

Jiang, W., Zhang, X., Guo, F., Chen, J., Wang, P., and Koh, L. H. (2020). Large-Signal Stability of Interleave Boost Converter System with Constant Power Load Using Sliding-Mode Control. *IEEE Trans. Ind. Electron.* 67 (11), 9450–9459. doi:10.1109/tie.2019.2955401

Kerdphol, T., Rahman, F. S., Mitani, Y., Watanabe, M., and Kufeoglu, S. (2018). Robust Virtual Inertia Control of an Islanded Microgrid Considering High Penetration of Renewable Energy. *IEEE Access* 6, 625–636. doi:10.1109/access.2017.2773486

Kong, X., Liu, X., Ma, L., and Lee, K. Y. (2019). Hierarchical Distributed Model Predictive Control of Standalone Wind/Solar/Battery Power System. *IEEE Trans. Syst. Man. Cybern. Syst.* 49 (8), 1570–1581. doi:10.1109/TSMC.2019.2897646

Li, D., Zhu, Q., Lin, S., and Bian, X. Y. (2017). A Self-Adaptive Inertia and Damping Combination Control of VSG to Support Frequency Stability. *IEEE Trans. Energy Convers.* 32 (1), 397–398. doi:10.1109/tec.2016.2623982

Li, X. (2019). Global Exponential Stability of Impulsive Delay Systems with Flexible Impulse Frequency. *IEEE Trans. Syst. Man. Cybern. Syst.* 49 (10), 2166–2174. doi:10.1109/tsmc.2017.2766260

Li, X., Xu, Q., and Blaabjerg, F. (2021). Adaptive Resilient Secondary Control for Islanded AC Microgrids with Sensor Faults. *IEEE J. Emerg. Sel. Top. Power Electron.* 9 (5), 5239–5248. doi:10.1109/jestpe.2020.2988509

Lin, L., Ma, H., and Bai, Z. (2017). An Improved Proportional Load-Sharing Strategy for Meshed Parallel Inverters System with Complex Impedances. *IEEE Trans. Power Electron.* 32 (9), 7338–7351. doi:10.1109/tpel.2016.2630709

Liserre, M., Sauter, T., and Hung, J. (2010). Future Energy Systems: Integrating Renewable Energy Sources into the Smart Power Grid through Industrial Electronics. *EEE Ind. Electron. Mag.* 4 (1), 18–37. doi:10.1109/mie.2010.935861

Liu, J., Miura, Y., and Ise, T. (2014). "Dynamic Characteristics and Stability Comparisons between Virtual Synchronous Generator and Droop Control in Inverter-Based Distributed Generators," in 2014 International Power Electronics Conference (IPEC-Hiroshima 2014 - ECCE ASIA) (Hiroshima, Japan: IEEE), 1536–1543. doi:10.1109/ipec.2014.6869789

Ma, D., Cao, X., Sun, C., Wang, R., Sun, Q., Xie, X., et al. (2021a). "Dual-Predictive Control with Adaptive Error Correction Strategy for AC Microgrids," in IEEE Transactions on Power Delivery (Early Access) (IEEE), 1. doi:10.1109/tpwrd.2021.3101198

Ma, D., Hu, X., Zhang, H., Sun, Q., and Xie, X. (2021b). A Hierarchical Event Detection Method Based on Spectral Theory of Multidimensional Matrix for Power System. *IEEE Trans. Syst. Man. Cybern. Syst.* 51 (4), 2173–2186. doi:10.1109/tsmc.2019.2931316

Ma, D., Liu, M., Zhang, H., Wang, R., and Xie, X. (2021c). "Accurate Power Sharing and Voltage Regulation for AC Microgrids: An Event-Triggered Coordinated Control Approach," in IEEE Transactions on Cybernetics (Early Access) (IEEE), 1–11. doi:10.1109/tcyb.2021.3095959

Meng, J., Wang, Y., Fu, C., and Wang, H. (2016). "Adaptive Virtual Inertia Control of Distributed Generator for Dynamic Frequency Support in Microgrid," in 2016 IEEE Energy Conversion Congress and Exposition (IEEE), 1–5. doi:10.1109/ecce.2016.7854825

Meng, K., Dong, Z. Y., Xu, Z., Zheng, Y., and Hill, D. J. (2019). Coordinated Dispatch of Virtual Energy Storage Systems in Smart Distribution Networks for Loading Management. *IEEE Trans. Syst. Man. Cybern. Syst.* 49 (4), 776–786. doi:10.1109/tsmc.2017.2690911

Mojica-Nava, E., Macana, C. A., and Quijano, N. (2014). Dynamic Population Games for Optimal Dispatch on Hierarchical Microgrid Control. *IEEE Trans. Syst. Man. Cybern. Syst.* 44 (3), 306–317. doi:10.1109/tsmcc.2013.2266117

Rene, V., Sjored, D., Pablo, V., and Klaas, V. (2009). "Grid Tied Converter with Virtual Kinetic Storage," in 2009 IEEE Bucharest PowerTech (IEEE), 1–7.

Simpson-Porco, J. W., Dörfler, F., and Bullo, F. (2013). Synchronization and Power Sharing for Droop-Controlled Inverters in Islanded Microgrids. *Automatica* 49 (9), 2603–2611. doi:10.1016/j.automatica.2013.05.018

Soni, N., Doolla, S., and Chandorkar, M. C. (2013). Improvement of Transient Response in Microgrids Using Virtual Inertia. *IEEE Trans. Power Deliv.* 28 (3), 1830–1838. doi:10.1109/TPWRD.2013.2264738

Tian, E., and Peng, C. (2020). Memory-Based Event-Triggering H ∞ Load Frequency Control for Power Systems under Deception Attacks. *IEEE Trans. Cybern.* 50 (11), 4610–4618. doi:10.1109/tcyb.2020.2972384

Wang, D., He, H., and Liu, D. (2017). Adaptive Critic Nonlinear Robust Control: A Survey. *IEEE Trans. Cybern.* 47 (10), 3429–3451. doi:10.1109/tcyb.2017.2712188.23

Wang, F., Zhang, L., Feng, X., and Guo, H. (2018). An Adaptive Control Strategy for Virtual Synchronous Generator. *IEEE Trans. Ind. Appl.* 54 (5), 5124–5133. doi:10.1109/TIA.2018.2859384

Wang R, R., Sun, Q., Ma, D., and Liu, Z. (2019). The Small-Signal Stability Analysis of the Droop-Controlled Converter in Electromagnetic Timescale. *IEEE Trans. Sustain. Energy* 10 (3), 1459–1469. doi:10.1109/tste.2019.2894633

Wang, R., Sun, Q., Hu, W., Li, Y., Ma, D., and Wang, P. (2021). SoC-Based Droop Coefficients Stability Region Analysis of the Battery for Stand-Alone Supply Systems with Constant Power Loads. *IEEE Trans. Power Electron.* 36 (7), 7866–7879. doi:10.1109/tpel.2021.3049241

Weng S, S., Yue, D., Dou, C., Shi, J., and Huang, C. (2019). Distributed Event-Triggered Cooperative Control for Frequency and Voltage Stability and Power Sharing in Isolated Inverter-Based Microgrid. *IEEE Trans. Cybern.* 49 (4), 1427–1439. doi:10.1109/tcyb.2018.2803754

Wu, W., Chen, Y., Luo, A., Zhou, L., Zhou, X., Yang, L., et al. (2017). A Virtual Inertia Control Strategy for DC Microgrids Analogized with

Virtual Synchronous Machines. *IEEE Trans. Ind. Electron.* 64 (7), 6005–6016. doi:10.1109/tie.2016.2645898

Yang, X., Su, J., Ding, M., Li, J., and Du, Y. (2011). "Control Strategy for Virtual Synchronous Generator in Microgrid," in 2011 4th International Conference on Electric Utility Deregulation and Restructuring and Power Technologies (IEEE), 1633–1637.

Zhang, X., Mao, F., Xu, H., Liu, F., and Li, M. (2017). An Optimal Coordination Control Strategy of Micro-grid Inverter and Energy Storage Based on Variable Virtual Inertia and Damping of Vsg. *Chin. J. Electr. Eng.* 3 (3), 25–33.

Zhong, Q., Nguyen, P., Ma, Z., and Sheng, W. (2014). Self-Synchronized Synchronverters: Inverters without a Dedicated Synchronization Unit. *IEEE Trans. Power Electron.* 29 (2), 617–630. doi:10.1109/tpel.2013.2258684

Zhao, Z., Yang, P., Guerrero, J. M., Xu, Z., and Green, T. C. (2016). Multiple-Time-Scales Hierarchical Frequency Stability Control Strategy of Medium-Voltage Isolated Microgrid. *IEEE Trans. Power Electron.* 31 (8), 5974–5991. doi:10.1109/tple.2015.249686910.1109/tpel.2015.2496869

Zhong, Q.-C., and Weiss, G. (2011). Synchronverters: Inverters that Mimic Synchronous Generators. *IEEE Trans. Ind. Electron.* 58 (4), 1259–1267. doi:10.1109/tie.2010.2048839

Conflict of Interest: The authors declare that the research was conducted in the absence of any commercial or financial relationships that could be construed as a potential conflict of interest.

frontiers | Frontiers in Energy Research

ORIGINAL RESEARCH
published: 28 June 2022
doi: 10.3389/fenrg.2022.939110

Two-Stage Robust Optimal Scheduling of "Nearly-Zero-Carbon Park" Considering the Synergy of Waste Disposal and Carbon Capture Gas-Fired Power Plants

Zongjun Yao[1], *Tieyan Zhang*[1]* *and Yan Zhao*[2,3]

[1]School of Electrical Engineering, Shenyang University of Technology, Shenyang, China, [2]Science and Technology Department, Shenyang Institute of Engineering, Shenyang, China, [3]Key Laboratory of Regional Multi-Energy System Integration and Control of Liaoning Province, Shenyang, China

Aiming at the demand characteristics of "Nearly-zero Carbon Parks" (NZCP) powered by all renewable energy for low-carbon emissions and waste reduction, a NZCP topology and a two-stage robust optimal scheduling model based on the Carbon Capture Gas-fired Power Plant (CCGPP)-Power to Gas(P2G)-Waste Disposal (WD) collaborative model are proposed in this paper. First, the relationship between WD, CCGPP and energy supply and demand that can be generated from renewable energy is studied, and according to the system energy regulation requirements, the energy flexibility of residential loads, small industrial loads and electric vehicles are considered, and the NZCP mathematical model based on the CCGPP-P2G-WD collaborative model is established. Secondly, NZCP energy supply and demand characteristics are studied, and an energy coordination model for NZCP energy conversion and storage powered by 100% renewable energy is established. Then, wind power, photovoltaic power, and combined demand response uncertainties are considered, and the NZCP two-stage robust hybrid optimal dispatch model is established based on second-order cone relaxation and dual theory. Finally, the simulation analysis is carried out based on the operation data of the integrated energy system of a park in a certain area in northern my country. The simulation results show that the proposed two-stage robust optimal scheduling model of NZCP coordinated with WD and CCGPP can effectively improve the economy of the system at a higher energy balance level, improve the absorption capacity of renewable energy, and provide better multi-time scale energy regulation characteristics for NZCP with a larger energy supply scale.

Keywords: nearly zero carbon park, carbon capture gas-fired power plants, waste disposal, demand side response, two-stage robust optimization

OPEN ACCESS

Edited by:
Qiuye Sun,
Northeastern University, China

Reviewed by:
He Ren,
Northeast Electric Power University, China
Xuguang Hu,
Northeastern University, China

****Correspondence:***
Tieyan Zhang
tyzhang62@163.com

Specialty section:
This article was submitted to Smart Grids, a section of the journal Frontiers in Energy Research

Received: *08 May 2022*
Accepted: *30 May 2022*
Published: *28 June 2022*

Citation:
Yao Z, Zhang T and Zhao Y (2022) Two-Stage Robust Optimal Scheduling of "Nearly-Zero-Carbon Park" Considering the Synergy of Waste Disposal and Carbon Capture Gas-Fired Power Plants. Front. Energy Res. 10:939110. doi: 10.3389/fenrg.2022.939110

INTRODUCTION

In the context of the zero-carbon strategy and the "dual-carbon" goal under the "14th Five-Year Plan" modern energy system plan, seeking low-carbon, diverse, interactive and sustainable energy coupling and transportation is the key to solving the problems of low-carbon development and transformation of energy in human society (National Development and Reform Commission, 2022).The "China Research Report on Carbon Neutrality Before 2060" pointed out that carbon capture, utilization and storage technology and biomass carbon capture and storage technology are important ways and key means to achieve the goal of carbon neutrality. Carbon capture and storage technology can effectively reduce carbon emissions and achieve zero and negative carbon emissions goals (Cheng et al., 2020; Hu et al., 2021; Wang et al., 2021a). However, most of the carbon capture power plants based on the transformation of traditional coal-fired power plants adopt the split-flow operation mode, and the working process of the absorption tower and the regeneration tower is coupled, resulting in the higher the power output, the greater the energy consumption of carbon capture, and the lack of carbon utilization mechanism. Therefore, considering the negative carbon emission characteristics of biomass waste treatment as a zero-carbon renewable energy and the energy space-time translation characteristics of P2G equipment with both source and load attributes, the establishment of NZCP based on CCGPP-P2G-WD collaborative mode is the key to improve the consumption of renewable energy, reduce carbon emissions and realize carbon recycling.

Carbon capture and storage technology is one of the main low-carbon technologies at the current stage, which can absorb abandoned wind and solar energy and achieve carbon emission reduction. At home and abroad, some researches have been carried out on the flexible operation mode of carbon capture power plants. Cui et al. (2021a) introduces a carbon storage device into the flue gas bypass of a carbon capture coal-fired power plant, shifts the wind power output in time, and proposes a flexible operation mode of coordination between wind power and carbon capture power plants, which improves the wind power consumption capacity; Cui et al. (2021b) introduces price-based demand response into a comprehensive energy system with carbon capture equipment, and adjusts the load to match the output of renewable energy, which reduces the carbon emissions of the system and improves the operating economy of the system; Zhou et al. (2018) proposed a combined operation mode of power-to-gas-carbon capture, which uses CO_2 captured by carbon capture equipment as a raw material for methane production in the power-to-gas process, which improves the carbon utilization level on the basis of ensuring economical efficiency.

NZCP fully dispatches zero-carbon resources in the comprehensive energy system of the park, and realizes rapid reduction of carbon emissions and approaches zero through multi-energy coupling and complementation, multi-load demand response, waste treatment and carbon capture and storage technologies. As a typical comprehensive energy application scenario, the park has carried out a lot of researches at home and abroad on the energy balance uncertainty of the park-level comprehensive energy system and the improvement of the energy supply regulation capacity. Zhou et al. (2018) established the topological structure of the integrated energy system of the park, considering the economic indicators of environment and energy efficiency, and proposed an optimization method of the integrated energy system of the park based on the improvement of efficiency and benefit; Fang et al. (2020) analyzes the time-delay characteristics of thermal loads, considers the comprehensive demand response mechanism of various electric heating loads, improves the flexibility of energy supply of the comprehensive energy system in the park, reduces wind and light abandonment, and realizes the coordination and optimization of the comprehensive energy system in the park; Jiang et al. (2021) considers the randomness of renewable energy output and load demand in multi-energy parks, and proposes an optimal scheduling method based on an improved deep deterministic policy gradient algorithm, which reduces the impact of source and load uncertainty on scheduling; According to fuzzy theory, Zhong et al. (2020) expresses wind power and load with fuzzy parameters, and transforms deterministic system constraints into fuzzy chance constraints to solve the source and load uncertainty problem in the optimal dispatch of carbon capture virtual power plants.

Biomass energy is also an important zero-carbon energy source, and a lot of efforts have been made at home and abroad in terms of WD energy supply characteristics and optimized operation. Wang et al. (2021b) studied the energy supply characteristics of waste incineration and sewage gas production, considering the processing capacity and waste output of waste treatment facilities, and proposed an operation strategy for waste treatment facilities to participate in power grid peak regulation; Yang et al. (2021) considers the low-carbon characteristics of waste treatment units and introduces a carbon quota trading mechanism, which improves the consumption capacity of renewable energy while taking into account the waste treatment; Zhou et al. (2019) considered the high energy consumption characteristics of flue gas treatment in waste incineration power plants, decoupled the power generation process from the flue gas treatment process, and used abandoned wind for flue gas treatment, which improved the operation flexibility of waste incineration power plants with a high proportion of wind power connected.

From the above analysis, it can be seen that the current domestic and foreign research on the energy balance characteristics and adjustment capacity of the integrated energy system under the low-carbon constraints mainly focus on the carbon capture technology of coal-fired power plants and the low-carbon economic dispatch considering the carbon quota trading mechanism. On the other hand, there are few studies on the collaborative optimization of CCGPP and WD and the improvement of power grid, heat grid, and gas grid regulation capacity.

Therefore, the NZCP structure based on the CCGPP-P2G-WD synergy model is proposed in this paper, which adopts a fully renewable energy supply method and makes full use of zero-carbon resources such as waste incineration, biogas treatment and multi-load demand response in the park. In addition, the energy supply and demand characteristics of NZCP are deeply analyzed. Firstly, the energy production and conversion model of each equipment is established based on the CCGPP-P2G-WD collaborative model. Secondly, an energy coordination model of NZCP energy conversion and storage is established by using the energy coupling matrix to map the multi-energy coupling method. Then, the NZCP two-stage robust optimal scheduling method is proposed, and the two-stage robust optimal scheduling model is processed based on the second-order cone relaxation and dual theory. Finally, the NZCP simulation model is established, and four scenes are proposed for simulation comparison analysis. The validity and economy of the model proposed in this paper are verified.

NEARLY-ZERO CARBON PARKS SYSTEM MODEL

The proposed NZCP considering the synergy of waste treatment and carbon capture gas-fired power plants is aimed at the zero-carbon demand and waste treatment demand of the integrated energy system of the park, and considers the energy transfer characteristics of waste incineration flue gas treatment and carbon capture gas-fired power plants carbon storage, which is sufficient. Coordinate zero-carbon resources such as waste treatment and demand-side response in the park, based on the coordinated coupling system between carbon capture, storage and utilization, energy storage medium material flow and energy flow. The CCGPP-P2G-WD collaborative method with multi-temporal scale and multi-energy regulation ability constructed in this paper and the NZCP energy coupling mode and connection relationship it serves are shown in **Figure 1**. NZCP includes renewable energy supply systems such as wind power generation, photovoltaic power generation, waste incineration and manure treatment, and the entire energy interaction network is composed of power grid, heat network, gas network and transportation network. NZCP realizes the recycling of carbon flow in the energy coupling link through the synergy of CCGPP, WD and P2G.

Waste Treatment System Model

For the waste treatment requirements of NZCP, the classified combustible waste is transported to a waste incineration power plant for waste incineration to generate electricity (Wang et al., 2021c). Biomass technology is used to convert the dry-wet separation of manure and waste into biogas, which is then purified and processed to obtain natural gas, which is used as the input of carbon capture gas-fired power plants and connected to the natural gas network at the same time (Zhang et al., 2020; Teng et al., 2021).

Considering that in the waste treatment system, waste incineration and manure treatment can support the multi-source regulation capacity of electric heating gas in the park, the energy conversion model is as follows:

$$\begin{bmatrix} P_{\mathrm{WD,E}} \\ P_{\mathrm{WD,H}} \\ P_{\mathrm{WD,G}} \end{bmatrix} = \begin{bmatrix} \eta_{\mathrm{WI,E}} a_{\mathrm{BG,E}} & 0 & 0 \\ \eta_{\mathrm{WI,H}} a_{\mathrm{BG,H}} & 0 & 0 \\ 0 & \eta_{\mathrm{FW,G}} a_{\mathrm{F,G}} \eta_{\mathrm{F,G}} & \eta_{\mathrm{SG,G}} a_{\mathrm{F,G}} \eta_{\mathrm{S,G}} \end{bmatrix} \begin{bmatrix} P_{\mathrm{BG}} \\ P_{\mathrm{FW}} \\ P_{\mathrm{SG}} \end{bmatrix} \tag{1}$$

where $P_{\mathrm{WD,E}}$, $P_{\mathrm{WD,H}}$ and $P_{\mathrm{WD,G}}$ are the electric energy, heat energy and natural gas energy provided by the waste treatment system respectively, $\eta_{\mathrm{WI,E}}$ and $\eta_{\mathrm{WI,H}}$ are the power supply and heating efficiency of the waste incineration power plant respectively, $a_{\mathrm{BG,E}}$ and $a_{\mathrm{BG,H}}$ are the conversion coefficients of electric energy and heat energy of the waste incineration power plant respectively, $\eta_{\mathrm{FW,G}}$ and $\eta_{\mathrm{SG,G}}$ are the treatment efficiency of the excrement treatment facility and the treatment efficiency of the sewage treatment facility respectively, $\eta_{\mathrm{F,G}}$ and $\eta_{\mathrm{S,G}}$ are the conversion coefficient of fecal waste and sewage waste into natural heat and gas energy respectively, $a_{\mathrm{F,G}}$ is biogas methanation efficiency, P_{BG}, P_{FW} and P_{SG} are the input amount of combustible waste, fecal waste and sewage waste, respectively.

During the working process of the waste incineration power plant, the exhaust gas needs to be discharged after the flue gas treatment reaches the standard (Xv et al., 2018). However, the energy consumption of flue gas treatment accounts for nearly 1/4 of its power generation, and if it is classified as plant power, it will affect the operating economy of the system (Cao et al., 2020).

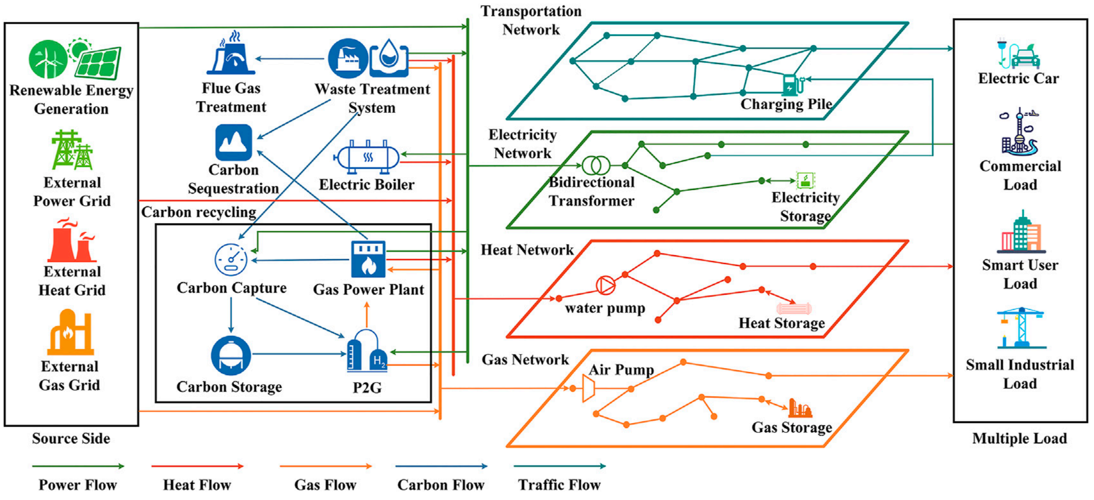

FIGURE 1 | "Nearly-zero carbon park" topology diagram.

Therefore, a flue gas storage device was introduced to decouple the waste incineration power generation process from the flue gas treatment process. The flue gas storage device divides the flue gas discharged from the waste incineration power plant. By adjusting the proportion of the flue gas entering the reaction tower and the flue gas storage device, the energy demand of the flue gas treatment can be shifted in time and space to realize the dynamic flue gas treatment at different time scales.

The amount of flue gas generated by waste incineration power generation can be expressed as:

$$V_{\mathrm{S,WI}} = v_{\mathrm{S,WI}} P_{\mathrm{WD,E}} = V_{\mathrm{S,RT}} + V_{\mathrm{S,MIGS}} \tag{2}$$

where $v_{\mathrm{S,WI}}$ is the unit flue gas coefficient of waste incineration power generation, $V_{\mathrm{S,RT}}$ is the amount of flue gas directly entering the reaction tower, $V_{\mathrm{S,MIGS}}$ is the amount of flue gas entering the gas storage device.

In addition to the energy consumption of flue gas treatment, there is energy consumption of the air pump in the filling and deflating behavior of the flue gas and the gas storage tank. The total energy consumption of flue gas treatment in waste incineration power plants can be expressed as:

$$P_{\mathrm{S,C,WI}} = s_{\mathrm{S,RT}} \left(V_{\mathrm{S,RT}} + V_{\mathrm{S,MIGS-RT}} \right) + s_{\mathrm{S,MIGS}} \left(V_{\mathrm{S,MIGS-RT}} + V_{\mathrm{S,MIGS}} \right) \tag{3}$$

where $s_{\mathrm{S,RT}}$ is the energy consumption coefficient of the reaction tower, $s_{\mathrm{S,MIGS}}$ is the energy consumption coefficient of the air pump, $V_{\mathrm{S,MIGS-RT}}$ is the amount of flue gas entering the reaction tower from the flue gas storage device.

CCGPP-P2G-WD Collaborative Mode

In the CCGPP-P2G-WD cooperative operation mode, the CO2 emitted by CCGPP-WD provides P2G with hydrogen methanation raw materials, and P2G-WD provides CCGPP with natural gas as fuel to realize the electricity-carbon-electricity cycle process.

During the working process of carbon capture gas power plants, carbon capture energy consumption is very high. In this paper, the carbon capture gas-fired power plant adopts the solution storage operation mode, and its specific operation mode and electric carbon characteristics refer to reference (Chen et al., 2012). The CCGPP power generation process is decoupled from the CO_2 absorption process by introducing a solution reservoir. The spatiotemporal shift of the energy demand of CCGPP-P2G is achieved, and the rate of CO_2 absorption and desorption is controlled.

The total amount of CO_2 captured by CCGPP-P2G at the moment is:

$$Q^{\Sigma}_{\mathrm{CCGPP-CO_2},t} = \theta_{\mathrm{CO_2},t} \eta_{\mathrm{CCGPP-CO_2},t} \left(P_{\mathrm{GD,E},t} + P_{\mathrm{CCGPP},t} \right) \tag{4}$$

where $\theta_{\mathrm{CO_2},t}$ is the carbon emission intensity processed at time t, $\eta_{\mathrm{CCGPP-CO_2},t}$ is the carbon capture rate of CCGPP capture CO2 at time t, $P_{\mathrm{GD,E},t}$ is the electricity provided by the waste treatment power plant at time t, $P_{\mathrm{CCGPP},t}$ is the output power of CCGPP at time t.

The total amount of CO_2 consumed by P2G at time t is:

$$Q^{\Sigma}_{\mathrm{P2G-CO_2},t} = \chi_{\mathrm{CO_2},t} \eta_{\mathrm{P2G}} P_{\mathrm{C,P2G},t} \tag{5}$$

where $\chi_{\mathrm{CO_2},t}$ is the amount of CO_2 required to generate unit capacity of natural gas, η_{P2G} is the gas production efficiency of P2G, $P_{\mathrm{C,P2G},t}$ is the energy consumption of the P2G device at time t.

The gas production of P2G at time t is:

$$V^{\Sigma}_{\mathrm{P2G-CH_4},t} = 3.6 \eta_{\mathrm{P2G}} P_{\mathrm{C,P2G},t} \big/ H_g \tag{6}$$

where H_g is natural gas calorific value.

The total energy consumption of CCGPP-P2G at time t is:

$$P_{\mathrm{C,CCGPP-P2G},t} = P_{\mathrm{C,CCGPP},t} + P_{\mathrm{C,P2G},t} + P_{\mathrm{F},t} \tag{7}$$

where $P_{\mathrm{C,CCGPP},t}$ is the energy consumption of CCGPP at time t, $P_{\mathrm{C,P2G},t}$ is the energy consumption of P2G at time t, $P_{\mathrm{F},t}$ is the energy consumption of system at time t.

The net output of CCGPP and net CO_2 emissions at time t are:

$$P^{\mathrm{net}}_{\mathrm{CCGPP},t} = P_{\mathrm{CCGPP},t} - P_{\mathrm{C,CCGPP},t} \tag{8}$$

$$Q^{\mathrm{net}}_{\mathrm{CCGPP-CO_2},t} = q_{\mathrm{CO_2}} P_{\mathrm{CCGPP},t} - Q^{\Sigma}_{\mathrm{CCGPP-CO_2},t} \tag{9}$$

where $P_{\mathrm{CCGPP},t}$ is the total output of CCGPP at time t, $q_{\mathrm{CO_2}}$ is the amount of CO_2 produced by unit power generation output.

Load Demand Response Model

Load demand response is an important zero-carbon resource, which can optimize the low-carbon performance of the mining system through source-load coordination and has good dispatchability (Wei et al., 2018). The main loads in the park include: smart users, small industrial loads, commercial loads and electric vehicles. Under the limitation of the scope of the park, the energy demand of electric vehicles is high, the battery capacity is small, and the scale of cluster operation is insufficient. This paper does not consider electric vehicles to discharge the grid. Smart users can adjust energy consumption behavior according to changes in electricity prices and reduce energy demand. The energy consumption period of small industrial loads is flexible, and the energy consumption period can be shifted. Commercial loads have a large energy demand. In addition to rigid demand response resources such as lighting, elevators and computers, flexible loads such as air conditioning and energy storage in commercial buildings can be mobilized to participate in the demand response to effectively improve the multiple regulation capacity of the park and reduce the peak-valley difference of load curves (Gao et al., 2019).

The types of demand response are divided into price demand response and incentive demand response. Price-based demand response guides users' energy consumption behavior through electricity prices, and the participants are mainly translatable loads (Wang et al., 2021d). Incentive demand response restricts users' energy consumption behavior through contracts, and the participants are mainly interruptible loads (He et al., 2019). Responding to changes in energy prices through load reduction and translation can match the energy demand of the park and promote the level of renewable energy consumption. The NZCP load demand response model is as follows:

$$L_{k,i,\mathrm{DR},t} = L^{\mathrm{int}}_{k,i,\mathrm{DR},t} + L^{\mathrm{shi}}_{k,i,\mathrm{DR},t}, i \in \{\mathrm{E},\mathrm{H},\mathrm{G}\} \tag{10}$$

$$L_{k,i,t} - L_{k,i,\mathrm{DR},t} \le L_{k,i,t,\max} \tag{11}$$

$$0 \le L^{\mathrm{int}}_{k,i,\mathrm{DR},t} \le \alpha^{\mathrm{int}}_{k,i,o,t} L_{k,i,t} \tag{12}$$

$$-\alpha^{\mathrm{shi}}_{k,i,t} L_{k,i,t} \le L^{\mathrm{shi}}_{k,i,\mathrm{DR},t} \le \alpha^{\mathrm{shi}}_{k,i,t} L_{k,i,t} \tag{13}$$

$$\sum_{t=1}^{T} L^{\mathrm{shi}}_{k,i,\mathrm{DR},t} = 0 \tag{14}$$

where i is the load type, that is, the electrical load, the thermal load, and the gas load respectively, k is the area type, residential area, small industrial area, commercial area and electric vehicle, respectively, $L_{k,i,\mathrm{DR},t}$, $L^{\mathrm{int}}_{k,i,\mathrm{DR},t}$, $L^{\mathrm{shi}}_{k,i,\mathrm{DR},t}$, $L_{k,i,t}$ and $L_{k,i,t,\max}$ are the load involved in demand response, interruptible load, transferable load, load forecast value, and maximum allowable load at time t in the k area respectively, $\alpha^{\mathrm{int}}_{k,i,o,t}$ and $\alpha^{\mathrm{shi}}_{k,i,t}$ are the interruptible load proportion of the oth stage at time t in the k area, and the transferable load proportion at time t in the k area respectively.

NEARLY-ZERO CARBON PARKS ENERGY SUPPLY AND DEMAND CHARACTERISTICS

The proposed NZCP takes the CCGPP-P2G-WD collaborative energy supply system as the core, takes wind power generation and photovoltaic power generation as the main energy supply methods, and realizes the conversion of various energy sources through P2G, CCGPP and Electric Boiler (EB), supplemented by the coordination of electricity storage, heat storage and gas storage devices.

The energy coupling matrix is used to describe the multi-energy conversion, storage and distribution relationship of NZCP:

$$\begin{bmatrix} L_{\mathrm{E}} - L_{\mathrm{E},\mathrm{DR},t} \\ L_{\mathrm{H}} - L_{\mathrm{H},\mathrm{DR},t} \\ L_{\mathrm{G}} - L_{\mathrm{G},\mathrm{DR},t} \end{bmatrix} = \begin{bmatrix} P_{\mathrm{E,W}} \\ P_{\mathrm{H,W}} \\ P_{\mathrm{G,W}} \end{bmatrix} + \begin{bmatrix} P_{\mathrm{ES}} \\ P_{\mathrm{HS}} \\ P_{\mathrm{GS}} \end{bmatrix} + \begin{bmatrix} 1 & 0 & 0 & \eta_{\mathrm{GE}} & 1 & 1 \\ 0 & 1 & 0 & \eta_{\mathrm{GE}}\eta_{\mathrm{GE,H}} & \varsigma_{\mathrm{WP},1}\eta_{\mathrm{EB}} & \varsigma_{\mathrm{PV},1}\eta_{\mathrm{EB}} \\ 0 & 0 & 1 & 0 & \varsigma_{\mathrm{WP},2}\eta_{\mathrm{P2G}} & \varsigma_{\mathrm{PV},2}\eta_{\mathrm{P2G}} \end{bmatrix} \times \begin{bmatrix} P_{\mathrm{WD,EW}} \\ P_{\mathrm{WD,HW}} \\ P_{\mathrm{WD,GW}} \\ P_{\mathrm{GE}} \\ P_{\mathrm{WP,EW}} \\ P_{\mathrm{PV,EW}} \end{bmatrix} \tag{15}$$

where $P_{\mathrm{E,W}}$, $P_{\mathrm{H,W}}$ and $P_{\mathrm{G,W}}$ are the electricity, heat and gas power purchased from the main network respectively, P_{ES}, P_{HS} and P_{GS} are the electricity, heat and gas power provided by the electricity storage, heat storage and gas storage devices respectively, η_{GE}, $\eta_{\mathrm{GE,H}}$, η_{EB} and η_{P2G} are CCGPP power supply efficiency, CCGPP thermoelectric ratio, EB heating efficiency, and P2G gas supply efficiency, $\varsigma_{\mathrm{WP},1}$ and $\varsigma_{\mathrm{WP},2}$ are the distribution coefficient of wind power supply EB and P2G respectively, $\varsigma_{\mathrm{PV},1}$ and $\varsigma_{\mathrm{PV},2}$ are the distribution coefficients of PV supply EB and P2G respectively, $P_{\mathrm{WD,EW}}$, $P_{\mathrm{WD,HW}}$ and $P_{\mathrm{WD,GW}}$ are the WD power supply, heating power, and gas supply power respectively, P_{GE} a is the total output of CCGPP, $P_{\mathrm{WP,EW}}$ and $P_{\mathrm{PV,EW}}$ are the on-grid power of wind power and the on-grid power of photovoltaics respectively.

NEARLY-ZERO CARBON PARKS COORDINATION OPTIMIZATION MODEL

Objective Function

In this paper, the NZCP optimal scheduling model considering the coordination of WD and CCGPP is established. Its essence is to realize carbon recycling through ccGPP-P2G-WD cooperative mode on the basis of considering the waste treatment and carbon reduction requirements of the park, and form a comprehensive energy system with near zero carbon emissions. The optimal goal of minimum net operating cost of the system was established, and the decision variables included total CCGPP output, WD equivalent output, P2G output, EB output, carbon capture energy consumption, flue gas treatment energy consumption, transfer load of demand response, interruption load of demand response and energy purchase from the main network.

$$\min\Big(C_{s-s} + C_{buy} + C_{\mathrm{W,PV}} + C_{\mathrm{L,DR}} + C_{\mathrm{EB}} + C_{\mathrm{P2G}} + C_{\mathrm{GD}} + C_{\mathrm{CCGPP}} + C_{\mathrm{CSE}} - R_{\mathrm{CCGPP}}\Big) \tag{16}$$

$$C_{s-s} = \sum_{ep}^{ALL} \sum_{t=1}^{T} \max\left\{0, ep_{i,t} - ep_{i,t-1}\right\} \gamma_{ep_i,t} \tag{17}$$

$$C_{buy} = \sum_{t=1}^{T} \partial_{\mathrm{E},t} P_{\mathrm{E,W}} + \sum_{t=1}^{T} \partial_{\mathrm{H},t} P_{\mathrm{H,W}} + \sum_{t=1}^{T} \partial_{\mathrm{G},t} P_{\mathrm{G,W}} \tag{18}$$

$$C_{\mathrm{WP,PV}} = \sum_{t=1}^{T} \gamma_{\mathrm{WP},t} P_{\mathrm{WP}} + \sum_{t=1}^{T} \gamma_{\mathrm{PV},t} P_{\mathrm{PV}} \tag{19}$$

$$C_{\mathrm{L,DR}} = \sum_{k}^{K} \sum_{i}^{I} \sum_{t=1}^{T} \sum_{o}^{O} b_{k,i,o,\mathrm{int},t} L^{\mathrm{int}}_{k,i,\mathrm{DR},t} + \sum_{k}^{K} \sum_{i}^{I} \sum_{t=1}^{T} b_{k,i,\mathrm{shi},t} L^{\mathrm{shi}}_{k,i,\mathrm{DR},t} \tag{20}$$

$$C_{\mathrm{EB}} = \sum_{t=1}^{T} \gamma_{\mathrm{EB},t} P_{\mathrm{EB},t} \tag{21}$$

$$C_{\mathrm{P2G}} = \sum_{t=1}^{T} \gamma_{\mathrm{P2G},t} P_{\mathrm{C,P2G},t} \tag{22}$$

$$C_{\mathrm{GD}} = \sum_{t=1}^{T} \left[a + b\left(P_{\mathrm{BG},t} + P_{\mathrm{FW},t} + P_{\mathrm{SG},t}\right) + c\left(P_{\mathrm{BG},t} + P_{\mathrm{FW},t} + P_{\mathrm{SG},t}\right)^2 \right] \tag{23}$$

$$C_{\mathrm{CCGPP}} = \sum_{t=1}^{T} \gamma_{\mathrm{CCGPP},t} P^{net}_{\mathrm{CCGPP},t} \tag{24}$$

$$C_{\mathrm{CSE}} = \sum_{t=1}^{T} \gamma_{\mathrm{CSE},t} Q_{\mathrm{CSE,CO_2},t} \tag{25}$$

$$R_{\mathrm{CCGPP}} = \sum_{t=1}^{T} \gamma_{\mathrm{C},t} \Big(a_{mount} P^{\mathrm{net}}_{\mathrm{CCGPP},t} - Q^{\mathrm{net}}_{\mathrm{CCGPP-CO_2},t} \Big) \tag{26}$$

$$Q_{\mathrm{CSE,CO_2},t} = Q^{\Sigma}_{\mathrm{CCGPP-CO_2},t} - Q_{\mathrm{P2G-CO_2},t} \tag{27}$$

where C_{s-s}, C_{buy}, $C_{\mathrm{WP,PV}}$, $C_{\mathrm{L,DR}}$, C_{EB}, C_{P2G}, C_{GD}, C_{CCGPP}, C_{CSE} and R_{CCGPP} are the total equipment start-up and shutdown cost, the main grid energy purchase cost, the operation and maintenance cost of renewable energy power generation equipment, the transferable load and interruptible load compensation cost, the EB operating cost, the P2G operating cost, the WD operating cost, the CCGPP operating cost, the carbon sequestration cost , and the income obtained by the carbon capture gas power plants by selling the emission credits that do not meet the carbon emission quotas. $ep_{i,t}$ is the start-stop state of the controllable device ep_i at time t, $\gamma_{ep_i,t}$ is the start-stop cost of the controllable device ep_i at time t, $\partial_{\mathrm{E},t}$, $\partial_{\mathrm{H},t}$ and $\partial_{\mathrm{G},t}$ is the price of electricity, heat and natural gas at time t, $\gamma_{\mathrm{WP},t}$ and $\gamma_{\mathrm{PV},t}$ are the unit operation and maintenance costs of wind power and photovoltaics at time t respectively, $b_{k,i,o,\mathrm{int},t}$ and $b_{k,i,\mathrm{shi},t}$ are the electric/heat/gas load interruption compensation price for the oth level participating in demand response at time t in the k area, and the electric/heat/gas load transfer compensation price for participating in the demand response at time t in the k area, $\gamma_{\mathrm{EB},t}$ and $\gamma_{\mathrm{P2G},t}$ are the operating cost coefficients of EB and P2G respectively, a, b, c are the cost factor for waste disposal, $\gamma_{\mathrm{CCGPP},t}$ is the operating cost coefficients of CCGPP, $\gamma_{\mathrm{CSE},t}$ is the unit cost of carbon sequestration, $Q_{\mathrm{CSE,CO_2},t}$ is the amount of CO_2 sequestered by the carbon sequestration device; $Q_{\mathrm{P2G-CO_2},t}$ is the amount of CO_2 captured for P2G devices, $\gamma_{\mathrm{C},t}$ is the carbon trading price, a_{mount} is the carbon emission benchmark quota per unit of electricity.

Restrictions

(1) Power balance constraints:

$$L_{\mathrm{E},t} = P_{\mathrm{E,W},t} + P_{\mathrm{WP},t} + P_{\mathrm{PV},t} + P_{\mathrm{WD,EW},t} + P_{\mathrm{CCGPP,E},t} + P_{\mathrm{ES},t} - P_{\mathrm{P2G},t} - P_{\mathrm{EB},t} \tag{28}$$

$$L_{\mathrm{H},t} = P_{\mathrm{H,W},t} + P_{\mathrm{WD,HW},t} + P_{\mathrm{CCGPP,H},t} + P_{\mathrm{HS},t} + P_{\mathrm{EB},t} \tag{29}$$

$$L_{\mathrm{G},t} = P_{\mathrm{G,W},t} + P_{\mathrm{WD,GW},t} + P_{\mathrm{P2G,H},t} + P_{\mathrm{GS},t} - P_{\mathrm{CCGPP},t} \tag{30}$$

where $P_{\mathrm{WP},t}$ and $P_{\mathrm{PV},t}$ are the output power of wind power and photovoltaic generators at time t respectively, $L_{\mathrm{E},t}$, $L_{\mathrm{H},t}$ and $L_{\mathrm{G},t}$ are the demand for electricity load, heat load, and gas load at the moment respectively, $P_{\mathrm{CCGPP,E},t}$ and $P_{\mathrm{CCGPP,H},t}$ are the power supply and heating power of CCGPP, respectively.

(2) CCGPP operating constraints:

$$P_{\mathrm{CCGPP,min}} \le P_{\mathrm{CCGPP},t} \le P_{\mathrm{CCGPP,max}} \tag{31}$$

$$\left|P_{\mathrm{CCGPP},t+1} - P_{\mathrm{CCGPP},t}\right| \le \Delta P_{\mathrm{CCGPP}} \tag{32}$$

where $P_{\mathrm{CCGPP,max}}$ and $P_{\mathrm{CCGPP,min}}$ are the upper and lower limits of CCGPP output respectively, $\Delta P_{\mathrm{CCGPP}}$ is the absolute value of the CCGPP ramp rate.

(3) WD operating constraints:

WD includes waste incineration power plants and manure treatment facility. The operation constraints of waste incineration power plants are:

$$\Delta P_{\mathrm{BG,\,min}} \le \Delta P_{\mathrm{BG,e},t} - P_{\mathrm{BG,e},t-1} \le \Delta P_{\mathrm{BG,\,max}} \tag{33}$$

$$0 \le P_{\mathrm{BG,e},t} \le P_{\mathrm{BG,e},rated} \tag{34}$$

where $\Delta P_{\mathrm{BG,\,max}}$ and $\Delta P_{\mathrm{BG,\,min}}$ are the upper limit and lower limit of the ramp rate of the waste incineration power plant respectively, $P_{\mathrm{BG,e},t}$ is the output power of the waste incineration power plant, $P_{\mathrm{BG,e},rated}$ is the rated power of the unit of the waste incineration power plant.

The operation constraints of manure treatment equipment are:

$$\Delta P_{\mathrm{FS,\,min}} \le \Delta P_{\mathrm{FS,g},t} - P_{\mathrm{FS,g},t-1} \le \Delta P_{\mathrm{FS,\,max}} \tag{35}$$

$$0 \le P_{\mathrm{FS,g},t} \le P_{\mathrm{FS,g},rated} \tag{36}$$

where $P_{\mathrm{FS,g},t}$ is the output power of the manure treatment equipment at time t, $\Delta P_{\mathrm{FS,\,max}}$ and $\Delta P_{\mathrm{FS,\,min}}$ are the ramp rate constraint of the manure treatment equipment, $P_{\mathrm{FS,g},rated}$ is the rated power of the manure treatment equipment.

(4) EB output and climbing constraints:

$$P_{\mathrm{EB,min}} \le P_{\mathrm{EB},t} \le P_{\mathrm{EB,max}} \tag{37}$$

$$\left|P_{\mathrm{EB},t+1} - P_{\mathrm{EB},t}\right| \le \Delta P_{\mathrm{EB}} \tag{38}$$

where $P_{\mathrm{EB,max}}$ and $P_{\mathrm{EB,min}}$ are the upper limit and lower limit of EB output respectively, ΔP_{EB} is the EB ramp rate constraint.

(5) EB output and climbing constraints:

$$0 \le P_{\mathrm{C,P2G},t} \le P_{\mathrm{P2G,max}} \tag{39}$$

$$\left|P_{\mathrm{P2G},t+1} - P_{\mathrm{P2G},t}\right| \le \Delta P_{\mathrm{P2G}} \tag{40}$$

where $P_{\mathrm{P2G,max}}$ is the upper limit of P2G output, ΔP_{P2G} is the P2G ramp rate constraint.

(6) Energy storage device operating constraints:

$$P_{\mathrm{ES},t} = (1 - \varsigma_{\mathrm{ES}})P_{\mathrm{ES},t-1} + \left(\eta_{\mathrm{ES}}^{\mathrm{ch}} P_{\mathrm{ES},t}^{\mathrm{ch}} - \frac{P_{\mathrm{ES},t}^{\mathrm{dis}}}{\eta_{\mathrm{ES}}^{\mathrm{dis}}}\right)\Delta t \tag{41}$$

$$P_{\mathrm{HS},t} = (1 - \varsigma_{\mathrm{HS}})P_{\mathrm{HS},t-1} + \left(\eta_{\mathrm{HS}}^{\mathrm{ch}} P_{\mathrm{HS},t}^{\mathrm{ch}} - \frac{P_{\mathrm{HS},t}^{\mathrm{dis}}}{\eta_{\mathrm{HS}}^{\mathrm{dis}}}\right)\Delta t \tag{42}$$

$$P_{\mathrm{GS},t} = (1 - \varsigma_{\mathrm{GS}})P_{\mathrm{GS},t-1} + \left(\eta_{\mathrm{GS}}^{\mathrm{ch}} P_{\mathrm{GS},t}^{\mathrm{ch}} - \frac{P_{\mathrm{GS},t}^{\mathrm{dis}}}{\eta_{\mathrm{GS}}^{\mathrm{dis}}}\right)\Delta t \tag{43}$$

where $P_{\mathrm{ES},t-1}$, $P_{\mathrm{HS},t-1}$ and $P_{\mathrm{GS},t-1}$ are the electricity storage, heat storage and gas storage capacity of the electricity storage device, heat storage device and gas storage device at time *t-1*, respectively, ς_{ES}, ς_{HS} and ς_{GS} are the energy loss rates of electricity storage devices, heat storage devices, and gas storage devices, respectively, $\eta_{\mathrm{ES}}^{\mathrm{ch}}$ and $\eta_{\mathrm{ES}}^{\mathrm{dis}}$ are the charging efficiency and discharging efficiency of the power storage device, respectively, $\eta_{\mathrm{HS}}^{\mathrm{ch}}$ and $\eta_{\mathrm{HS}}^{\mathrm{dis}}$ are the charging efficiency and discharging efficiency of the heat storage device, respectively, $\eta_{\mathrm{GS}}^{\mathrm{ch}}$ and $\eta_{\mathrm{GS}}^{\mathrm{dis}}$ are the charging efficiency and discharging efficiency of the gas storage device, respectively, $P_{\mathrm{ES},t}^{\mathrm{ch}}$ and $P_{\mathrm{ES},t}^{\mathrm{dis}}$ are the charging power and discharging power of the power storage device, respectively, $P_{\mathrm{HS},t}^{\mathrm{ch}}$ and $P_{\mathrm{HS},t}^{\mathrm{dis}}$ are the charging power and discharging power of the heat storage device, respectively, $P_{\mathrm{GS},t}^{\mathrm{ch}}$ and $P_{\mathrm{GS},t}^{\mathrm{dis}}$ are the charging power and discharging power of the gas storage device, respectively.

NEARLY-ZERO CARBON PARKS TWO-STAGE ROBUST OPTIMAL SCHEDULING MODEL

Optimized Scheduling Model

NZCP is powered by all renewable energy sources, but wind power, photovoltaic power and multiple loads have strong uncertainties. According to the traditional polyhedral uncertainty set form, the uncertainty factors are expressed as (Sun et al., 2020):

$$P_t^{\mathrm{WP}} \in \left[\hat{P}_t^{\mathrm{WP}} - \Delta P_t^{\mathrm{WP}}, \hat{P}_t^{\mathrm{WP}} + \Delta P_t^{\mathrm{WP}}\right] \tag{44}$$

$$\sum_{t=1}^{T} \frac{\hat{P}_t^{\mathrm{WP}} - P_t^{\mathrm{WP}}}{\Delta P_t^{\mathrm{WP}}} \leq \Gamma^{\mathrm{WP}} \tag{45}$$

$$P_t^{\mathrm{PV}} \in \left[\hat{P}_t^{\mathrm{PV}} - \Delta P_t^{\mathrm{PV}}, \hat{P}_t^{\mathrm{PV}} + \Delta P_t^{\mathrm{PV}}\right] \tag{46}$$

$$\sum_{t=1}^{T} \frac{\hat{P}_t^{\mathrm{PV}} - P_t^{\mathrm{PV}}}{\Delta P_t^{\mathrm{PV}}} \leq \Gamma^{\mathrm{PV}} \tag{47}$$

$$L_{i,t} \in \left[\hat{L}_{i,t} - \Delta L_{i,t}, \hat{L}_{i,t} + \Delta L_{i,t}\right] \tag{48}$$

$$\sum_{t=1}^{T} \frac{\hat{L}_{i,t} - L_{i,t}}{\Delta L_{i,t}} \leq \Gamma^{L_i} \tag{49}$$

where P_t^{WP}, $\hat{P}_t^{\mathrm{WP}}$ and ΔP_t^{WP} are the output uncertainty, forecast value and fluctuation deviation value of wind power at time t respectively, P_t^{PV}, $\hat{P}_t^{\mathrm{PV}}$ and ΔP_t^{PV} are the PV output uncertainty, predicted value, and fluctuation deviation value at time t respectively, $L_{i,t}$, $\hat{L}_{i,t}$ and $\Delta L_{i,t}$ are the uncertainty, predicted value and fluctuation deviation value of i load at time t respectively, $i \in [E, H, G]$, Γ^{WP}, Γ^{PV} and Γ^{L_i} are the uncertain adjustment parameters introduced for wind power output, photovoltaic output, and load power, respectively, the value range is an integer within the period 0–24.

After the polyhedron uncertainty set is established, the model changes from a single stage to a two-stage model, and **Eq. 16** is transformed into the following two-stage robust hybrid optimal scheduling model:

$$\min_{x \in X} c^{\mathrm{T}} x + \max_{z \in Z} \min_{y \in Y} b^{\mathrm{T}} y \tag{50}$$

$$\begin{aligned} s.t.\quad & Ax \leq h \\ & By + Cz = d \\ & My + Nz \leq u \\ & \|Qy\| \leq q \end{aligned} \tag{51}$$

where x is the first-stage optimization variable, corresponding to the start-stop state of each controllable device, the start-up state of the equipment is 1, and the stop state is 0, y and z is the second-stage optimization variable, representing the output, wind, and load uncertain variables corresponding to each equipment respectively, c and b is the coefficient matrix corresponding to the objective function, A, B, C, M, N and Q are a sparse matrix of variables under the corresponding constraints, h, d, u and q are constant column vector.

The established NZCP two-stage robust optimal scheduling model decomposes the two-stage problem into the first-stage main problem and the second-stage sub-problem. The main problem is to optimize the start-stop state of each controllable device at each time period under extreme conditions of wind and solar output and original load. The sub-problem is based on the optimization scheme obtained from the main problem, and the output of each equipment in the NZCP is adjusted according to the uncertain variables of wind power, photovoltaic power generation and load to achieve the optimization goal of minimum net cost.

Solution Method

The C&CG algorithm is used to decompose the above two-stage robust optimal scheduling model into a main problem and sub-problems (Liu et al., 2018). The main problem is:

$$\min_{x \in X} c^{\mathrm{T}} x + \bar{\lambda} \tag{52}$$

$$\begin{aligned} s.t.\quad & Ax \leq h \\ & \bar{\lambda} \geq b^{\mathrm{T}} y^k \\ & By^k + Cz^k = d \\ & My^k + Nz^k \leq u \\ & \|Qy^k\| \leq q \end{aligned} \tag{53}$$

where k is the current iteration number, y^k is the variable at the kth iteration, z^k is the value of the uncertain variable z in extreme scenarios obtained after the kth iteration.

The sub-problems is:

$$\max_{z \in Z} \min_{y \in Y} b^{\mathrm{T}} y \tag{54}$$

$$\begin{aligned} s.t.\quad & Ax^* \leq h \\ & By + Cz = d \\ & My + Nz \leq u \\ & \|Qy\| \leq q \end{aligned} \tag{55}$$

In a given scenario, the inner min problem is a second-order cone programming problem, which is obtained by combining dual theory with the outer max problem:

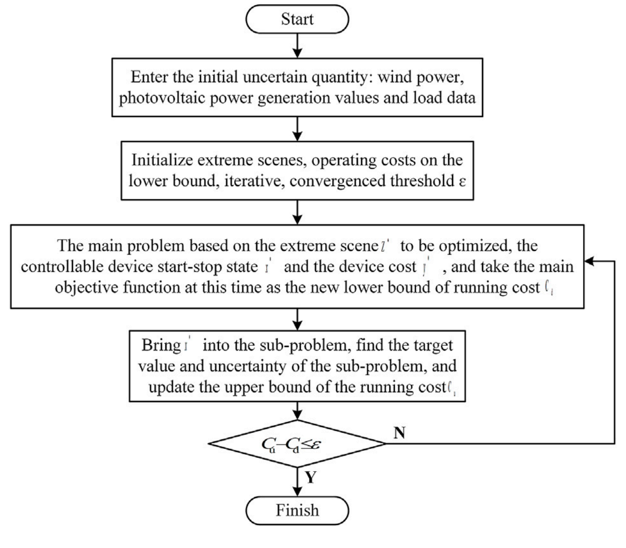

FIGURE 2 | Algorithm flow chart.

$$\max_{z\in Z,\vartheta_1,\vartheta_2,\vartheta_3} (d - Cz)^{\mathrm{T}}\vartheta_1 + (u - Nz)^{\mathrm{T}}\vartheta_2 + q^{\mathrm{T}}\vartheta_3 \tag{56}$$

$$\begin{aligned} s.t.\quad & B^{\mathrm{T}}\vartheta_1 + M^{\mathrm{T}}\vartheta_2 + Q^{\mathrm{T}}\vartheta_3 \le b \\ & \vartheta_1 \ge 0, \vartheta_2 \ge 0, \vartheta_3 \ge 0 \end{aligned} \tag{57}$$

When **Fq. 56** takes the maximum value, the value of the uncertain variable z should be at the boundary of the uncertainty set fluctuation interval established in this paper (Wang et al., 2019). At the same time, when the wind and solar output is at the lower limit and the load is at a peak, the system operating cost is the highest, that is, in an extreme scenario, which can be expressed as:

$$\begin{aligned} z_{\mathrm{WP}} &= \frac{\hat{P}_t^{WP} - P_t^{WP}}{\Delta P_t^{WP}} \\ z_{\mathrm{PV}} &= \frac{\hat{P}_t^{PV} - P_t^{PV}}{\Delta P_t^{PV}} \\ z_{i,L} &= \frac{\hat{L}_{i,t}^{i,L} - L_{i,t}^{i,L}}{\Delta L_{i,t}^{i,L}} \end{aligned} \tag{58}$$

where z_{WP}, z_{PV} and $z_{i,\mathrm{L}}$ are the binary variable. When the value is 1, it means that the boundary of the interval is obtained. At this time, **Eqs 56**, **57** are rewritten as:

$$\max_{z,\vartheta_1,\vartheta_2,\vartheta_3} (d - C\hat{z})^{\mathrm{T}}\vartheta_1 + (u - N\hat{z})^{\mathrm{T}}\vartheta_2 + q^{\mathrm{T}}\vartheta_3 + \Delta z Z_m \tag{59}$$

$$\begin{aligned} s.t.\quad & B^{\mathrm{T}}\vartheta_1 + M^{\mathrm{T}}\vartheta_2 + Q^{\mathrm{T}}\vartheta_3 \le b \\ & 0 \le Z_m \le \bar{\vartheta} z \\ & \sum_{t=1}^{T} z_{\mathrm{WP}} \le \Gamma^{\mathrm{WP}} \\ & \sum_{t=1}^{T} z_{\mathrm{PV}} \le \Gamma^{\mathrm{PV}} \\ & \sum_{t=1}^{T} z_{i,\mathrm{L}} \le \Gamma^{L_i} \\ & \vartheta_1 \ge 0, \vartheta_2 \ge 0, \vartheta_3 \ge 0 \end{aligned} \tag{60}$$

where $\bar{\vartheta}$ is the upper bound of the dual variable.

After the above derivation and transformation, the two-stage robust optimization scheduling model is finally decoupled from the main problem **(52)** and the sub-problem **(59)**, and then solved by the C&CG algorithm, in which the sub-problem can be solved by calling the Cplex solver on the Matlab platform, the algorithm flow is shown in **Figure 2**. CCGPP carbon emission intensity a; P2G-CCGPP fixed energy consumption b; carbon emission allowance price c.

CASE SIMULATION

Example Basic Data

The simulation analysis is based on the operation data of the Park Integrated Energy System in a region of northern China. In NZCP, the forecast curves of wind power and photovoltaic power generation are shown in **Figure 3**; The daily load forecast curve is shown in **Figure 4**; the energy price forecast curve is shown in **Figure 5**; the operating parameters of the energy conversion equipment and energy storage equipment are shown in **Table 1**; The daily load forecast curve is shown in **Figure 4**; the energy price forecast curve is shown in **Figure 5**; the

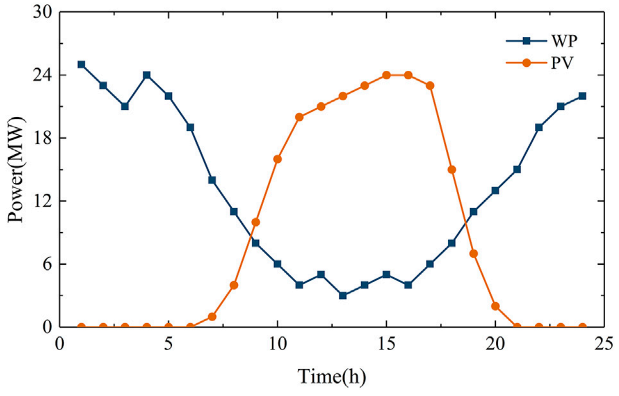

FIGURE 3 | Forecast curve of wind power and photovoltaic power generation.

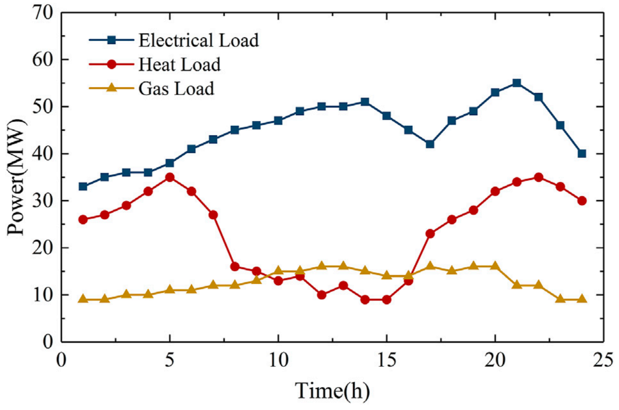

FIGURE 4 | Forecast curve of wind power and photovoltaic power generation.

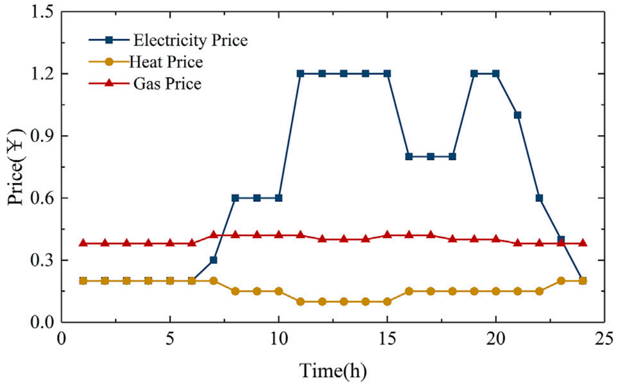

FIGURE 5 | Forecast curve of electricity, heat and gas prices.

TABLE 1 | Operating parameters of energy conversion equipment and energy storage equipment.

Equipment Type	Power upper limit/MW	Power lower limit/MW	Ramp rate/(MW/min)
EB	0	20	1
ES	0	35	—
HS	0	15	—
GS	0	5	—
P2G	4	30	2

operating parameters of the energy conversion equipment and energy storage equipment are shown in **Table 1**; CCGPP carbon emission intensity $\theta_{CO_2,t} = 0.76/\mathrm{MW}\cdot\mathrm{h}$; P2G-CCGPP fixed energy consumption $P_{F,t} = 15\mathrm{MW}$; carbon emission allowance price $\gamma_{C,t} = 129E/\mathrm{t}$; The waste treatment capacity of Waste Incineration power generation equipment is 1500t/d, and the rated power is 30 MW; The manure treatment capacity of the Manure Treatment facility is 350t/d, and the rated power is 6 MW.

Optimizing Results Analysis

In order to verify the effectiveness of the proposed CCGPP-P2G-WD collaborative model and the NZCP two-stage robust optimal scheduling model, the following four scenes are set up to simulate and analyze the optimal model proposed in this paper:

Scene 1. Only P2G is considered to participate in the coordinated operation of the park's comprehensive energy system, and all energy shortages are purchased from the external network.

Scene 2. WD is added On the basis of Scene 1, but the synergy between its energy transfer characteristics and the comprehensive energy system of the park is not considered.

Scene 3. CCGPP is added on the basis of Scene 1, but the synergy between its energy transfer characteristics and the comprehensive energy system of the park is not considered.

Scene 4. Adopt the proposed CCGPP-WD-P2G collaborative operation mode, and use the proposed operation strategy to coordinate and optimize with the park's comprehensive energy system.

On the basis of meeting the NZCP load requirements, the multi-energy optimization operation effect of each device in Scene 4 is shown in **Figures 6–8**.

In Scene 4, the CCGPP-WD-P2G collaborative mode provides certain energy support for the power grid, heat grid, and gas grid. Combined with the forecast curve of electricity, heat and gas load of renewable energy, it can be seen that in the period of 16–18 and 23–6, the system is in a low period of electricity consumption, and the power generation of renewable energy cannot be fully absorbed. Because of the introduction of a flue gas storage device, the high energy consumption of flue gas treatment of WD provides a way to absorb abandoned wind. At the same time, CCGPP transfers the energy consumption of carbon capture during the peak period of energy consumption to the period of low load by introducing solution storage, which further absorbs the abandonment of wind and light on the basis of ensuring the reliability of energy supply during the peak period. Then, the CO_2 captured by CCGPP is used as the raw material in the P2G production process, and the waste electricity is fully absorbed by P2G. It can be seen from **Figure 5** that the electricity price at this time is relatively low. On the basis of fully absorbing the abandoned wind and solar energy, the electricity storage equipment is charged by purchasing energy from the external network to adjust the load peak period.

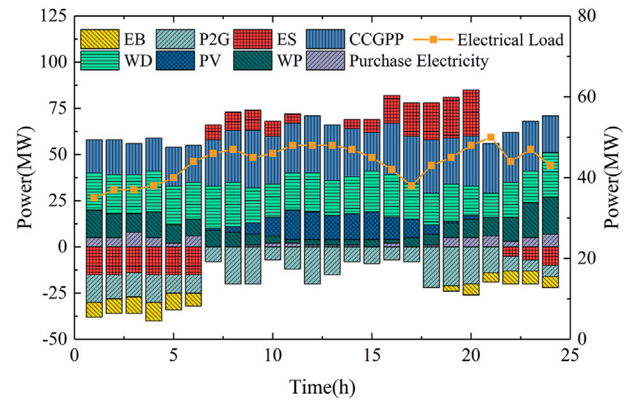

FIGURE 6 | Power balance curve of Scene 4.

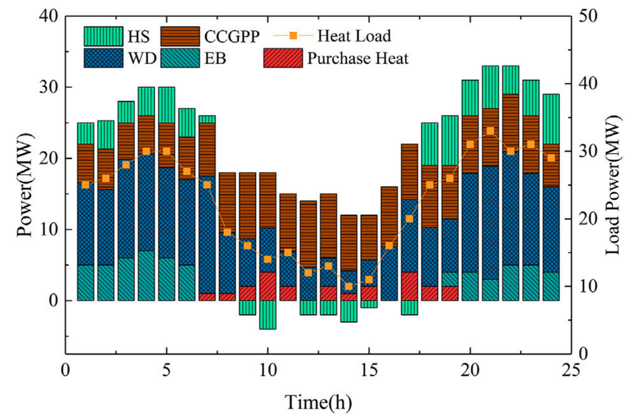

FIGURE 7 | Thermal balance curve of Scene 4.

During the period of 7–10, the output of wind power decreases. It can be seen from **Figures 6–10** that CCGPP-WD is the main power source at this time. At the same time, the energy consumption of carbon capture and flue gas treatment is transferred to the load trough period, which improves the

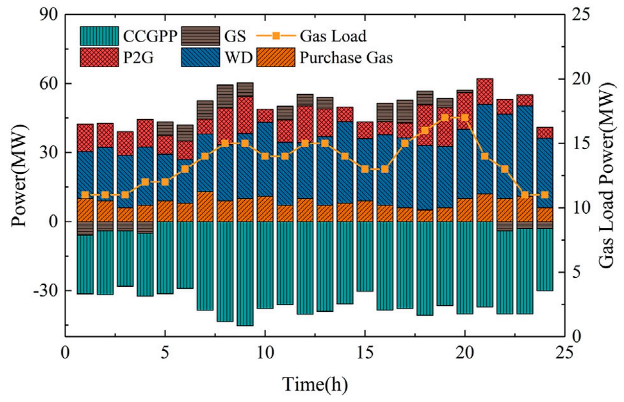

FIGURE 8 | Gas balance curve of Scene 4.

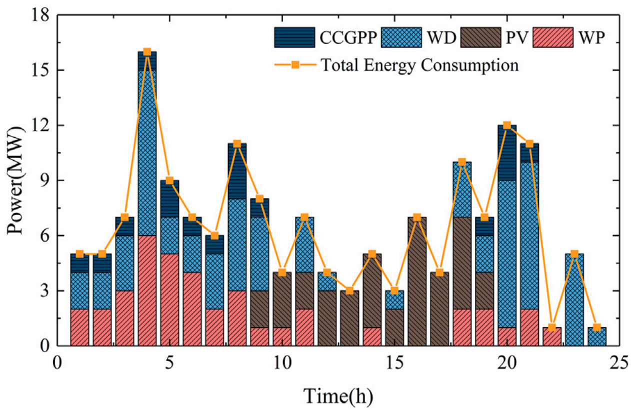

FIGURE 10 | Flue gas treatment energy consumption curve.

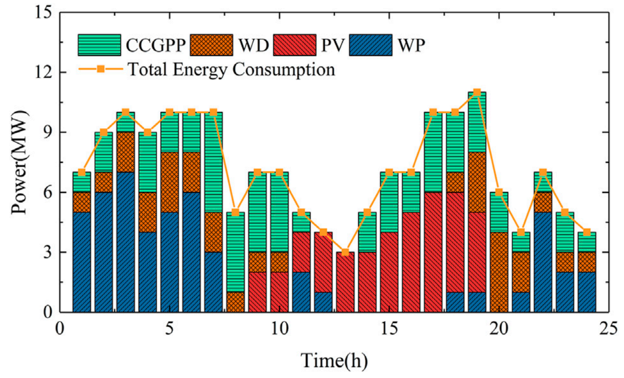

FIGURE 9 | Carbon capture energy consumption curve.

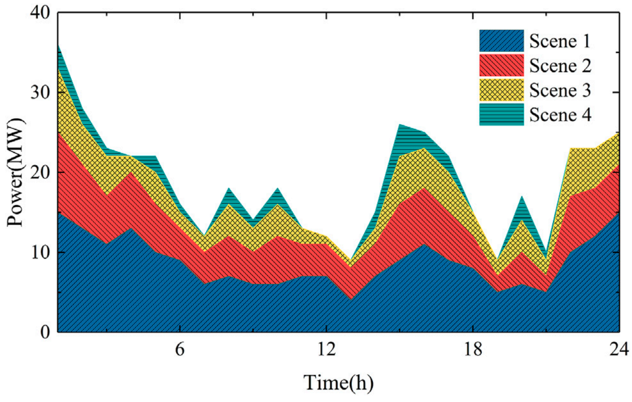

FIGURE 11 | Wind power and photovoltaic power curtailment in various scenes.

energy supply efficiency of CCGPP-WD. The heat load demand is low, and the heat energy provided by the CCGPP-WD is stored by the heat storage device. During the 18-6 period, the heat load is at the peak period, and the heat storage device cooperates with CCGPP-WD and EB to supply energy for the heat load.

The manure treatment equipment in WD obtains natural gas by purifying biogas, and P2G converts electricity into natural gas through CO_2 captured by CCGPP as a raw material. These two types of gas sources provide natural gas for CCGPP. The gas shortfall is purchased from the mainnet.

Combining **Figures 6–8**, it can be seen from the optimized load curve that, compared with the load prediction curve before optimization, the load peak-to-valley difference in Scene 4 is smaller. Therefore, the CCGPP-WD-P2G cooperative mode realizes load shaving peaks and valleys.

From **Figures 9**, **10**, it can be seen that during the period 10–16, the output of photovoltaic power generation is mainly used for carbon capture and flue gas treatment. The volatility problem of photovoltaics is well resolved by the CCGPP-WD-P2G synergistic mode introduced into solution storage and flue gas storage devices.

It can be seen from **Figure 11** that in Scene 1, P2G and energy storage devices are limited by capacity constraints and ramp rate constraints, resulting in a large amount of power abandonment, and the power abandonment rate reaches 40.19%. In Scene 2, the WD flue gas treatment process consumes a certain amount of abandoned wind and light, and the abandoned electricity rate is 24.19%. In Scene 3, the carbon capture process of CCGPP absorbs a lot of abandoned wind and light, and the electricity abandonment rate is 16.57%. Scene 4 adopts the CCGPP-WD-P2G collaborative mode to shift the energy consumption of carbon capture and flue gas treatment in time and space, and mainly uses abandoned wind and sunlight for energy supply, so the system has the strongest ability to absorb renewable energy in this scene, the power abandonment rate is only 5.33%. It can be seen that the CCGPP-WD-P2G collaborative mode improves the renewable energy consumption capacity on the basis of ensuring the balance of energy supply and demand in the system. The optimization results of each unit cost and total net cost of the four scenes proposed in this paper are shown in **Table 2**. Compared with Scene 1, the introduction of WD reduces the cost of electricity purchase by 7.96×10^3 ¥, the heating cost of 6.29×10^3 ¥ and the gas purchase cost of 5.79×10^3 ¥, and the total cost is reduced by 3.72×10^3 ¥. Combining with **Table 2** and **Figure 12**, it can be seen that although WD provides energy support for the power grid, heat grid and gas grid in the process of realizing waste reduction, the

TABLE 2 | Comparison of optimization results in different scenes (*10^3¥).

Type	Scene 1	Scene 2	Scene 3	Scene 4
Electricity purchase cost	81.19	73.23	58.16	38.41
Heat purchase cost	20.46	14.17	10.13	6.97
Gas purchase cost	23.42	17.63	32.41	20.58
Equipment start and stop costs	12.16	14.32	15.79	16.11
Operation and maintenance costs of renewable energy power generation equipment	8.95	8.32	7.69	7.11
Transferable and interruptible load compensation costs	14.45	17.62	19.36	27.55
EB operating cost	4.19	4.07	3.99	3.96
P2G operating costs	11.31	10.26	8.10	7.07
WD operating cost	0	7.52	0	4.24
CCGPP operating costs	0	0	6.49	6.72
Carbon sequestration cost	0	0	10.13	20.16
Carbon emission allowance revenue	6.34	1.07	10.16	16.12
Net cost	169.79	166.07	162.09	142.76

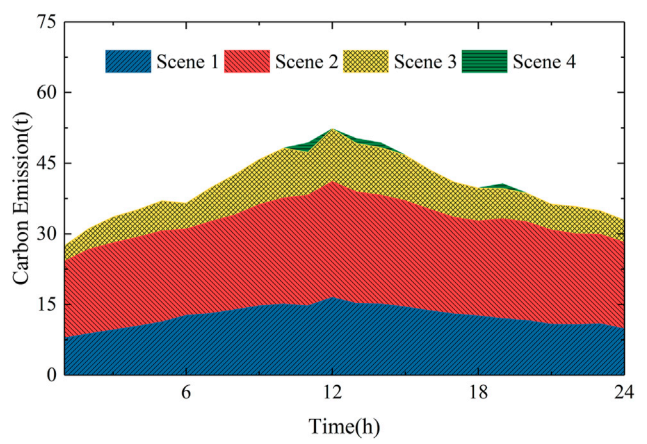

FIGURE 12 | Carbon emissions in each scene.

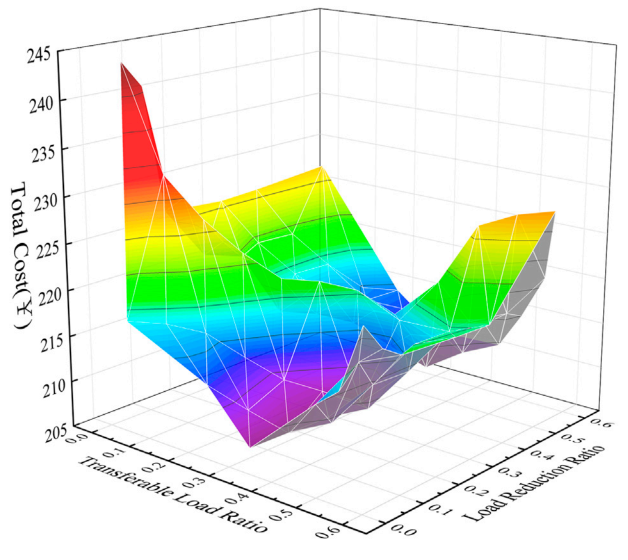

FIGURE 13 | The relationship between demand response load proportional coefficient and cost.

carbon emission increases by 64.47%. Compared with Scene 1, in Scene 3, the electricity purchase cost is reduced by 23.03×10^3 ¥, the heat purchase cost is reduced by 10.33×10^3 ¥, and the gas purchase cost is increased by 8.99×10^3 ¥. It can be seen that CCGPP provides a certain energy support for the system, but the gas source in the system is insufficient, which increases the cost of gas purchase. Combined with **Table 2** and **Figure 12**, it can be seen that after the introduction of CCGPP, carbon emissions were reduced by 41.83% through carbon capture and carbon sequestration. Combining **Table 2** and **Figures 11**, **12**, it can be seen that Scene 4 adopts the CCGPP-WD-P2G collaborative mode proposed in this paper, which reduces the cost of electricity purchase by 42.78×10^3 ¥, the cost of sufficient heat by 13.49×10^3 ¥ and 2.84×10^3 ¥ gas purchase cost. It can be seen that carbon capture provides P2G with a large amount of CO_2 as a raw material for gas production, which saves gas purchase costs and P2G operating costs. Because carbon capture and carbon sequestration technology reduces carbon emissions, NZCP's participation in carbon emission allowance trading increases revenue by 9.724×10^3 ¥, which in turn reduces the total cost by 27.03×10^3 ¥. At the same time, the absorbing capacity of renewable energy has been increased by 86.73%, and the carbon emission has been reduced by 98.33%, which has improved the absorbing capacity of renewable energy, and achieved the goal of near-zero carbon emission while maintaining a high energy balance in the system.

According to **Figure 13**, it can be seen that the load that can be reduced and the load that can be shifted can affect the net cost. It can be seen that with the increase of the proportional coefficient of demand response, the operating cost of the system is gradually reduced. When the proportional coefficient of the demand response of the shiftable load is 0.3 and the proportional coefficient of the demand response of the curtailable load is 0.2, the operating cost of the system is the lowest. With the gradual increase of the proportional coefficient of the translatable load demand response, the operating cost of the system also increases gradually. Therefore, an appropriate proportion of loads participating in demand response is beneficial for multi-time-scale energy regulation of NZCP. However, an excessively high load demand response proportional coefficient will lead to an increase in energy regulation compensation, and at the same time, it will affect the normal operation of small industrial loads and commercial loads in the park, and reduce system benefits.

CONCLUSION

In order to fully dispatch zero-carbon resources, form a production system for carbon recycling, and achieve near-zero carbon emissions while improving system revenue. In this paper, the CCGPP-WD-P2G collaborative model is proposed on the basis of full renewable energy supply, which realizes the collaborative optimization of zero-carbon resources in the park. Four groups of scenes were proposed and compared, and the following conclusions were drawn:

1) The CCGPP-WD-P2G collaborative mode is proposed to participate in the optimal scheduling of NZCP, which makes full use of the adjustment ability of zero-carbon resources in the system and improves the economy of the system maintaining a high energy balance level.
2) In the CCGPP-WD-P2G collaborative mode, the captured CO_2 is used as the raw material for P2G gas production, which reduces carbon emissions while reducing the operating cost of P2G, and provides gas source support for CCGPP, realizing the recycling of CO_2.
3) The flue gas storage device and the CO_2 solution storage device are respectively introduced to decouple the flue gas treatment link, the carbon capture link and the power generation link, and the renewable energy output is shifted in time and space. The load peak-valley curve is effectively stabilized, the renewable energy consumption capacity is improved, and the energy supply pressure on the upper energy grid is reduced.
4) A reasonable proportion of interruptible loads and transferable loads can be used to participate in scheduling, which can effectively reduce the net cost of system operation and improve the flexibility of energy supply and demand in the system.

DATA AVAILABILITY STATEMENT

The raw data supporting the conclusion of this article will be made available by the authors, without undue reservation.

AUTHOR CONTRIBUTIONS

ZY was responsible for the modeling and writing work of the paper. TZ was responsible for the main idea of the paper. YZ was responsible for the simulation part.

FUNDING

This work was supported by Key R&D Program of Liaoning Province (2020JH2/10300101), Liaoning Revitalization Talents Program (XLYC1907138) and Key R&D Program of Shenyang (GG200252).

REFERENCES

Cao, W., Wang, Z., Huang, J., Wu, B., Tai, J., Zhao, J., et al. (2020). Disposal Pattern of Municipal Solid Waste and Influencing Factors: Based on Data of 134 Countries [J]. *Acta Sci. Circumstantiae* 40 (8), 3062. doi:10.13671/.hjkxxb.2020.0044

Chen, Q. J. Z., Kang, C., and Ming, H. (2012). Analysis on Relation Between Power Generation and Carbon Emission of Carbon Capture Power Plant in Different Operation Modes[J]. *Automation Electr. Power Syst.* 36 (18), 109r. doi:10.3969/j.issn.1000-1026.2012.18.020

Cheng, Y., Du, E., Tian, X., Zhang, N., and Kang, C. (2020). Carbon Capture Power Plants in Power Systems: Review and Latest Research Trends[J]. *J. Glob. Energy Interconnect.* 3 (4), 33. doi:10.19705/j.cnki.issn2096-5125.2020.04.003

Cui, Y., Zeng, P., Wang, Z., Wang, M., Zhang, J., and Zhao, Y. (2021b). Low-Carbon Economic Dispatch of Electricity-Gas-Heat Integrated Energy System with Carbon Capture Equipment Considering Price-Based Demand Response[J]. *Power Syst. Technol.* 45 (2), 447. doi:10.13335/j.1000-3673.pst.2020.0100a

Cui, Y., Zeng, P., Wang, Z., Wang, M., Zhang, J., and Zhao, Y. (2021a). Multiple Time Scales Scheduling Strategy of Wind Power Accommodation Considering Energy Transfer Characteristics of Carbon Capture Power Plant[J]. *Proc. CSEE* 41 (3), 946. doi:10.13334/j.0258-8013.pcsee.200120

Fang, S., Zhou, R., Xu, F., Feng, J., Cheng, Y., and Li, B. (2020). Optimal Operation of Integrated Energy System for Park Micro-Grid Considering Comprehensive Demand Response of Power and Thermal Loads[J]. *Proc. CSU-EPSA* 32 (1), 50. doi:10.19635/j.cnki.csu-epsa.000217

Gao, S., Zou, Z., and Liu, Y. (2019). Coordination and Optimization of Combined Heat and Power System Considering Multi-Type Demand-Response Load[J]. *Electr. Power Constr.* 40 (10), 9. doi:10.3969/j.issn.1000-7229.2019.10.002

He, C., Zhang, X., Liu, T., and Wu, L. (2019). Distributionally Robust Scheduling of Integrated Gas-Electricity Systems with Demand Response. *IEEE Trans. Power Syst.* 34 (5), 3791–3803. doi:10.1109/tpwrs.2019.2907170

Hu, X., Zhang, H., and Ma, D. (2021). A tnGAN-Based Leak Detection Method for Pipeline Network Considering Incomplete Sensor Data. *IEEE Trans. Instrum. Meas.* 70 (1-10), 3510610. doi:10.1109/tim.2020.3045843

Jiang, M., Cheng, G., and Zhao, J. (2021). Research on the Improvement of DDPG Multifunctional Industrial Park Typical Daily Scheduling[J/OL]. *Power Syst. Technol.*, 1. doi:10.13335/j.1000-3673.pst.2021.0998

Liu, Y., Guo, L., and Wang, C. (2018). Economic Dispatch of Microgrid Based on Two Stage Robust Optimization[J]. *Proc. CSEE* 38 (14), 4013

National Development and Reform Commission (2022). National Energy Board. Notice on Printing and Distributing the "14th Five-Year Plan for Modern Energy System"[EB/OL]. https://www.ndrc.gov.cn/xwdt/tzgg/202203/t20220322_1320017.html?code=&state=123.

Sun, K., Zhang, Q., Wang, L., Li, H., Lu, M., and Hu, Z. (2020). Two-Stage Robust Planning for Microgrid Considering Security Margin. *Power Syst. Technol.* 44 (12), 4617. doi:10.13335/j.1000-3673.pst.2020.0292a

Teng, Y., Sun, P., Hui, Q., and Chen, Z. (2021). Optimal Operation Model of Micro-Energy Network Considering Classification and Disposal of Biomass Waste. *[J] Automation Electr. Power Syst.* 45 (15), 55. doi:10.7500/AEPS20200726003

Wang, R., Sun, Q., Hu, W., Li, Y., Ma, D., and Wang, P. (2021c). SoC-Based Droop Coefficients Stability Region Analysis of the Battery for Stand-Alone Supply Systems with Constant Power Loads. *IEEE Trans. Power Electron.* 36 (7), 7866–7879. doi:10.1109/tpel.2021.3049241

Wang, R., Sun, Q., Ma, D., and Liu, Z. (2019). The Small-Signal Stability Analysis of the Droop-Controlled Converter in Electromagnetic Timescale. *IEEE Trans. Sustain. Energy* 10 (3), 1459–1469. doi:10.1109/tste.2019.2894633

Wang, R., Sun, Q., Tu, P., Xiao, J., Gui, Y., and Wang, P. (2021a). Reduced-Order Aggregate Model for Large-Scale Converters with Inhomogeneous Initial Conditions in DC Microgrids. *IEEE Trans. Energy Convers.* 36 (3), 2473–2484. doi:10.1109/tec.2021.3050434

Wang, Z., Teng, Y., Hu, H., and Chen, Z. (2021d). Multi-Energy System Optimal Model in Consideration of Coordinate Disposal of Power Grid and Gas Network and Waste[J]. *High. Volt. Eng.* 47 (1), 63. doi:10.13336/j.1003-6520.hve.20201329

Wang, Z., Teng, Y., Hui, Q., and Chen, Z. (2021b). A Sustainable Development Multi-Energy System Planning Method Incorporating the Demand of Waste Disposal and Peak Shaving[J]. *Proc. CSEE* 41 (11), 3781. doi:10.13334/j.0258-8013.pcsee.201021

Wei, C., Xu, J., Liao, S., Sun, Y., Jiang, Y., Ke, D., et al. (2018). A Bi-Level Scheduling Model for Virtual Power Plants with Aggregated Thermostatically Controlled Loads and Renewable Energy. *Appl. Energy* 224, 659–670. doi:10.1016/j.apenergy.2018.05.032

Xv, J., Shi, J., Zhang, J., Hao, R., and Chen, Q. (2018). Bi-Level Optimization of Urban Integrated Energy System Based on Biomass Combined Heat and Power Supply[J]. *Automation Electr. Power Syst.* 42 (14), 23. doi:10.7500/AEPS20170817003

Yang, H., Xie, M., Huang, W., Zhang, M., Shi, B., Hong, Y., et al. (2021). Low-Carbon Economic Operation of Urban Integrated Energy System Including Waste Treatment[J]. *Power Syst. Technol.* 45 (9), 3545. doi:10.13335/j.1000-3673.pst.2020.1676

Zhang, H., Wang, L., Van herle, J., Maréchal, F., and Desideri, U. (2020). Techno-Economic Evaluation of Biomass-To-Fuels with Solid-Oxide Electrolyzer. *Appl. Energy* 270, 115113. doi:10.1016/j.apenergy.2020.115113

Zhong, W., Huang, S., Cui, Y., Xu, J., and Zhao, Y. (2020). W-S-C Capture Coordination in Virtual Power Plant Considering Source-Load Uncertainty[J]. *Power Syst. Technol.* 44 (9), 3424. doi:10.13335/j.1000-3673.pst.2019.1986

Zhou, C., Zheng, J., Jing, Z., Wu, Q., and Zhou, X. (2018). Multi-Objective Optimal Design of Integrated Energy System for Park-Level Microgrid[J]. *Power Syst. Technol.* 42 (6), 1687. doi:10.13335/j.1000-3673.pst.2018.0280

Zhou, R., Chen, Y., Yang, W., Wang, Y., Xu, J., and Zhu, J. (2019). Two-Stage Optimal Dispatching of Wind Power-Waste Incineration Virtual Power Plant with Flue Gas Storage Device[J]. *Electr. Power* 52 (2), 78. doi:10.11930/j.issn.1004-9649.201806147

Zhou, R., Xiao, J., Tang, X., Zheng, Q., Lu, J., and Cao, J. (2018). Coordinated Optimization of Carbon Utilization Between Power-To-Gas Renewable Energy Accommodation and Carbon Capture Power Plant [J]. *Electr. Power Autom. Equipmen.* 38 (7), 61. doi:10.16081/j.issn.1006-6047.2018.07.008

Conflict of Interest: The authors declare that the research was conducted in the absence of any commercial or financial relationships that could be construed as a potential conflict of interest.

frontiers | Frontiers in Energy Research

ORIGINAL RESEARCH
published: 22 July 2022
doi: 10.3389/fenrg.2022.952420

A Transformer-Based Multi-Entity Load Forecasting Method for Integrated Energy Systems

Zhiyu Wang , Zhen Zhu , Geyang Xiao, Bing Bai and Yinjie Zhang*

Intelligent Network Research Institute, Zhejiang Lab, Hangzhou, China

Energy load forecasting is a critical component of energy system scheduling and optimization. This method, which is classified as a time-series forecasting method, uses prior features as inputs to forecast future energy loads. Unlike a traditional single-target scenario, an integrated energy system has a hierarchy of many correlated energy consumption entities as prediction targets. Existing data-driven approaches typically interpret entity indexes as suggestive features, which fail to adequately represent interrelationships among entities. This paper, therefore, proposes a neural network model named Cross-entity Temporal Fusion Transformer (CETFT) that leverages a cross-entity attention mechanism to model inter-entity correlations. The enhanced attention module is capable of mapping the relationships among entities within a time window and informing the decoder about which entity in the encoder to concentrate on. In order to reduce the computational complexity, shared variable selection networks are adapted to extract features from different entities. A data set obtained from 13 buildings on a university campus is used as a case study to verify the performance of the proposed approach. Compared to the comparative methods, the proposed model achieves the smallest error on most horizons and buildings. Furthermore, variable importance, temporal correlations, building relationships, and time-series patterns in data are analyzed with the attention mechanism and variable selection networks, therefore the rich interpretability of the model is verified.

Keywords: integrated energy system, time-series forecasting, multi-entity forecasting, load forecasting, neural networks, transformer network

Edited by:
Qiuye Sun,
Northeastern University, China

Reviewed by:
Jingwei Hu,
State Grid Liaoning Power Company Limited Economic Research Institute, China
Tianyi Li,
Aalborg University, Denmark
Ning Zhang,
Anhui University, China

****Correspondence:***
Geyang Xiao
xgyalan@outlook.com

Specialty section:
This article was submitted to Smart Grids, a section of the journal Frontiers in Energy Research

Received: *25 May 2022*
Accepted: *10 June 2022*
Published: *22 July 2022*

Citation:
Wang Z, Zhu Z, Xiao G, Bai B and Zhang Y (2022) A Transformer-Based Multi-Entity Load Forecasting Method for Integrated Energy Systems. Front. Energy Res. 10:952420. doi: 10.3389/fenrg.2022.952420

1 INTRODUCTION

The integrated energy system (IES) is regarded as one of the most important forms of modern energy systems (Tahir et al., 2021). A comprehensively optimized IES is capable of delivering considerable energy savings, pollution reduction advantages, better system stability, etc. (Zhang et al., 2020; Wang et al., 2022). One key specification of IES is the demand pattern of the energy end-users. Therefore, demand forecasting can provide insights to enhance system design, scheduling strategy, and control optimization for IES (Dittmer et al., 2021).

Statistic and machine learning techniques have long been applied for the demand forecasting of end-users. The former techniques are straightforward strategies that focus on the target time series' statistics. The latter techniques are trained with a period of load data accompanied with auxiliary information before making predictions based on recent data. Typical statistic models include the simple linear regression model, moving average (MA) strategy, and autoregression (AR) algorithm. Auto-Regressive Integrated Moving Average (ARIMA) is a combination of MA and AR, which includes stationary stochastic variables in the non-stationary stochastic process. As a result, it is capable of reproducing time series patterns (Newsham and Birt, 2010). Notable traditional machine learning methods include Partial Least Squares Regression (PLSR), Ridge Regression (RR), and Support Vector Regression (SVR). PLSR basically uses the covariance between the input and output variables instead of analyzing the hyperplanes with the least variance between the dependent and independent variables (Hosseinpour et al., 2016). In RR models, a shrinkage estimator is added to the diagonal elements of the correlation matrix (Sun et al., 2019). SVR leverages kernel functions for modeling the nonlinear transformation. These models often ignore the chronological order of variables and struggle to properly model the temporal features in the data.

Time-series forecasting approaches based on deep learning have significantly grown in recent years, with the development in neural network algorithms, available data, and hardware power. Recurrent neural networks (RNN) (Rumelhart and McClelland, 1987) is a category of neural network suitable for time-series modeling. RNNs use hidden states that are iteratively supplied back to the network for temporary time-related information representation and storage, as implied by the name (Tang et al., 2021). This gives the model memory for temporal properties. However, RNN suffers from the vanishing gradient problem (Ribeiro et al., 2020). The hidden state will gradually degrade during simulation for long-term sequences. To alleviate this problem, improved implementation of RNN including Long Short-Term Memory (LSTM) (Hochreiter and Schmidhuber, 1997) and GRU Gated Recurrent Unit (GRU) (Chung et al., 2014) have been proposed. These networks introduce a gate for controlling time-series information. The gates assist the network in selecting critical data that requires long-term memory. As a result, both networks can make predictions for extended periods of time before the vanishing gradient problem appears Ayodeji et al. (2022).

The Transformer (Vaswani et al., 2017), which employs an attention mechanism to describe cross-time interactions for time series, has recently become one of the most popular network architectures. The attention module accepts all time frame inputs and provides weights that directly map the impact of the previous time frame on future targets. Therefore, the gradient vanishing problem due to long-time dependence is eliminated. Another benefit of the transformer is that the network grants better interpretability. Natural language processing (Tetko et al., 2020) and computer vision (Dosovitskiy et al., 2021), two of the most important domains of artificial intelligence, have both benefited greatly from the transformer. The better modeling capabilities of this model, however, come at the cost of more computation. The computational complexity of attention to explicitly simulate the cross-time relationship is $O(n^2)$, where n is the scale of time frames. In comparison, the computational complexity of most neural network implementations, such as GRU and LSTM, is $O(n)$. Meanwhile, while the transformer solves the problem of time dependence, it does not support input selection inside a single time frame.

Combining LSTM and Transformer, the Temporal Fusion Transformer (TFT) proposed by Lim et al. (2021) is a state-of-the-time model for multi-horizon forecasting. TFT leverages a backbone network based on LSTM layers for variable selection and encoding. The attention module receives the output from LSTM at all time frames as input, which addresses LSTM's disadvantage by efficiently modeling time dependence.

For time-series forecasting including multiple entities, the TFT uses entity encodings to distinguish entities and independent networks to produce predictions, without modeling the correlation between entities. As a result, TFT may not cope well with the correlation among entities across different time steps, which is crucial for IES load forecasting (Feng and Zhang, 2020; Wang R. et al., 2021).

Therefore, the Cross-Entity Temporal Fusion Transformer (CETFT) was developed in this research as an improved version of the Transformer structure geared to energy load forecasting with correlations across distinct entities. The cross-entity attention module and entity encoding networks based on shared variable selection blocks are two innovative methods offered to adapt the network to multi-entity prediction tasks. This allows for simultaneous quantification of correlation across entities and time domains. Experiments on 13 buildings on a university campus are conducted to compare the proposed method to existing predicting algorithms. Future analyses are taken to comprehensively evaluate the interpretability of the network, Including cross-time correlations, cross-entity correlations, special attention to unconventional time-series trends, and variable importance.

The remaining of this paper is organized as follows: **Section 2** gives an introduction and mathematical definition of IES and time series forecasting; In **Section 3**, the structure of the proposed CETFT and its submodules are explained in detail; **Section 4** carried out a case study based on the campus building data set evaluating the performance and interpretability of the proposed model; and **Section 5** briefly concludes this paper.

2 PRELIMINARY

2.1 Integrated Energy Systems

The IES is mainly composed of multiple energy supply, exchange, storage, and consumption entities (Lin and Fang, 2019). These entities could transmit energy to each other according to a certain scheduling strategy to achieve a balance within the system and minimize the overall energy usage and expense. One major concern in achieving this goal is forecasting loads of consumption entities in advance, and the interdependence of entities is critical to achieving this goal.

2.2 Time-Series Forecasting

As illustrated in **Figure 1**, the goal of load forecasting can be framed as a supervised learning problem on time-series data. The data are a sequence of observations with equal time intervals, including targets and auxiliary information. The object of the

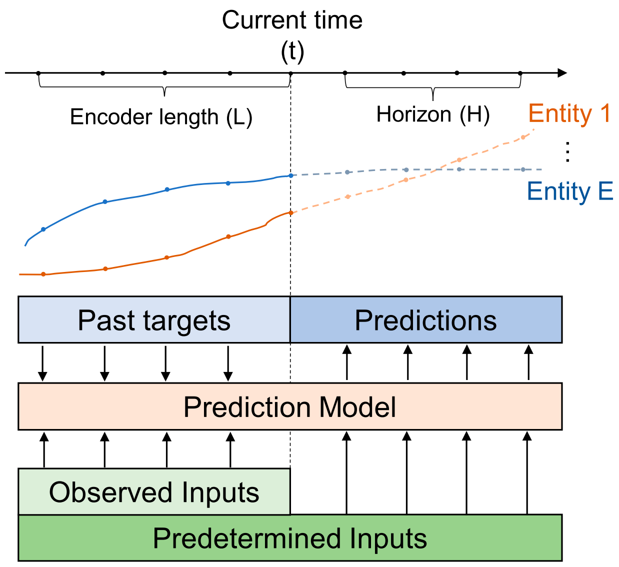

FIGURE 1 | Demonstration of a time-series forecasting problem with multiple entities.

problem is to forecast future target values based on historical data.

These data are organized in chronological order and grouped into a series of time windows of equal lengths. Each time window is further divided into two parts by a given forecast time frame t. In the inference phase, it is typically sufficient to take as input data a short period before the prediction time to encode the current state. The length of the data window as inputs is denoted by L. Those after the forecast time are outputs of the problem. The forecasting horizon is given by H, which is the number of time frames to be forecast.

In an IES, there are typically multiple entities that are correlated to each other. Let E be the number of unique entities in the system, e.g., different buildings on a campus, indexed by $1, 2, \ldots, E$. The target is the energy load $y_{i,t} \in \mathbb{R}$ of entity $i \in E$ at time step t in the future time window $[t, t^{\mathrm{F}}]$, where $t^{\mathrm{F}} = t + H$.

From the perspective of accessibility, the features $\boldsymbol{\chi}_t = [\boldsymbol{u}_t; \boldsymbol{x}_t]$ are divided into known features that can be predetermined ahead of time (e.g., calendar features) and unknown features $\boldsymbol{u}_t$ that are observed and must be predicted for future values (e.g., meteorological information). Typically, the targets are also a subset of the unknown features. The features $\boldsymbol{\chi}_i$ associated with a certain entity i include the private property of that entity and public features that affect the entire area.

The object of the problem is to construct a model $f(\cdot)$ to forecast future outputs for each entity in a time period, which is denoted by:

$$\hat{y}_i(t,\tau) = f\left(\tau, y_{t^{\mathrm{S}}:t}, \boldsymbol{z}_{t^{\mathrm{S}}:t}, \boldsymbol{x}_{t^{\mathrm{S}}:t^{\mathrm{F}}}\right), \tag{1}$$

where $f(\cdot)$ is the proposed prediction model. The output $\hat{y}_i(t,\tau)$ is the forecast value at time $t + \tau$, given known variables spanning from starting time frame $t^{\mathrm{S}} = t - L + 1$. Finally, the output of the model is the targets of all entities at the time frame $t + \tau$, which is a set of targets $\hat{\boldsymbol{y}}(t,\tau) = \{\hat{y}_1(t,\tau), \ldots, \hat{y}_E(t,\tau)\}$, where $\tau = 1, 2, \ldots, H$.

3 METHODOLOGY

The basic idea of neural networks is to apply weights to inputs through serial layers, in the form of:

$$\text{Layer}(\boldsymbol{z}) = \text{Activation}(\boldsymbol{W}\boldsymbol{z} + \boldsymbol{b}), \tag{2}$$

where $\boldsymbol{z} \in \mathbb{R}^{d_{\text{input}}}$ is input of the layer, $\boldsymbol{W} \in \mathbb{R}^{d_{\text{layer}} \times d_{\text{input}}}$ is weight, $\boldsymbol{b} \in \mathbb{R}^{d_{\text{layer}}}$ is bias, and Activation$(\cdot)$ is a proper activation function that enhances the otherwise linear matrix multiplication and addition operation with non-linearity. Typically, the training process of neural networks is to optimize the weights and biases to fit the training data set and minimize metrics or losses. Usually, a batch of input vectors will be stacked into a matrix and processed at the same time, and $\boldsymbol{b}$ will be horizontally broadcast to fit the shape.

The weights are hard parameters that only change during learning and are insistent during inferences. In contrast, recently developed neural networks tend to utilize "soft" weights to simulate the cognitive attention to inputs, of which a typical example is the attention mechanism (Vaswani et al., 2017). These networks leverage additional branch layers to adaptively calculate weights from inputs, which are again multiplied by the inputs at the layer at the main route.

The proposed CETFT utilizes two of these modules. First is the cross-entity attention module, which builds associations between each entity at different times. The second is the variable selection network (Lim et al., 2021) used for entity encoding, which simulates the importance of features for understanding the state of each entity at each time. In this paper, both these modules have been improved to adapt to the cross-entity situation. This section will provide a detailed definition of these two key modules and also the overall architecture of the network.

3.1 CETFT Architecture

The CETFT can be roughly separated into three sequential submodules, as shown in **Figure 2**: 1) the cross-entity attention, 2) the entity encoding network, and 3) the output layers. Gated residual networks are used to connect adjacent sub-modules and further process intermediate variables. These modules will be defined in this section.

3.2 Cross-Entity Attention

In order to model the correlation among entities as well as time steps at the same forecast time, A cross-entity attention mechanism is employed for the temporal fusion transformer. The attention module receives encoded vectors from entity encoding networks and generates temporally enhanced feature vectors for the output layer. Before the module, an encoded vector of d_{input} will be generated for all entities from all times. For a system with E entities, L encoder length, and H decoder length, the number of vectors available is $E(L + H)$. The attention module receives two matrics as input: $\boldsymbol{Z}_1 \in \mathbb{R}^{d_{\text{input}} \times E(L+H)}$ composed of all encoded vectors stacked, and $\boldsymbol{Z}_2 \in \mathbb{R}^{d_{\text{input}} \times EH}$ within the predicted time period. Adapted from the implementation of the attention mechanism called scaled dot-product attention (Vaswani et al., 2017), the process is represented as:

$$\text{CEAttention}\left(\boldsymbol{Q},\boldsymbol{K},\boldsymbol{V}\right) = \text{Softmax}\left(\frac{\boldsymbol{Q}\boldsymbol{K}^{\text{T}}}{\sqrt{d_k}} \odot \tilde{\boldsymbol{M}}\right)\boldsymbol{V} \tag{3}$$

$$\boldsymbol{Q}^{\text{T}} = \boldsymbol{W}_Q \boldsymbol{Z}_2, \tag{4}$$

$$\boldsymbol{K}^{\text{T}} = \boldsymbol{W}_K \boldsymbol{Z}_1, \tag{5}$$

$$\boldsymbol{V}^{\text{T}} = \boldsymbol{W}_V \boldsymbol{Z}_1, \tag{6}$$

where $\boldsymbol{Q} \in \mathbb{R}^{EH\times d_k}$, $\boldsymbol{K} \in \mathbb{R}^{E(L+H)\times d_k}$, and $\boldsymbol{V} \in \mathbb{R}^{E(L+H)\times d_v}$ are the query, key and value matrices, respectively, and $\boldsymbol{W}_Q \in \mathbb{R}^{d_k\times d_{\text{input}}}$, $\boldsymbol{W}_K \in \mathbb{R}^{d_k\times d_{\text{input}}}$, $\boldsymbol{W}_V \in \mathbb{R}^{d_v\times d_{\text{input}}}$, are learnable weights. The $\odot$ symbol denotes Hadamard product, and the mask matrix $\tilde{\boldsymbol{M}} \in \mathbb{R}^{EH\times E(L+H)}$ provides information accessibility control for the module, which will be defined later The Softmax function is a function that scales a input vector $\boldsymbol{z} \in \mathbb{R}^{d_{\text{input}}}$ into the range $(0,1)$, and keeps the sum of the elements equal to 1:

$$\text{Softmax}(\boldsymbol{z})_j = \frac{\exp\left(z_j\right)}{\sum_{i=1}^{d_{\text{input}}}\exp\left(z_i\right)}, \tag{7}$$

where $\exp(\cdot)$ is the power with natural base. The output of the whole module is with dimension $EH \times d_v$.

The process can be interpreted as a weighted sum of the features. The weights are calculated by multiplying the keys from all time and queries within the prediction horizon. The module scale the feature vectors according to the relationship among time frames and scale the input according to the estimated attention.

For time series forecasting, a decoding mask $\boldsymbol{M}$ should be applied to define the causal relationships between embeddings (Li et al., 2019). The encoding embeddings, however, are available to all time frames. Therefore, the mask for a single-entity attention mask is shaped like a right-angled trapezoid. The lengths of the top base and the bottom base are equal to the size of encoder embeddings and the size of all embeddings, respectively. The mask is described as a matrix $\boldsymbol{M} \in \mathbb{R}^{H\times(L+H)}$, where its elements are:

$$\boldsymbol{M}_{i,j} = \begin{cases} 1 & j \le L+i \\ -\infty & j > L+i \end{cases}, \text{for } 1 \le i \le H, 1 \le j \le L+H. \tag{8}$$

The mask matrix is illustrated in the left sub-figure in **Figure 3**.

To adapt to a multiple-entity application, the attention mask should be repeated by the number of entities both horizontally and vertically, which is illustrated in **Figure 3**. Mathematically, the cross-entity mask is defined as:

$$\tilde{\boldsymbol{M}}_{i,j} = \begin{cases} 1 & j \bmod (L+H) \le L + i \bmod H, \\ -\infty & \text{otherwise}, \end{cases} \\ \text{for } 1 \le i \le EH, 1 \le j \le E(L+H). \tag{9}$$

Furthermore, to increase the representative capability of the attention mechanism, it is common to stack multiple attention heads into a multi-head attention module, which is defined as:

$$\text{MultiHead}\left(\boldsymbol{Q},\boldsymbol{K},\boldsymbol{V}\right) = \boldsymbol{W}_h\left[\boldsymbol{H}_1;\ldots;\boldsymbol{H}_{m_h}\right], \tag{10}$$

$$\boldsymbol{H}_h = \text{CEAttention}_h\left(\boldsymbol{Q},\boldsymbol{K},\boldsymbol{V}\right), \tag{11}$$

where h is the index of attention head, m_h is the number of heads, and $\boldsymbol{W}_h \in \mathbb{R}^{m_h d_v \times d_v}$ is a weight parameter matrix.

3.3 Entity Encoding Networks

The entity encoding modules are a set of networks for producing encoded vectors from raw inputs, which are passed to the attention layer. The network consists of two components in series. Firstly, the shared variable selection network filters important variables in the input, and then the LSTM layers will initially extract the time information.

3.3.1 Shared Variable Selection

At different times, the variables that have the main impact on the forecast are different. The variable selection networks are intended to screen valuable variables and apply weights to those variables based on their projected importance.

The inputs will be categorized according to distinct entities initially, as indicated in **Figure 2**. Each input will be sent into a single variable selection network at each time frame. All of these networks' outputs will be collected and organized in the same hierarchy as their inputs.

Before being fed into the networks, the numerical inputs are normalized. The categorical inputs will be encoded using a normalized vector whose length is determined by the number of available values. After this process, it makes no difference to the network whether the input is continuous or discrete, except that discrete variables are represented as a vector rather than a single value. Without loss of generality, the following definition will be based on a single continuous variable.

In practice, the variable selection network modules can be reused if the same features are shared across time or entities, which is similar to how the modules were shared for encoders and decoders in the original TFT model. Different from the original TFT implementation, the variable selection networks are shared among entities to reduce the complexity of the network. These networks rely on the idea of a Gated Residual Network (GRN) defined by Lim et al. (2021) as follows:

$$\text{GRN}_\omega\left(z_3\right) = \text{LayerNorm}\left(z_3 + \text{GLU}_\omega\left(\eta_1\right)\right), \tag{12}$$

$$\eta_1 = \boldsymbol{W}_{1,\omega}\eta_2 + b_{1,\omega}, \tag{13}$$

$$\eta_2 = \text{ELU}\left(\boldsymbol{W}_{2,\omega} z_3 + b_{2,\omega}\right) \tag{14}$$

where ω is an identifier of the network that corresponds to a certain input element, LayerNorm is a standard layer normalizer by Ba et al. (2016), and η_1, $\eta_2 \in \mathbb{R}^{d_{\text{layer}}}$ are intermediate variables, $\boldsymbol{W}_{1,\omega}$, $\boldsymbol{W}_{2,\omega}$, $b_{1,\omega}$, $b_{2,\omega}$ are learnable weights and biases of the

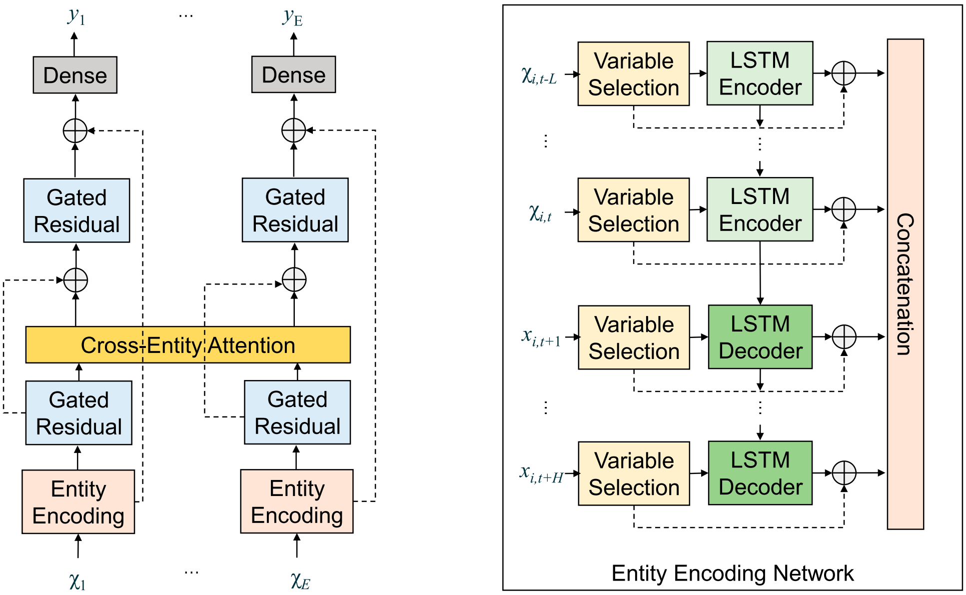

FIGURE 2 | CETFT architecture. Entity encoding networks receive inputs directly related to theirs corresponding entity, and the outputs are concatenated chronologically. The cross-entity attention integrates information from all entities and time frames. Gated residual layers provide enhancement to skip connections. Dense layers generate forecasting results.

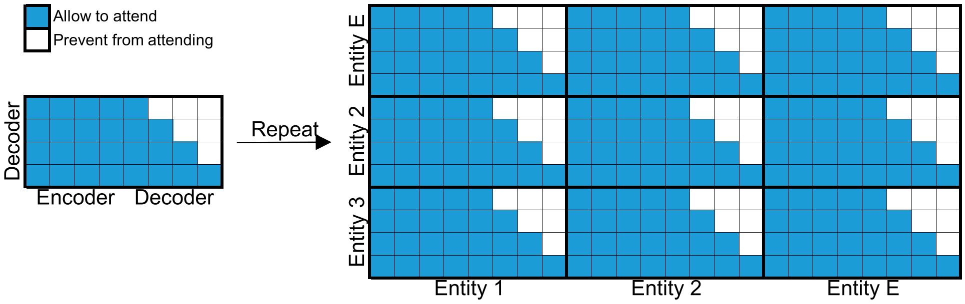

FIGURE 3 | Left: The original self-attention mask for TFT. **Right:** The cross-entity attention mask for CETFT, generated by repeating the single-entity attention mask by *E* times both horizontally and vertically.

layers, and Exponential Linear Unit (ELU) is a type of activation function defined as (Clevert et al., 2016):

$$\text{ELU} = \begin{cases} x & \text{if } x > 0 \\ \exp(x) - 1 & \text{if } x \leq 0, \end{cases} \tag{15}$$

The Gated Linear Unit (GLU) is (Dauphin et al., 2017):

$$\text{GLU}_\omega(z) = \sigma\left(\boldsymbol{W}_{3,\omega} z + b_{3,\omega}\right) \odot \left(\boldsymbol{W}_{4,\omega} z + b_{4,\omega}\right), \tag{16}$$

where $\sigma(\cdot)$ is the sigmoid function and $\odot$ is Hadamard product, $\boldsymbol{W}_{3,\omega}$. $\boldsymbol{W}_{4,\omega}$, $b_{3,\omega}$, $b_{4,\omega}$ are learnable layer parameters.

In practice, individual shared variable selection networks are built for each element in the model input. Let $\chi_{j,t}$ be j-th normalized or encoded input variable at time frame t, the variable selection layer is:

$$v_{\chi_{j,t}} = \text{Softmax}\left(\text{GRN}_{v_{\chi_j}}\left(\chi_{j,t}\right)\right), \tag{17}$$

where $v_{\chi_{j,t}}$ identifiers the network with parameters for j-th variable at given time t.

On the other hand, the input $\chi_{j,t}$ is handled by an extra GRN layer associated with itself:

$$\tilde{\chi}_{j,t} = \text{GRN}_{\tilde{\chi}_{j,t}} \chi_{j,t}, \tag{18}$$

Individual variable selection networks corresponding to the inputs connected with a certain entity are collected based on predefined entity attributes, and their outputs are aggregated into a single vector. Let V_t^i be the set of variables associated with entity i at time t, and the variable selection network for entity i produces the following output:

$$\tilde{\chi}_t^i = \sum_{j \in V_t^i} v_{\chi_{j,t}} \tilde{\chi}_{j,t} \tag{19}$$

TABLE 1 | Building categories and energy load patterns.

No.	Category	Pattern
B1	Administration	Varies from 8 a.m. to 5 p.m.
B2	Lecture hall	Relatively small but chaotic load
B3–B7	Classroom/Lab	Varies from 8 a.m. to 10 p.m.
B8	Library	The largest and most stable load
B9	Parking structure with photovoltaic panels	Negative load during the daytime
B10–B13	Student residence hall	Diverse load

Note that aside from inside the entity encoding networks, the GRN blocks also act as connectors of the main modules in the CETFT network.

3.3.2 LSTM Layers

LSTM layers are a type of RNN layers that receive inputs of the current time and also hidden inputs from past time. The mathematical definition of LSTM can be found in the paper by Hochreiter and Schmidhuber (1997). The LSTM layers generate two parts of return values, namely the output vector and the hidden vector. The output vector, as indicated by the name, is the variable passed to other modules. On the other hand, the hidden vector is passed back to the layer.

In CETFT, the LSTM layers are used to further process the features of each time output by the variable selection network to initially extract the time information. The past inputs $\tilde{\chi}^i_{t^{\mathrm{S}}:t}$ are fed into LSTM encoders to get output and hidden vectors for each frame, and the latter is further inputs $\tilde{\chi}^i_{t+1:t^{\mathrm{F}}}$ to LSTM decoders. The outputs of LSTM encoders and decoders are grouped chronologically into a vector $\tilde{\chi}^i$. Finally, the outputs from all entities are aggregated and flattened into a big vector, which is the attention layer's input, to align with the cross-entity attention module.

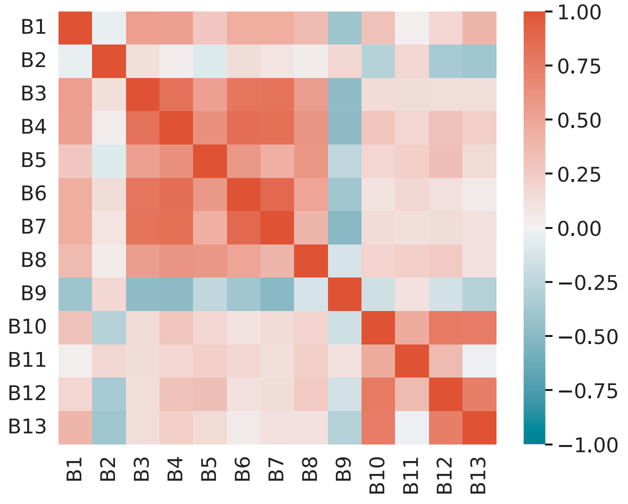

FIGURE 4 | Pearson correlation of building loads.

3.4 Output Layer

The outputs of the attention module will pass through another GRN before a set of dense layers are introduced to generate quantile outputs for the model. The model will generate multiple outputs corresponding to the forecasted values of each entity at each prediction time. In addition, the quantile loss by Sharda et al. (2021) summed across all outputs is used to train CETFT.

4 CASE STUDY

4.1 Dataset and Evaluation Setting

The data set is a collection of energy loads of 13 buildings at the University of Texas at Dallas, accompanied by 21 columns of auxiliary variables including meteorological records and calendar information[1]. The recordings span from January 2014 to December 2015 with a 1-h sample interval, providing a total of 17,520 records.

The buildings can be separated into six categories, as listed in **Table 1**. B9 is a site equipped with photovoltaic panels, whose load drops to negative numbers during the daytime. B2 is a lecture hall. Its load is relatively small and drops to 0 about 30% of the time. All other buildings have higher loads during the day and lower loads at night, but their load patterns vary with different categories. The correlations among these buildings can be clearly seen from Pearson analysis illustrated in **Figure 4**. A list of auxiliary features and their accessibility and types are shown in **Table 2**. The correlations among meteorological variables are illustrated in **Figure 5**. The heat map indicates high correlations among the variables related to irradiance and temperature, while they share a negative correlation with the solar zenith angle and relative humidity.

The categorical inputs are converted to encoding vectors, while continuous inputs are normalized. These inputs are concatenated into a vector for each entity at each time step. The data sets are chronologically divided into training/validation/test sets with a ratio of 0.7:0.15:0.15. The forecast horizons are selected as 1, 6, 12, and 24 h ahead. This horizon configuration is based on the daily periodicity of the time series and is commonly adopted by recent works (Arsov et al., 2021; He et al., 2022). In

---

[1] The data is accessible on the website of IEEE Data Port (https://dx.doi.org/10.21227/jdw5-z996).

TABLE 2 | Feature and target specification in the UTD dataset.

Variable	Accessibility	Type
Holiday	Predetermined	Categorical
Day	Predetermined	Categorical
HOD (Hour of Day)	Predetermined	Categorical
DOW (Day of Week)	Predetermined	Categorical
MOY (Month of Year)	Predetermined	Categorical
Cloud type	Unknown	Categorical
DHI (Diffuse Horizontal Irradiance)	Unknown	Continuous
DNI (Direct Normal Irradiance)	Unknown	Continuous
GHI (Global Horizontal Irradiance)	Unknown	Continuous
Clearsky DHI	Unknown	Continuous
Clearsky DNI	Unknown	Continuous
Clearsky GHI	Unknown	Continuous
Dew point	Unknown	Continuous
Temperature	Unknown	Continuous
Pressure	Unknown	Continuous
Relative humidity	Unknown	Continuous
Solar zenith angle	Unknown	Continuous
Precipitable water	Unknown	Continuous
Wind direction	Unknown	Continuous
Wind speed	Unknown	Continuous
Load	Target	Continuous

the test data set, there are 1460 and 846 missing data of buildings B2 and B9 out of 2628 records, respectively, and therefore the two buildings are excluded from forecast targets during model evaluation.

The hyperparameters CETFT and TFT are tuned with the Optuna framework (Akiba et al., 2019). The range of the hyperparameters are: network layer size range in [8, 256], attention head size in [1, 16], learning rate range in [1e-5, 0.1], dropout range in [0.1, 0.3]. The model is optimized based on the loss on the evaluation set, and the optimized model is further evaluated on the test set. The Ranger optimizer is adopted for training, with the batch size equal to 128 and a max epoch of 300. The learning rate is divided by 10 if the evaluation loss has stopped reducing for 4 epochs, and the training will early stop after 10 epochs without performance improvement.

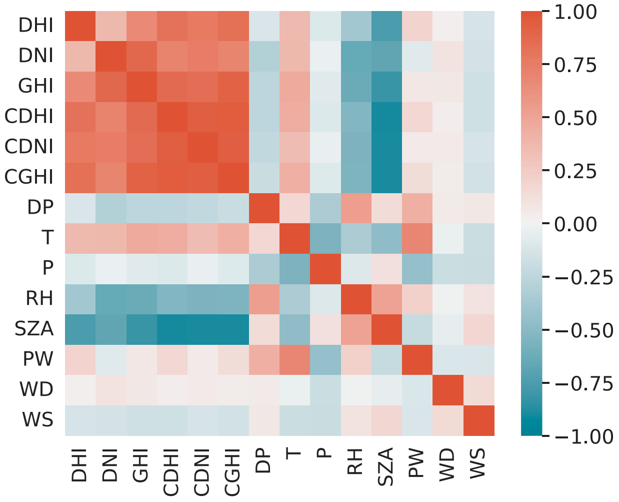

FIGURE 5 | Pearson correlation of meteorological variables. CDHI, clearsky DHI; CDNI, clearsky DNI; CGHI, clearsky GHI; DP, dew point; T, temperature; P, pressure; RH, relative humidity; SZA, solar zenith angle; PW, precipitable water; WD, wind direction; WS, wind speed.

The models to be compared are roughly divided into three categories: identification-based methods, of which a representative algorithm ARIMA; traditional statistical methods, including PLSR, RR and SVR; and deep-learning-based methods, including LSTM, GRU and TFT. The metric used for evaluation is Symmetric Mean Absolute Percentage Error (sMPAE) which is commonly used in time-series forecasting in the field of energy (Demir et al., 2021; Meira et al., 2021; Putz et al., 2021):

$$\mathrm{sMAPE} = \frac{1}{n}\sum_{i=1}^{n}\left|\frac{y_i - \hat{y}_i}{\left(y_i + \hat{y}_i\right)/2}\right| \tag{20}$$

where n is the amount of prediction made. A smaller value of the metric indicates a better performance of the model.

4.2 Comparison With Baseline

Table 3 collects the sMAPE error of all testing scenarios, covering different horizons, models, and buildings. The best model is marked in bold in each line. It can be seen that CETFT has achieved the best performance in 37 tests out of 44. The remaining best results were achieved by TFT, RR, and ARIMA, respectively. From an architectural point of view, CETFT achieves the best results for all horizons with the exception of B1, B5, and B8. In terms of computational complexity, our network takes 3 h and 27 min to train, while TFT takes 1 h and 25 min on an Nvidia A100 GPU with 40 GiB memory.

All models' predictive power declines as the horizon lengthen, which is to be expected given the limited amount of information available for future forecasts. ARIMA is the model that suffers the most as the horizon lengthens. Although ARIMA performed best on B8 when horizon = 1, it quickly became the model with the biggest error as the horizon was extended. When the horizon is increased from 12 to 24, however, the ARIMA error does not greatly rise, which can be explained by the cyclical pattern of energy usage throughout the day.

Statistical machine learning models including PLSR, RR, and SVR have obtained similar results. The RR model's accuracy gradually drops as the horizon lengthens, whereas PLSR and SVR remain reasonably stable. When horizon = 1, however, the latter two already have bigger errors. As a result, the RR model has a superior overall performance. There is a more remarkable phenomenon regarding these models, that is, their performance on buildings B12 and B13 is rather poor. These statistical models may fail to capture special patterns related to certain entities in the time series, resulting in inaccurate forecasts.

LSTM and GRU, the two RNN-based models, have relatively similar model performance. The accuracy of these two models is relatively little influenced by the prediction horizon. These two models outperform statistical machine learning techniques for B10–B13 prediction, but they don't have any evident advantages in other buildings. In general, neither of these

TABLE 3 | SMAPE on the UTD dataset.

horizon = 1

Entity	ARIMA	PLSR	RR	SVR	LSTM	GRU	TFT	CETFT
B1	3.73%	7.87%	4.73%	8.65%	6.99%	6.38%	3.80%	**3.13%**
B3	5.28%	11.47%	7.95%	10.51%	8.25%	6.83%	5.92%	**4.93%**
B4	3.05%	4.78%	2.45%	6.38%	4.79%	3.89%	2.88%	**2.12%**
B5	3.89%	7.21%	**3.59**%	6.50%	9.38%	8.65%	6.86%	6.79%
B6	5.17%	8.55%	5.14%	8.92%	8.95%	6.91%	4.96%	**3.27%**
B7	9.18%	15.14%	8.63%	14.05%	12.88%	8.55%	6.59%	**3.92%**
B8	**1.35%**	2.85%	1.77%	3.42%	3.47%	2.68%	2.40%	1.72%
B10	6.93%	11.64%	7.10%	11.90%	6.43%	6.98%	5.44%	**4.79%**
B11	7.38%	11.70%	6.50%	14.13%	8.37%	7.34%	7.60%	**6.41%**
B12	6.76%	30.21%	18.98%	30.49%	7.38%	7.70%	6.27%	**5.60%**
B13	15.28%	42.78%	25.13%	39.11%	9.34%	10.19%	7.79%	**6.06%**

horizon = 6

Entity	ARIMA	PLSR	RR	SVR	LSTM	GRU	TFT	CETFT
B1	10.67%	9.18%	6.04%	9.11%	7.68%	7.90%	4.94%	**3.88%**
B3	17.62%	12.10%	7.35%	10.93%	8.98%	8.89%	7.05%	**5.66%**
B4	10.62%	5.58%	3.48%	6.74%	5.45%	5.35%	3.60%	**2.44%**
B5	9.85%	8.88%	**7.07%**	7.95%	10.62%	9.80%	7.45%	7.41%
B6	15.60%	9.48%	5.07%	9.40%	10.12%	9.88%	6.39%	**4.00%**
B7	31.97%	16.20%	10.08%	14.34%	13.17%	12.11%	7.06%	**4.34%**
B8	2.95%	3.19%	2.38%	3.60%	3.73%	3.49%	2.60%	**1.82%**
B10	13.80%	12.79%	9.40%	12.24%	7.86%	9.19%	6.73%	**5.66%**
B11	13.22%	12.19%	9.56%	14.37%	8.60%	7.70%	7.80%	**6.83%**
B12	13.34%	30.95%	28.21%	30.88%	8.46%	9.42%	7.39%	**6.51%**
B13	29.73%	44.31%	24.39%	40.14%	10.37%	14.15%	10.05%	**7.85%**

horizon = 12

Entity	ARIMA	PLSR	RR	SVR	LSTM	GRU	TFT	CETFT
B1	16.52%	9.67%	7.70%	9.31%	8.93%	8.98%	**4.49%**	4.94%
B3	28.70%	12.45%	8.55%	11.10%	10.33%	10.41%	6.59%	**6.49%**
B4	18.15%	5.97%	4.47%	6.87%	6.57%	5.99%	3.03%	**2.79%**
B5	14.47%	9.66%	8.58%	8.78%	11.49%	10.84%	**7.67%**	8.12%
B6	25.18%	9.82%	5.95%	9.64%	12.29%	11.74%	5.73%	**5.10%**
B7	51.33%	16.57%	11.44%	14.51%	15.34%	14.62%	6.56%	**5.39%**
B8	3.93%	3.32%	2.71%	3.68%	3.88%	3.81%	2.62%	**2.02%**
B10	19.33%	13.52%	10.71%	12.56%	8.54%	8.47%	7.14%	**6.93%**
B11	17.82%	12.44%	10.16%	14.53%	8.68%	7.98%	8.08%	**7.16%**
B12	18.91%	31.42%	29.24%	31.23%	9.52%	9.05%	8.25%	**7.80%**
B13	41.54%	46.41%	29.22%	41.23%	12.04%	13.22%	10.71%	**10.14%**

horizon = 24

Entity	ARIMA	PLSR	RR	SVR	LSTM	GRU	TFT	CETFT
B1	17.64%	10.03%	8.52%	9.61%	9.52%	9.19%	**4.95%**	5.03%
B3	31.18%	12.86%	9.26%	11.29%	10.66%	10.30%	6.74%	**6.14%**
B4	20.25%	6.25%	4.74%	7.02%	6.00%	5.96%	3.07%	**2.65%**
B5	15.53%	10.13%	9.31%	9.43%	11.53%	11.87%	**7.87%**	8.40%
B6	26.50%	9.85%	6.33%	9.86%	11.84%	11.44%	6.05%	**4.38%**
B7	51.93%	17.26%	12.25%	14.75%	14.82%	13.48%	6.34%	**4.83%**
B8	4.36%	3.48%	2.96%	3.76%	4.00%	4.07%	2.64%	**2.15%**
B10	20.27%	14.51%	12.25%	13.07%	8.48%	8.66%	7.73%	**7.08%**
B11	17.96%	12.64%	10.49%	14.79%	8.66%	9.16%	8.15%	**7.91%**
B12	20.38%	31.90%	30.43%	31.81%	9.47%	9.78%	8.94%	**8.73%**
B13	48.58%	49.93%	35.14%	43.14%	12.52%	13.14%	11.49%	**11.01%**

The best model in each row is marked in bold.

two models may be particularly favorable for multi-entity forecasting.

The TFT is the closest to the proposed CETFT in terms of performance. But on most buildings, especially buildings including B6 and B7, CETFT still shows a clear advantage, where the error is reduced by about 1–2 percentage points. When the horizon is smaller, CETFT offers more visible advantages than TFT. This reflects CETFT's superiority over TFT in extracting information from entities. In general, CETFT delivers the best overall forecasting performance by combining the advantages of TFT for time-series forecasting with advances based on multi-entity forecasting.

4.3 Model Interpretability

It is feasible to interpret the model by examining the runtime weights during prediction thanks to the incorporation of two soft-weight-based network structures, namely the cross-entity attention module and shared variable selection network. Both of these networks will assign bigger weights to the more important inputs each time the model makes a prediction (Ding et al., 2020; Niu et al., 2021). As a result, a probabilistic assessment of the contribution or importance of a particular object (i.e., a variable/entity/time frame) to the prediction can be made by aggregating the soft weights pertaining to that object across the whole data set (Lim et al., 2021).

Several use cases, including 1) variable importance assessment, 2) cross-entity relationship evaluation, 3) cross-time relationship evaluation, and 4) time-series pattern identification, will be exhibited in this section to evaluate the model's interpretability.

4.3.1 Variable Importance Assessment

By aggregating the weights of the shared variable selection networks, it is possible to assess the importance of different variables to the network. The importance of all variables and known variables can be determined by aggregating the weights of the variable selection network in the encoder and decoder sections, respectively. The two classes of importance are normalized so that their sum is equal to 1, and the result is recorded in **Tables 4**, **5**. In these two tables, the importance percentages greater than 5% and 10% are, respectively marked in bold, indicating key variables for encoding and decoding.

TABLE 4 | Importance of variable importance for past inputs.

Variable	Importance
Holiday	**7.66%**
Day	**5.90%**
HOD	**7.71%**
DOW	2.45%
MOY	4.78%
Cloud type	2.71%
DHI	3.38%
DNI	3.39%
GHI	**7.37%**
Clearsky DHI	**6.10%**
Clearsky DNI	3.29%
Clearsky GHI	**9.18%**
Dew point	2.76%
Temperature	1.99%
Pressure	**5.40%**
Relative humidity	3.19%
Solar zenith angle	1.03%
Precipitable water	**8.13%**
Wind direction	4.69%
Wind speed	3.40%
Load	**5.48%**

Aggregation of variable selection network weights and normalized to sum to 1. Percentages greater than 5% are marked in bold.

TABLE 5 | Importance of variable importance for future inputs.

Variable	Importance
Holiday	**26.77%**
Day	7.66%
HOD	**50.13%**
DOW	**11.78%**
MOY	3.67%

Aggregation of variable selection network weights and normalized to sum to 1. Percentages greater than 10% are marked in bold.

Holiday, day, HOD, GHI, clearsky DHI, clearsky GHI, Pressure, precipitable water, and load are critical factors in the encoder stage, according to the model. Because the load has a clear daily periodicity and is considerably affected by holidays, the impact of holidays and hours on the forecast is interpretable. The variables related to sunlight are strongly correlated, and the importance of clearsky GHI is the highest for all variables, but some of the variables are of low importance. This could be because the variable selection network identifies redundant features and reduces dimensionality. It is worth noting that the importance of the load itself is not at its peak. This illustrates the importance of auxiliary variables in load forecasting.

On the decoder side, Holidays and hours still have a very important impact on the prediction. However, the rank of date and DOW is the opposite of those of the encoder. This may be due to the fact that the information of DOW is partially contained in the Day variable, and the network decreases the dimensionality of the two and retains the influence of one of the variables for the same reason as the sunlight-related variables.

4.3.2 Cross-Entity Relationship Evaluation

The cross-entity relationship is evaluated by aggregating and normalizing the weights of the attention module per entity, as illustrated in **Figure 6**. The figure maps the normalized attention from different buildings to predicate to the encoded feature vectors of different buildings. High, medium, and low attention are indicated by the colors red, white, and green, respectively. Note that the attention is not necessarily synced with correlation, as the former more likely represents the model's assessment of causality between variables (Wang X. et al., 2021; Yang et al., 2021).

It can be seen that B9 has received the most attention from other buildings. This makes sense because B9 has photovoltaic panels installed, which is the only building with electricity generating capacity, and its energy consumption pattern differs

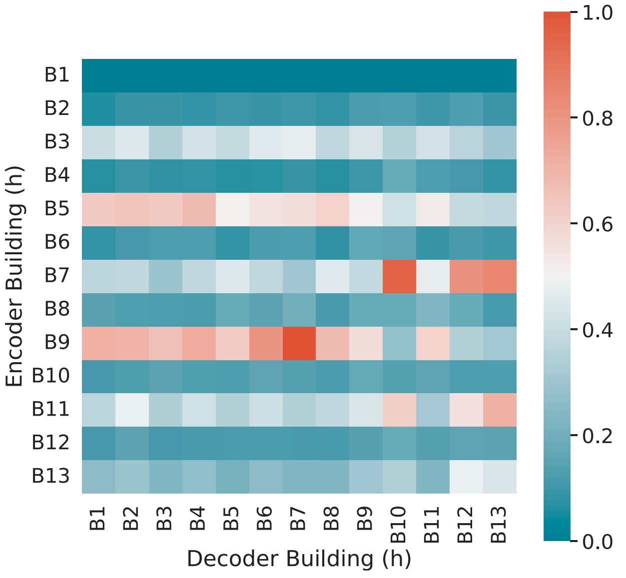

FIGURE 6 | Heatmap of attention weights aggregated per entity. The horizontal axis represents the entity being input, and the vertical axis denoted the entity being predicted.

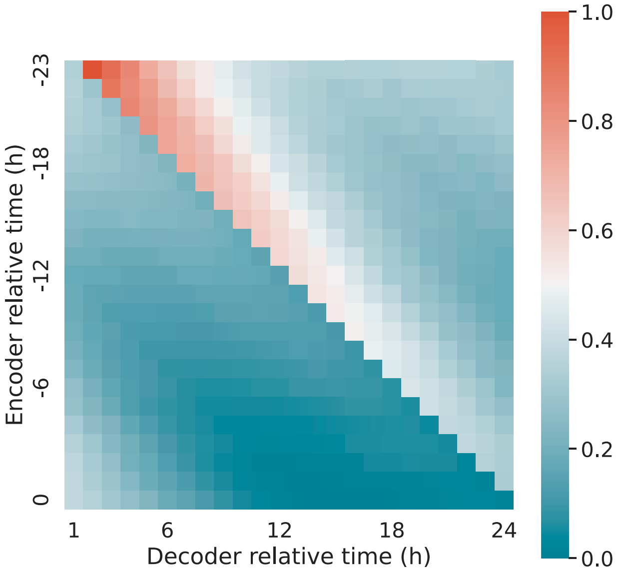

FIGURE 7 | Heatmap of attention weights aggregated per time. The horizontal axis represents the entity being input, and the vertical axis denoted the entity being predicted.

significantly from the others. Higher weights are given to three classroom/lab buildings (B3, B5, and B7), as well as two student living halls (B11, B13). This reflects the model's selection of variables with a similar pattern. The administration building (B1), the lecture hall (B2), and the library (B8) are three structures that are reasonably independent or utilize a consistent amount of energy. As a result, their contribution to the prediction is minor.

4.3.3 Cross-Time Relationship Evaluation

Similar to the cross-entity relationship, it is also possible to identify the cross-time relationship by aggregating the attention weights per time. The heatmap is shown as **Figure 7**. This relationship is expressed in relative time rather than absolute time, and the axis tick tables represent hours relative to the current time.

A diagonal line running from the upper left to the lower right is clearly visible in the figure. This shows that the network is mostly interested in information from the same hour the day before. Each time frame's attention in the encoder peaks right of the diagonal line, then gradually decreases and again increases in chronological order. This is primarily owing to the variable's periodic character. The majority of inputs of interests occur at the same time the day before, as well as a few hours ahead of the prediction time.

This figure also demonstrates the difficulty in long-term series forecasting. While the attention mechanism can directly model correlations across time frames, the amount of attention the network can provide diminishes over time. Maximum attention is given to the first prediction, while the attention level becomes increasingly distracted over time. As a result, longer-period projections are still insufficiently informative and perform poorly.

4.3.4 Time-Series Pattern Identification

Attention weights can also be aggregated in terms of absolute time frames. This allows time-series pattern identification by providing a picture of how much each actual time frame contributes to the model output.

Figure 8 uses the attention provided at different past times collected from building B4, B5, B6, and B12 for demonstration of this capability of the network. The horizontal axis represents the number of hours elapsed since Sunday, 13 September 2015, which is the first day in the test data set. The load of B6 is shown in red, while the overall attention is shown in cyan. It can be seen that loads of the four buildings all show obvious periodic characteristics within a cycle of 24 h. For B4, B5, and B6, the loads show consistent behavior during workdays, but a different pattern occurs each weekend. The first such change occurs at about 100 h. Therefore, there is also a cyclical feature with a period of a week (i.e., 168 h). Simultaneously, the network's attention has shown a similar periodicity, with a notable spike over the weekend. The time-series pattern for B12 is a bit different. The load for B12 does not show a clear periodicity based on weeks. Instead, the load generally shows an upward trend over time. Corresponding to this characteristic, the attention to B12 experienced a rise when the load dropped. These analyses demonstrate how the attention module reacts to the input time-series patterns and pays particular attention to particular changes. This provides insight for automatic analysis of the time-series characteristics and significant events.

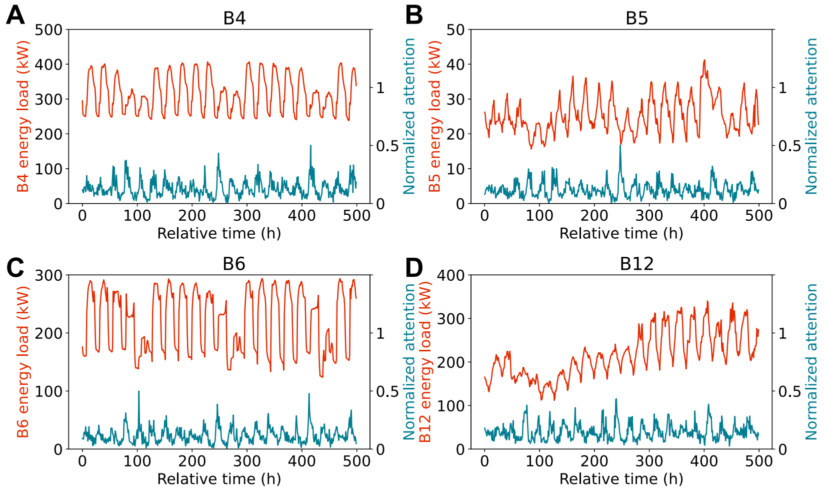

FIGURE 8 | Load and normalized attention to building **(A)** B4, **(B)** B5, **(C)** B6, and **(D)** B12 for 500 h since 13 September 2015.

5 CONCLUSION

This paper presents a deep-learning-based model named CETFT for multi-entity energy load forecasting. Entity encoding networks and a cross-entity attention module are defined. In a case study involving 13 buildings on a university campus, the proposed model achieves the minimum errors on all buildings given different prediction horizons. Further analyses are performed to assess the model's interpretability, revealing the relevance of variables, linkages between entities and time frames, and time-series features. The concept of selection networks could be used in future work to address the complexity of cross-entity attention processes and strike a balance between model correctness and computation overhead, along with improved fine-grained input categories for better adaption to a wider variety of time-series data.

DATA AVAILABILITY STATEMENT

The original contributions presented in the study are included in the article/supplementary material, further inquiries can be directed to the corresponding author.

AUTHOR CONTRIBUTIONS

ZW and ZZ developed the CETFT model and implement the computer code and wrote the initial draft, GX revised and edited the draft. BB validated the experiments and results, YZ prepared visualization and data presentation.

FUNDING

This work is supported by Key Research Project of Zhejiang Lab (No. 2021LE0AC02).

REFERENCES

Akiba, T., Sano, S., Yanase, T., Ohta, T., and Koyama, M. (2019). "Optuna," in Proceedings of the ACM SIGKDD International Conference on Knowledge Discovery and Data Mining, 2623–2631. doi:10.1145/3292500.3330701

Arsov, M., Zdravevski, E., Lameski, P., Corizzo, R., Koteli, N., Gramatikov, S., et al. (2021). Multi-horizon Air Pollution Forecasting with Deep Neural Networks. *Sensors* 21, 1–18. doi:10.3390/s21041235

Ayodeji, A., Wang, Z., Wang, W., Qin, W., Yang, C., Xu, S., et al. (2022). Causal Augmented ConvNet: A Temporal Memory Dilated Convolution Model for Long-Sequence Time Series Prediction. *ISA Trans.* 123, 200–217. doi:10.1016/j.isatra.2021.05.026

Ba, J. L., Kiros, J. R., and Hinton, G. E. (2016). "Layer Normalization," in 4th International Conference on Learning Representations, ICLR 2016 - Conference Track Proceedings. doi:10.48550/arXiv.1607.06450

Chung, J., Gulcehre, C., Cho, K., and Bengio, Y. (2014). "Empirical Evaluation of Gated Recurrent Neural Networks on Sequence Modeling," in *NIPS 2014 Workshop on Deep Learning*, 1–9. doi:10.48550/arXiv.1412.3555

Clevert, D. A., Unterthiner, T., and Hochreiter, S. (2016). "Fast and Accurate Deep Network Learning by Exponential Linear Units (ELUs)," in 4th International Conference on Learning Representations, ICLR 2016 - Conference Track Proceedings. doi:10.48550/arXiv.1511.07289

Dauphin, Y. N., Fan, A., Auli, M., and Grangier, D. (2017). "Language Modeling with Gated Convolutional Networks," in 34th International Conference on Machine Learning, ICML 2017, 1551–1559. 2. doi:10.48550/arXiv.1612.08083

Demir, S., Mincev, K., Kok, K., and Paterakis, N. G. (2021). Data Augmentation for Time Series Regression: Applying Transformations, Autoencoders and Adversarial Networks to Electricity Price Forecasting. *Appl. Energy* 304, 117695. doi:10.1016/j.apenergy.2021.117695

Ding, Y., Zhu, Y., Feng, J., Zhang, P., and Cheng, Z. (2020). Interpretable Spatio-Temporal Attention LSTM Model for Flood Forecasting. *Neurocomputing* 403, 348–359. doi:10.1016/j.neucom.2020.04.110

Dittmer, C., Krümpel, J., and Lemmer, A. (2021). Power Demand Forecasting for Demand-Driven Energy Production with Biogas Plants. *Renew. Energy* 163, 1871–1877. doi:10.1016/j.renene.2020.10.099

Dosovitskiy, A., Beyer, L., Kolesnikov, A., Weissenborn, D., Zhai, X., Unterthiner, T., et al. (2021). "An Image Is Worth 16x16 Words: Transformers for Image Recognition at Scale," in *International Conference on Learning Representations*, 1–22. doi:10.48550/arXiv.2010.11929

Feng, C., and Zhang, J. (2020). Assessment of Aggregation Strategies for Machine-Learning Based Short-Term Load Forecasting. *Electr. Power Syst. Res.* 184, 106304. doi:10.1016/j.epsr.2020.106304

He, X., Shi, S., Geng, X., and Xu, L. (2022). Information-aware Attention Dynamic Synergetic Network for Multivariate Time Series Long-Term Forecasting. *Neurocomputing* 500, 143–154. doi:10.1016/j.neucom.2022.04.124

Hochreiter, S., and Schmidhuber, J. (1997). Long Short-Term Memory. *Neural Comput.* 9, 1735–1780. doi:10.1162/neco.1997.9.8.1735

Hosseinpour, S., Aghbashlo, M., Tabatabaei, M., and Khalife, E. (2016). Exact Estimation of Biodiesel Cetane Number (Cn) from its Fatty Acid Methyl Esters (Fames) Profile Using Partial Least Square (Pls) Adapted by Artificial Neural Network (Ann). *Energy Convers. Manag.* 124, 389–398. doi:10.1016/j.enconman.2016.07.027

Li, S., Jin, X., Xuan, Y., Zhou, X., Chen, W., Wang, Y. X., et al. (2019). "Enhancing the Locality and Breaking the Memory Bottleneck of Transformer on Time Series Forecasting," in *Advances in Neural Information Processing Systems 32 (NeurIPS 2019)*.

Lim, B., Arık, S., Loeff, N., and Pfister, T. (2021). Temporal Fusion Transformers for Interpretable Multi-Horizon Time Series Forecasting. *Int. J. Forecast.* 37, 1748–1764. doi:10.1016/j.ijforecast.2021.03.012

Lin, R., and Fang, F. (2019). "Energy Management Method on Integrated Energy System Based on Multi-Agent Game," in 2019 International Conference on Sensing, Diagnostics, Prognostics, and Control (SDPC), 564–570. doi:10.1109/SDPC.2019.00107

Meira, E., Cyrino Oliveira, F. L., and de Menezes, L. M. (2021). Point and Interval Forecasting of Electricity Supply via Pruned Ensembles. *Energy* 232. doi:10.1016/j.energy.2021.121009

Newsham, G. R., and Birt, B. J. (2010). "Building-level Occupancy Data to Improve ARIMA-Based Electricity Use Forecasts," in *BuildSys'10 - Proceedings of the 2nd ACM Workshop on Embedded Sensing Systems for Energy-Efficiency in Buildings*, 13–18. doi:10.1145/1878431.1878435

Niu, Z., Zhong, G., and Yu, H. (2021). A Review on the Attention Mechanism of Deep Learning. *Neurocomputing* 452, 48–62. doi:10.1016/j.neucom.2021.03.091

Putz, D., Gumhalter, M., and Auer, H. (2021). A Novel Approach to Multi-Horizon Wind Power Forecasting Based on Deep Neural Architecture. *Renew. Energy* 178, 494–505. doi:10.1016/j.renene.2021.06.099

Ribeiro, A. H., Tiels, K., Aguirre, L. A., and Schön, T. (2020). "Beyond Exploding and Vanishing Gradients: Analysing Rnn Training Using Attractors and Smoothness," in *Proceedings of the Twenty Third International Conference on Artificial Intelligence and Statistics*. Editors Chiappa, S., and Calandra, R., 108, 2370–2380. PMLR of Proceedings of Machine Learning Research.

Rumelhart, D. E., and McClelland, J. L. (1987). *Learning Internal Representations by Error Propagation*. MIT Press, 318–362.

Sharda, S., Singh, M., and Sharma, K. (2021). RSAM: Robust Self-Attention Based Multi-Horizon Model for Solar Irradiance Forecasting. *IEEE Trans. Sustain. Energy* 12, 1394–1405. doi:10.1109/TSTE.2020.3046098

Sun, M., Ghorbani, M., Chong, E. K., and Suryanarayanan, S. (2019). "A Comparison of Multiple Methods for Short-Term Load Forecasting," in *51st North American Power Symposium, NAPS 2019*. doi:10.1109/NAPS46351.2019.8999984

Tahir, M. F., Chen, H., and Han, G. (2021). A Comprehensive Review of 4E Analysis of Thermal Power Plants, Intermittent Renewable Energy and Integrated Energy Systems. *Energy Rep.* 7, 3517–3534. doi:10.1016/j.egyr.2021.06.006

Tang, Y., Yu, F., Pedrycz, W., Yang, X., Wang, J., and Liu, S. (2021). Building Trend Fuzzy Granulation Based LSTM Recurrent Neural Network for Long-Term Time Series Forecasting. *IEEE Trans. Fuzzy Syst.* 30, 1599–1613. doi:10.1109/TFUZZ.2021.3062723

Tetko, I. V., Karpov, P., Van Deursen, R., and Godin, G. (2020). State-of-the-art Augmented NLP Transformer Models for Direct and Single-step Retrosynthesis. *Nat. Commun.* 11. doi:10.1038/s41467-020-19266-y

Vaswani, A., Shazeer, N., Parmar, N., Uszkoreit, J., Jones, L., Gomez, A. N., et al. (2017). "Attention Is All You Need," in *Advances in Neural Information Processing Systems*, 30. Long Beach, USA: NIPS 2017, 1–11.

Wang, R., Sun, Q., Sun, C., Zhang, H., Gui, Y., and Wang, P. (2021a). Vehicle-Vehicle Energy Interaction Converter of Electric Vehicles: A Disturbance Observer Based Sliding Mode Control Algorithm. *IEEE Trans. Veh. Technol.* 70, 9910–9921. doi:10.1109/TVT.2021.3105433

Wang, R., Sun, Q., Zhang, H., Liu, L., Gui, Y., and Wang, P. (2022). Stability-Oriented Minimum Switching/Sampling Frequency for Cyber-Physical Systems: Grid-Connected Inverters under Weak Grid. *IEEE Trans. Circuits Syst. I Regul. Pap.* 69, 946–955. doi:10.1109/TCSI.2021.3113772

Wang, X., Xu, X., Tong, W., Roberts, R., and Liu, Z. (2021b). InferBERT: A Transformer-Based Causal Inference Framework for Enhancing Pharmacovigilance. *Front. Artif. Intell.* 4, 1–11. doi:10.3389/frai.2021.659622

Yang, X., Zhang, H., Qi, G., and Cai, J. (2021). *Causal Attention for Vision-Language Tasks*, 9842–9852. doi:10.1109/CVPR46437.2021.00972

Zhang, D., Jianhua, B., Sun, X., and You, P. (2020). "Research on Operational Economics of the Integrated Energy System," in 2020 4th International Conference on Power and Energy Engineering (ICPEE), 251–255. doi:10.1109/ICPEE51316.2020.9310986

Conflict of Interest: The authors declare that the research was conducted in the absence of any commercial or financial relationships that could be construed as a potential conflict of interest.

NOMENCLATURE

$\boldsymbol{\tau}$	prediction time offset
$\boldsymbol{\chi_t}$	initial input
$\boldsymbol{\omega}$	shared variable selection network identifier
$\boldsymbol{b}$	layer bias
$\boldsymbol{d}_{input}$	input dimension
$\boldsymbol{d}_{layer}$	layer dimension
$\boldsymbol{d_k}$	dimension of key
$\boldsymbol{d_v}$	dimension of value
$\boldsymbol{E}$	number of entities
$\boldsymbol{f}(\cdot)$	prediction model
$\boldsymbol{H}$	attention head
H	prediction Horizon
$\boldsymbol{i}$	entity index
$\boldsymbol{K}$	key matrix
$\boldsymbol{L}$	encoder length
$\boldsymbol{M}$	attention mask matrix
$\tilde{\boldsymbol{M}}$	cross-entity attention mask matrix
$\boldsymbol{m_h}$	number of attention head
$\boldsymbol{n}$	amount of predictions
$\boldsymbol{Q}$	query matrix
$\boldsymbol{t}$	time frame
$\boldsymbol{t}^{\mathrm{F}}$	end of future time window
$\boldsymbol{t}^{\mathrm{S}}$	starting time of input
$\boldsymbol{u_t}$	observed input
$\boldsymbol{V}$	value matrix
$\boldsymbol{v}$	input identifier
$\boldsymbol{W}$	layer weight
$\boldsymbol{x_t}$	predetermined input
$\boldsymbol{y_i}$	actual target value
$\hat{y}_i$	predicted target value
$\boldsymbol{z}$	layer input vector
$\boldsymbol{Z}$	layer input matrix

ORIGINAL RESEARCH
published: 22 July 2022
doi: 10.3389/fenrg.2022.939376

An Improved Dual-Loop Feedforward Control Method for the Enhancing Stability of Grid-Connected PV and Energy Storage System Under Weak Grids

Chunxu Li[1], **Xinrui Liu**[1]*, **Rui Wang**[1], **Yi Zhang**[2] **and Li Zhang**[3]

[1]*The College of Information Science and Engineering, Northeastern University, Shenyang, China,* [2]*State Key Laboratory of Alternate Electrical Power System with Renewable Energy Sources, North China Electric Power University, Beijing, China,* [3]*School of Electrical and Electronic Engineering, Nanyang Technological University, Singapore*

Edited by:
Qihe Shan,
Dalian Maritime University, China

Reviewed by:
Kenneth E. Okedu,
National University of Science and Technology (Muscat), Oman
Tianyi Li,
Aalborg University, Denmark
Jianguo Zhou,
Tsinghua University, China

***Correspondence:**
Xinrui Liu
liuxinrui@ise.neu.edu.cn

Specialty section:
This article was submitted to Smart Grids, a section of the journal Frontiers in Energy Research

Received: 09 May 2022
Accepted: 30 May 2022
Published: 22 July 2022

Citation:
Li C, Liu X, Wang R, Zhang Y and Zhang L (2022) An Improved Dual-Loop Feedforward Control Method for the Enhancing Stability of Grid-Connected PV and Energy Storage System Under Weak Grids. Front. Energy Res. 10:939376. doi: 10.3389/fenrg.2022.939376

Although the stability of the grid-connected photovoltaics (PV) and energy storage systems under weak grids has been widely researched, the classical improvement methods focus more on suppressing the harmonics introduced by the phase-locked loop (PLL). Furthermore, the current distortion caused by the DC voltage loop is difficult to be eliminated. In this study, based on the hybrid energy storage system of battery-supercapacitor, a dual-loop compensation method is proposed. First, the small-signal model and output impedance matrix are built in d-q axis. Second, for different disturbance loops, a DC voltage loop disturbance compensation method based on power feedforward is proposed to suppress the harmonics caused by the DC voltage controller (DVC). In addition, a voltage feedforward PLL disturbance compensation method is proposed, which can reduce the PLL perturbations and revise the output impedance to improve system stability. Finally, the output impedance frequency characteristic analysis and the hardware-in-the-loop (HIL) simulation results show that the proposed control method can effectively improve the stability of the system under weak grids.

Keywords: PV and energy storage system, weak power grids, grid-connected inverter, phase-locked loop, stability analysis

1 INTRODUCTION

Renewable energy sources such as PV have the characteristics of intermittency and randomness. In order to ensure the stability of the microgrid system, certain capacity energy storage devices need to be configured in the microgrid system. The battery-supercapacitor (SC)–based hybrid energy storage system (HESS) has been proposed to mitigate the impact of dynamic power exchanges on the battery's lifespan (Jing et al., 2017). Aiming at the control of the PV and energy storage microgrid, (Akram et al., 2018), proposed an iterative search algorithm to improve the optimal size of the PV and energy storage systems in the microgrid. (Tricarico et al., 2020) made improvements on the microgrid topology. In (Xu and Cen, 2021), a coordinated control strategy was used to suppress the power fluctuations of grid-connected PV power generation systems. Due to the interaction between the inverter and grid impedance, will cause a decrease in system stability. Therefore, considering the

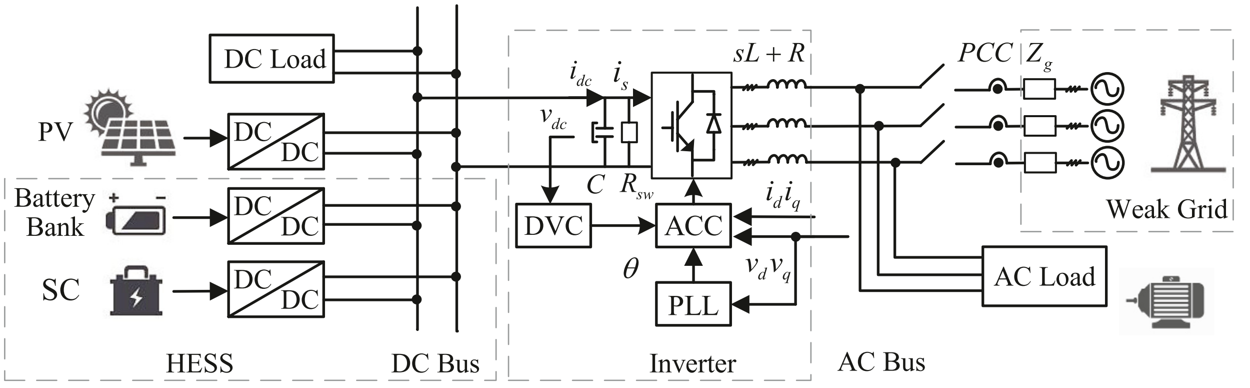

FIGURE 1 | Grid-connected PV and energy storage system.

weak grid conditions, the research on stable control of grid-connected inverters is particularly important.

The impedance analysis is widely used in the stability analysis of grid-connected inverters. (Sun, 2011) pointed out that if the ratio of the grid impedance to the inverter output impedance satisfies the Nyquist stability criterion, the system will remain stable. (Wen et al., 2014) analyzed the control of the voltage controller in the low-frequency range, the output impedance decreases as the voltage loop bandwidth increases, and the wider will be the frequency range of the negative impedance. In this regard, (Xu et al., 2017), proposed an adaptive control method, which adjusts the voltage feedforward signal through an adaptive criterion to improve the stability. (Lu et al., 2018) revealed that the dc-link voltage control may cause high-frequency oscillations in the inverter. (Yuan et al., 2017) pointed out that controller parameters of DVC affect the oscillation. In addition, (Harnefors et al., 2015), suggested not to select the bandwidths of DVC, unnecessarily large, to avoid oscillation. (Dong et al., 2014); (Wen et al., 2015a); (Wen et al., 2015b); (Bakhshizadeh et al., 2016); (Yang et al., 2019); (Nicolini et al., 2020) mainly analyzed the influence of the PLL on the stability of the inverter and pointed out that the PLL is one of the main factors that affect the stability of the system. The method of introducing a feedforward function was used by (Wang et al., 2010); (Xue et al., 2012); (Zhang et al., 2018) to improve stability.

To solve the influence of PLL on system stability, (Cespedes and Sun, 2014); (Yang et al., 2014); (Zhou et al., 2014); (Davari and Mohamed, 2016) made different attempts. In (Zhou et al., 2014), a small-signal model of the control system including the PLL was established. It was discussed that the gain of the PLL has a greater effect on the stability of the inverter, and a method is proposed to reduce the bandwidth of the PLL to solve this problem. (Yang et al., 2014) used virtual impedance to regulate the output impedance instead of adjusting the current loop gain to improve the inverter's harmonic suppression and stability robustness. The current control loop can be independently designed. (Wang et al., 2014) reviewed the control methods of VSCs and CSCs based on virtual impedance. (Cao et al., 2017) proposed an impedance matrix modeling method, which simplifies the stability judgment process. However, the impact of the DC side voltage fluctuation is ignored. For PV grid-connected systems, the DC side voltage will fluctuate under the influence of factors such as intensity of light. Therefore, it is necessary to take DC voltage fluctuations into consideration.

This study aims at the stability of weak grid-connected PV and energy storage systems. To meet the dynamic response requirements, a HESS is adopted. For the grid-connected inverter, the small-signal analysis and impedance method are used to analyze the stability of the system, including the influence of the PLL and the voltage loop controller. The main contributions are as follows:

1) Considering the State of Charge (SoC) of the battery, an adaptive bandwidth frequency low-pass filter (LPF) is proposed, smoothing the low-frequency power from the battery, ensuring DC bus voltage stability.
2) A DC voltage loop disturbance compensation control based on power feedforward is added to the DVC to reduce the perturbation signals caused by the controller parameters.
3) To eliminate the negative effects introduced by PLL, a disturbance compensation method based on voltage feedforward is proposed, which further improves the stability of grid connections.

The rest of this article is organized as follows. Section 3 establishes the impedance model of the grid-connected inverter. Section 4 discusses the proposed control method and analyzes the control effect. Section 5 builds a HIL platform to verify that the proposed method can reduce the frequency range of the negative impedance characteristics. The conclusion is given in Section 6.

2 GRID-CONNECTED PV AND ENERGY STORAGE SYSTEM UNDER WEAK GRIDS

Figure 1 is a weak grid-connected PV and energy system. PV and HESS are connected to the DC bus through DC/DC converters. Therefore, the DC bus voltage becomes a key indicator for stable

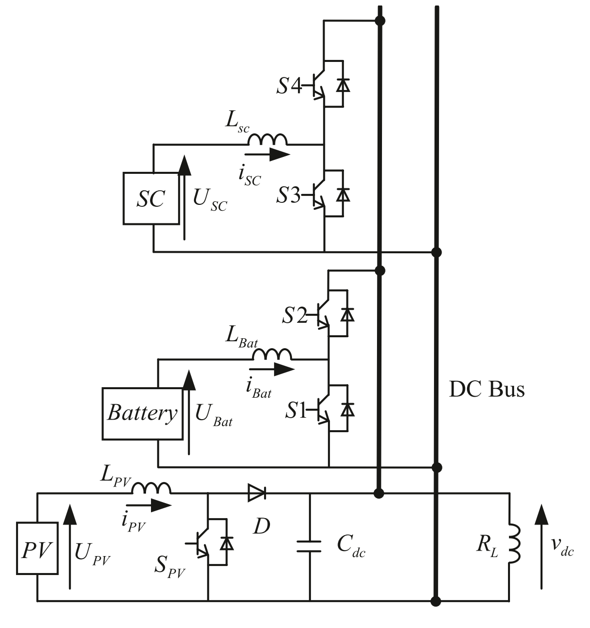

FIGURE 2 | DC microgrid structure.

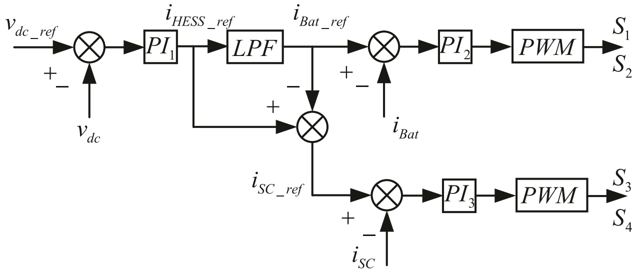

FIGURE 3 | Structure of voltage stabilization control.

operation. L is the filter inductance on the inverter side, and R is the parasitic resistance on the inductance. The grid impedance is represented by Z_g, which comprises an inductance L_g and a resistance R_g, and θ is the phase angle of the PLL. DC bus voltage and current are represented by v_{dc} and i_{dc}, respectively. The control system of the inverter comprises a DVC, an AC current controller (ACC), and PLL.

2.1 Structure Design of HESS

The PV array is connected to the DC microgrid through a boost converter, which adopts the MPPT control algorithm. The HESS uses a bidirectional DC/DC converter to connect to the DC microgrid. Due to the imbalance between power generation and load demand, the HESS is proposed to maintain the DC bus voltage v_{dc} stability.

In **Figure 2**, R_L represents the load of the DC bus, U_{PV}, i_{PV}, U_{Bat}, i_{Bat}, U_{SC}, and i_{SC} represent the voltage and output current of PV array, battery, and SC; L_{PV}, L_{Bat}, and L_{SC} are the filter inductance of the converter; C_{PV} is the filter capacitor; and S_1, S_2, S_3, S_4, and S_{PV} are the control switches.

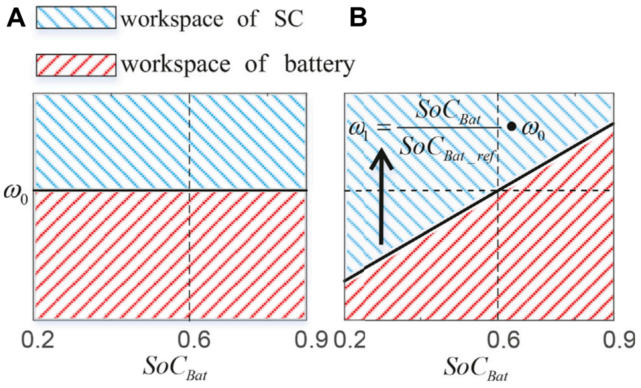

FIGURE 4 | (A) Traditional LPF power distribution diagram, **(B)** self-adaptive LPF power distribution diagram considering SoC_{Bat}.

2.2 Self-Adaptive LPF Considering SoC_{Bat}

The control block diagram of the voltage stabilization control strategy is shown in **Figure 3**. The basic idea of this control strategy is that the battery supports the low-frequency part of power changes and the SC supports the high-frequency part of power changes. Therefore, v_{dc} is compared with its reference value v_{dc_ref}, and the total current i_{HESS_ref} is provided by the PI controller. A low-pass filter (LPF) is used to divide the total current into a steady-state power component and a dynamic power component. The steady-state power component is used as the reference value i_{Bat_ref} for battery current control, and the dynamic power component is used as the reference value i_{SC_ref} for SC current control.

The smaller the bandwidth frequency of the LPF, the smoother the power borne by the battery after P_{HESS} passes through the LPF, and the more the power borne by the SC. Therefore, the power distribution effect of the LPF can be optimized by changing the size of bandwidth frequency.

On the basis of the traditional power distribution method, the SoC of the HESS is considered, and the bandwidth of the LPF is changed in real time according to its SoC value to realize the reasonable distribution of the power in HESS.

We set the improved self-adaptive bandwidth frequency ω_1 as follows:

$$\omega_1 = \frac{SoC_{Bat}}{SoC_{Bat\_ref}} \cdot \omega_0, \tag{1}$$

where $0.2 < SoC_{Bat} < 0.9$, ω_0 is the initial bandwidth frequency of the LPF, and SoC_{Bat_ref} is the optimal SoC of the battery, with a magnitude of 0.6.

In **Figure 4**, the power with a frequency lower than ω_1 is borne by the battery, and the power with a frequency higher than ω_1 is borne by the SC. **Figure 4A** shows the power distribution under the traditional LPF, where $\omega_1 = \omega_0$. **Figure 4B** shows that the larger SoC_{Bat} means larger ω_1, and the battery bears more range of power output. When the battery power is low, ω_1 decreases with SoC_{Bat}. SC takes on more range of power output so as to extend the working time of HESS and protect the battery.

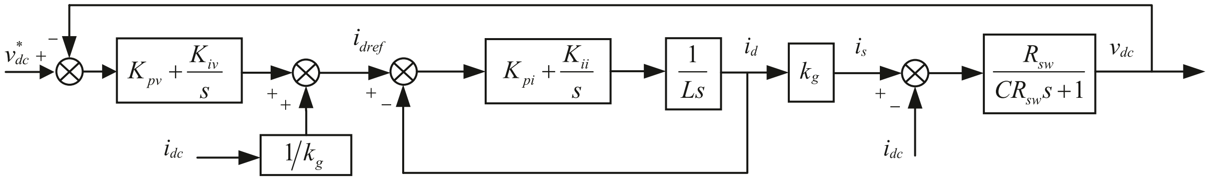

FIGURE 5 | Dual-loop control structure of the inverter.

With the self-adaptive LPF power distribution method, the new reference current i_{Bat_ref} andi_{SC_ref} are obtained. By sending these parameters to the PI controllers, we can get the bidirectional DC/DC control signals.

2.3 System Power Distribution

In the power distribution control strategy, the DC bus voltage is controlled by the PV and the HESS. P_{inv} is the power at the input of the inverter, and P_L is the power of DC load. P_{dc} represents the output power from the DC bus side. P_C is the power of the DC bus capacitor.

$$P_{dc} = P_{inv} + P_L. \tag{2}$$

$$P_C = P_{PV} + P_{HESS} - P_{dc}. \tag{3}$$

$$P_C = v_{dc} \cdot C_{dc} \frac{dv_{dc}}{dt}. \tag{4}$$

In order to stabilize the DC bus voltage, $dv_{dc}/d_t = 0$, which means $P_{HESS} = P_{DC} - P_{PV}$. The HESS is responsible for balancing the power between the DC bus side and the PV. The power of the HESS is allocated to the battery and the SC.

$$P_{HESS} = P_{Bat} + P_{SC}. \tag{5}$$

When the energy emitted by the system can satisfy (5), v_{dc} can remain stable.

3 DESIGN OF THE GRID-CONNECTED INVERTER

3.1 Design of Inverter Controllers

Figure 5 is the dual-loop control block diagram with a power feedforward. The proportional and integral gain of the PI controllers are k_{pv} and k_{pi}; k_{iv} and k_{ii}.

According to **Figure 1**, the mathematical model of the grid-connected inverter under the dq axis is as follows:

$$\begin{cases} C\dfrac{dv_{dc}}{dt} + \dfrac{v_{dc}}{R_{sw}} = i_{dc} - i_s \\ \\ L\dfrac{di_d}{dt} - \omega L i_q + u_d = v_d \\ \\ L\dfrac{di_q}{dt} + \omega L i_d + u_q = v_q \end{cases}, \tag{6}$$

where i_d and i_q are the dq-axis components of the grid-connected current at the PCC point, u_d and u_q are the dq-axis components of the PCC voltage, v_d and v_q are the inverter output voltage, and ω is the grid angle frequency. We usually set $v_q = 0$, $i_q = 0$. The topology diagram of the control system is shown in **Figure 6**. According to the power conservation at the input and output of the inverter, we can get

$$P_{inv} = i_{dc}v_{dc} {=} P_{out} = \frac{3v_d i_d}{2}. \tag{7}$$

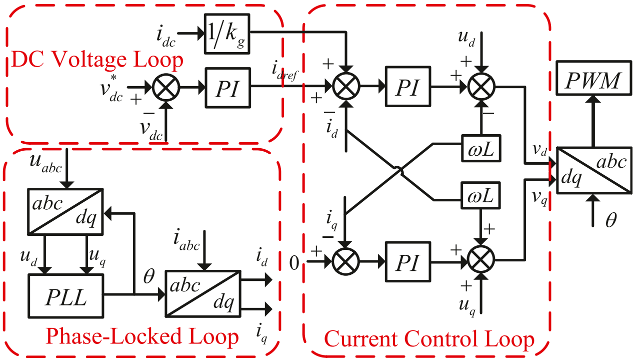

FIGURE 6 | Topology diagram of the control system.

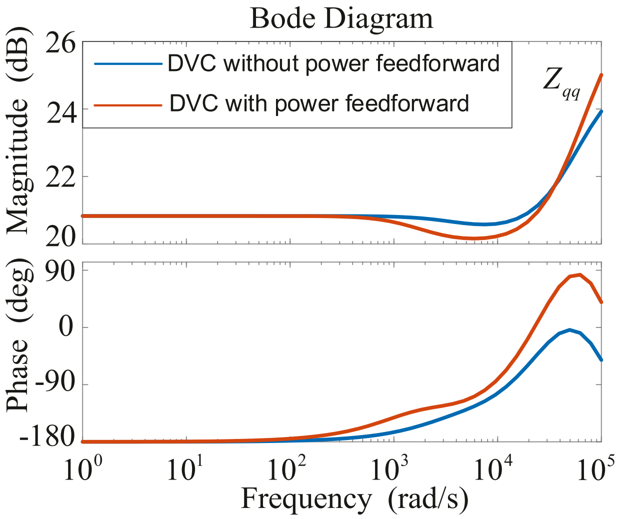

FIGURE 7 | Frequency characteristics of Z_{qq} with and without power feedforward.

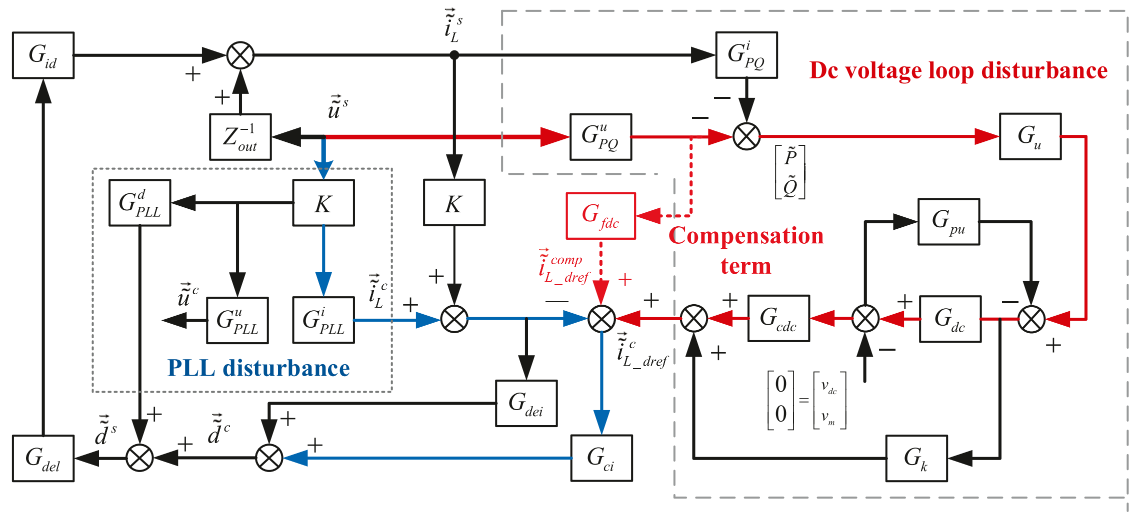

FIGURE 8 | Small signal model of the grid-connected inverter with PLL, ACC, and DVC.

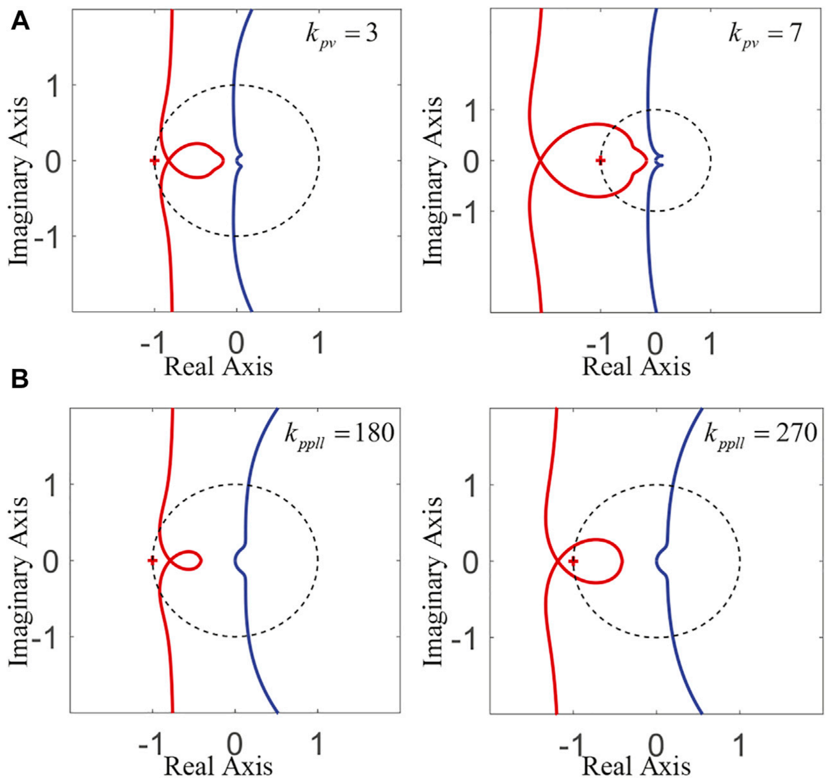

FIGURE 9 | (A) Impedance ratio curves of different k_{pv}; **(B)** impedance ratio curves of different k_{pll}.

According to (7), i_d can be expressed as follows:

$$i_d = i_{dc} \cdot \frac{2v_{dc}}{3v_d}. \tag{8}$$

According to (8), the power feedforward item $1/k_g = 2v_{dc}/3v_d$ is introduced into the DVC.

The voltage loop control is to maintain the power balance and stabilize the DC side voltage (Harnefors et al., 2007). The

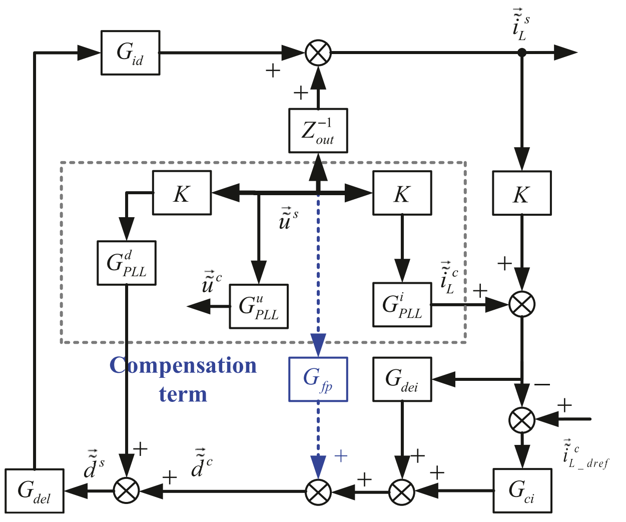

FIGURE 10 | Small-signal model of the grid-connected inverter.

introduction of a power feedforward link will reduce the signal of the outer loop voltage control command, thereby reducing the steady-state error of vdc, improving the response speed. **Figure 7** compares the frequency characteristic curve of Z_{qq} with and without power feedforward. It can be seen that the range of negative impedance characteristics of Z_{qq} is reduced with the addition of power feedforward, which indicates that the feedforward in DVC will improve the stability of the system.

3.2 Modeling of Output Impedance

The model of output impedance is built in d-q axis. In order to distinguish the variables of the system and the control loop, the superscript c represents the control loop variable, and the superscript s represents the system variable.

$$Z_{out} = \begin{bmatrix} Z_{dd} & Z_{dq} \\ Z_{qd} & Z_{qq} \end{bmatrix} = \begin{bmatrix} Ls + R & -\omega L \\ \omega L & Ls + R \end{bmatrix}. \tag{9}$$

K is the transfer function of the filter:

$$K = \begin{bmatrix} \dfrac{\omega_n^2}{s^2 + 2\zeta\omega_n s + \omega_n^2} & 0 \\ 0 & \dfrac{\omega_n^2}{s^2 + 2\zeta\omega_n s + \omega_n^2} \end{bmatrix} \frac{1}{2}. \tag{10}$$

G_{del} is the time delay caused by the control loop and PWM modulation, which can be expressed as follows:

$$G_{del} = \begin{bmatrix} \dfrac{1 - 0.5T_{del}s}{1 + 0.5T_{del}s} & 0 \\ 0 & \dfrac{1 - 0.5T_{del}s}{1 + 0.5T_{del}s} \end{bmatrix}. \tag{11}$$

In the formula, $T_{del} = 1/f_{sw}$, f_{sw} is the switching frequency. G_{id} is the transfer function from duty ratio $\vec{\tilde{d}}^s$ to inductor current $\vec{\tilde{i}}_L$, and G_{id} is as (Wen et al., 2015a) follows:

$$G_{id} = \frac{-V_{dc}}{(Ls + R)^2 + (\omega L)^2} \begin{bmatrix} Ls + R & \omega L \\ -\omega L & Ls + R \end{bmatrix}. \tag{12}$$

As mentioned, the inverter uses PLL to obtain the phase information of the grid voltage. The angle output by the PLL will then be used for the d-q axis conversion inside the inverter, so the dynamic characteristics of the PLL will affect the output voltage, current, and duty ratio signals of the inverter, which in turn affects its output impedance (Bakhshizadeh et al., 2016) **Eq. 13** is the transfer function of PLL.

$$G_{PLL} = \frac{k_{ppll} + k_{ipll}/s}{s + U_d^s\left(k_{ppll} + k_{ipll}/s\right)}, \tag{13}$$

where, k_{ppll} and k_{ipll} are the PI controller parameters in the PLL.

When a small signal disturbance is applied to the output voltage, the relationship between the control loop voltage $\vec{\tilde{u}}^c$ and the system voltage $\vec{\tilde{u}}^s$ is as follows:

$$\begin{bmatrix} \tilde{u}_d^c \\ \tilde{u}_q^c \end{bmatrix} \approx \underbrace{\begin{bmatrix} 1 & U_q^s G_{PLL} \\ 0 & 1 - U_d^s G_{PLL} \end{bmatrix}}_{\mathbf{G}_{PLL}^u} \begin{bmatrix} \tilde{u}_d^s \\ \tilde{u}_q^s \end{bmatrix}. \tag{14}$$

In the same way, the duty ratio signal has the following relationship:

$$\begin{bmatrix} \tilde{d}_d^s \\ \tilde{d}_q^s \end{bmatrix} \approx \underbrace{\begin{bmatrix} 0 & -D_q^s G_{PLL} \\ 0 & D_d^s G_{PLL} \end{bmatrix}}_{\mathbf{G}_{PLL}^d} \begin{bmatrix} \tilde{u}_d^s \\ \tilde{u}_q^s \end{bmatrix} + \begin{bmatrix} \tilde{d}_d^c \\ \tilde{d}_q^c \end{bmatrix}. \tag{15}$$

For the control loop inductor current, there is the following relationship:

$$\begin{bmatrix} \tilde{i}_d^c \\ \tilde{i}_q^c \end{bmatrix} \approx \underbrace{\begin{bmatrix} 0 & I_q^s G_{PLL} \\ 0 & -I_d^s G_{PLL} \end{bmatrix}}_{\mathbf{G}_{PLL}^i} \begin{bmatrix} \tilde{u}_d^s \\ \tilde{u}_q^s \end{bmatrix} + \begin{bmatrix} \tilde{i}_d^s \\ \tilde{i}_q^s \end{bmatrix}. \tag{16}$$

G_{PLL}^u , G_{PLL}^d, and G_{PLL}^i respectively, represent the influence of PLL on system voltage, duty ratio, and current.

The ACC control loop in **Figure 8** is realized by converting the system output current $\vec{\tilde{i}}_L^s$ into the current of the control loop $\vec{\tilde{i}}_L^c$ under the action of the filter and PLL and then through G_{dei} and G_{ci}. G_{dei} is the feedforward decoupling link:

$$G_{dei} = \begin{bmatrix} 0 & -\dfrac{3\omega L}{V_{dc}} \\ \dfrac{3\omega L}{V_{dc}} & 0 \end{bmatrix}. \tag{17}$$

G_{ci} is the current controller:

$$G_{ci} = \begin{bmatrix} k_{pi} + k_{ii}\dfrac{1}{s} & 0 \\ 0 & k_{pi} + k_{ii}\dfrac{1}{s} \end{bmatrix} \tag{18}$$

Ignoring the power loss of switching devices, the active power balance equation is as follows:

$$v_{dc} i_s = \frac{3}{2}\left(u_d i_d + u_q i_q\right). \tag{19}$$

Add a small signal disturbance the $\vec{u}^s$ helps obtain the power equation:

$$P = P_0 + \tilde{P}. \tag{20}$$

$$Q = Q_0 + \tilde{Q}. \tag{21}$$

In the formula, P_0 and Q_0 and $\tilde{P}$ and $\tilde{Q}$ are

$$\begin{bmatrix} P_0 \\ Q_0 \end{bmatrix} = \frac{3}{2} \cdot \begin{bmatrix} U_d & U_q \\ U_q & -U_d \end{bmatrix} \begin{bmatrix} I_d \\ I_q \end{bmatrix}. \tag{22}$$

$$\begin{bmatrix} \tilde{P} \\ \tilde{Q} \end{bmatrix} = \frac{3}{2} \cdot \begin{bmatrix} U_d & U_q \\ U_q & -U_d \end{bmatrix} \begin{bmatrix} \tilde{i}_d \\ \tilde{i}_q \end{bmatrix} + \frac{3}{2} \cdot \begin{bmatrix} I_d & I_q \\ -I_q & I_d \end{bmatrix} \begin{bmatrix} \tilde{u}_d \\ \tilde{u}_q \end{bmatrix}. \tag{23}$$

The input current i_s of the inverter is

$$i_s = \frac{P}{v_{dc}}. \tag{24}$$

$$\tilde{i}_s = \frac{\tilde{P}}{V_{dc}} - \frac{P_0}{V_{dc}^2} \tilde{v}_{dc}. \tag{25}$$

Set $G_u = 1/V_{dc}$ and $G_{pu} = P_0/V_{dc}^2$. G_{dc} represents the loss of DC side capacitance and switching device:

$$G_{dc} = \begin{bmatrix} R_{sw}/(CR_{sw}s + 1) & 0 \\ 0 & R_{sw}/(CR_{sw}s + 1) \end{bmatrix}. \tag{26}$$

The transfer function matrix G_{PQ}^i and G_{PQ}^u is defined and used for power calculation as

$$G_{PQ}^i = \frac{3}{2} \cdot \begin{bmatrix} U_d & U_q \\ U_q & -U_d \end{bmatrix}. \tag{27}$$

$$G_{PQ}^u = \frac{3}{2} \cdot \begin{bmatrix} I_d & I_q \\ -I_q & I_d \end{bmatrix}. \tag{28}$$

To obtain the impedance model of the inverter, supposing that on the DC side of the inverter, besides the DC voltage v_{dc}, there is also a voltage corresponding to it, which is defined as v_m. G_{cdc} is the voltage controller:

$$G_{cdc} = \begin{bmatrix} k_{pv} + k_{iv}\frac{1}{s} & 0 \\ 0 & k_{pv} + k_{iv}\frac{1}{s} \end{bmatrix}. \tag{29}$$

Let the power feedforward term $G_k = \begin{bmatrix} 1/k_g \\ 0 \end{bmatrix}$.

Therefore, according to **Figure 8**, the output impedance matrix of the grid-connected inverter small-signal model can be derived as follows:

$$Z_{out\_dc} = (I + G_1 + G_3)\left(G_2 + G_4 + Z_{out}^{-1}\right)^{-1}. \tag{30}$$

$$G_1 = KG_{del}G_{id}(G_{ci} - G_{dei}). \tag{31}$$

$$G_2 = KG_{PLL}^i G_{del} G_{id}(G_{ci} - G_{dei}) + KG_{PLL}^d G_{del} G_{id}. \tag{32}$$

$$G_3 = G_{PQ}^i G_u G_{ci} G_{del} G_{id}(G_{dc}G_{cdc} + G_k) + G_{dc}G_{pu}. \tag{33}$$

$$G_4 = -G_{PQ}^u G_u G_{ci} G_{del} G_{id}(G_{dc}G_{cdc} + G_k). \tag{34}$$

4 DUAL-LOOP COMPENSATION CONTROL

4.1 The Influence of the Proportional Gain of DVC on the Stability of the System

Under weak grid conditions, the increase of k_{pv} will easily cause DC bus voltage fluctuations and grid-side current distortions.

In **Figure 9A**, the Nyquist curves of the impedance ratio are shown. As k_{pv} increases, the impedance ratio curve gradually includes the (−1, j0) point. It shows that k_{pv} will affect the stability of the system.

4.2 The Influence of the Proportional Gain of PLL on the Stability of the System

In a weak grid, the PLL and the grid impedance are coupled with each other, and the voltage at the PCC point is distorted. The increase in k_{ppll} also increases the output error and reduces the system stability.

In **Figure 9B**, it can be seen that as k_{ppll} increases, the impedance ratio curve gradually includes the (−1, j0) point. It shows that the increase in k_{ppll} will make the grid-connected system unstable.

Aiming at the problem that the grid impedance, the PLL, and the DC voltage loop are coupled with each other, corresponding control methods need to be adopted to suppress unstable factors.

4.3 Disturbance Compensation Method of DVC

The disturbance path of the DC voltage loop in **Figure 8** shows that $\overrightarrow{u}^s$ affects $\overrightarrow{\tilde{i}}_{L\_dref}$ through the DC voltage loop and then affects the system output current through the current loop. Adding a compensation matrix G_{fdc} at the output of the DVC can offset the disturbance signal. Based on the small-signal model, the compensation matrix can be obtained as follows:

Compensation signal:

$$G_{fdc} = G_u \cdot G_{dc} \cdot G_{cdc}. \tag{35}$$

$$\overrightarrow{i}_{L\_dref}^{comp} = -\left(\overrightarrow{u}^s \cdot G_{PQ}^u\right) G_{fdc}. \tag{36}$$

Since G_{PQ}^u only affects the d-axis, the control signal can be obtained as follows:

$$i_{dref}^{comp} = -\frac{3}{2} \cdot u_d \cdot i_d \cdot G_{fdc}. \tag{37}$$

Disturbance Compensation Method of PLL

Figure 10 shows the disturbance path of the PLL, where the voltage at the PCC point passes through the transfer matrix G_{PLL}^i and then affects the output voltage command through the current loop. Therefore, a compensation matrix G_{fp} can be added at the ACC to offset the disturbance signal.

According to **Figure 10**, let the compensation term G_{fp} be

$$G_{fp} = K \cdot G_{PLL}^i \cdot G_{ci}. \tag{38}$$

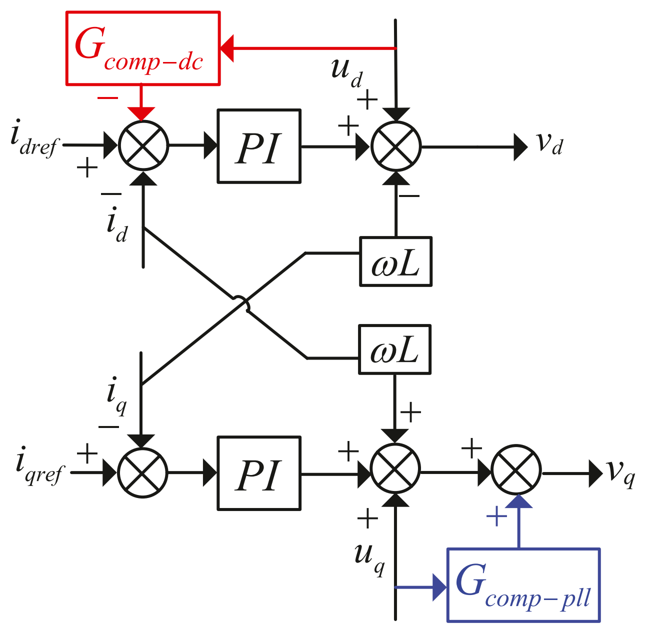

FIGURE 11 | Diagram of the current loop control system with compensation terms.

Due to the control voltage being $\vec{\tilde{u}}^c$, therefore according to the relationship between the control loop voltage $\vec{\tilde{u}}^c$ and the system voltage $\vec{\tilde{u}}^s$, the actual feedforward term can be obtained:

$$G^*_{fp} = K \cdot G_{IREF} \cdot G_P \cdot G_{ci}, \tag{39}$$

where

$$G_{IREF} = \begin{bmatrix} 0 & i_{qref} \\ 0 & -i_{dref} \end{bmatrix}. \tag{40}$$

$$G_P = \frac{\left(k_{ppll} + k_{ipll}/s\right)}{s}. \tag{41}$$

Since G^i_{PLL} only affects the q-axis current, the improved current control equation of the inverter can be expressed as follows:

$$\begin{cases} v_d = \left(k_p + \dfrac{k_i}{s}\right)\left(i_{dref} + i^{comp}_{dref} - i_d\right) - \omega L i_q + u_d \\ v_q = \left(k_p + \dfrac{k_i}{s}\right)\left(i_{qref} - i_q\right) + \omega L i_d + u_q + u_q \cdot K \cdot G_{fpq} \end{cases}. \tag{42}$$

The adjustment gain ξ is used to adjust the magnitude of the compensation signal, and G_{fpq} can be expressed as follows:

$$G_{fpq} = \frac{-i_{dref} \cdot \left(k_{ppll} + k_{ipll}/s\right) \cdot G_{ci} \cdot \xi}{s}. \tag{43}$$

Figure 11 of the current loop control system with compensation terms is shown in, where $G_{comp-dc} = 3/2 \cdot i_d \cdot G_{fdc}$, $G_{comp-pll} = K \cdot G_{fpq}$.

TABLE 1 | Grid-Connected system parameters.

Parameter	Symbol	Value
Filter inductance	L	19mH
Filter capacitance	C	0V
Filter impedance	R_{sw}	100Ω
DC voltage	v_{dc}	600V
D-axis grid voltage	v_d	200V
Q-axis grid voltage	v_q	0V
D-axis I current reference	i_{dref}	−20A
Q-axis current reference	i_{qref}	0A

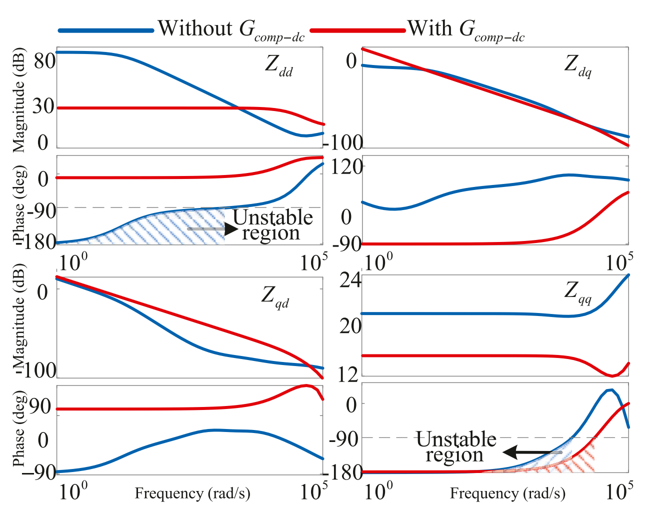

FIGURE 12 | Impedance frequency characteristics with and without $G_{comp-dc}$.

4.5 Analysis of Output Impedance

This section uses the data in **Table 1** to analyze the frequency characteristics of the inverter output impedance based on the previous deduction.

Comparison of simulation results of impedance frequency characteristics with and without $G_{comp-dc}$ is shown in **Figure 12**.

It can be seen from the figure that when the PLL is acting, the output angle of the PLL is affected by the q-axis voltage, and Z_{qq} characteristic is negative. The DVC and ACC use the angle to transform the coordinates and then introduce the negative influence of PLL to the d-axis. Z_{dd} presents a negative characteristic, and its amplitude is related to the output power of the inverter.

After adding $G_{comp-dc}$, Z_{dd} presents the frequency characteristic of positive impedance, which shows that the voltage loop compensation strategy proposed in this study effectively eliminates DVC's negative effects on the d-axis. Z_{qq} still presents negative impedance characteristics.

Figure 13 shows the impedance frequency characteristics with and without $G_{comp-pll}$, and after adding the PLL disturbance compensation, Z_{qq} presents the positive characteristic, and the

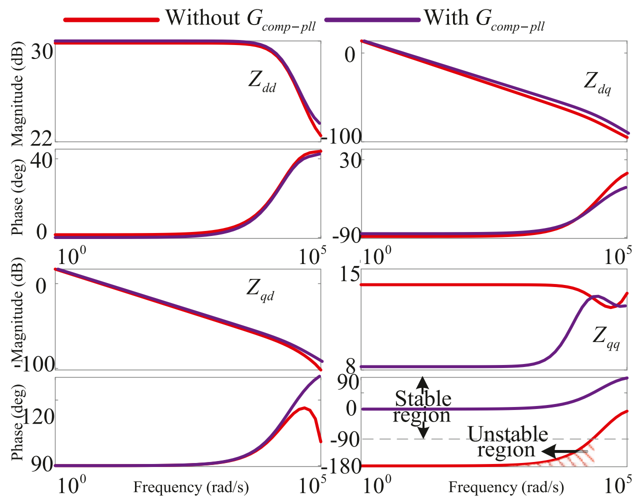

FIGURE 13 | Impedance frequency characteristics with and without $G_{comp-pll}$.

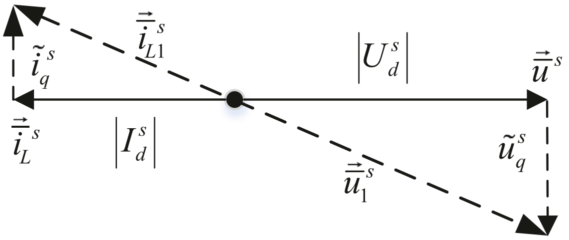

FIGURE 14 | Phasor diagram of the inverter when perturbation happens in q channel.

control method effectively eliminates the negative influence of PLL on the q-axis and improves the stability of the system.

The negative influence of PLL on the q-axis makes Z_{qq} exhibit negative characteristics. As the bandwidth of PLL increases, the range of frequency characteristics of negative impedance on Z_{qq} becomes larger, while the bandwidth of PLL has little effect on the amplitude of Z_{qq}. Its amplitude is related to the output power of the inverter.

As shown in **Figure 14**, the inverter current vector is synchronized with the grid voltage vector. Assuming that the inverter only delivers active power to the grid, when the disturbance occurs on the q-axis, the voltage vector will transition from the original equilibrium state $\vec{u}^{\,s}$ to the new equilibrium state $\vec{u}^{\,s}_1$. Similarly, the inverter current vector will be synchronized with the grid voltage vector and transition from the original equilibrium state $\vec{i}^{\,s}_L$ to the new equilibrium state $\vec{i}^{\,s}_{L1}$. In the low-frequency band, the calculation formula of Z_{qq} is as follows:

$$Z_{qq} = -\frac{|\tilde{v}_q^s|}{|\tilde{i}_q^s|} = -\frac{|V_d^s|}{|I_d^s|}. \tag{44}$$

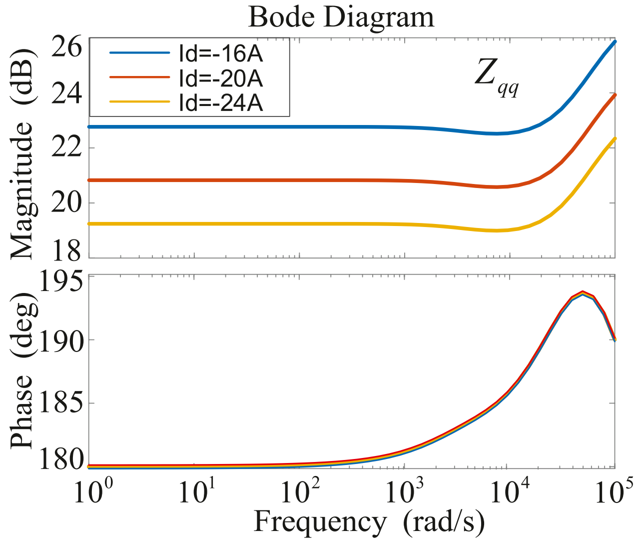

FIGURE 15 | Frequency characteristics of Z_{qq} under different grid-connected power.

The amplitude of grid voltage remains unchanged, and as the grid-connected power becomes larger, the amplitude of Z_{qq} becomes smaller. When the grid-connected power changes, the frequency characteristic curve of Z_{qq} is shown in **Figure 15**.

In **Figure 15**, different grid-connected power has no effect on the phase angle of Z_{qq}, and as the grid-connected power becomes larger, the amplitude of Z_{qq} becomes smaller.

In **Figure 13**, the addition of the compensation term not only eliminates the negative impedance characteristic of Z_{qq} but also reduces the amplitude of Z_{qq} in the low-frequency band and increases the output power of the inverter.

5 EXPERIMENTS

In order to verify the validity of the proposed control strategy, a HIL simulation platform was built in the OPAL-RT real-time simulation system which comprises an external controller and simulation computer. **Figure 16** is the OPAL-RT HIL system structure diagram. The host computer (Host PC) is used to build the system model and download it to the target computer (OP5600) through the TPC/IP channel; the target computer uploads information to the Host PC to monitor the operation of the model in real time. The grid-connected inverter controller adopts the TMS320F28335 digital signal processor (DSP). The DSP controller is responsible for collecting model output signals, performing real-time calculations, and generating PWM signals to send to the I/O board of the target machine to control the inverter.

When the output power of the PV array fluctuates:

Figure 17 shows the control experiment results of the PV and energy storage system under case 1. $P_{dc} = 4$ kW. By changing light intensity, in the first 2s, $P_{PV} > P_{dc}$, the battery is charged

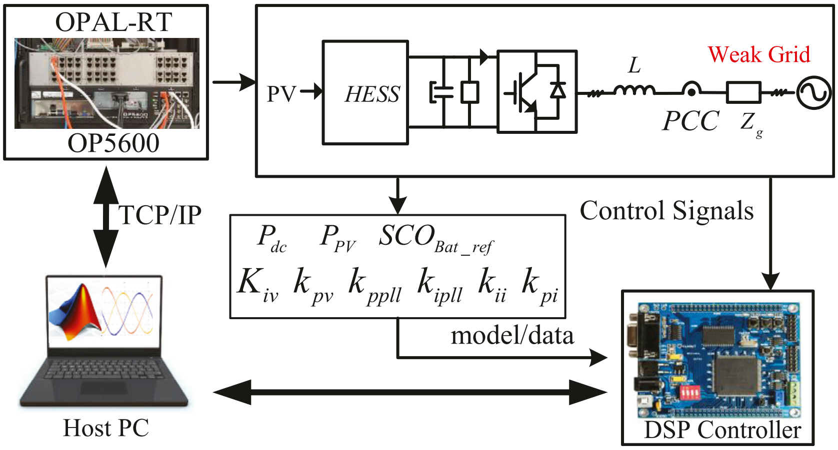

FIGURE 16 | HIL experiment topology.

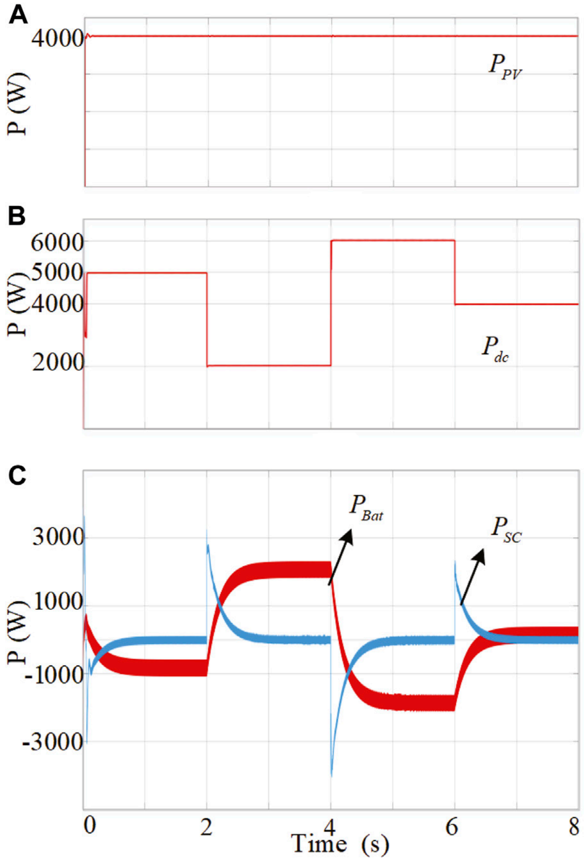

FIGURE 17 | (A) DC bus output power P_{dc}; **(B)** PV array output power P_{PV}; **(C)** HESS output power.

smoothly. At 2s, P_{dc} reduces to 2kW, $P_{PV} < P_{dc}$, SC discharges quickly to compensate for the power fluctuation of the system, and the battery discharges smoothly. At 4s, P_{PV} increases to 6kW, SC absorbs the power impact, and the battery is charged smoothly. During 6–8s, $P_{PV} = P_{dc}$, HESS works steadily.

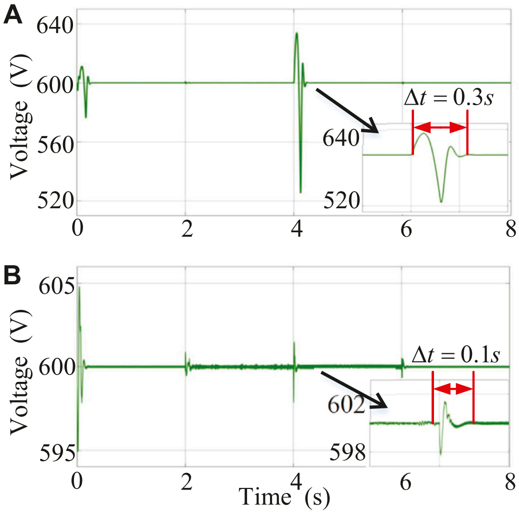

FIGURE 18 | (A) v_{dc} of the system without SC in case 1; **(B)** v_{dc} of HESS in case 1.

Figure 18 compares the waveforms of the vdc in different energy storage systems versus P_{PV} in case 1. It can be seen that v_{dc} has different degrees of fluctuation and is finally stabilized at 600 V. At 4 s, the fluctuation is the most obvious. The system without SC is stable after 0.3 s with larger fluctuation amplitude; HESS is stable after 0.1 s, and the fluctuation amplitude is smaller. It proves that when P_{PV} fluctuates, the HESS has faster dynamic response performance and higher stability than battery energy storage systems due to introduction of supercapacitors with higher power density.

When the output power of the DC bus fluctuates:

Figure 19 shows the control experiment results of the PV and energy storage system in case 2. At first $P_{PV} < P_{dc}$, the

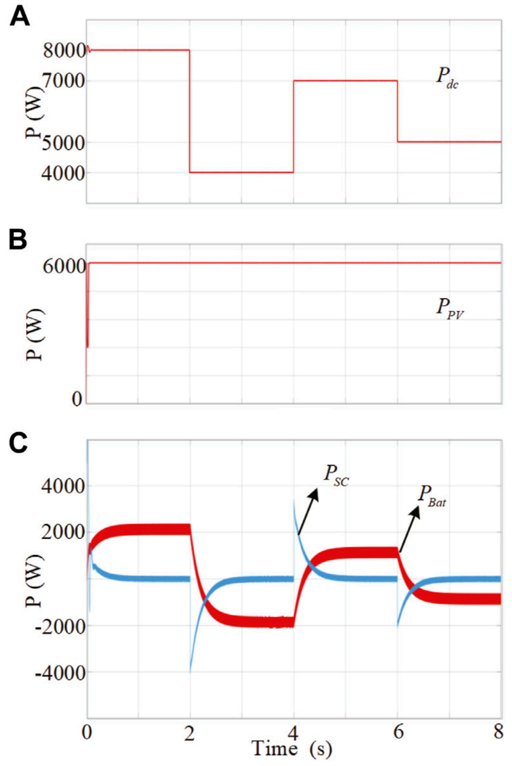

FIGURE 19 | (A) DC bus output power P_{dc}; **(B)** PV array output power P_{PV}; **(C)** HESS output power.

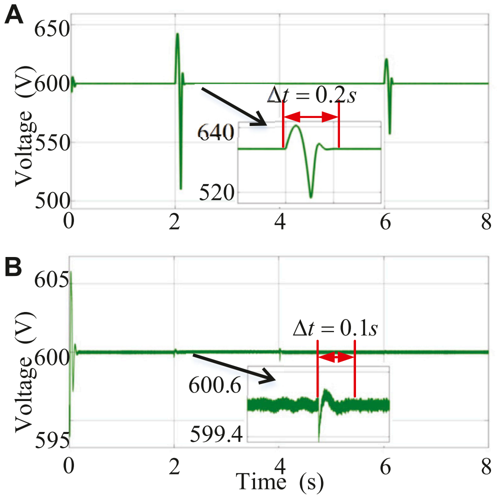

FIGURE 20 | (A) v_{dc} of the system without SC in case 2; **(B)** v_{dc} of HESS in case 2.

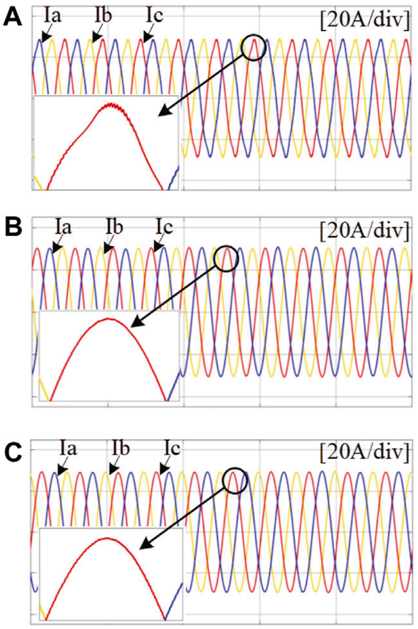

FIGURE 21 | Grid-connected current waveform; **(A)** without compensation; **(B)** with DVC compensation; **(C)** with PLL compensation.

battery is in a stable discharge state. Due to load reduction, P_{dc} decreases, SC is charged quickly to compensate for the power fluctuation, and the battery absorbs the remaining power smoothly. When P_{dc} suddenly increases, the SC provides sudden power to offset the impact, during which the battery discharges smoothly.

Figure 20 compares the waveforms of the v_{dc} in case 2. The most obvious fluctuation happens at 2s, the battery energy storage system takes 0.2 s to get stable, and the fluctuation amplitude is larger. The HESS takes 0.1 s to get stable with a smaller fluctuation. The HESS can overcome the shortcoming of the slow response of the battery system to the sudden change of load demand and effectively and quickly reduce the influence of system power fluctuation v_{dc}.

In order to suppress the negative impact of DVC and PLL, the experimental results of the improved method for the traditional inverter control strategy are as follows. **Figures 21, 22** show the simulation results of the grid-connected current before and after the compensation control is added to the inverter. The addition of the DVC compensation proposed in this article effectively eliminates the negative impact of the DC voltage loop, and the harmonic distortion rate of the grid-connected current is reduced from 4.18% to 1.02%. The system becomes stable and meets the grid-connected standards. The harmonic distortion rate of the grid-connected current is reduced from 1.02% to 0.68% when the negative influence of the PLL is compensated on the q-axis, which proves the validity of the control method proposed in this study.

In **Figure 23**, the experimental results show that in the very weak-grid condition, after compensation is added at 0.5 s, the distortion of the grid current is suppressed. The grid-connected system is restored to a stable state.

The common fault in the grid-connected operation of the PV system is simulated. The single-phase grounding fault current is measured at the PCC point. When a single-phase ground fault

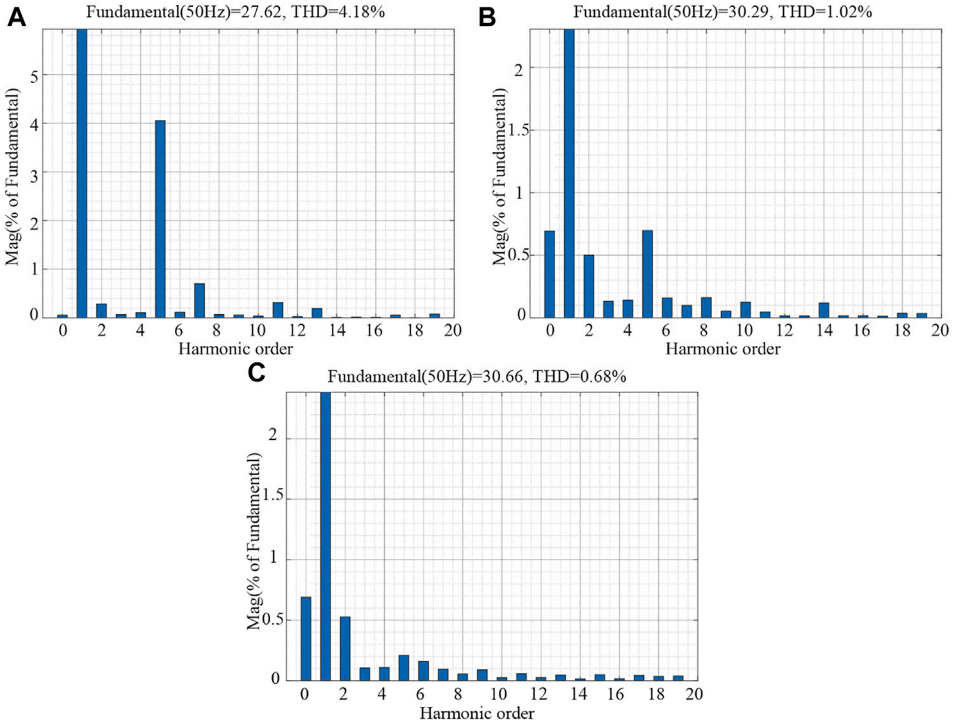

FIGURE 22 | Grid-connected current THD; **(A)** traditional control without compensation; **(B)** with DVC compensation; **(C)** with PLL compensation.

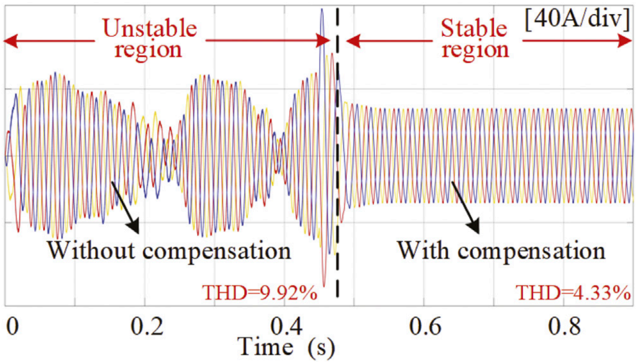

FIGURE 23 | Grid-connected current under very weak-grid.

occurs at the PCC point, the grid-connected current will change rapidly. A-phase ground fault occurs at 0.9 s. At 1.2 s, the A-phase ground fault is eliminated. The experimental results are shown in **Figure 24**. When phase A is grounded, it increases rapidly and distorts. After the fault is eliminated, the current can quickly recover to the current waveform before the A phase is grounded in about 0.01 s. After adding compensation, due to the negative feedback signal in the DVC compensation, the output current is greatly reduced when the fault occurs, and the current waveform is almost stable. The experimental results show that the proposed control method has a certain anti-interference ability to single-phase ground fault.

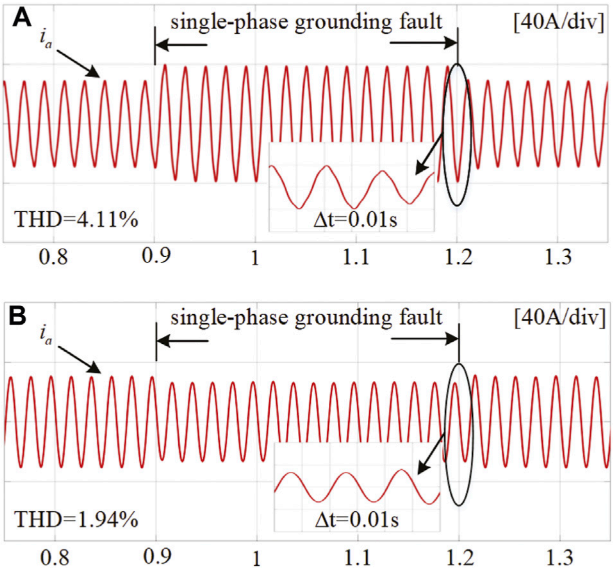

FIGURE 24 | Phase-A grounding fault current; **(A)** without compensation; **(B)** with compensation.

6 CONCLUSION

Aiming at the DC side voltage disturbance of the PV and energy storage system, this study adopts a HESS with a self-adaptive LPF to quickly and effectively stabilize the DC bus voltage. A small-signal model of the grid-connected inverter is established in the dq coordinate system, and the influence of the DC voltage loop and PLL on the output impedance of the inverter is discussed. The DC voltage loop disturbance compensation method based on power feedforward and the PLL disturbance compensation method based on voltage feedforward are proposed. The analysis results of the impedance frequency characteristics and HIL experiment show that the proposed method can reduce the range that the output impedance appears as a negative characteristic, thereby improving the stability of the system.

DATA AVAILABILITY STATEMENT

The original contributions presented in the study are included in the article/Supplementary Material; further inquiries can be directed to the corresponding author.

AUTHOR CONTRIBUTIONS

XL: Investigation, Conceptualization, Methodology, Validation, and Writing—review and editing. CL: Investigation, Conceptualization, Methodology, Software, Writing—original draft, and Writing—review and editing. RW: Supervision and Validation. YZ: Validation and Writing. LZ: Validation and review and editing.

FUNDING

This study is supported by the National Key R&D Program of China under grant (2018YFA0702200), the National Natural Science Foundation of China (62173074), the Key Project of National Natural Science Foundation of China (U20A2019), the State Key Laboratory of Alternate Electrical Power System with Renewable Energy Sources (Grant No. LAPS22002).

REFERENCES

Akram, U., Khalid, M., and Shafiq, S. (2018). Optimal Sizing of a Wind/solar/battery Hybrid Grid-connected Microgrid System. *IET Renew. Power Gener.* 12, 72–80. doi:10.1049/iet-rpg.2017.0010

Bakhshizadeh, M. K., Wang, X., Blaabjerg, F., Hjerrild, J., Kocewiak, Ł., Bak, C. L., et al. (2016). Couplings in Phase Domain Impedance Modeling of Grid-Connected Converters. *IEEE Trans. Power Electron.* 31, 6792–6796. doi:10.1109/TPEL.2016.2542244

Cao, W., Ma, Y., Yang, L., Wang, F., and Tolbert, L. M. (2017). D-Q Impedance Based Stability Analysis and Parameter Design of Three-Phase Inverter-Based AC Power Systems. *IEEE Trans. Ind. Electron.* 64, 6017–6028. doi:10.1109/tie.2017.2682027

Cespedes, M., and Sun, J. (2014). Adaptive Control of Grid-Connected Inverters Based on Online Grid Impedance Measurements. *IEEE Trans. Sustain. Energy* 5, 516–523. doi:10.1109/tste.2013.2295201

Davari, M., and Mohamed, Y. A.-R. I. (2016). Robust Vector Control of a Very Weak-Grid-Connected Voltage-Source Converter Considering the Phase-Locked Loop Dynamics. *IEEE Trans. Power Electron.* 32, 977–994. doi:10.1109/TPEL.2016.2546341

Dong, D., Wen, B., Boroyevich, D., Mattavelli, P., and Xue, Y. (2014). Analysis of Phase-Locked Loop Low-Frequency Stability in Three-phase Grid-Connected Power Converters Considering Impedance Interactions. *IEEE Trans. Industrial Electron.* 62, 310–321. doi:10.1109/TIE.2014.2334665

Harnefors, L., Bongiorno, M., and Lundberg, S. (2007). Input-admittance Calculation and Shaping for Controlled Voltage-Source Converters. *IEEE Trans. Ind. Electron.* 54, 3323–3334. doi:10.1109/tie.2007.904022

Harnefors, L., Wang, X., Yepes, A. G., and Blaabjerg, F. (2015). Passivity-based Stability Assessment of Grid-Connected Vscs—An Overview. *IEEE J. Emerg. Sel. Top. Power Electron.* 4, 116–125. doi:10.1109/JESTPE.2015.2490549

Jing, W., Hung Lai, C., Wong, S. H. W., and Wong, M. L. D. (2017). Battery-supercapacitor Hybrid Energy Storage System in Standalone DC Microgrids: Areview. *IET Renew. Power Gener.* 11, 461–469. doi:10.1049/iet-rpg.2016.0500

Lu, D., Wang, X., and Blaabjerg, F. (2018). Impedance-based Analysis of Dc-Link Voltage Dynamics in Voltage-Source Converters. *IEEE Trans. Power Electron.* 34, 3973–3985. doi:10.1109/TPEL.2018.2856745

Nicolini, A., Pinheiro, H., Carnielutti, F., and Massing, J. (2020). PLL Parameters Tuning Guidelines to Increase Stability Margins in Multiple Three-phase Converters Connected to Weak Grids. *IET Renew. Power Gener.* 14, 2232–2244. doi:10.1049/iet-rpg.2020.0028

Sun, J. (2011). Impedance-based Stability Criterion for Grid-Connected Inverters. *IEEE Trans. Power Electron.* 26, 3075–3078. doi:10.1109/tpel.2011.2136439

Tricarico, T., Gontijo, G. F., Aredes, M., Dias, R., and Guerrero, J. M. (2020). New Hybrid-microgrid Topology Using a Bidirectional Interleaved Converter as a Robust Power Interface Operating in Grid-connected and Islanded Modes. *IET Renew. Power Gener.* 14, 134–144. doi:10.1049/iet-rpg.2019.0626

Wang, X., Li, Y. W., Blaabjerg, F., and Loh, P. C. (2014). Virtual-impedance-based Control for Voltage-Source and Current-Source Converters. *IEEE Trans. Power Electron.* 30, 7019–7037. doi:10.1109/TPEL.2014.2382565

Wang, X., Ruan, X., Liu, S., and Tse, C. K. (2010). Full Feedforward of Grid Voltage for Grid-Connected Inverter with Lcl Filter to Suppress Current Distortion Due to Grid Voltage Harmonics. *IEEE Trans. Power Electron.* 25, 3119–3127. doi:10.1109/tpel.2010.2077312

Wen, B., Boroyevich, D., Burgos, R., Mattavelli, P., and Shen, Z. (2015a). Analysis of Dq Small-Signal Impedance of Grid-Tied Inverters. *IEEE Trans. Power Electron.* 31, 675–687. doi:10.1109/TPEL.2015.2398192

Wen, B., Boroyevich, D., Burgos, R., Mattavelli, P., and Shen, Z. (2014). Small-signal Stability Analysis of Three-phase Ac Systems in the Presence of Constant Power Loads Based on Measured Dq Frame Impedances. *IEEE Trans. Power Electron.* 30, 5952–5963. doi:10.1109/TPEL.2014.2378731

Wen, B., Dong, D., Boroyevich, D., Burgos, R., Mattavelli, P., and Shen, Z. (2015b). Impedance-based Analysis of Grid-Synchronization Stability for Three-phase Paralleled Converters. *IEEE Trans. Power Electron.* 31, 26–38. doi:10.1109/TPEL.2015.2419712

Xu, D., and Cen, H. (2021). A Hybrid Energy Storage Strategy Based on Multivariable Fuzzy Coordinated Control of Photovoltaic Grid-connected Power Fluctuations. *IET Renew. Power Gener.* 15, 1826–1835. doi:10.1049/rpg2.12152

Xu, J., Xie, S., Qian, Q., and Zhang, B. (2017). Adaptive Feedforward Algorithm without Grid Impedance Estimation for Inverters to Suppress Grid Current Instabilities and Harmonics Due to Grid Impedance and Grid Voltage Distortion. *IEEE Trans. Ind. Electron.* 64, 7574–7586. doi:10.1109/tie.2017.2711523

Xue, M., Zhang, Y., Kang, Y., Yi, Y., Li, S., and Liu, F. (2012). Full Feedforward of Grid Voltage for Discrete State Feedback Controlled Grid-Connected Inverter with Lcl Filter. *IEEE Trans. Power Electron.* 27, 4234–4247. doi:10.1109/tpel.2012.2190524

Yang, D., Ruan, X., and Wu, H. (2014). Impedance Shaping of the Grid-Connected Inverter with Lcl Filter to Improve its Adaptability to the Weak Grid Condition. *IEEE Trans. Power Electron.* 29, 5795–5805. doi:10.1109/tpel.2014.2300235

Yang, L., Chen, Y., Luo, A., Chen, Z., Zhou, L., Zhou, X., et al. (2019). Effect of Phase-locked Loop on Small-signal Perturbation Modelling and Stability Analysis for Three-phase LCL-type Inverter Connected to Weak Grid. *IET Renew. Power Gener.* 13, 86–93. doi:10.1049/iet-rpg.2018.0072

Yuan, H., Yuan, X., and Hu, J. (2017). Modeling of Grid-Connected Vscs for Power System Small-Signal Stability Analysis in Dc-Link Voltage Control Timescale. *IEEE Trans. Power Syst.* 32, 3981–3991. doi:10.1109/tpwrs.2017.2653939

Zhang, X., Xia, D., Fu, Z., Wang, G., and Xu, D. (2018). An Improved Feedforward Control Method Considering Pll Dynamics to Improve Weak Grid Stability of Grid-Connected Inverters. *IEEE Trans. Ind. Appl.* 54, 5143–5151. doi:10.1109/tia.2018.2811718

Zhou, J. Z., Ding, H., Fan, S., Zhang, Y., and Gole, A. M. (2014). Impact of Short-Circuit Ratio and Phase-Locked-Loop Parameters on the Small-Signal Behavior of a Vsc-Hvdc Converter. *IEEE Trans. Power Deliv.* 29, 2287–2296. doi:10.1109/tpwrd.2014.2330518

Conflict of Interest: The authors declare that the research was conducted in the absence of any commercial or financial relationships that could be construed as a potential conflict of interest.

frontiers | Frontiers in Energy Research

TYPE Original Research
PUBLISHED 08 August 2022
DOI 10.3389/fenrg.2022.971725

EDITED BY
Qihe Shan,
Dalian Maritime University, China

REVIEWED BY
Guangzheng Yu,
Shanghai University of Electric Power, China
Ping Hu,
EPFL, Switzerland
Peiyin Chen,
Tianjin University, China

*CORRESPONDENCE
Jun'e Li,
jeli@whu.edu.cn

SPECIALTY SECTION
This article was submitted to Smart Grids,
a section of the journal
Frontiers in Energy Research

RECEIVED 17 June 2022
ACCEPTED 12 July 2022
PUBLISHED 08 August 2022

CITATION
Li J, Liang J, Liu Q, Qi D, Zhang J and Chen Y (2022), Research on situation assessment of active distribution networks considering cyberattacks. *Front. Energy Res.* 10:971725.
doi: 10.3389/fenrg.2022.971725

Research on situation assessment of active distribution networks considering cyberattacks

Jun'e Li[1]*, Jiaqi Liang[1], Quanying Liu[1], Donglian Qi[2], Jianliang Zhang[2] and Yangrong Chen[1]

[1]Key Laboratory of Aerospace Information Security and Trusted Computing, Ministry of Education, School of Cyber Science and Engineering, Wuhan University, Wuhan, China, [2]College of Electrical Engineering, Zhejiang University, Hangzhou, China

With the rapid development of integrated energy system, the large-scale and high-permeability access of distributed generations (DGs) is making the distribution networks develop into active distribution networks (ADNs). The increased complexity of ADNs also increases the vulnerabilities for cyberattacks. It is a new challenge how to evaluate the situation of an ADN so as to support the decision-making of grid control policies in the condition of cyberattacks probably occur. Hence, in this paper, we proposed a method of situation assessment for ADNs considering cyberattacks. This method is aggregated by two parts. 1) An index system is presented, which includes the indexes of DGs stability, the indexes of security risk considering cyberattacks along with the traditional safety indexes. 2) The entropy weight method is used to assign weights to each index, and taking the normal operation status of ADNs as the reference scenario, an operating situation assessment method for ADNs is proposed based on grey correlation analysis method. Finally, in order to verify the effectiveness of the proposed index system and assessment method, 12 attack scenarios are established from three categories: attacks on DGs, attacks on controllable loads and attacks on both of them, and the situation of the ADN, a case based on IEEE 33-node standard distribution system, is evaluated under each scenario.

KEYWORDS

integrated energy systems, active distribution network, situation assessment, cyberattack, index system, assessment method

1 Introduction

The rapid development of integrated energy systems alleviate the energy crisis, but also brings security threats to the power system. However, situation assessment of power grid can help to grasp the operation status of power grid in time, provides basis for the projection and early warning of power grid situation, and assists the operation control decision of power grid so as to ensure the safe and stable operation of power grid (Lin et al., 2018; Russell, et al., 2018; Wang et al., 2019; Wang et al., 2020; Lai et al., 2022).

As a substantial component of ADNs, the large integration of DGs, controllable loads (CLs), and distributed energy storages (DESs) have caused severe challenges for the safe and stable operation of the ADNs. 1) In terms of DGs, power flows are now bidirectional rather than unidirectional, and it also alters the architecture of the conventional distribution network (Sultan et al., 2013). Furthermore, different manufacturers of DG use different communication protocols (Wang X. et al., 2017). Attackers could substantially threaten the safe and stable operation of ADNs and even cause power outages if they successfully utilize communication protocol vulnerabilities and other crucial information (Ismail et al., 2020). 2) In terms of CLs, with the uninterrupted improvement of inhabitants' living standards, household terminal load is changed into household CLs via the Internet of Things. However, some household equipment cyber security protection measures are inadequate. When attackers utilize vulnerabilities to launch cyber attacks on large-scale household CLs, it may causes ADNs voltage overruns, frequency oscillations, circuit breaker disconnection, and power outage in severe case (Gallo et al., 2020). 3) In terms of DESs, the essential protocol standards for DESs access into ADNs are still in the initial stage, and communication management has not attracted much attention. Taking the electric vehicle charging and discharging station as an example, due to the user side of information security protection is relatively vulnerable, the attackers are more likely to use parking intelligent terminal embedded system vulnerabilities embedded malicious code and send malicious control command via the Internet, which can destroy the mode of electric vehicle charging and discharging, cause the power quality problems and ADNs power balance of demand and supply in severe cases (McLaughlin et al., 2016). It can be seen that the attackers launch cyber attacks through using the cyber security vulnerability, the adverse impact on ADNs can not be underestimated. Hence, in order to ensure the safe and stable operation of the ADNs, it is urgent to establish the operation situation assessment method of ADNs considering cyberattacks, so as to adjust the operation status of power grid, formulate control strategies and emergency plans.

At present, situation assessment as the core content of power grid situation awareness, the study of situation assessment can be mainly divided into three categories. 1) From the perspective of power grid dispatching control center, the situation awareness technology to the power grid operation control, and an intelligent dispatching system based on situation awareness are applied by Lai et al. (2020), Shahsavari et al. (2019) and Li et al. (2015). 2) The operation situation assessment and projection methods of power grid based on massive data collected by wide-area measurement system are studied by Li et al. (2020), Liu et al. (2018), Li et al. (2021), Jena et al. (2017) and Ren et al. (2019). 3) The main components and functional hierarchy of power grid situation awareness system are analyzed by Li et al. (2019), Wang and Govindarasu. (2020) and Zhao et al. (2019), and propose the smart grid situation awareness model and conceptual design. The above studies mainly focus on the power grid operation safety status assessment and the theoretical framework of power grid situation awareness, but the situation awareness methods are rarely discussed in detail and need to be further studied.

In the study of power grid situation awareness, there are relatively few studies about situation awareness of ADNs. A framework of ADNs situation awareness, constructs an optimal dispatching framework based on analysis of the linkage relationship between situation awareness and optimal dispatching, and elaborates the key technology for optimal dispatching of ADNs (Wang H. et al., 2017). From the initiative perspective of ADNs, a framework of situation awareness and points out the key problem should be solved in realizing situation awareness is given by Lin et al. (2016). Huang et al. (2017) mines a large amount of historical data values of ADNs, adds the ADNs virtual measurement information data, so as to improve the accuracy of state estimation and provides technical support for the online status perception of ADNs. Tao et al. (2020) proposes a situation awareness system of ADNs based on distributed monitoring and multi-source information fusion, and elaborates the situation awareness technology of ADNs based on multi-source information fusion. Above all, most of the above research works focus on the theoretical level of the ADNs situation awareness system framework, the key technologies such as multi-source information fusion ADNs situation assessment and projection methods are not in-depth enough studied, and there are rarely relevant study of considering cyberattacks and operation law of ADNs.

In order to evaluate the operation status of ADNs effectively, this paper studies the situation assessment method of ADNs considering cyberattack. The main contributions are as follows.

(1) Considering the uncertain outputs of DGs and the vulnerabilities for cyberattacks to DGs and controllable loads, the indexes of DGs stability and the indexes of security risk considering cyberattacks along with the traditional safety indexes are employed as the indexes of situation assessment of ADNs.
(2) On the basis of the proposed index system, the operation situation assessment method of ADNs is established based on the entropy weight method and grey relation method. This method can quantitative assessment the operation safety status of ADNs to provide the basis for operation situation projection and operation control decision of ADNs.
(3) Twelve attack scenarios of the ADN, a case based on IEEE 33-node standard distribution system, are established from three categories: attacks on DGs, attacks on controllable loads and attacks on both of them to verify the effectiveness of the proposed index system and assessment method.

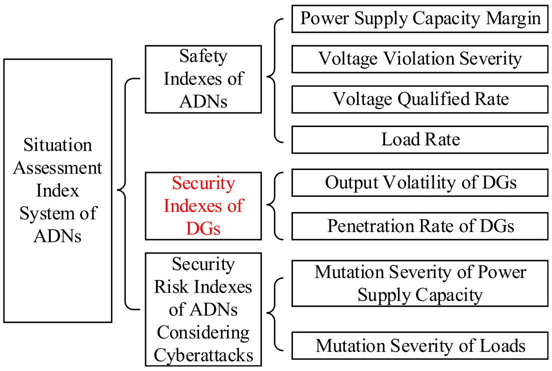

FIGURE 1
Situation assessment index system of ADNs.

The rest of paper is organized as follows. Section 2 proposes situation assessment index system. Sections 3 investigates situation assessment method of ADNs based on entropy weight method and grey correlation analysis method. Section 4 verifies the proposed method in IEEE 33-node active distribution system. And conclusions are presented in Section 5.

2 Situation assessment index system

The safe and stable operation of ADNs depends on its safety characteristics during operation, the stability of DGs in ADNs and the risk when it suffering cyberattacks (Canizes et al., 2017). On the one hand, the normal operation of ADNs require sufficient capacity margin to maintain the normal level of the voltage and frequency. The voltage value should not deviate too much from the rated voltage, and the number of voltage qualified nodes should not be less than the normal operation status standards. The branch line should not run under heavy load for a long period. The output of the DGs should not fluctuate too much in operation status. On the other hand, the cyberattack events against power system in recent years show that the potential cyberattacks risks also have a crucial impact on the safe and stable operation of ADNs. Therefore, we present the situation assessment index system of ADNs as shown in Figure 1.

2.1 Safety indexes of ADNs

The safe operation characteristics of ADNs are related to the power supply capacity margin, the voltage violation severity, the voltage qualification rate and the load rate (Fauzan et al., 2019). Those indexes can reflect the security margin of power supply capacity, the harmful degree of system voltage fluctuation and the security risk of ADNs.

2.1.1 Power supply capacity margin

The power supply capacity margin represents the percentage of the loads that can be increased based on the current loads. It can be defined as follows:

$$\eta = \frac{S_{\max} - L_{total}}{S_{\max}} \times 100\% \tag{1}$$

In Eq. 1, $S_{\max}$ represents the maximum of power supply capacity, which is the sum of the capacity of the main transformer and the output of each DG in the ADNs. L_{total} represents the total load value in the ADNs.

2.1.2 Voltage violation severity

The voltage violation severity represents the degree of voltage deviation from the rated voltage. While the power grid failure has happened, the voltage value also be impacted, and the operation voltage value deviates from the normal voltage may aggravate the vulnerability of the ADNs. In severe cases, it directly impacts the safe and stable operation status of the ADNs. Hence, voltage violation severity can be defined as follows:

$$\omega_i = \begin{cases} 0.95 - u_i & u_i < 0.95 \\ 0 & u_i < 1.05 \\ u_i - 0.95 & u_i > 1.05 \end{cases} \tag{2}$$

In Eq. 2, u_i represents the ratio of the ith node to rated voltage in ADNs.

2.1.3 Voltage qualified rate

Voltage qualified nodes need to satisfied the following requirements: 1) Power supply voltage exist on the nodes. 2) The nodes voltage value do not exceed the threshold. The voltage qualification rate refers to the percentage of voltage qualified nodes account for the total number nodes of the ADNs. Voltage qualified rate also reflects the comprehensive voltage quality during the operation status of ADNs. To some extent, it represents characterizes the security of ADNs operation status. Hence, voltage qualified rate can be defined as follows:

$$f = 1 - \frac{N_{exceed}}{N_{all}} \times 100\% \tag{3}$$

In Eq. 3, N_{exceed} represents the number of nodes exceed the voltage threshold or lost the function of power supply. N_{all} represents the total number nodes of ADNs.

2.1.4 Load rate

If the load rate of the main transformer approaches the threshold or run with heavy loads, once the distribution network suffered cyberattacks or failures happened, it may cause the load changed or large-scale power flow of a certain node transfer into another node. Therefore, it may lead to the overload of the main transformer and large-scale cascading failures happened in the future in severe case. From the perspective of safe operation of ADNs, no matter whether the failure of ADNs happened or not, we expect that the main transformer running in a safe range, and security risk decreases as the load rate decreases. Hence, the load rate can be defined as follows:

$$\gamma = \frac{S_T}{S_{T\max}} \tag{4}$$

In Eq. 4, S_T represents the actual transmission capacity of main transformer in ADNs. S_{Tmax} represents the max transmission capacity of main transformer in ADNs.

2.2 Security indexes of DGs

The distribution network contains a large number of renewable energy DGs. Such as photovoltaic power stations, wind farms and so on. The output of those kinds of DGs are greatly impacted by climate, and climate can lead to uncertain output of DGs (Arya, 2016). What's more, DGs are more likely to fluctuate under all kinds of disturbance, those disturbances can cause the change of the direction and value of the power flow in the distribution network, and even result in the fluctuation of the system voltage and bring the challenge to itself safe operations status. At the same time, due to many uncertain factors of DGs, the high permeability of DGs may increase the risk of stable operation of the ADNs and result in different degrees of impact on the ADNs security. Therefore, the output volatility and the penetration rate of DGs are play an important role in index evaluating the security risks of ADNs.

2.2.1 Output volatility of DGs

Output volatility of DGs can be defined as follows:

$$\zeta_{DG} = \frac{S_{DG}(t+1) - S_{DG}(t)}{S_{DG}(t)} \tag{5}$$

In Eq. 5, $S_{DG}(t+1)$ represents the actual output of all DGs at time ($t+1$). $S_{DG}(t)$ represents the actual output of all DGs at time t.

2.2.2 Penetration rate of DGs

Penetration rate of DGs can be defined as follows:

$$\lambda = \frac{S_{DG}}{L_{total}} \times 100\% \tag{6}$$

In Eq. 6, S_{DG} represents the actual output of all DGs in ADNs. L_{total} represents the total load of ADNs.

2.3 Risk indexes

According to the three elements of network security proposed by the National Institute of Standards and Technology (Zhao et al., 2019), cyberattacks can be classified into three categories according to their consequences as follows: 1) Destroying the confidentiality; 2) Destroying the integrity; 3) Destroying the availability. Among them, the first category of attacks aims to steal data and does not directly impact the power grid. The second category of attacks aims to control the power generations or loads maliciously by tampering or falsifying measurement data or control commands, which can directly impact the operation status of the power grid. The third category of attacks makes the cyber system partially or completely lose control of the power grid by blocking communication or increasing time delay, which mainly impacts the observability and controllability of the power grid. It can be seen that only the second category of attacks can be awareness through the operation status data of the power grid. Therefore, this paper established ADNs security risk index for second category of attacks.

2.3.1 Mutation severity of power supply capacity

Cyberattacks can cause the main transformers and DGs out of running, aggravate the power supply burden of the remaining transformers, and result the output shortage or voltage collapse of ADNs. Cyberattacks can also lead to increase output of DGs, aggravate the instability of ADNs, and excessive reactive power output can cause the voltage to exceed the safe operation range. The sudden changes of power supply capacity can impact the reliability and quality of ADNs, which may bring hidden impact to the safe operation status of the ADNs (Liang et al., 2021).

Therefore, the mutation severity index of power supply capacity can be defined as follows:

$$\alpha = \frac{S_{\max}(t+1) - S_{\max}(t)}{S_{\max}(t)} \tag{7}$$

In Eq. 7, $S_{max}(t+1)$ represents the maximum power supply capacity of distribution network in time (t+1). $S_{max}(t)$ represents the maximum power supply capacity of distribution network in time t.

2.3.2 Mutation severity of loads

Cyberattacks can lead to the large-scale controllable loads casting/dropping synchronously or frequent and synchronous casting and dropping, threaten the safe and stable operation of the ADNs(Kurt et al., 2018; Wei et al., 2020; Liang et al., 2021). Hence, we use the mutation severity of loads represent the impact of the cyberattacks.

The index of mutation severity of loads can be defined as follows:

$$\beta = \frac{\sum_{i=1}^{M} |L_i(t+1) - L_i(t)|}{L_{total}(t)} \tag{8}$$

In Eq. 8, $L_i(t+1)$ represents the loads of node i in time ($t+1$). $L_i(t)$ represents the loads of node i in time t. $L_{total}(t+1)$ is the total loads of ADNs in time t.

3 Situation assessment method

In this section, the basic thought of the situation assessment method of ADNs is as follows: first, after establishing the ADNs situation assessment indexes according to Section 2, the weights are assigned to the indexes according to the impact degree of each index on the assessment results; then, the normal operation status of ADN is taken as the reference scenario, and the correlation degrees between the attack scenarios to be assessed and the reference scenario are calculated based on the grey correlation analysis method; finally, the security risk levels of those scenarios can be determined according to the pre-defined criteria.

3.1 Calculating the weights of situation assessment indexes based on entropy weight method

In the situation assessment of ADNs, each index has different functions and impacts on the assessment results, so it is necessary to assign corresponding weights to different indexes. The index weight reflects the importance in the index systems, and a reasonable weight distribution is the basis for accurately assessing the operating situation of the ADNs. The entropy weight method needs to calculate only once, which can help to obtain the suitable index weight to each evaluation object, so that the calculation of the weights are no longer complexity, and that is a most widely used objective weight method. To sum up, this paper adopts this method to obtain the weight of each index.

Suppose that there are m indexes, and n samples, $x_{ij}\,(i \in [1,n], j \in [1,m])$ represents the *jth* index of the *ith* sample, then each original data sample can be represented as follows:

$$X_i = (x_{i1}, x_{i2}, \cdots, x_{im}) \tag{9}$$

The original data assessment matrix can be represented as follows:

$$X_{nm} = [X_1, X_2, \cdots X_n]^T \tag{10}$$

The process of calculating the weights of situation assessment indexes based on entropy weight method is as follows.

(1) Standardizing the index values. The index system proposed in this paper includes positive indexes and negative indexes. Among them, the positive index has property that the larger the index value is, the better the index will be. However, the negative index has property that the smaller the index value is, the better the index will be. In the ADNs safety index system, we should consider the impact of cyberattacks. Therefore, the voltage qualification rate and the power supply capacity margin should be included in the positive index system. Similarly, the voltage violation severity, the load factor, the output volatility of DGs, the permeability of DGs, the power supply capacity mutation severity and the load mutation severity should be included in the negative index system. The range transformation method is used to standardize the original calculated values of each index in the safety index system of ADNs considering cyberattacks. If the *kth* index is positive index, it can be calculated as follows:

$$x_{ik}^{'}= \frac{x_{ik} - \min(x_{1k}, x_{2k}, \cdots, x_{nk})}{\max(x_{1k}, x_{2k}, \cdots, x_{nk}) - \min(x_{1k}, x_{2k}, \cdots, x_{nk})} \tag{11}$$

If the *kth* index is negative index, it can be calculated as follows:

$$x_{ik}^{'}= \frac{\max(x_{1k}, x_{2k}, \cdots, x_{nk}) - x_{ik}}{\max(x_{1k}, x_{2k}, \cdots, x_{nk}) - \min(x_{1k}, x_{2k}, \cdots, x_{nk})} \tag{12}$$

(2) Calculating the entropy of each index. The entropy of each index can be calculated as follows:

$$E_j = \frac{\sum_{i=1}^{n} x_{ij}^{'} ln\, x_{ij}^{'}}{lnn} \tag{13}$$

It shows, when $x_{ij}^{'}= 0, x_{ij}^{'} ln\, x_{ij}^{'}= 0$.

(3) Calculating the weight of each index. The weight of each index can be calculated as follows:

$$w_j = \frac{1 - E_j}{\sum_{j=1}^{m} \left(1 - E_j\right)} \tag{14}$$

3.2 Situation assessment method based on grey correlation

Grey correlation analysis method is an important part of grey system theory. The essence of grey correlation analysis method is to judge the correlation degree between the reference sequence curve and the research sequence curve according to their similarity degree. Compared with the method of mathematical statistics in system analysis, this method does not require a large number of sample data and it also does not satisfies the rule of typical probability distribution either. Meanwhile, this method has uncomplicated calculation processing, and the calculation results are consistent with the results of qualitative analysis, so as to this method is widely used.

However, there are some limitations in the grey correlation analysis method, such as its need to select reference sequence, that is, to determine the optimal value of each index, which is too subjective. At the same time, it is difficult to determine the optimal value of part of indexes. In the processing of situation assessment of ADNs, the data in the normal operation status can be taken as a reference sequence, and this reference sequence without any strong subjectivity. So it is best choices to apply in situation assessment of ADNs.

The main steps and methods are as follows.

(1) Selecting the reference sequence. It is necessary to draft the reference sequence before doing grey correlation analysis, and reference sequence should be an ideal reference standard. We use the data sample when the ADNs is not suffering from attacks as the reference sequence. Suppose that there are m indexes and n samples, according to Eq. 9, the reference sequence can be represented as follows:

$$X_0 = (x_{01}, x_{02}, \cdots, x_{0m}) \tag{15}$$

(2) Calculating the difference sequences and determine the maximum and minimum values of the difference sequence. Calculate the absolute difference between each element of the original data sequences and the reference sequences, which can be used to form the difference sequence, it can be calculated as follows:

$$\left|x_{0j} - x_{ij}\right| \tag{16}$$

(3) Calculating the correlation coefficient according to the maximum value $\underset{i}{max}\,\underset{j}{\max}|x_{0j} - x_{ij}|$ and the minimum value $\underset{i}{min}\,\underset{j}{min}|x_{0j} - x_{ij}|$ of the difference sequences, it can be calculated as follows:

$$\xi(j) = \frac{\underset{i}{min}\ \underset{j}{min}\left|x_{0j} - x_{ij}\right| - \rho\,\underset{i}{max}\ \underset{j}{max}\left|x_{0j} - x_{ij}\right|}{\left|x_{0j} - x_{ij}\right| + \rho\,\underset{i}{max}\ \underset{j}{max}\left|x_{0j} - x_{ij}\right|} \tag{17}$$

In Eq. 17, ρ is the resolution coefficient, and its value range is (0, 1). Usually, ρ is set to 0.5.

(4) Calculating the correlation degree. The correlation degree can be calculated as follows:

$$r\left(x_{0j} - x_{ij}\right) = \sum_{j=1}^{m} w_j \xi_i(j) \tag{18}$$

In the above Equation, the value of the weight w_j directly impacts the correlation degree, that is, the result of the situation assessment of the ADNs. The w_j in this paper takes the objective weight of each index, which can be calculated by entropy weight method in 3.1.

3.3 Grading the risk level of ADNs situations

According to the situation assessment method of the ADNs, the situation security risk degree of the ADNs can be determined by the correlation degree. It means if the security risk degree is high, the correlation degree will be low. Therefore, according to the numerical range of the correlation degree, the security risk level can be graded into 6 levels, namely 0, 1, 2, 3, 4 and 5. The numerical range of the correlation degree of each security risk level is shown in Table 1.

4 Case study

In this section, we select the IEEE 33-node standard distribution system as a basis case, and connect DGs to it to form an ADN case for study. As shown in Figure 2, we take photovoltaic power (PV) as an example of renewable energy DGs, and connect PVs to the node 18 and node 22. In addition, micro gas turbine units are connected to the node 33.

Firstly, 12 attack scenarios are presented based on the possible cyberattacks on the ADN. Then, the security risk level of the ADN under each attack scenario is evaluated according the proposed method. Where, the operation parameters of the ADN for the calculation are obtained through simulations. Finally, we theoretically analyze the security risk of the ADN under the comparing attack scenarios to illustrate the rationality of the assessment results.

All the experiments are programmed on toolbox Matpower, and all the simulations run on a Dell PC with a 3.3 GHz CPU and 16 GB ram.

4.1 Attack scenarios

Based on the possible cyberattacks on the ADN, we envisage 12 attack scenarios from three categories: attacks on DGs, attacks on controllable loads and attacks on both of them, which can be shown in Table 2. In addition, we take the ADN operation status in normal as the reference scenario and set it as scenario 0.

4.2 Situation assessment under attack scenarios

In this part, we firstly obtain the operation parameters of the ADN under each scenario through simulations, and then calculate the indexes according to Eqs 1–8.

Taking scenario 1 as an example. The operation parameters obtained by simulation are shown in Table 3. It should be noted that the operating parameters need to be obtained from the measurement system in practice.

Then, according to Eqs 1–8, the situation assessment indexes are calculated as shown in Table 4.

TABLE 1 Security risk level grading of ADNs situations.

r	$0.9 < r \leq 1$	$0.8 < r \leq 0.9$	$0.7 < r \leq 0.8$	$0.6 < r \leq 0.7$	$0.5 < r \leq 0.6$	$r \leq 0.5$
Risk level	0	1	2	3	4	5

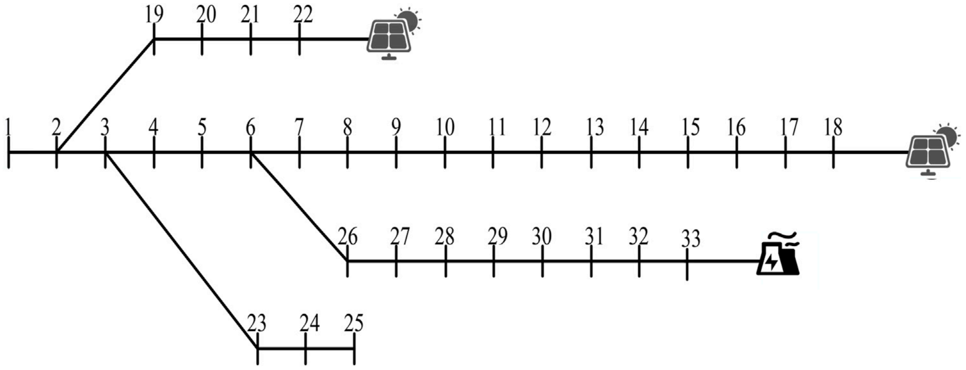

FIGURE 2
An ADN based on IEEE 33-node standard distribution system.

TABLE 2 Cyberattack scenarios.

Attack target	Scenario	Attack strategy
DGs	1	Remove the PV of node 18
	2	Remove the PV of node 22
	3	Remove the micro gas turbine of node 33
	4	Remove the PV and the micro gas turbine of node 18, 22, 33 synchronously
Loads	5	Increase the load of nodes 12, 13, 14, 15, 16, 17 and 18 by 60 kW synchronously
	6	Increase the load of nodes 2, 19, 20, 21, 22, 32 and 33 by 60 kW synchronously
	7	Reduce the load of nodes 12, 13, 14, 15, 16, 17 and 18 by 60 kW synchronously
	8	Cut off the branch line after node 17
	9	Cut off the branch line after node 15
	10	Cut off the branch line after node 6
DGs and Loads	11	Cut off all of the DGs, and increase the load of nodes 12, 13, 14, 15, 16, 17 and 18 by 60 kW synchronously
	12	Cut off all of the DGs, and reduce the load of nodes 12, 13, 14, 15, 16, 17 and 18 by 60 kW synchronously

TABLE 3 Simulation results of operation parameters of the ADN under scenario 1.

S_{max}	L_{total}	u_i/u_n	N_{exceed}	S_T
6.744	4.4522	0.9367	7	3.168
S_{Tmax}	$S_{DG}(t)$	$S_{DG}(t-1)$	$S_{max}(t-1)$	$L_{total}(t-1)$
4.52	2.2241	2.3821	6.9021	4.4024

TABLE 4 Calculation result of situation assessment indexes of the ADN under scenario 1.

η	ω	φ	γ	ζ_{DG}	λ	α	β
0.3398	0.0133	0.7879	0.7009	0.0663	0.4996	0.0229	0.0113

Similarly, we can calculate the situation assessment indexes of other scenarios, and the final calculation results are shown in Table 5.

The power supply capacity margin and voltage qualified rate can be standardized by Eq. 11, and voltage violation severity, load rate, output volatility of DGs, penetration rate of DGs, mutation severity of power supply capacity

TABLE 5 Situation assessment indexes of the ADN under different cyberattack scenarios.

Scenario	η	ω	φ	γ	ζ_{DG}	λ	α	β
0	0.362	0.000	1.000	0.631	0.000	0.541	0.000	0.000
1	0.3398	0.0133	0.7879	0.7009	0.0663	0.4996	0.0229	0.0113
2	0.3321	0.0000	1.0000	0.6991	0.1303	0.4706	0.0450	0.0000
3	0.1316	0.0234	0.4848	0.8595	0.7412	0.1382	0.2558	0.0132
4	0.0021	0.0359	0.3939	0.9979	1.0000	0.0000	0.3451	0.0246
5	0.3259	0.0090	0.7879	0.7144	0.0663	0.5337	0.0229	0.0811
6	0.3281	0.0000	1.0000	0.7080	0.0538	0.5315	0.0186	0.0729
7	0.4070	0.0000	1.0000	0.5306	0.0867	0.5480	0.0299	0.0982
8	0.3596	0.0013	0.9091	0.6646	0.0995	0.5026	0.0343	0.0304
9	0.3659	0.0000	0.9394	0.6515	0.1119	0.5028	0.0386	0.0443
10	0.4862	0.0000	0.6364	0.4497	0.3178	0.5147	0.1097	0.2828
11	0.0620	0.0313	0.3939	0.9365	0.7412	0.1279	0.2558	0.0943
12	0.2157	0.0079	0.8182	0.7677	0.7412	0.1530	0.2558	0.0850

TABLE 6 Standardized situation assessment indexes of the ADN under different cyberattack scenarios.

Scenario	η	ω	φ	γ	ζ_{DG}	λ	α	β
0	0.7438	1.0000	1.0000	0.6692	1.0000	0.0126	1.0000	1.0000
1	0.6976	0.6295	0.6500	0.5418	0.9337	0.0884	0.9337	0.9600
2	0.6817	1.0000	1.0000	0.5450	0.8697	0.1413	0.8697	1.0000
3	0.2674	0.3482	0.1500	0.2525	0.2588	0.7478	0.2588	0.9532
4	0.0000	0.0000	0.0000	0.0000	0.0000	1.0000	0.0000	0.9131
5	0.6688	0.7493	0.6500	0.5172	0.9337	0.0261	0.9337	0.7132
6	0.6735	1.0000	1.0000	0.5288	0.9462	0.0301	0.9462	0.7421
7	0.8365	1.0000	1.0000	0.8524	0.9133	0.0000	0.9133	0.6529
8	0.7384	0.9638	0.8500	0.6081	0.9005	0.0829	0.9005	0.8925
9	0.7515	1.0000	0.9000	0.6320	0.8881	0.0824	0.8881	0.8434
10	1.0000	1.0000	0.4000	1.0000	0.6822	0.0607	0.6822	0.0000
11	0.1238	0.1281	0.0000	0.1120	0.2588	0.7665	0.2588	0.6664
12	0.4413	0.7799	0.7000	0.4200	0.2588	0.7207	0.2588	0.6995

TABLE 7 The weight of assessment indexes of the ADN.

Index	η	ω	φ	γ	ζ_{DG}	λ	α	β
w	0.107	0.116	0.129	0.110	0.112	0.279	0.112	0.035

and mutation severity of load can be standardized by Eq. 12. The situation assessment indexes after standardization are shown in Table 6.

The weight of different situation assessment index in situation assessment can be calculated by Eqs 13–14, and the calculation results are shown in Table 7.

Taking scenario 0 as the reference scenario, and calculate the correlation coefficient of each situation assessment index between the reference scenario and the different attack scenarios according to the Eqs 15-17. The calculation results are shown in Table 8.

The correlation degree of each scenario with references scenario 0 is calculated by Eq. 18, and the calculation results are shown in Table 9.

Based on the security risk level graded in Table 1, the correlation degree calculation under each attack scenario is determined in the interval, and the final security risk level of the ADNs model under different attack scenarios is obtained, which can be shown in Table 10.

TABLE 8 Correlation coefficient of each situation assessment index under different cyberattack scenarios.

scenario	η	ω	φ	γ	ζ_{DG}	λ	α	β
0	1.000	1.000	1.000	1.000	1.000	1.000	1.000	1.000
1	0.891	1.000	1.000	0.805	0.793	0.825	0.793	1.000
2	0.917	0.725	0.588	0.801	0.883	0.889	0.883	0.926
3	0.517	0.600	0.370	0.552	0.403	0.453	0.403	0.914
4	0.406	0.495	0.333	0.434	0.333	0.381	0.333	0.852
5	0.702	0.449	0.476	0.532	0.719	0.942	0.719	0.368
6	0.673	1.000	1.000	0.578	0.992	0.793	0.992	0.431
7	0.866	1.000	1.000	0.798	0.877	0.978	0.877	0.631
8	0.649	1.000	0.714	0.589	0.931	0.726	0.931	0.393
9	0.888	1.000	0.714	0.911	0.815	0.836	0.815	0.949
10	0.665	1.000	0.455	0.608	0.611	0.927	0.611	0.333
11	0.647	0.333	0.476	0.459	0.784	0.857	0.784	0.345
12	0.934	1.000	1.000	0.992	0.780	0.896	0.780	0.655

4.3 Analysis

In this part, we illustrate the rationality of the assessment results shown in Table 9 and Table 10 through theoretically analyzing the security risk of the ADN under the comparing attack scenarios.

(1) Comparing Scenario 1 with Scenario 2. In those two scenarios, the types and the total output power of the removed DGs in scenario 1 is consistency with scenario 2. But in scenario 1, the distance of the removed DGs from the main power supply of the distribution network is farther than in Scenario 2, and the result of calculating security risk higher than scenario 2. The reason is that the removed DGs far away from the main power source, and it have the heavier task of the local ADN power balancing, so as to the security risk level of scenario 1 is higher than scenario 2 while the ADN suffered cyberattacks.

(2) Comparing scenario 1 with scenario 3. The total output power of the removed DGs in scenario 1 is consistency with scenario 3, and the distance of the removed DGs in scenario 1 is farther from the main power supply than scenario 3, which lead to the security risk level of scenario 3 is higher than scenario 1, and the security risk of scenario 3 is level 4. The micro gas turbine serving as PV node in scenario 3 outputs more reactive power than the PV power supply serving as PQ node in scenario 1. Therefore, it has heavier task of balancing the reactive power and maintains voltage level in ADN, the security risk level of scenario 3 is higher after suffering attacked. So as to the security risk of scenario 3 is higher than scenario 1 after the ADN suffered cyberattacks.

(3) Comparing scenario 1, scenario 2, scenario 3 and scenario 4. Removing all of the DGs lead to the security risk of the ADN is level 5 in scenario 4. The reason is that the more DGs are removed, the more power will be loss, and the total of demand of power on the power grid become very high. At the meantime, the capacity of the power grid to maintain the voltage balance have decreased and results the voltage fluctuations.

(4) Comparing scenario 5 with scenario 6. During the normal operation of the ADN, the voltage of nodes 12, 13, 14 and 15 are lower than reference value, but the voltage of nodes 18, 19, 20 and 21 are close to the reference voltage value. While increasing the same loads, the security risk of increasing loads of the nodes with low voltage value is higher than increasing loads of the nodes with close to the reference voltage value. The low voltage nodes are more likely to exceed the voltage limit and become the voltage unqualified nodes. While nodes with voltage value are close to the baseline voltage value, it have greater margin and not likely to exceed the voltage limit, so as to the security risk of scenario 5 is higher than scenario 6.

(5) Comparing scenario 5 with scenario 7. Simultaneous increasing loads lead to the higher security risk than simultaneous removing loads. The increasing of loads aggravate the distribution network burden of the power supply and reducing the node voltage. When the loads are removed, the load rate of the main transformers are reduced after the fluctuation become stabilization, the power supply pressure also alleviated, the nearby node voltage value is closer to the reference value. It is more beneficial to the stable operation of the distribution network, and not easy to cause security risks, so as to the security risk of scenario 5 is higher than scenario 7.

(6) Comparing scenario 8, scenario 9 and scenario 10. When the cut off line contains little load, the security risk decreases slightly with increasing of the cut off line loads. The security risk level increased as the load contained by the cut line increasing substantially. When the cut off line contains a small amount of loads, and the length of lines are slightly longer (the

TABLE 9 Correlation degree of each cyberattack scenario to the reference scenario.

Scenario	1	2	3	4	5	6	7	8	9	10	11	12
r	0.788	0.872	0.541	0.39	0.812	0.930	0.915	0.858	0.875	0.699	0.357	0.525

TABLE 10 Security risk level of each cyberattack scenario.

Scenario	1	2	3	4	5	6	7	8	9	10	11	12
Risk level	2	1	4	5	1	0	0	1	1	3	5	4

amount of load contained is slightly increasing), which are benefit for alleviating the power demand pressure of the power supply. Making the power supply for other node loads are more stable, and the voltage is closer to the reference voltage value. Therefore, it can be explained that why the security risk of scenario 9 is slightly lower than that of scenario 8 (see Table 9). With the total of the loads contained in the cut off line are increased substantially, the adverse effects of the long line being cut off and the fluctuations and user losses will exceed the beneficial effects of the load reduction. The security risk level increase accordingly, thus the security risk of scenario 10 is higher than scenario 8 and scenario 9.

(7) Comparing scenario 11 with scenario 12. Removing DGs and aggravating loads value may lead to security risk of the ADN become highest. Removing DGs and shedding loads synchronously may lead to security risk of the ADN become relatively low. After removing the DGs and increasing loads, it may aggravate the burden of power supply. However, shedding a certain amount of loads can alleviate the power supply capacity decline that caused by removing DGs, and make the ADN relatively difficult to have security risks, so the security risk of scenario 12 is lower than scenario 11.

Through the above comparative analysis, it can be seen that the situation assessment results of all attack scenarios are consistent with the theoretical analysis conclusions, which verified the effectiveness and practicability of the situation assessment index system and assessment methods of ADNs that we proposed in this paper.

5 Conclusion

With the rapid development of integrated energy system, the large-scale and high-permeability access of DGs is making the distribution networks develop into ADNs. The increased complexity of ADNs also increases the vulnerabilities for cyberattacks, and the factors of cyberattacks should be considered in situation assessment system. At present, research on the situation awareness of ADNs is relatively preliminary, there are few relevant study considering cyberattacks and the operation rules of ADNs. Therefore, in this paper, the index system and assessment method of situation assessment for ADNs considering cyberattacks are proposed and verified through the IEEE 33-node ADN system. The characteristics of this work are as follows:

(1) The index system includes three parts: safty indexes of ADNs, security indexes of DGs and the security risk indexes of ADNs suffering from cyberattacks.
(2) The assessment method includes three steps. Firstly, the entropy weight method is used to assign weights to each assessment index according to its impact on the assessment results, which avoids the subjectivity of the traditional expert weight method. Then, the normal operation status of ADNs is taken as the reference scenario, and the grey correlation analysis method is used to calculate the correlation degree of the scenario to be evaluated to the reference scenario. Finally, the security risk level of the scenario to be evaluated is assessed based on the pre-established grading standard for ADNs situations.
(3) For case study, 12 attack scenarios are established considering cyberattacks that the DGs and controllable loads in ADNs might suffering, the situation of each attack scenario are assessed using our proposed method, and the rationality of the assessment results is illustrated by the theoretical analysis. By the case study, the effectiveness of the proposed index system and assessment method are verified.

This paper can provide a practical method for the on-line operation situation assessment of ADNs. The assessment results can help the operation and maintenance staff to grasp the real-time operation status of ADNs, and provide a basis for the situation projection and early warning of ADNs. It can also support for off-line research on the projection and early warning method, operation control strategy and network planning of ADNs. The results of the case study can directly provide reference for the study of situation awareness and planning of ADNs.

The future work will conduct the study on situation projection method for ADNs considering cyberattacks to complete the ADNs situation awareness system.

Data availability statement

The original contributions presented in the study are included in the article/supplementary material, further inquiries can be directed to the corresponding author.

Author contributions

JL and JL has done the main theory research work. JL and JL conceived the project and wrote the manuscript. JL, JL, JZ and DQ designed and participated in the experiment. All authors discussed the results, read, and commented on the manuscript.

Funding

This work was supported by the National Natural Science Foundation of China (no. 51977155).

Conflict of interest

The authors declare that the research was conducted in the absence of any commercial or financial relationships that could be construed as a potential conflict of interest.

Publisher's note

References

Arya, R. (2016). Determination of customer perceived reliability indices for active distribution systems including omission of tolerable interruption durations employing bootstrapping. *IET Generation Transmission &. Distribution* 10 (15), 3795–3802. doi:10.1049/iet-gtd.2016.0198

Canizes, J., Soares, J., Vale, Z., and Lobo, C (2017). Optimal Approach for Reliability Assessment in Radial Distribution Networks. *IEEE Systems Journal* 11 (3), 1846–1856. doi:10.1109/JSYST.2015.2427454

Fauzan, H., Victor, W., and Jaesung, J. (2019). State-of-the-art review on power grid resilience to extreme weather events: Definitions, frameworks, quantitative assessment methodologies, and enhancement strategies. *Applied Energy* 239, 1049–1065. doi:10.1016/j.apenergy.2019.02.017

Gallo, J., Turan, S., Boem, F., Parisini, T., and Ferrari, T. (2020). A Distributed Cyber-attack Detection Scheme with Application to DC Microgrids. *IEEE Trans. Automat. Contr.* 65 (9), 3800–3815. doi:10.1109/tac.2020.2982577

Huang, M., Wei, Z., Sun, G., Zang, H., and Huang, Q. (2017). A Novel Situation Awareness Approach Based on Historical Data-Mining Model in Distribution Network. *Power Syst. Tech.* 41 (4), 1139–1145. doi:10.13335/j.1000-3673.pst.2016.2813

Ismail, M., Shaaban, F., Naidu, M., and Serpedin, E. (2020). Deep Learning Detection of Electricity Theft Cyber-attacks in Renewable Distributed Generation. *IEEE Trans. Smart Grid* 11 (4), 3428–3437. doi:10.1109/TSG.2020.2973681

Jena, M., Panigrahi, B., and Samantaray, S. (2017). A New Approach to Power System Disturbance Assessment Using Wide-Area Postdisturbance Records. *IEEE Trans. Ind. Inf.* 14 (3), 1253–1261. doi:10.1109/TII.2017.2772081

Kurt, M., Yilmaz, Y., and Wang, X. (2018). Distributed Quickest Detection of Cyberattacks in Smart Grid. *IEEE Trans. Inform. Forensic. Secur.* 13 (8), 2015–2030. doi:10.1109/TIFS.2018.2800908

Lai, J., Lu, X., Dong, Z., and Cheng, S. (2022). Resilient Distributed Multiagent Control for AC Microgrid Networks Subject to Disturbances. *IEEE Trans. Syst. Man Cybern. Syst.* 52 (1), 43–53. doi:10.1109/TSMC.2021.3056559

Lai, J., Lu, X., Yu, X., and Monti, A. (2020). Stochastic Distributed Secondary Control for AC Microgrids via Event-Triggered Communication. *IEEE Trans. Smart Grid* 11 (4), 2746–2759. doi:10.1109/TSG.2020.2966691

Li, H., Liu, Z., and Song, Z. (2015). Real-time Static Security Situational Awareness of Power Systems Based on Relevance Vector Machine. *Proceedings of the CSEE* 35 (2), 294–301. doi:10.13334/j.0258-8013.pcsee.2015.02.005

Li, Q., Tang, H., Liu, Z., Li, J., Xu, X., Sun, W., et al. (2021). Optimal Resource Allocation of 5G Machine-Type Communications for Situation Awareness in Active Distribution Networks. *IEEE Syst. J.* 10 (6), 1–11. doi:10.1109/JSYST.2021.3110502

Li, Y., Gao, W., Gao, W., Zhang, H., and Zhou, J. (2020). A Distributed Double-Newton Descent Algorithm for Cooperative Energy Management of Multiple Energy Bodies in Energy Internet. *IEEE Trans. Ind. Inf.* 17 (9), 5993–6003. doi:10.1109/TII.2020.3029974

Li, Y., Zhang, H., and LiangHuang, X, B. (2019). Event-triggered Based Distributed Cooperative Energy Management for Multienergy Systems. *IEEE Trans. Ind. Inf.* 15 (14), 2008–2022. doi:10.1109/TII.2018.2862436

Liang, J., Wu, Y., Li, J., Chen, X., Tong, H., Ni, M., et al. (2021). Security Risk Analysis of Active Distribution Networks with Large-Scale Controllable Loads under Malicious Attacks. *Complexity* 2021, 1–12. doi:10.1155/2021/6659879

Lin, J., Wan, C., Song, Y., Huang, R., Chen, X., and Guo, W. (2016). Situation Awareness of Active Distribution Network: Roadmap, Technologies, and Bottlenecks. *CSEE Jour. Power & Ener. Syst.* 2 (3), 35–42. doi:10.17775/CSEEJPES.2016.00033

Lin, Z., Wen, F., Ding, Y., Xue, Y., Liu, S., Zhao, Y., et al. (2018). WAMS-based Coherency Detection for Situational Awareness in Power Systems with Renewables. *IEEE Trans. Power Syst.* 33 (5), 5410–5426. doi:10.1109/TPWRS.2018.2820066

Liu, W., Zhang, D., Wang, X., Hou, J., and Liu, L. (2018). A Decision Making Strategy for Generating Unit Tripping under Emergency Circumstances Based on Deep Reinforcement Learning. *Proceedings of the CSEE* 38 (1), 109–119. doi:10.13334/j.0258-8013

McLaughlin, S., Konstantinou, C., Wang, X., Davi, L., Sadeghi, A., Maniatakos, M., et al. (2016). The Cybersecurity Landscape in Industrial Control Systems. *Proc. IEEE* 104 (5), 1039–1057. doi:10.1109/JPROC.2015.2512235

Ren, C., Xu, Y., Zhang, Y., and Zhang, Rui. (2019). A Hybrid Randomized Learning System for Temporal Adaptive Voltage Stability Assessment of Power Systems. *IEEE Trans. Ind. Inf.* 16 (6), 3672–3684. doi:10.1109/TII.2019.2940098

Russell, L., Goubran, R., Kwamena, F., and Knoefel, F. (2018). Agile IoT for Critical Infrastructure Resilience: Cross-Modal Sensing as Part of a Situational Awareness Approach. *IEEE Internet Things J.* 5 (6), 4454–4465. doi:10.1109/JIOT.2018.2818113

Shahsavari, A., Farajollahi, M., Stewart, E., Cortez, E., and Mohsenian, H. (2019). Situational Awareness in Distribution Grid Using Micro-PMU Data: A Machine Learning Approach. *IEEE Trans. Smart Grid* 10 (6), 6167–6177. doi:10.1109/TSG.2019.2898676

Sultan, K., Hatem, Z., and Vinod, K. (2013). Planning Active Distribution Networks Considering Multi-DG Configurations. *IEEE Trans. Power Syst* 29 (2), 785–793. doi:10.1109/PESGM.2014.6939178

Tao, X., Kong, K., Zhao, F., Cheng, S., and Wang, S. (2020). An Efficient Method for Network Security Situation Assessment. *Int. J. Distrib. Sens. Netw.* 16 (11), 155014772097151. doi:10.1177/1550147720971517

Wang, H., Shi, L., and Ni, Y. (2017b). Distribution system planning incorporating distributed generation and cyber system vulnerability. *J. Eng. (Stevenage).* 3, 2198–2202. doi:10.1049/joe.2017.0720

Wang, P., and Govindarasu, M. (2020). Multi-agent based attack-resilient system integrity protection for smart grid. *IEEE Trans. Smart Grid* 11 (4), 3447–3456. doi:10.1109/TSG.2020.2970755

Wang, Q., Bu, S., He, Z., and Dong, Z. (2020). Toward the prediction level of situation awareness for electric power systems using CNN-LSTM network. *IEEE Trans. Ind. Inf.* 17 (10), 6951–6961. doi:10.1109/TII.2020.3047607

Wang, S., Dehghanian, P., and Li, L. (2019). Power grid online surveillance through PMU-embedded convolutional neural networks. *IEEE Trans. Ind. Appl.* 56 (2), 1146–1155. doi:10.1109/TIA.2019.2958786

Wang, X., Chen, N., Li, Y., Wang, C., and Pu, T. (2017a). Multi-source optimal dispatch architecture for active distribution network based on situational linkage power. *Power Syst. Tech.* 41 (2), 349–354. doi:10.13335/j.1000-3673.pst.2016.2913

Wei, F., Wan, Z., and He, H. (2020). Cyberattack recovery strategy for smart grid based on deep reinforcement learning. *IEEE Trans. Smart Grid* 11 (3), 2476–2486. doi:10.1109/TSG.2019.2956161

Zhao, J., Gómez, A., Netto, M., Mili, L., Abur, A., Terzija, V., et al. (2019). Power system dynamic state estimation: Motivations, definitions, methodologies, and future work. *IEEE Trans. Power Syst.* 34 (4), 3188–3198. doi:10.1109/TPWRS.2019.2894769

frontiers | Frontiers in Energy Research

TYPE Original Research
PUBLISHED 12 August 2022
DOI 10.3389/fenrg.2022.956672

OPEN ACCESS

EDITED BY
Qiuye Sun,
Northeastern University, China

REVIEWED BY
Yao Weitao,
Nanyang Technological University,
Singapore
Xiaokang Liu,
Huazhong University of Science and
Technology, China
Yu Wang,
Imperial College London,
United Kingdom

*CORRESPONDENCE
Biheng Wang,
bihengwang2022@163.com

SPECIALTY SECTION
This article was submitted to Smart
Grids,
a section of the journal
Frontiers in Energy Research

RECEIVED 30 May 2022
ACCEPTED 07 July 2022
PUBLISHED 12 August 2022

CITATION
Wang B (2022), Resilient cooperative control for optimal current sharing and voltage regulation of microgrid-based distribution network under FDI attacks.
Front. Energy Res. 10:956672.
doi: 10.3389/fenrg.2022.956672

Resilient cooperative control for optimal current sharing and voltage regulation of microgrid-based distribution network under FDI attacks

Biheng Wang*

NARI Technology Nanjing Control System Co., Ltd., Nanjing, China

In this study, the security secondary control problems are considered for optimal current sharing and voltage restoration of a microgrid distribution network under false data injection (FDI) attacks. To solve these problems, a resilient secondary control method is provided. Specifically, a resilient secondary controller is designed by introducing an adaptive parameter based on the adaptive technique. Then, a theoretical analysis method is provided to show that the designed resilient secondary controller can ensure optimal current sharing and voltage regulation under FDI attacks.

KEYWORDS

resilient control, voltage regulation, current sharing, adaptive control, FDI attacks

Introduction

In recent years, microgrids (MGs) have received a lot of attention (Wang et al., 2021a; Yao et al., 2022; Wang et al., 2021c; Wang et al., 2020). Specifically, a direct current (DC) MG has been widely investigated owing to it is favorable to the alternating current (AC) MG such as higher reliability and efficiency (Dragicevic et al., 2016; Deng et al., 2022a; Liu et al., 2021). By fully utilizing the inherent DC nature of the distributed generators (DGs) and DC loads, the DC MG avoids multiple conversions between DC/AC and AC/DC to improve the efficiency. According to the current report, the DC MG has been proved to have a 10%–22% improvement in efficiency in comparison to the AC MG. For the DC MG, the control issues mainly include voltage restoration and current sharing. A hierarchical control framework including primary, secondary, and tertiary control is widely adopted to solve such control issues (Ding et al., 2020; Rui et al., 2020; Deng et al., 2021a; Wang et al., 2021b; Lin et al., 2021). The primary control rapidly responds for system disturbance based on the local controller. The secondary control is to eliminate the voltage deviation caused by primary control through certain information exchange. The tertiary control aims to achieve economic dispatch and optimal power flow (Liang et al., 2016). In this study, the secondary control in the islanded DC MG is the main focus.

Recently, distributed secondary control for voltage restoration and current sharing of the DC MG gains more attention due to its flexibility, scalability, and reliability.

Compared with centralized control, distributed 26 controls need no central controller and only peer-to-peer information exchange is required (Guo et al., 2020). In recent works, many distributed controllers have been proposed. For example, a distributed finite-time controller is proposed in Guo et al. (2018a) to achieve average voltage regulation and accurate current sharing. Deng et al. (2020) introduced an event-trigger controller to significantly reduce the communication burden. In addition, a fast model predictive control is proposed (Lian et al., 2021a) to regulate the voltage and desired current flows in a DC MG, in which the proposed controller is based on a distributed alternating direction method of the multipliers method.

Although many distributed control methods have been proposed, it should be noted that all the aforementioned distributed secondary control results assume that the communication between networks is reliable. However, network communication between DGs is often sensitive to cyber attacks. Typically, the classical attack modes can be divided into false data injection (FDI) attacks (Yang and Dong, 2019; Yang et al., 2022) and denial-of-service (DoS) attacks (Deng et al., 2021; Ma et al., 2021; Yang et al., 2021; Deng et al., 2022b). FDI attacks are usually launched by attacker injecting some false data, while DoS attacks usually occur by jamming network communication. Recently, some results on FDI attacks for MGs have received considerable attention. The main focuses contain attack detection (Hetel et al., 2017; Sahoo et al., 2020; Habibi et al., 2021a), impact mitigation (Zhang et al., 2021; Habibi et al., 2021b), and resilient controller design (Jiang et al., 2021; Karimi et al., 2021; Cecilia et al., 2022). The detection problem is usually formalized as identifying a change in sets of inferred candidate invariants, which can be solved by the classic analytical method (Hetel et al., 2017; Sahoo et al., 2020) or AI-based algorithm (Habibi et al., 2021a). The attack impact mitigation is another critical concern, which can be achieved by replacing the attacked signal with a reconstructed signal (Zhang et al., 2021) or artificial neural network–based method (Habibi et al., 2021b). In addition, resilient controller design is another effective method to against FDI attacks. The existing methods include observer-based methodology (Cecilia et al., 2022), high-order differentiator–based distributed controller (Jiang et al., 2021), and adaptive controller (Karimi et al., 2021).

Note that in Habibi et al. (2021b), Jiang et al. (2021), Karimi et al. (2021), and Cecilia et al. (2022), current sharing ratios are only set as the inverse of droop gains. However, the optimal current sharing ratios may change online with the change in power generation costs and the updated user demands. Thus, how to develop an optimal current sharing method with the function of resilient the influence of FDI attacks is an interesting and open work. In proposing this method, the following challenges are encountered: 1) the existing secondary control methods for current sharing and voltage regulation are available under the condition that the secondary control information is reliable. However, under the influence of FDI attacks, the accurate information of the secondary control cannot be achieved and thus leading to the voltage deviating from the normal value and the current sharing can be also influenced. Therefore, the first challenge is how to develop a resilient control method to correct the voltage deviation and current sharing derivation caused by FDI attacks. 2) It is difficult to build a linearization model of MG and the closed-loop model of the MG becomes more complex under the influence of FDI attacks. Therefore, another challenge caused by the considered problem is how to propose a stability analysis method for the nonlinear MG under FDI attacks.

To solve this issue, a resilient cooperative control method is proposed to achieve the optimal current sharing and voltage regulation problem for MG based distribution network in the presence of FDI attacks. In this study, the main contributions can be summarized as follows.

1 Based on the designed resilient secondary control method, the DC MG both achieve optimal current sharing and restore the bus voltage simultaneously even under the influence of FDI attacks. In addition, with the help of the designed adaptive parameter, the effects of FDI attacks on MG can be eliminated, which makes the method resilient to FDI attacks. Therefore, both the resilient and the system performance can be improved.

2 Based on the Lyapunov theory, a stability analysis method is established for the overall closed-loop MG system to show that the designed resilient secondary controller can resist the influence of FDI attacks theoretically. In addition, a guideline for the controller design is introduced to facilitate implementation for the designer.

Problem formulation

In this section, the main contents will be elaborated as follows: 1) modeling of the DC MG; 2) introducing the FDI attacks; and 3) presenting the control objectives.

DC MG system

As shown in Figure 1, current and voltage control loops and droop control are the primary control of each DG in the physical layer. As known, the dynamic responses of voltage and current control are much faster than that of the droop control. Therefore, the droop control can decisively indicate the dynamics of the primary control. Based on this analysis, the model of the DG with primary control is given by

$$V_m = -d_m I_m + V^*, \tag{1}$$

where V_m represents the voltage reference of the mth DG, V^* is the nominal DC voltage, d_m indicates the droop gain, and I_m

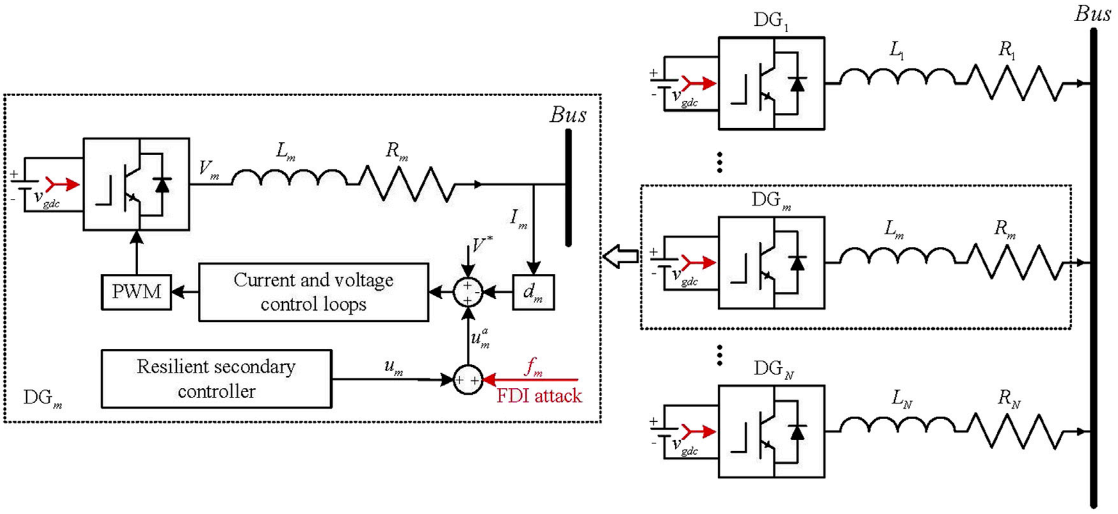

FIGURE 1
DC MG model under FDI attacks.

represents the current output. Since the voltage and current control loops have clever designs, the voltage output of the converter V_m^o can track V_m rapidly. According to the aforementioned statement, V_m can be written as follows:

$$V_m = V_m^o. \tag{2}$$

According to the relationship between DC bus voltage V_b and V_m^o can be expressed mathematically as follows:

$$V_b = -R_m I_m + V_m^o, \tag{3}$$

where R_m denotes the resistance of the line between common bus and DG. Based on Wang et al. (2021a) (3), the relationship between current I_m and the DC bus voltage V_b immediately is known:

$$V_b = -(d_m + R_m I_m + V^*). \tag{4}$$

If the values of the line resistance R_m $m = 1,2,...,N$ are much less than d_m, that is, $R_m \ll d_m$, the following equation holds

$$\frac{I_m}{I_n} = \frac{R_n + d_n}{R_m + d_m} \approx \frac{d_n}{d_m}, \forall i = 1, \ldots, N. \tag{5}$$

If the effects of line resistance R_m in ([]) is ignored, then the current sharing ratio and the droop gain d_m are inversely proportional. Nevertheless, using droop control to solve the current sharing problem also exists.

Some drawbacks, including: 1) line resistance R_m $m = 1,2,...,N$ affect the current sharing accuracy inevitably; 2) larger droop gains d_m $m = 1,2,...,N$ may improve the current sharing accuracy, while a larger deviation of DC bus voltage V_b may be generated; 3) with the change in operational condition of DC MG, the optimal current sharing ratio obtained from the tertiary layer will be different, and thus it does not always hold the expected relationship Figure 1.

False data injection attacks in cyber layer

In some situation, the attackers may launch FDI attacks on the control input, which will make the voltage deviates from the normal value and the current sharing can be also influenced. Under FDI attacks, the input u_m may be regulated to u_m^a, that is,

$$u_m^a(t) = u_m + f_m, \tag{6}$$

where f_m is an unknown and time-varying attack signal injected by attackers. In this study, the FDI attacks may occur in any control input u_m, and the constrain of FDI attacks is that the attack signal f_m is bounded, that is, the following assumption is satisfied.

Assumption 1. It is assumed that $f = [f_1, f_2, \ldots, f_N]^T$ is bounded, that is, $|f_m| \leq \overline{f_m}$ with $\overline{f_m}$ being an unknown constant for m = 1,...,N.

Control objectives

From (Eq. 4), it is obvious that, since V_m= 0 when the system tends to stable, there exists error between bus voltage $V_b(t)$ and the nominal value V^*. Then, a secondary controller u_m will add into the mth DG, which can be summarized as follows,

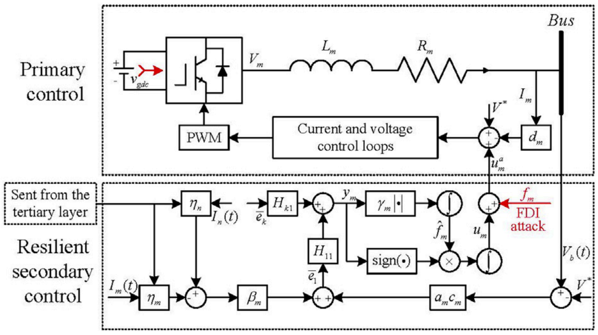

FIGURE 2
Framework of the resilient secondary controller.

$$V_b = u_m - (d_m + R_m)I_m + V^*. \tag{7}$$

According to the relationship among I_m, I_j, d_j, and d_m in (Eq. 5), it is known that the droop gains d_m for $m = 1,2,...,N$ should be selected large enough to ignore the influence of line resistance R_m. Unfortunately, larger droop gains d_m will lead to larger deviation of bus voltage of (Eq. 4). In addition, optimal current sharing ratios obtained from the tertiary layer will change with the change in the external environment of the MG, which may lead to the failure of the inversely proportional. Thus, the objectives of this study can be summarized as follows;

1 Voltage restoration:

$$\lim_{t\to\infty} v_b(t) = V^*; \tag{8}$$

2 Current sharing:

$$\lim_{t\to\infty}\left(\frac{I_n^*}{\eta_m(t)} - \frac{I_m^*}{\eta_n(t)}\right) = 0, \forall n \neq m, \tag{9}$$

where the piecewise constant function $\eta_m(t)$ represents the optimal current sharing ratio obtained from the tertiary layer and I_m^* represents the current value at the steady state.

Secondary current sharing and voltage regulation control

In this section, a resilient secondary current sharing and voltage restoration controller will be designed and then provide a stability analysis method based on the Lyapunov stability theory.

Resilient controller design

To achieve control objectives (Ding et al., 2020; Rui et al., 2020), the resilient controller is designed as follows:

$$u_m = \int\left(\operatorname{sign}(y_m) = \widehat{f_m} + u_m\right)dt \tag{10}$$

where sign (y_m) denotes the sign function of y_m, which satisfies

$$\operatorname{sign}(y_m) = \begin{cases} 1, & y_m > 0, \\ 0, & y_m = 0, \\ -1, & y_m < 0. \end{cases} \tag{11}$$

The symbol y_m is denoted by $y_m = \sum_{k=1}^{N} \overline{e_k} H_{km}$ with H_{km} being the element in row k and column i of the matrix H (the definition of matrix H and variable $\bar{e}_k$ will be given later). The term $\hat{f}_m{}^{(t)}$ is an adaptive parameter and is updated by

$$\widehat{f_m} = \gamma_m |y_m|, \tag{12}$$

where the parameter γ_m is chosen as an arbitrary positive constant. To show the controller more intuitively, the secondary current sharing and voltage restoration controller will be presented in Figure 2.

Remark 1. Different from the existing results on secondary control (Guo et al., 2018b; Lian et al., 2021b), a resilient secondary control method is proposed in this study. By introducing an adaptive parameter f_m in the resilient controller u_m, the advantage of the designed controller is that the FDI attacks can be resisted, that is, the designed controller can ensure that optimal current sharing and voltage regulation can be achieved even under the influence of FDI attacks. The specific effect will be shown in the simulation section.

Stability analysis

Before giving the main result, the model of the DC MG will be firstly derived. Define $e^V(t) = V^* - V_b(t)$. According to Liu et al. (2021), it has

$$e^V(t)1_N = -u(t) + (d + R)I(t), \tag{13}$$

where $u(t) = col\{u_m(t)\}$ and $I(t) = col\{I_m(t)\}$ with $col\{u_m(t)\}$ representing a column vector composed of elements $u_1, u_2, ..., u_N$. In addition, $d = \operatorname{diag}\{d_m\}$ and $R = \operatorname{diag}\{R_m\}$ with $\operatorname{diag}\{d_m\}$ representing a diagonal matrix with diagonal elements $d_1, d_2, ..., d_N$.

As discussed in Guo et al. (2020), it assumes that the resistance R_L integrates the loads and the resistances between lines. Then, it has

$$\frac{V_b(t)}{R_L} = 1_N^T I(t) \tag{14}$$

Substituting Guo et al. (2020) into Liang et al. (2016), one gets

$$I(t) = A^{-1}u(t) + A^{-1}V^* 1_N, \tag{15}$$

where the matrix $A = R_L 1_N 1_N^T + d + R$ is invertible, as discussed in Guo et al. (2018a). Based on Liang et al. (2016) and Guo et al. (2018a), it has

$$e^V(t)1_N = -R_L 1_N 1_N^T H^{-1} u(t) + (d+R)H^{-1}V^* 1_N.$$

Define $\bar{e} = \alpha c e^V(t)1_N - \beta \mathrm{L} \eta I(t)$ with $\alpha = \mathrm{diag}\{\alpha_m\}$, c = diag $\{c_m\}$, $\beta = \mathrm{diag}\{\beta_m\}$, and $\eta = \mathrm{diag}\{\eta_m\}$. Then, it has

$$\dot{\bar{e}}(\mathrm{t}) = H(\dot{u} + f), \tag{16}$$

where $H = -(\alpha c R_L 1 N 1_N^T A^{-1} + \beta L \eta A^{-1})$ is a Hurwitz matrix (Guo et al., 2020).

Theorem 1. Consider the DC MG under FDI attacks satisfying Assumption 1. If the resilient secondary controller $\mathrm{u_m}$ in Deng et al. (2021a) with adaptive parameter $\hat{\mathrm{f}}_\mathrm{m}$ updated by Lin et al. (2021) is used and arbitrary positive constants γ_m for m = 1,2,...,N are chosen and then the resilient optimal current sharing and voltage regulation problems can be solved, that is, the control objectives Ding et al. (2020) and Rui et al. (2020) can be achieved simultaneously.

Proof: Define $V = \frac{1}{2}\|\bar{e}\|^2$. The derivative of V along (Deng et al., 2020) yields

$$\dot{V} = \bar{e}^T H \dot{u} + \bar{e}^T H f, \tag{17}$$

where

$$\begin{aligned}\bar{e}^T H \dot{u} &= [\bar{e}1\,\bar{e}1 \cdots \bar{e}N]\begin{bmatrix} H_{11} & H_{12} & \cdots & H_{1N} \\ H_{21} & H_{22} & \cdots & H_{2N} \\ \vdots & \vdots & \cdots & \vdots \\ H_{N1} & H_{N2} & \cdots & H_{NN}\end{bmatrix}\dot{u}, \\ &\left[\sum\nolimits_{k=1}^{N} \bar{e}_k H_{k1} \sum\nolimits_{k=1}^{N} \bar{e}_k H_{k2} \cdots \sum\nolimits_{k=1}^{N} \bar{e}_k H_{kN}\right]\dot{u}, \\ &= \sum_{m=1}^{N}\sum_{k=1}^{n} \overline{e_k} H_{km} \dot{u}_m. \end{aligned} \tag{18}$$

By using the similar method, it has

$$\begin{aligned}\bar{e}^T H f &= \left[\overline{e_1 e_1} \cdots \overline{e_N}\right]\begin{bmatrix} H_{11} & H_{12} & \cdots & H_{1N} \\ H_{21} & H_{22} & \cdots & H_{2N} \\ \vdots & \vdots & \cdots & \vdots \\ H_{N1} & H_{N2} & \cdots & H_{NN}\end{bmatrix} f, \\ &= \left[\sum\nolimits_{k=1}^{N} \bar{e}_k H_{k1} \sum\nolimits_{k=1}^{N} \bar{e}_k H_{k2} \cdots \sum\nolimits_{k=1}^{N} \bar{e}_k H_{kN}\right] f, \\ &= \sum_{m=1}^{N}\sum_{k=1}^{N} \bar{e}_k H_{km} f_m. \end{aligned} \tag{19}$$

Substituting Yang et al. (2022) and Yang and Dong (2019) into Lian et al. (2021a), it has

$$\dot{V}(t) = \sum_{m=1}^{N}\left(\sum_{k=1}^{N} \bar{e}_k H_{km} \dot{u}_m + \sum_{k=1}^{N} \bar{e}_k H_{km} f_m\right). \tag{20}$$

Define $y_m = \sum_{k=1}^{N} \overline{e_k} H_{km}$. Then, Deng et al. (2022b) can be rewritten as follows:

$$\dot{V}(t) = \sum_{m=1}^{N} (y_m \dot{u}_m + y_m f_m). \tag{21}$$

According to Assumption 1, it has

$$\dot{V}(\mathrm{t}) \le \sum_{\mathrm{m=1}}^{\mathrm{N}} y_m \dot{u}_m + \sum_{\mathrm{m=1}}^{\mathrm{N}} |y_m| \bar{f}_m. \tag{22}$$

Substituting (Eq. 14) into (Eq. 13), one gets

$$\dot{V}(t) \le -\sum_{m=1}^{N} |y_m| \left(\hat{f}_m - \hat{f}_m\right). \tag{23}$$

To achieve the main result, the following Lyapunov function is introduced:

$$W(t) = V(t) + \frac{1}{2\gamma_m}\sum_{m=1}^{N}\left(\hat{f}_m - \hat{f}_m\right)^2. \tag{24}$$

The derivative of $W(t)$ is

$$\dot{W}(t) = \dot{V}(t) + \frac{1}{\gamma_m}\sum_{m=1}^{N}\left(\hat{f}_m - \hat{f}_m\right)\hat{f}_m. \tag{25}$$

Substituting Ma et al. (2021) into Sahoo et al. (2020), one gets

$$\dot{W}(t) \le -\sum_{m=1}^{N} |y_m| \left(\hat{f}_m - \hat{f}_m\right) + \frac{1}{\gamma_m}\sum_{m=1}^{N}\left(\hat{f}_m - \hat{f}_m\right)\hat{f}_m. \tag{26}$$

Substituting Lin et al. (2021) into Habibi et al. (2021a), one gets

$$\dot{W}(t) \le -\sum_{m=1}^{N} |y_m| \left(\hat{f}_m - \bar{f}_m\right) + \sum_{m=1}^{N}\left(\hat{f}_m - \bar{f}_m\right)|y_m| \tag{27}$$

By applying the LaSalle–Yoshizawa theorem, it is easy to show that

$$\lim_{t\to\infty} \bar{e}(t) = 0. \tag{28}$$

According to Deng et al. (2020) and Habibi et al. (2021b), it yields

$$\lim_{t\to\infty}\left(\alpha \mathbf{c} e^v(t)1_N - \beta \boldsymbol{L} \eta I(t)\right) = 0.$$

Thus, it has

$$\lim_{t\to\infty} \alpha \mathbf{c} e^v(t)1_N = \lim_{t\to\infty} \beta \boldsymbol{L} \eta I(t). \tag{29}$$

By multiplying $1_{N\times 1}^T$ on each side of Cecilia et al. (2022), one has

$$\lim_{t\to\infty} e^v(t)\sum_{i=1}^{N} \alpha_m c_m = \lim_{t\to\infty} 1_N^T \times 1\beta \boldsymbol{L} \eta I(t). \tag{30}$$

If β_m (m = 1,2,...,N) such that $b_m = b_n, \forall m,n = 1,\ldots,N$, then

$$\lim_{t\to\infty} 1_{N\times 1}^T \beta \boldsymbol{L} \eta I(t) = 0. \tag{31}$$

TABLE 1 Parameters on controllers and the MG system.

	DGs:1, 2, & 3			
DG	**VDC**	**48 V**	**fs**	**20 kHz**
Droop gain	d1 = 8, d2 = 4, d3 = 2			
Proposed controller	α1 = α2 = α3 = 1			
	β1 = β2 = β3 = 0.5			
	γ1 = γ2 = γ3 = 3			
Load	$R_L = 5\Omega\ R$			
Nominal voltage	$V^* = 48$ V			

According to $\sum_{i=1}^{N}\alpha_m c_m > 0$, then it is obtained that

$$\lim_{t\to\infty}\left(V^* - V_b(t)\right) = 0, \tag{32}$$

$$\lim_{t\to\infty}\beta \boldsymbol{L}\eta I(t) = 0. \tag{33}$$

Thus, it has shown that bus voltage regulation and optimal current sharing can be achieved by using the designed resilient secondary controller (Deng et al., 2021a) with adaptive updated law (Lin et al., 2021) even under the influence of FDI attacks.

Remark 2. In Theorem 1, a new stability analysis method is provided to show that the resilient secondary controller (Deng et al., 2021a) can resist FDI attacks theoretically. In particular, the term $\frac{1}{2\gamma_m}\sum_{m=1}^{N}(\widehat{f_m} - f_m)^2$ is introduced in the Lyapunov function W(t). Then, the control objectives of voltage regulation and optimal current sharing can be achieved.

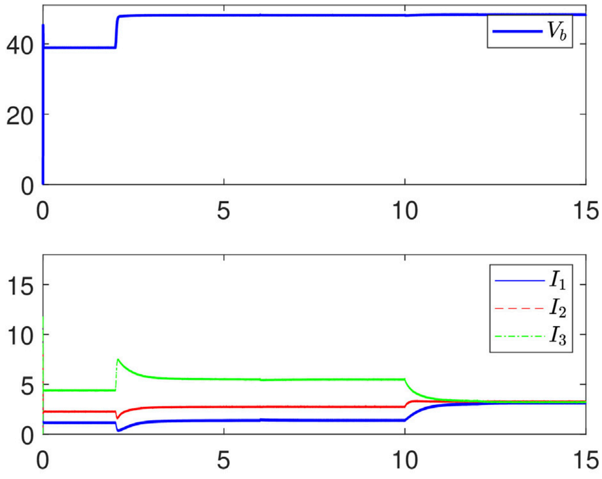

FIGURE 3
Trajectories of the voltage and the current with load added in.

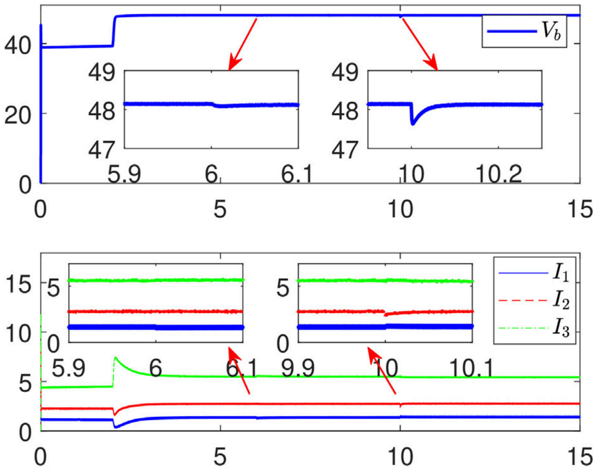

FIGURE 4
Trajectories of the voltage and the current under our method.

Simulation results

To verify the advantage of our designed resilient secondary controller, it is first shown that the developed method is effective to achieve the optimal current sharing and voltage regulation. Then, it is further to prove the effectiveness of our method by comparing with the existing secondary method in Lian et al. (2021b). In the simulation, the detailed DG parameters are given in Table 1 and the Laplacian matrix L is chosen as follows:

$$L = \begin{bmatrix} 2 & -1 & -1 \\ -1 & 1 & 0 \\ -1 & 0 & 1 \end{bmatrix}.$$

Resilient optimal current sharing and voltage regulation

In this subsection, the verification of our resilient secondary controller (Deng et al., 2021a) against FDI attacks is shown. In this case, there is no attacker to destroy the system, that is, $f_m \equiv 0$ for $m = 1,2,\ldots,N$.

1) Consider 0–10 s, the experimental results are shown in Figure 3 by using the resilient secondary controller (Deng et al., 2021a). From Figure 3, it is shown that the proposed controller ensures that the bus voltage 156 can be regulated to V^* after introducing the secondary controller (Deng et al., 2021a). In addition, the ratios of I_m for $m = 1,2,3$ are maintained as I_1:I_2:I_3 ≈ 1:2:4 after introducing the secondary controller (Deng et al., 2021a).

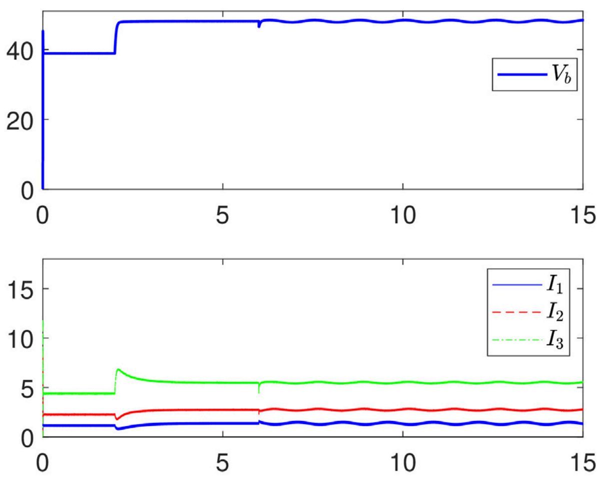

FIGURE 5
Trajectories of the voltage and the current under the method in Lian et al. (2021b).

2) Consider 10–15 s, an extra load $R_L = 5\ \Omega$ is added to the MG. According to the solution at the tertiary layer, the optimal sharing ratio is changed to $I_1{:}I_2{:}I_3 = 1{:}1{:}1$ when the load is changed. Thus, the parameter η_i (i = 1, 2, 3) of the resilient secondary controller is adjusted to $\eta_1{:}\eta_2{:}\eta_3 = 1{:}1{:}1$. Then, the bus voltage will be regulated to V^* by using the automatic adjustment function of the resilient secondary controller (Deng et al., 2021a). In addition, the current sharing ratio will also alter to $I_1{:}I_2{:}I_3 \approx 1{:}1{:}1$ through our controller.

Comparison studies

In this case, the designed resilient secondary method and the secondary control method in Lian et al. (2021b) are both applied to solve the optimal current and voltage regulation for DC MG under FDI attacks. Specifically, the secondary controllers are added into the DC MC at $t = 2$ s. The FDI attack $f_1 = \sin(0.1t)$ is added into the 1 st DG at $t = 6$ s and the FDI attacks $f_2 = 2\sin(0.1t)$ and $f_3 = 3\sin(0.1t)$ for DGs 2 and 3 are added at $t = 10$ s. Under our resilient secondary controller and the secondary controller in Lian et al. (2021b), the simulation results are shown in Figures 4,5.

1) Consider 0–6 s, it can be seen that both methods can ensure that the bus voltage be regulated to V^* and the ratios of I_m for $m = 1,2,3$ are maintained as $I_1{:}I_2{:}I_3 \approx 1{:}2{:}4$ after introducing the secondary controller at $t = 2$ s.
2) Consider 6–10 s, the FDI attack is added into the 1 st DG at this interval. Our method can ensure that the bus voltage regulates to V^* by using the resilient secondary controller (Deng et al., 2021a). In addition, the current 176 sharing ratio will also retain to $I_1{:}I_2{:}I_3 \approx 1{:}2\ 4$ through our controller. However, the bus voltage will deviate to V^* by using the resilient secondary controller (Deng et al., 2021a), and the current sharing ratio will fluctuate with the addition of attacks under the secondary controller (Lian et al., 2021b).
3) Consider 10–15 s, the FDI attacks are added into all DG attacks at this interval. Our method can still ensure that voltage regulates to V^* and the current sharing ratio will also hold. However, the method in Deng et al. (2021a) does not guarantee these two objectives. Thus, it has shown that the developed method is effective to resist FDI attacks.

Conclusion

In this article, it has solved the security secondary control problems for optimal current sharing and voltage restoration of an islanded DC MG under FDI attacks. To solve these problems, a resilient secondary control method has been provided. First, a resilient secondary controller has been designed by introducing an adaptive parameter based on the adaptive technique. Then, a theoretical analysis method has been provided to show that the designed resilient secondary controller can ensure optimal current sharing and voltage regulation under FDI attacks. Finally, a simulation example is given by using the MATLAB testing platform to verify the developed resilient secondary control method. Now, this result cannot be extended to the directed network case due to that the Laplacian matrix is no longer a symmetric matrix under directed network case. Therefore, it is my further work to extend this result to the directed network case.

Data availability statement

The original contributions presented in the study are included in the article/Supplementary Material; further inquiries can be directed to the corresponding author.

Author contributions

The author confirms being the sole contributor of this work and has approved it for publication.

Conflict of interest

Author BW was employed by the company NARI Technology Nanjing Control System Co., Ltd.

Publisher's note

References

Cecilia, A., Sahoo, S., Dragiceviõ c, T., Costa-Castell´ o, R., and Blaabjerg, F. (2022). On addressing the security and´ stability issues due to false data injection attacks in DC microgrids—an adaptive observer approach. *IEEE Trans. Power Electron.* 37 (3), 2801–2814. doi:10.1109/tpel.2021.3114990

Deng, C., Jin, X. -Z., Che, W. -W., and Wang, H. (2021). Learning-based distributed resilient fault-tolerant control method for heterogeneous MASs under unknown leader dynamic. *IEEE Trans. Neural Netw. Learn. Syst.*, 1–10. doi:10.1109/tnnls.2021.3070869

Deng, C., Wang, Y., Wen, C., Xu, Y., and Lin, P. (2021). Distributed resilient control for energy storage systems in cyber–physical microgrids. *IEEE Trans. Ind. Inf.* 17 (2), 1331–1341. doi:10.1109/tii.2020.2981549

Deng, C., Er, M. J., Yang, G., and Wang, N. (2020). Event-triggered consensus of linear multiagent systems with time-varying communication delays. *IEEE Trans. Cybern.* 50 (7), 2916–2925. doi:10.1109/tcyb.2019.2922740

Deng, C., Guo, F., Wen, C., Yue, D., and Wang, Y. (2022). Distributed resilient secondary control for DC microgrids against heterogeneous communication delays and DoS attacks. *IEEE Trans. Ind. Electron.* 69, 11560–11568. to be published. doi:10.1109/TIE.2021.3120492

Deng, C., Zhang, D., and Feng, G. (2022). Resilient practical cooperative output regulation for MASs with unknown switching exosystem dynamics under DoS attacks. *Automatica*, 110172. doi:10.1016/j.automatica.2022.110172

Dragicevic, T., Lu, X., Vasquez, J. C., and Guerrero, J. M. (2016). DC microgrids—Part I: A review of control´ strategies and stabilization techniques. *IEEE Trans. Power Electron.* 31 (7), 4876–4891. doi:10.1109/tpel.2015.2478859

Ding, L., Han, Q., Ning, B., and Yue, D. (2020). Distributed resilient finite-time secondary control for heterogeneous battery energy storage systems under denial-of-service attacks. *IEEE Trans. Ind. Inf.* 16 (7), 4909–4919. doi:10.1109/tii.2019.2955739

Guo, F., Wang, L., Wen, C., Zhang, D., and Xu, Q. (2020). Distributed voltage restoration and current sharing control in islanded DC microgrid systems without continuous communication. *IEEE Trans. Ind. Electron.* 67 (4), 3043–3053. doi:10.1109/tie.2019.2907507

Guo, F., Xu, Q., Wen, C., Wang, L., and Wang, P. (2018). Distributed secondary control for power allocation and voltage restoration in islanded DC microgrids. *IEEE Trans. Sustain. Energy* 9 (4), 1857–1869. doi:10.1109/tste.2018.2816944

Guo, F., Xu, Q., Wen, C., Wang, L., and Wang, P. (2018). Distributed secondary control for power allocation and voltage restoration in islanded DC microgrids. *IEEE Trans. Sustain. Energy* 9 (4), 1857–1869. doi:10.1109/tste.2018.2816944

Habibi, M. R., Baghaee, H. R., Dragiceviõ c, T., and Blaabjerg, F. (2021). Detection of false data injection´ cyber-attacks in DC microgrids based on recurrent neural networks. *IEEE J. Emerg. Sel. Top. Power Electron.* 9 (5), 5294–5310. doi:10.1109/jestpe.2020.2968243

Habibi, M. R., Baghaee, H. R., Dragiceviõ c, T., and Blaabjerg, F. (2021). False data injection cyber-attacks´ mitigation in parallel DC/DC converters based on artificial neural networks. *IEEE Trans. Circuits Syst. Ii.* 68 (2), 717–721. doi:10.1109/tcsii.2020.3011324

Hetel, L., Fiter, C., Omran, H., Seuret, A., Fridman, E., Richard, J. P., et al. (2017). Recent developments on the stability of systems with aperiodic sampling: An overview. *Automatica* 76, 309–335. doi:10.1016/j.automatica.2016.10.023

Jiang, Y., Yang, Y., Tan, S. -C., and Hui, S. Y. R. (2021). A high-order differentiator based distributed secondary control for DC microgrids against false data injection attacks. *IEEE Trans. Smart Grid*, 1. to be published. doi:10.1109/TSG.2021.3135904

Karimi, A., Ahmadi, A., Shahbazi, Z., Shafiee, Q., and Bevrani, H. (2021). in A resilient control method against false data injection attack in DC microgrids," 2021 7th International Conference on Control (Tabriz, Iran: Instrumentation and Automation (ICCIA), 1–6.

Liu, X. K., Wen, C., Xu, Q., and Wang, Y. W. (2021). Resilient control and analysis for dc microgrid system under DoS and impulsive FDI attacks. *IEEE Trans. Smart Grid* 12 (5), 3742–3754. doi:10.1109/tsg.2021.3072218

Lian, Z., Guo, F., Wen, C., Deng, C., and Lin, P. (2021). Distributed resilient optimal current sharing control for an islanded DC microgrid under doS attacks. *IEEE Trans. Smart Grid* 12 (5), 4494–4505. doi:10.1109/tsg.2021.3084348

Lin, P., Deng, C., Yang, Y., Lee, C. H. T., and Tay, W. P. (2021). Resilience-oriented control for cyber-physical hybrid energy storage systems using a semi-consensus scheme: Design and practice. *IEEE Trans. Ind. Electron.*, 1. to be published. doi:10.1109/TIE.2021.3102397

Liang, G., Weller, S. R., Zhao, J., Luo, F., and Dong, Z. (2016). The 2015 Ukraine blackout: Implications for false data injection attacks. *IEEE Trans. Power Syst.* 32 (4), 3317–3318, Nov. doi:10.1109/tpwrs.2016.2631891

Lian, Z., Deng, C., Wen, C., Guo, F., Lin, P., and Jiang, W. (2021). Distributed event-triggered control for frequency restoration and active power allocation in microgrids with varying communication time delays. *IEEE Trans. Ind. Electron.* 68 (9), 8367–8378. doi:10.1109/tie.2020.3016272

Ma, Y. -S., Che, W. -W., Deng, C., and Wu, Z. -G. (2021). Distributed model-free adaptive control for learning nonlinear MASs under DoS attacks. *IEEE Trans. Neural Netw. Learn. Syst.*, 1–10. doi:10.1109/TNNLS.2021.3104978

Rui, W., Qiuye, S., Pinjia, Z., Yonghao, G., Dehao, Q., and Peng, W. (2020). Reduced-order transfer function model of the droop-controlled inverter via Jordan continued-fraction expansion. *IEEE Trans. Energy Convers.* 35 (3), 1585–1595. doi:10.1109/tec.2020.2980033

Sahoo, S., Peng, J. C., Devakumar, A., Mishra, S., and Dragiceviõ c, T. (2020). On detection of false data in´ cooperative DC microgrids—a discordant element approach. *IEEE Trans. Ind. Electron.* 67 (8), 6562–6571. doi:10.1109/tie.2019.2938497

Wang, Y., Mondal, S., Satpathi, K., Xu, Y., Dasgupta, S., and Gupta, A. (2021). Multi-Agent distributed power management of DC shipboard power systems for optimal fuel efficiency. *IEEE Trans. Transp. Electrific.* 7, 3050–3061. doi:10.1109/TTE.2021.3086303

Wang, R., Sun, Q., Sun, C., Zhang, H., Gui, Y., and Wang, P. (2021). Vehicle-vehicle energy interaction converter of electric vehicles: A disturbance observer based sliding mode control algorithm. *IEEE Trans. Veh. Technol.* 70 (10), 9910–9921. doi:10.1109/tvt.2021.3105433

Wang, R., Sun, Q., Han, J., Zhou, J., Hu, W., Zhang, H., et al. (2021c). Energy-management strategy of battery energy storage systems in DC microgrids: A distributed dynamic event-triggered H_∞ consensus control. *IEEE Trans. Syst. Man, Cybern. Syst.* doi:10.1109/TSMC.2021.3129184

Wang, Y., Deng, C., Xu, Y., and Dai, J. (2020), Unified real power sharing of generator and storage in islanded microgrid via distributed dynamic event-triggered control. *IEEE Trans. Power Syst.* 36 (3), 1713–1724. doi:10.1109/TPWRS.2020.3039530

Yao, W., Wang, Y., Xu, Y., Deng, C., and Wu, Q. (2022). Distributed weight-average-prediction control and stability analysis for an islanded microgrid with communication time delay. *IEEE Trans. Power Syst.* 37 (1), 330–342. doi:10.1109/tpwrs.2021.3092717

Yang, Y., Qian, Y., and Yue, W. (2022). A secure dynamic event-triggered mechanism for resilient control of multi-agent systems under sensor and actuator attacks. *IEEE Trans. Circuits Syst. I.* 69 (3), 1360–1371. doi:10.1109/tcsi.2021.3132153

Yang, Y., and Dong, Y. (2019). Observer-based decentralized adaptive NNs fault-tolerant control of a class of large-scale uncertain nonlinear systems with actuator failures. *IEEE Trans. Syst. Man. Cybern. Syst.* 49 (3), 528–542. doi:10.1109/tsmc.2017.2744676

Yang, Yang, Li, Yanfei, Yue, Dong, Tian, Yu-Chu, and Ding, Xiaohua (2021). Distributed secure consensus control with event-triggering for multi-agent systems under DoS attacks. *IEEE Trans. Cybern.* 51 (6), 2916–2928. doi:10.1109/tcyb.2020.2979342

Zhang, J., Sahoo, S., Peng, J. C. -H., and Blaabjerg, F. (2021). Mitigating concurrent false data injection attacks in cooperative DC microgrids. *IEEE Trans. Power Electron.* 36 (8), 9637–9647. doi:10.1109/tpel.2021.3055215

frontiers | Frontiers in Energy Research

ORIGINAL RESEARCH
published: 15 August 2022
doi: 10.3389/fenrg.2022.956768

Electricity Demand Forecasting With a Modified Extreme-Learning Machine Algorithm

Chen Chen*, Chuangang Ou , Mingxiang Liu and Jingtao Zhao

NARI Technology Co., Ltd., Nanjing, China

To operate the power grid safely and reduce the cost of power production, power-load forecasting has become an urgent issue to be addressed. Although many power load forecasting models have been proposed, most still suffer from poor model training, limitations sensitive to outliers, and overfitting of load forecasts. The limitations of current load-forecasting methods may lead to the generation of additional operating costs for the power system, and even damage the distribution and network security of the related systems. To address this issue, a new load prediction model with mixed loss functions was proposed. The model is based on Pinball–Huber's extreme-learning machine and whale optimization algorithm. In specific, the Pinball–Huber loss, which is insensitive to outliers and largely prevents overfitting, was proposed as the objective function for extreme-learning machine (ELM) training. Based on the Pinball–Huber ELM, the whale optimization algorithm was added to improve it. At last, the effect of the proposed hybrid loss function prediction model was verified using two real power-load datasets (Nanjing and Taixing). Experimental results confirmed that the proposed hybrid loss function load prediction model can achieve satisfactory improvements on both datasets.

Keywords: outliers, whale optimization algorithm, load forecasting, Pinball–Huber regression, extreme-learning machine

Edited by:
Qihe Shan,
Dalian Maritime University, China

Reviewed by:
Yang Yang,
Nanjing University of Posts and Telecommunications, China
Jinran Wu,
Queensland University of Technology, Australia
Li Xi'An,
Shanghai Jiao Tong University, China

****Correspondence:***
Chen Chen
chenchen3@sgepri.sgcc.com.cn

Specialty section:
This article was submitted to Smart Grids,
a section of the journal Frontiers in Energy Research.

Received: *30 May 2022*
Accepted: *17 June 2022*
Published: *15 August 2022*

Citation:
Chen C, Ou C, Liu M and Zhao J (2022) Electricity Demand Forecasting With a Modified Extreme-Learning Machine Algorithm. Front. Energy Res. 10:956768. doi: 10.3389/fenrg.2022.956768

1 INTRODUCTION

As an integrated system that can optimize the allocation of energy resources according to the regional energy structure and energy reserves, integrated energy systems have become an important way to accelerate the global sustainable energy transformation (Wu et al., 2019, 2021). Power-load forecasting is an important part of the power system (Ahmad et al., 2020; Yang et al., 2022b). Accurate power-load forecasting can arrange the start and stop of generator sets more economically and reasonably to maintain power supply and demand balance (Shi et al., 2021), and maintain the safety and stability of power grid operation (Dynge et al., 2021). In addition, it can effectively reduce the cost of power generation, transmission, and distribution; improve economic and social benefits; and ensure the operation of the society (Chu et al., 2021; Lin and Shi, 2022). The existing mainstream power load forecasting methods are mainly divided into two categories: statistical (Rehman et al., 2022) and artificial intelligence methods (Aslam et al., 2021). Factors such as seasons (van der Meer et al., 2018), climates (Alipour et al., 2019), and temperature (Yang et al., 2022d) have a direct impact on power load. Statistical methods are a very effective solution to such systems with trends, seasons, and periodic changes. Many scholars have carried out research on power load forecasting based on these methods such as the auto regressive (AR) (Louzazni et al., 2020), auto regressive moving average (Yan and Chowdhury, 2014), and auto regressive integrated moving average models (Asadi et al., 2012). The statistical methods usually take power load or energy as a single input series, while the artificial intelligence methods consider the relationship between the output and multiple influencing factors. Under the condition of sufficient historical samples, artificial intelligence methods usually have high forecast accuracy and strong generalization ability, such as the support vector machine (Yang et al., 2022a) and neural networks (NNs) (Huang et al., 2002; Oreshkin et al., 2021). Extreme-learning machine (ELM) is an emerging generalized single-hidden-layer feed-forward neural-network-learning algorithm, which can generate hidden variable parameters at random to calculate output weights, and it is widely used in forecast. Liu and Wang (2022) proposed a transfer-learning-based probabilistic wind power forecasting method. Model-based transfer learning is utilized to construct the multilayer extreme-learning machine. The enhanced Crow search algorithm–ELM (ENCSA–ELM) model was proposed to accurately forecast short-term wind power to improve the utilization efficiency of clean energy in Li et al. (2021). ELM is more efficient, has lower computational costs, and has greater generalization than shallow learning systems.

Both time series and artificial intelligence methods usually take the loss function as the training objective. The existing literature mainly uses the mean absolute error (L1 loss), mean absolute percentage error (MAPE), and root mean square error (RMSE) to evaluate the effect of power load forecasting. Furthermore, to develop an algorithmic framework capable of handling data containing outliers, a robust loss function, Huber–Loss (Ge et al., 2019), has been introduced. Compared with other loss functions, this function has different sensitivity to abnormal data and is more tolerant to noise. Furthermore, the loss function can adjust the robustness of the model according to the tuning parameters τ, and it can better suppress the influence of outliers.

However, these improved evaluation indicators are still mostly based on the absolute value criterion, only considering the size of the error, but not the direction of the error. They also do not fully account for the different consequences of positive and negative errors. In fact, the positive and negative errors of the power load forecasting affect the reliability and economy of power differently, so the error evaluation indicators should be differentiated. The improvement of the abovementioned traditional indicators is mainly reflected in the improvement of the mathematical form, the introduction or construction of new statistics, and the construction of a multiindicator evaluation system.

Hybrid algorithmic frameworks have been developed and widely used in power-load forecasting. However, these algorithmic frameworks have hyperparameters that need to be carefully optimized before forecasting. The optimized values of these algorithms determine the performance of the forecast (Yang et al., 2022c). Grid search, gradient descent, and cross validation are commonly used methods for optimizing the parameters of forecast models. The studies have also proposed nature-inspired meta-heuristic optimization algorithms to efficiently optimize these parameters. Geng et al. (2015) proposed a load-forecasting model hybridizing the seasonal SVR and chaotic cloud simulated annealing algorithm to receive more accurate forecasting performance. Xie et al. (2020) proposed a method combined Elman neural network and the particle swarm optimization for the short-term power load forecasting. Heydari et al. (2020) proposed a hybrid model that considers price and load forecasting, including variational mode decomposition, generalized regression NNs, and gravitational search algorithms.

In summary, the current requirement for power load forecasting is increasing from the following perspectives: 1) the forecasting accuracy needs to be improved; 2) a robust loss function is required to develop machine learning framework that can fully account for the different consequences of positive and negative errors and outliers; and 3) more advanced optimization methods are needed to improve model parameters. The contributions of this article are the following: 1) A new hybrid model was proposed to improve the load-forecasting accuracy and prevent overfitting, which combines the Pinball–Huber–ELM with WOA. In specific, in our proposed Pinball–ELM, WOA is employed to search weights and thresholds, which provide good training results for load prediction; and 2) an improved ELM was developed to handle data with outliers. Due to its excellent properties, the Pinball–Huber loss was incorporated into the ELM as the objective function for its training.

The rest of this article is organized as follows. In **Section 2**, we review the basic ELM and propose our powerful ELM. Next, **Section 3** introduces WOA. **Section 4** then illustrates our proposed hybrid loss function load prediction model and presents the model-training process for cross validation of tuning parameters. In **Section 5**, the testing of the proposed hybrid load-forecasting model WOA–Pinball–Huber–ELM using two datasets from Nanjing and Taixing is described. **Section 6** concludes the article.

2 PINBALL–HUBER EXTREME-LEARNING MACHINE

2.1 Extreme-Learning Machine

Unlike traditional NNs, ELM is a single-hidden-layer feed-forward NN that randomly selects its input weights and thresholds. The number of nodes in the input layer, hidden layer, and output layer are N, L, and M, respectively. Under the action of the activation function, the hidden layer output matrix H is as follows:

$$H = \begin{bmatrix} g(\omega_1 \cdot x_1 + b_1) & g(\omega_2 \cdot x_1 + b_2) & \cdots & g(\omega_L \cdot x_1 + b_L) \\ g(\omega_1 \cdot x_2 + b_1) & g(\omega_2 \cdot x_2 + b_2) & \cdots & g(\omega_L \cdot x_2 + b_L) \\ \vdots & \vdots & \ddots & \vdots \\ g(\omega_1 \cdot x_N + b_1) & g(\omega_2 \cdot x_N + b_2) & \cdots & g(\omega_L \cdot x_N + b_L) \end{bmatrix}_{N\times L}, \tag{1}$$

where x is the input matrix, ω is the input weight matrix, and b is the threshold in the hidden layer, which are randomly generated in ELM. The output T of the ELM is then

$$T = [t_1, t_2, \ldots, t_N]_{M\times N} = \begin{bmatrix} t_{1j} \\ t_{2j} \\ \vdots \\ t_{Mj} \end{bmatrix}_{M\times L} = \begin{bmatrix} \sum_{i=1}^{t} \beta_{i1} \cdot g\left(\omega_i \cdot x_j + b_i\right) \\ \sum_{i=1}^{t} \beta_{i2} \cdot g\left(\omega_i \cdot x_j + b_i\right) \\ \vdots \\ \sum_{i=1}^{t} \beta_{iM} \cdot g\left(\omega_i \cdot x_j + b_i\right) \end{bmatrix}_{M\times L} \quad (j = 1, 2, \ldots, N), \qquad (2)$$

where β is the correlation weight matrix between the hidden and output layers.

ELM mainly uses the randomly generated ω and b, and it selects the least square method to complete the calculation of the β. The algorithm does not need to perform multiple solving operations, which greatly reduces the complexity of the operation.

According to the two theorems in Zhang et al. (2020), when the activation function is differentiable, it is not necessary to adjust all parameters in ELM. At last, the solution of β can be obtained as follows:

$$\beta = H^{-1} T', \qquad (3)$$

where H^{-1} is the generalized inverse matrix of H.

2.2 Regression Loss Function

The regression loss function represents the gap between the predicted and actual value. If the gap is larger, the value of the loss function is larger; otherwise, its value is smaller. During the optimization process, through continuous learning and training, the value of the loss function is gradually reduced, so that the performance of the model is continuously improved.

2.2.1 $L2$ Loss

In the training of forecast models, the most commonly used loss function is $L2$ loss (mean squared error), which is defined as

$$L2 = \frac{1}{M} \sum_{i=1}^{M} (y_i - \hat{y}_i)^2, \qquad (4)$$

where M is the number of output samples in the training set, y_i represents the expected output of the training set, and $\hat{y}_i$ represents the forecast output of the training set. For models using the $L2$ loss, the convergence is fast when the error is large. However, the $L2$ loss is sensitive to outliers, which affects the performance of the forecast model.

2.2.2 $L1$ Loss

The $L1$ loss (mean absolute error) is more robust to outliers than the $L2$ loss, which is defined as

$$L1 = \frac{1}{M} \sum_{i=1}^{M} |y_i - \hat{y}_i|, \qquad (5)$$

where M is the number of output samples in the training set, y_i represents the expected output of the training set, and $\hat{y}_i$ represents the forecast output of the training set. Although the $L1$ loss enhances robustness, it is not smooth and nondifferentiable at zero, and it converges slowly.

2.2.3 Huber Loss

Huber loss is a combination of the $L2$ and $L1$ losses, which includes a parameter δ. δ determines the degree of inclination of the Huber loss on the $L1$ and $L2$ losses; that is, it is used to control the quadratic and linear range of the loss function. The Huber loss combines the advantages of the $L1$ and $L2$ losses, and it is more robust to outliers than the $L2$ loss, while converging faster.

Huber loss reduces the penalty for outliers, so it is a commonly used robust loss function. It is defined as

$$\rho_\delta(r) = \begin{cases} \frac{1}{2} r^2 & |r| \le \delta \\ |r|\delta - \frac{\delta^2}{2} & |r| > \delta, \end{cases} \qquad (6)$$

where r represents the absolute value of the difference between the expected output and predicted output. δ represents the tuning parameter, which is used to determine the behavior of the model to deal with outliers.

2.2.4 Pinball Loss

Pinball loss is mostly used in regression analysis problems, which is related to the quantile distance and is not sensitive to outliers. The Pinball loss used is defined as

$$L_\tau = \begin{cases} (y_i - \hat{y}_i)\tau & y_i \ge \hat{y}_i \\ (\hat{y}_i - y_i)(1-\tau) & y_i < \hat{y}_i, \end{cases} \qquad (7)$$

where $\tau \in [0, 1]$ is the target quantile to adjust for the positive and negative errors in the forecast. y_i and $\hat{y}_i$ are defined as above. When $\tau = 0.5$, the Pinball loss is the same as the L1 loss, and it can be considered as a generalized L1 loss. When $\tau \ne 0.5$, the Pinball loss has different penalties for positive and negative errors.

2.2.5 Proposed Pinball–Huber Loss

To implement different penalties for positive and negative errors during training, and enhance the robustness of the loss function, thereby improving the accuracy, the proposed improved loss function named the Pinball–Huber loss is

$$V(r) = \begin{cases} \frac{1}{2}\tau r^2 & -\delta \le r < 0 \\ \frac{1}{2}(1-\tau) r^2 & 0 \le r \le \delta \\ \tau\left(|r|\delta - \frac{\delta^2}{2}\right) & r < -\delta \\ (1-\tau)\left(|r|\delta - \frac{\delta^2}{2}\right) & r > \delta, \end{cases} \qquad (8)$$

where $\tau \in [0, 1]$ is the target quantile to adjust for the positive and negative errors in the forecast. δ represents the threshold, which is used to determine the behavior of the model to deal with outliers. r represents the absolute value of the difference between the expected output and predicted output. Compared with Huber loss, the Pinball–Huber loss maintains its low sensitivity to outliers in the data and implements different penalties for positive and negative errors, considering the direction of errors. In power load forecasting, since there are often outliers in power load data, and positive and negative errors should be distinguished, our proposed Pinball–Huber is expected to improve the forecasting accuracy and convergence speed.

2.3 Pinball–Huber–Extreme-Learning machine

The presence of data outliers can affect the prediction performance of ELM. The Pinball–Huber loss obtained by introducing the pinball feature based on the Huber loss can effectively distinguish the effects of positive and negative errors and further improve the accuracy of prediction, while maintaining robustness. Therefore, this study introduces the Pinball–Huber loss into the traditional ELM and uses the Pinball–Huber loss as the objective function to train the ω and b of ELM. When dealing with power data with outliers, the model shows quite good robustness, and greatly improves the ELM effect regarding the prediction accuracy. The improved model named the Pinball–Huber–ELM is as follows:

$$
\begin{aligned}
&\min_{\omega,b} \quad MHL = \frac{1}{M}\sum_{i=1}^{M} V\left(r_i\right) \\
&s.t. \quad V\left(r\right) = \begin{cases} \frac{1}{2}\tau r^2 & -\delta \le r < 0 \\ \frac{1}{2}\left(1-\tau\right) r^2 & 0 \le r \le \delta \\ \tau\left(|r|\delta - \frac{\delta^2}{2}\right) & r < -\delta \\ \left(1-\tau\right)\left(|r|\delta - \frac{\delta^2}{2}\right) & r > \delta \end{cases} \\
&\qquad \omega_i = \left[\omega_{i1}, \omega_{i2}, \ldots, \omega_{iN}\right]^T \\
&\qquad b = \left[b_1, b_2, \ldots, b_L\right]^T.
\end{aligned}
\tag{9}
$$

3 WHALE OPTIMIZATION ALGORITHM

The whale optimization algorithm was inspired by the unique bubble net prey method of the whale population (Mirjalili et al., 2016). It searches for the optimal solution through the following three mechanisms: surrounding the prey, searching for the prey, and attacking the prey by the spiral bubble net.

3.1 Surround Prey

1) Whale swimming toward the optimal position

Whale groups can find out the coordinates of their prey and surround them during hunting. In WOA, it is assumed that the position of the optimal individual whale in the current population is the position of the prey, and the optimal whale is surrounded by other whales. The mathematical model is

$$D = \left|C \cdot X^{*}\left(t\right) - X\left(t\right)\right|, \tag{10}$$

$$X\left(t+1\right) = X^{*}\left(t\right) - A \cdot D. \tag{11}$$

In **Eqs. 10** and **11**, t is the current iteration; $X*(t)$ is the best-obtained solution in the previous iteration; $X(t)$ is the solution in the current iteration; and $X(t)$ is the solution in the next iteration. The specific formulas of the coefficient vectors A and C are

$$A = 2a \cdot r_2 - a, \tag{12}$$

$$C = 2 \cdot r_1. \tag{13}$$

In **Eqs. 12** and **13**, r_1, r_2 are the two numbers randomly selected in the range of $[-1, 1]$, and a is the convergence factor. As the solution is updated, the value of a decreases linearly from 2 to 0. The formula is

$$a = 2 - 2\left(\frac{t}{t_{\max}}\right), \tag{14}$$

where $t_{\max}$ is the maximum number of iterations.

Equation 11 shows that it can be updated on the basis of the current optimal individual position (X^{*}, Y^{*}) and continue to search for the individual position (X, Y). Y^{*} represents the fitness value obtained from position X^{*}. Y represents the fitness value obtained from position X. By adjusting the values of the A and C vectors, we can achieve various positions around the best position relative to the current position. Any individual whale is allowed to update its position near the current optimal solution and simulate surrounding the prey.

2) Whales swimming toward random locations

In the process of searching for prey, the method that the vector A changes with the iterative process can be used. In effect, humpback whales randomly explore the solution space based on each other's positions. Therefore, A is used in the global exploration phase to update the whale position so as to stay away from the current individual when the random value is >1 or <1.

In contrast to the local development phase, in the global exploration phase, the positions of individual whales are upgraded based on randomly selected individuals, rather than the best whales found so far. This mechanism focuses on exploration. Thus, when $|A| > 1$, the WOA algorithm performs a global exploration operation. During the prey-hunting phase, the location of the prey is unknown to the whale population. This mechanism focuses on optimization. Thus, when $|A| < 1$, the whales obtain the location of the prey through collective cooperation. Whales use random individual positions in the population as navigation targets to find food, and the mathematical model is described as follows:

$$D = \left|C \cdot X_{rand} - X\right|, \tag{15}$$

$$X\left(t+1\right) = X_{rand} - A \cdot D. \tag{16}$$

In **Eqs. 15** and **16**, X_{rand} represents the position of the whales randomly selected in the current whale population.

The WOA algorithm begins execution with a random set of whale swarm locations. The shrinking envelope is achieved as the convergence factor a decreases. The fluctuation range of the coefficient vector A also decreases as the convergence factor a decreases. That is, when the convergence factor a decreases from 2 to 0 during the iteration, the fluctuation of the coefficient vector A also decreases; its range is $[-a, a]$.

In each iteration, the whale individual updates its position using the randomly selected whale position information or the whale individual position information with the best fitness value obtained so far. As the parameter a decreases from 2 to 0, the transition of the algorithm between the global exploration phase and local development phase is realized. When $|A| > 1$, we randomly select a whale in the population; when $|A| < 1$, we select the current whale with the best fitness value to update the position of the individual whale. Given the value of p, WOA has the ability to swap between helical or circular motion. At last, satisfying a termination condition terminates the WOA algorithm.

3.2 Bubble Net Chase

Two methods were used to build a mathematical model of the predation behavior of whales in bubble nets. The first is the reduction of the wraparound mechanism, which is achieved by reducing the value of a in **Eq. 14**, where the fluctuation range of A also decreases accordingly. In other words, A represents a random value in the interval $[-a, a]$, where a decreases from 2 to 0 during the iteration. Defining a random value of A in $[-1, 1]$, the new position of the individual whale can be defined somewhere between the whale's original position and the current best whale position. The shrinking and wrapping mechanism of whale group predation can be represented by a two-dimensional space $(0 \leq A \leq 1)$. This space contains all possible positions to transform from (X, Y) to (X^{*}, Y^{*}).

The second is the spiral update position mechanism. The method first calculates the distance between the whale located at (X, Y) and the prey located at (X^{*}, Y^{*}). Between the location of the whale and prey, the researchers used a spiral equation to mimic the spiral of a humpback whale shape motion. Its mathematical model is described as

$$X(t+1) = D' \cdot e^{bl} \cdot cos(2\pi l) + X^{*}(t). \tag{17}$$

In **Eq. 17**, $D' = |X^{*}(t) - X(t)|$ represents the distance between the optimal whale individual and current whale individual in the tth iteration; b represents the constant of the logarithmic spiral equation; l is the random value between $[-1, 1]$ number; and "$\cdot$" is element-wise multiplication.

Whales follow a spiral path while swimming around their prey in a shortened circle. To obtain a model that simulates this behavior, it is assumed that there is a 50% probability during the optimization process to randomly choose between the encircling mechanism and spiral updating position mechanism to update the positions of individual whales. Its mathematical model is

$$X(t+1) = \begin{cases} X^{*}(t) - A \cdot D, & p < 0.5 \\ D' \cdot e^{bl} \cdot cos(2\pi l) + X^{*}(t), & p \leq 0.5. \end{cases} \tag{18}$$

In **Eq. 18**, p represents the random number between [0, 1]. After the bubble net chase pattern, the humpback whales begin to randomly search for prey.

4 PROPOSED FORECASTING MODEL

In this section, we propose a hybrid loss function power load forecasting model. This model combines a powerful ELM with an improved Pinball–Huber loss function. To optimize the effect of the improved algorithm, we need to obtain the optimal solution of the tuning parameters of Huber loss through two cross validation in advance.

At last, the implementation flow of our hybrid loss function prediction model is as follows:

1) We obtain the original data and preprocess them. We divide the data into training and test sets appropriately.
2) The training set is then divided into five subsets. Any nonrepetitive part of the five subsets (i.e., any subset) is used as the training set; the remaining four parts of the training set (i.e., the remaining subsets) are used as the test set. We compute MSE_i using the test set and employ a different subset as the test set each time. We use five-fold cross validation for parameters δ and τ. We divide the value range of a into five equal parts. Then we randomly pick a value from each interval and obtain five values, denoted as $[0, 0.2], [0.2, 0.4], [0.4, 0.6], [0.6, 0.8], [0.8, 1]$. Experiments were performed five times with different values for each test set used. We use five δ-values and five τ-values to combine 25 experimental data.
3) We first assign empirical parameter values, then apply 2 five-fold cross-validations to average the 25 values of MSE_i to obtain the final average MSE, called CV, $CV = \left(\sum_{i=1}^{k} MSE_i\right)/k$. Twenty-five MSE_i's were compared, and the minimum value of MSE is selected to be substituted into the Pinball–Huber loss regression function.
4) In the training set, we take the minimum value of the Pinball–Huber as the goal, use WOA to solve the optimal parameters ω_i, b_j of ELM, and substitute them into formula to obtain β_{jk}.
5) The input weight of the model, the threshold of intermediate nodes, and the output weight of the model are all brought into the ELM model, and then the input of the test set is substituted into the model to obtain the prediction output of the test set.

5 CASE STUDIES

We performed power-load forecasts for Nanjing and Taixing power data. We recorded Nanjing's power load data (total load power of the grid/MW every 15 min) every half an hour. Nanjing data have 1920 data points (2003.2.18.00:00–2003.3.29.23:30). The training set included 1,152 data points, and the test set included 768 data points. We record Taixing's electricity load data (daily electricity consumption/10,000 kwh) every other day. Taixing data have 1,175 data points (2018.5.13–2021.8.2). The training set includes 705 data points, and the test set includes 470 data points. The specific situation is shown in the **Table 1**.

An evaluation is performed in this subsection; the performance of our proposed WOA–Pinball–Huber–ELM algorithm is evaluated using the power load data of Nanjing and Taixing, as shown in **Tables 2** and **3**. The actual electrical load power and the WOA–Pinball–Huber–ELM-based electrical load forecast result graph for Nanjing's data are shown in **Figure 1**. The

TABLE 1 | Characteristics of experimental data in Nanjing and Taixing.

	Dataset	Size	Min	Max	Median	Mean	Std.
Nanjing	Total data	1920	2,362.152	5,276.500	3,879.217	3,802.732	607.709
	Training data	1,152	2,564.228	5,151.652	3,991.129	3,860.526	635.217
	Testing data	768	2,362.152	5,276.500	3,775.403	3,716.042	553.120
Taixing	Total data	1,175	1,210.872	2,875.318	1,893.728	1,902.926	249.797
	Training data	705	1,210.872	2,516.598	1,799.584	1,795.856	203.690
	Testing data	470	1,424.918	2,875.318	2,040.657	2,063.533	225.466

TABLE 2 | Evaluation index of Nanjing data is obtained from three prediction algorithm experiments.

	Train			Test		
	RMSE	MAE	MAPE	RMSE	MAE	MAPE
WOA-ELM	191.52	178.92	0.04	202.42	187.02	0.04
WOA-L1-ELM	168.93	120.63	0.04	194.06	155.35	0.04
WOA-L2-ELM	161.20	120.82	0.04	193.94	152.58	0.04
WOA-Pinball-ELM	182.92	141.66	0.04	192.49	150.48	0.04
WOA-HUBER-ELM	172.50	136.45	0.04	188.21	149.17	0.04
WOA-Pinball-Huber-ELM	153.69	115.11	0.03	186.05	146.58	0.04

TABLE 3 | Evaluation index of Taixing data is obtained from three prediction algorithm experiments.

	Train			Test		
	RMSE	MAE	MAPE	RMSE	MAE	MAPE
WOA-ELM	58.56	43.78	0.02	74.04	60.25	0.02
WOA-L1-ELM	59.50	41.47	0.02	69.67	58.04	0.02
WOA-L2-ELM	57.71	41.68	0.02	73.91	57.45	0.02
WOA-Pinball-ELM	58.49	42.00	0.02	70.79	51.62	0.02
WOA-HUBER-ELM	57.44	41.30	0.02	73.36	54.72	0.03
WOA-Pinball-Huber-ELM	57.62	41.58	0.02	69.57	51.48	0.02

actual electrical load power and the WOA–Pinball–Huber–ELM-based electrical load forecast result graph for Taixing data are shown in **Figure 2**.

As far as the power load data in Nanjing are concerned, we use the proposed algorithm (WOA–Pinball–Huber–ELM) and the compared algorithms (WOA–ELM, WOA–L1–ELM, WOA–L2–ELM, WOA–Pinball–ELM, WOA–Huber–ELM) for experiments, and the experimental results are shown in **Table 2**. From the experimental results of the test set in **Table 2**, the four (improved based on the basic WOA–ELM) algorithms and the basic WOA–electric power data predicted by ELM algorithm. The above four improved algorithms corresponding to the calculated three evaluation indicators (RMSE, MAE, and MAPE) data are mostly better than the three calculated by the basic WOA–ELM algorithm.

The Pinball–Huber loss function is obtained by combining the Pinball and Huber loss. We improved the WOA–Pinball–Huber–ELM, WOA–Pinball–ELM, WOA–Huber–ELM, WOA–L1–ELM, and WOA–L2–ELM algorithms from the Pinball–Huber, Pinball loss, Huber loss, and L1 and L2, respectively. Furthermore, we used these algorithms to predict the electric power data and calculate the corresponding three evaluation indicators. The three evaluation indexes calculated by the WOA–Pinball–Huber–ELM algorithm were better than the three evaluation indexes calculated by the improved WOA–Pinball–ELM and WOA–Huber–ELM algorithms. In addition, the three evaluation indexes calculated by the WOA–Pinball–Huber–ELM algorithm were better than the three evaluation indexes calculated by the improved WOA–L1–ELM and WOA–L2–ELM algorithms.

Considering the power load data of Taixing, the experimental results are presented in **Table 3**. From the experimental results of the test set in **Table 3**, it can be seen that the four improved algorithms and the basic WOA–ELM algorithm predict the power load prediction power data. The power data obtained by the above four improved algorithms correspond to the calculated

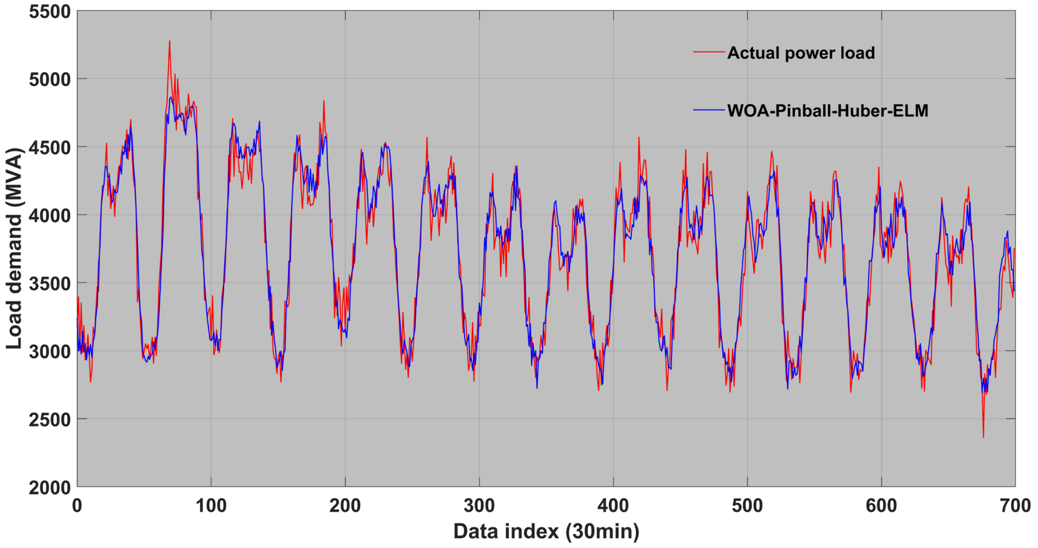

FIGURE 1 | Actual power and prediction result graph based on WOA–Pinball–Huber–extreme-learning machine (ELM) in Taixing.

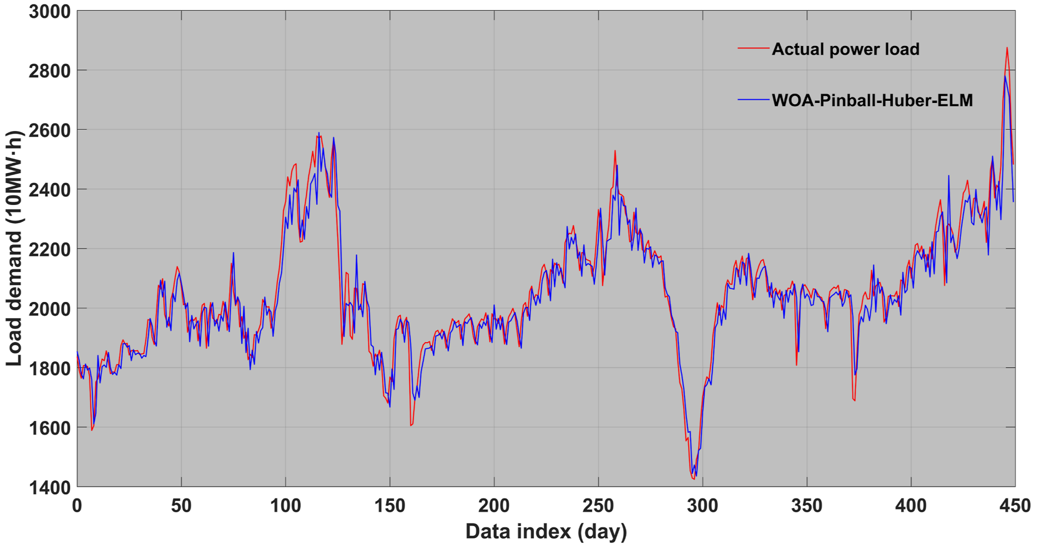

FIGURE 2 | Actual power and prediction result graph based on WOA–Pinball–Huber–ELM in Taixing.

three evaluation indicators RMSE, MAE, and MAPE data than the three calculated using the basic WOA–ELM algorithm. The evaluation index data are small, and the effect is better.

It is obvious from **Table 3** that the three evaluation indexes calculated using the WOA–Pinball–Huber–ELM algorithm were better than the three evaluation indexes calculated by the improved WOA–Pinball–ELM and WOA–Huber–ELM algorithms. At last, the three evaluation metrics calculated by the WOA–Pinball–Huber–ELM algorithm are better than those calculated by the improved WOA–L1–ELM and WOA–L2–ELM algorithms.

6 CONCLUSION

To ensure the safe operation of the grid, we must confirm that the power-load forecast is accurate and effective. However, the complexity of the grid structure brings many difficulties to future power-load forecasting, and the current popular forecasting methods cannot handle all the difficulties. To address this challenge, this study proposed a new hybrid loss function load prediction model, the WOA–Pinball–Huber–ELM. It is a combination of the Pinball–Huber ELM and whale optimization algorithm. The Pinball–Huber loss, which is insensitive to outliers and largely prevents overfitting, is treated as the objective function for our optimized ELM training. Based on two real power load forecasting datasets in Nanjing and Taixing and comparative experiments with two improved algorithms, our WOA–Pinball–Huber–ELM model shows great advantages in handling outliers and improving forecasting accuracy.

In future work, our proposed framework can be employed for other forecasting problems in environmental science (Zhang et al., 2021, 2022) and bioinformatics (Miao et al., 2022).

DATA AVAILABILITY STATEMENT

The original contributions presented in the study are included in the article/Supplementary Material. Further inquiries can be directed to the corresponding author.

AUTHOR CONTRIBUTIONS

CC: supervision, investigation, project administration; CO: software, visualization, formal analysis, writing–original draft; ML: writing–review and editing; JZ: formal analysis, writing–review and editing

FUNDING

This research was funded by the National Key Research and Development Program of China under Grant No. 2021YFB2401303.

REFERENCES

Ahmad, T., Zhang, H., and Yan, B. (2020). A Review on Renewable Energy and Electricity Requirement Forecasting Models for Smart Grid and Buildings. *Sustain. Cities Soc.* 55, 102052. doi:10.1016/j.scs.2020.102052

Alipour, P., Mukherjee, S., and Nateghi, R. (2019). Assessing Climate Sensitivity of Peak Electricity Load for Resilient Power Systems Planning and Operation: A Study Applied to the texas Region. *Energy* 185, 1143–1153. doi:10.1016/j.energy.2019.07.074

Asadi, S., Tavakoli, A., and Hejazi, S. R. (2012). A New Hybrid for Improvement of Auto-Regressive Integrated Moving Average Models Applying Particle Swarm Optimization. *Expert Syst. Appl.* 39, 5332–5337. doi:10.1016/j.eswa.2011.11.002

Aslam, S., Herodotou, H., Mohsin, S. M., Javaid, N., Ashraf, N., and Aslam, S. (2021). A Survey on Deep Learning Methods for Power Load and Renewable Energy Forecasting in Smart Microgrids. *Renew. Sustain. Energy Rev.* 144, 110992. doi:10.1016/j.rser.2021.110992

Chu, W., He, W., Jiang, Q., Zhang, S., Hu, Z., Xu, G., et al. (2021). Optimization of Operation Strategy for a Grid Interactive Regional Energy System. *Energy Build.* 250, 111294. doi:10.1016/j.enbuild.2021.111294

Dynge, M. F., Crespo del Granado, P., Hashemipour, N., and Korpås, M. (2021). Impact of Local Electricity Markets and Peer-To-Peer Trading on Low-Voltage Grid Operations. *Appl. Energy* 301, 117404. doi:10.1016/j.apenergy.2021.117404

Ge, J., Li, H., Wang, H., Dong, H., Liu, H., Wang, W., et al. (2019). Aeromagnetic Compensation Algorithm Robust to Outliers of Magnetic Sensor Based on Huber Loss Method. *IEEE Sensors J. PP* 1–1. doi:10.1109/jsen.2019.2907398

Geng, J., Huang, M.-L., Li, M.-W., and Hong, W.-C. (2015). Hybridization of Seasonal Chaotic Cloud Simulated Annealing Algorithm in a Svr-Based Load Forecasting Model. *Neurocomputing* 151, 1362–1373. doi:10.1016/j.neucom.2014.10.055

Heydari, A., Majidi Nezhad, M., Pirshayan, E., Astiaso Garcia, D., Keynia, F., and De Santoli, L. (2020). Short-term Electricity Price and Load Forecasting in Isolated Power Grids Based on Composite Neural Network and Gravitational Search Optimization Algorithm. *Appl. Energy* 277, 115503. doi:10.1016/j.apenergy.2020.115503

Huang, H.-C., Hwang, R.-C., and Hsieh, J.-G. (2002). A New Artificial Intelligent Peak Power Load Forecaster Based on Non-fixed Neural Networks. *Int. J. Electr. Power & Energy Syst.* 24, 245–250. doi:10.1016/s0142-0615(01)00026-6

Li, L.-L., Liu, Z.-F., Tseng, M.-L., Jantarakolica, K., and Lim, M. K. (2021). Using Enhanced Crow Search Algorithm Optimization-Extreme Learning Machine Model to Forecast Short-Term Wind Power. *Expert Syst. Appl.* 184, 115579. doi:10.1016/j.eswa.2021.115579

Lin, B., and Shi, L. (2022). New Understanding of Power Generation Structure Transformation, Based on a Machine Learning Predictive Model. *Sustain. Energy Technol. Assessments* 51, 101962. doi:10.1016/j.seta.2022.101962

Liu, Y., and Wang, J. (2022). Transfer Learning Based Multi-Layer Extreme Learning Machine for Probabilistic Wind Power Forecasting. *Appl. Energy* 312, 118729. doi:10.1016/j.apenergy.2022.118729

Louzazni, M., Mosalam, H., Khouya, A., and Amechnoue, K. (2020). A Non-linear Auto-Regressive Exogenous Method to Forecast the Photovoltaic Power Output. *Sustain. Energy Technol. Assessments* 38, 100670. doi:10.1016/j.seta.2020.100670

Miao, M., Wu, J., Cai, F., and Wang, Y.-G. (2022). A Modified Memetic Algorithm with an Application to Gene Selection in a Sheep Body Weight Study. *Animals* 12, 201. doi:10.3390/ani12020201

Mirjalili, S., Lewis, A., and Andrew, S. (2016). The Whale Optimization Algorithm. *Adv. Eng. Softw.* 95, 51–67. doi:10.1016/j.advengsoft.2016.01.008

Oreshkin, B. N., Dudek, G., Pełka, P., and Turkina, E. (2021). N-Beats Neural Network for Mid-term Electricity Load Forecasting. *Appl. Energy* 293, 116918. doi:10.1016/j.apenergy.2021.116918

Rehman, A., Zhu, J.-J., Segovia, J., and Anderson, P. R. (2022). Assessment of Deep Learning and Classical Statistical Methods on Forecasting Hourly Natural Gas Demand at Multiple Sites in spain. *Energy* 244, 122562. doi:10.1016/j.energy.2021.122562

Shi, Y., Li, Y., Zhou, Y., Xu, R., Feng, D., Yan, Z., et al. (2021). Optimal Scheduling for Power System Peak Load Regulation Considering Short-Time Startup and Shutdown Operations of Thermal Power Unit. *Int. J. Electr. Power. Energy Syst.* 131, 107012. doi:10.1016/j.ijepes.2021.107012

van der Meer, D. W., Munkhammar, J., and Widén, J. (2018). Probabilistic Forecasting of Solar Power, Electricity Consumption and Net Load: Investigating the Effect of Seasons, Aggregation and Penetration on Prediction Intervals. *Sol. Energy* 171, 397–413. doi:10.1016/j.solener.2018.06.103

Wu, J., Cui, Z., Chen, Y., Kong, D., and Wang, Y.-G. (2019). A New Hybrid Model to Predict the Electrical Load in Five States of australia. *Energy* 166, 598–609. doi:10.1016/j.energy.2018.10.076

Wu, J., Wang, Y.-G., Tian, Y.-C., Burrage, K., and Cao, T. (2021). Support Vector Regression with Asymmetric Loss for Optimal Electric Load Forecasting. *Energy* 223, 119969. doi:10.1016/j.energy.2021.119969

Xie, K., Yi, H., Hu, G., Li, L., and Fan, Z. (2020). Short-term Power Load Forecasting Based on Elman Neural Network with Particle Swarm Optimization. *Neurocomputing* 416, 136–142. doi:10.1016/j.neucom.2019.02.063

Yan, X., and Chowdhury, N. A. (2014). Mid-term Electricity Market Clearing Price Forecasting Utilizing Hybrid Support Vector Machine and Auto-Regressive Moving Average with External Input. *Int. J. Electr. Power & Energy Syst.* 63, 64–70. doi:10.1016/j.ijepes.2014.05.037

Yang, Y., Tao, Z., Qian, C., Gao, Y., Zhou, H., Ding, Z., et al. (2022a). A Hybrid Robust System Considering Outliers for Electric Load Series Forecasting. *Appl. Intell.* 52, 1630–1652. doi:10.1007/s10489-021-02473-5

Yang, Y., Wang, Z., Gao, Y., Wu, J., Zhao, S., and Ding, Z. (2022b). An Effective Dimensionality Reduction Approach for Short-Term Load Forecasting. *Electr. Power Syst. Res.* 210, 108150.

Yang, Y., Zhou, H., Wu, J., Ding, Z., and Wang, Y.-G. (2022c). Robustified Extreme Learning Machine Regression with Applications in Outlier-Blended Wind-Speed Forecasting. *Appl. Soft Comput.* 122, 108814. doi:10.1016/j.asoc.2022.108814

Yang, Y., Zhou, H., Wu, J., Liu, C.-J., and Wang, Y.-G. (2022d). A Novel Decompose-Cluster-Feedback Algorithm for Load Forecasting with Hierarchical Structure. *Int. J. Electr. Power & Energy Syst.* 142, 108249. doi:10.1016/j.ijepes.2022.108249

Zhang, B., Tan, R., and Lin, C. J. (2020). Forecasting of E-Commerce Transaction Volume Using a Hybrid of Extreme Learning Machine and Improved Moth-Flame Optimization Algorithm. *Appl. Intell.* 1–14, 1840. doi:10.1007/s10489-020-01840-y

Zhang, S., Wu, J., Jia, Y., Wang, Y.-G., Zhang, Y., and Duan, Q. (2021). A Temporal Lasso Regression Model for the Emergency Forecasting of the Suspended Sediment Concentrations in Coastal Oceans: Accuracy and Interpretability. *Eng. Appl. Artif. Intell.* 100, 104206. doi:10.1016/j.engappai.2021.104206

Zhang, S., Wu, J., Wang, Y.-G., Jeng, D.-S., and Li, G. (2022). A Physics-Informed Statistical Learning Framework for Forecasting Local Suspended Sediment Concentrations in Marine Environment. *Water Res.* 218, 118518. doi:10.1016/j.watres.2022.118518

Conflict of Interest: Authors CC, CO, ML, and JZ were employed by the company NARI Technology Co., Ltd.

frontiers | Frontiers in Energy Research

TYPE Original Research
PUBLISHED 02 September 2022
DOI 10.3389/fenrg.2022.977854

*CORRESPONDENCE
Weiguo Zhang,
230209330@seu.edu.cn

SPECIALTY SECTION
This article was submitted to Smart Grids, a section of the journal Frontiers in Energy Research

RECEIVED 25 June 2022
ACCEPTED 11 July 2022
PUBLISHED 02 September 2022

CITATION
Zhang W, Gu L, Shi Y, Luo X and Zhou H (2022), A hybrid SVR with the firefly algorithm enhanced by a logarithmic spiral for electric load forecasting.
Front. Energy Res. 10:977854.
doi: 10.3389/fenrg.2022.977854

A hybrid SVR with the firefly algorithm enhanced by a logarithmic spiral for electric load forecasting

Weiguo Zhang [1,2]*, Linlin Gu [2], Yang Shi [3], Xiaodong Luo [3] and Hu Zhou [4]

[1]Southeast University, Nanjing, China, [2]Nari Technology Co., Ltd, Najing, China, [3]State Grid Xiong'an Integrated Energy Service Co, Ltd, Baoding, China, [4]Nanjing University of Posts and Telecommunications, Nanjing, China

Accurate forecasting of an electric load is vital in the effective management of a power system, especially in flourishing regions. A new hybrid model called logarithmic spiral firefly algorithm-support vector regression (LS-FA-SVR) is proposed to promote the performance of electric load forecasting. The new hybrid model is acquired by combining the support vector regression, firefly algorithm, and logarithmic spiral. Half-hourly electric load from five main regions (NSW, QLD, SA, TAS, and VIC) of Australia are used to train and test the proposed model. By comparing the model results with observed data on the basis of the root mean squared error (RMSE), mean absolute error (MAE), and mean absolute percent error (MAPE), the performance of the proposed hybrid model is the most outstanding among all the considered benchmark models. Hence, the results of this study show that the hybrid model LS-FA-SVR is preferable and can be applied successfully because of its high accuracy.

KEYWORDS

electric load, time series forecasting, firefly algorithm, support vector regression, logarithmic spiral, management of power system

1 Introduction

As an integrated system that can optimize the allocation of energy resources according to the regional energy structure and energy reserves, an integrated energy system has become an important way to accelerate the global sustainable energy transformation. Accurate load forecasting not only plays a decisive role in the comprehensive planning, operation, management and cascade use of energy system but is also a key technology to promote the development of the energy market (Wang et al., 2018; Chen and Wang, 2021; Yang et al., 2022c). Hence, technology for the smart and efficient management of grid uncertainty has attracted research interest. In particular, load forecasting is a core factor of smart grid applications, such as demand response, as it can accurately predict the demand flexibility and potential problems in a grid. In addition, load forecasting can contribute to the efficient integration and wide allocation of distributed energy resources and their coordination to accommodate supply and demand (Kaur et al., 2016). Therefore, the prediction of the short-term load has become the chief task in power dispatching and power planning (Wu et al., 2021; Yang et al., 2022d).

However, high accuracy in predicting a short-term load is difficult to obtain because the electric load time series is complex and shows vacillating behavior with many variables considered. In order to deal with this problem, regression models, stochastic process models, and exponential smoothing are employed to forecast the electric load in traditional methods (Zhang et al., 2021, 2022b,a). However, the traditional methods scarcely acquire the complexity of the system. Hence, artificial intelligence approaches are extensively used to predict the power load, such as artificial neural networks, support vector machines, and nature-inspired meta-heuristic algorithms.

Among all the data mining techniques based on artificial intelligence, artificial neural networks have become hot techniques in the research of forecasting electric load. Yang et al. (2022a) developed a highly accurate short-term load forecasting method using non-linear auto-regressive artificial neural networks with exogenous multi-variable input. Yang et al. (2022b) presented a novel approach for short-term electrical load forecasting by the radial basis function neural networks, and the result showed that the application of neural networks in short-term load forecasting is encouraging. Wang et al. (2016) proposed an outstanding model based on a wavelet neural network to address the complex nonlinearities and uncertainties in forecasting the electric load, and the accuracy of the proposed model is better than the considered models. Yang et al. (2021b) proposed a new hybrid model to forecast electric load series with outliers, which is based on a robust extreme learning machine and an improved whale optimization algorithm. An et al. (2013) presented a novel approach based on a feed-forward neural network to predict the electricity demand with high accuracy and demonstrated that the proposed model improved the forecasting accuracy noticeably. Yang et al. (2021a) applied the radial basis function neural network (RBFNN) to generate accurate predictions for nonlinear time series. In recent years, with the development of the deep learning theory and hardware equipment, the technology based on deep learning is widely used in power load forecasting. Kong et al. (2017) established a forecasting framework based on LSTM for residential load forecasting. In particular, the recurrent neural network (RNN) and its variants (long short-term memory (LSTM) and gated recurrent unit (GRU)) have been widely used because of their outstanding ability to deal with time series. Feng developed a two-step short-term load forecasting (STLF) model which designed a Q-learning-based dynamic model selection. This model can provide reinforced deterministic and probabilistic load forecasts (DLFs and PLFs) (Feng et al., 2019). Afrasiabi et al. (2020) proposed a model for conditional probability density forecasting of residential loads based on an end-to-end composite model comprising convolution neural networks (CNNs) and a gated recurrent unit (GRU).

Although neural networks and deep learning methods have been widely used in load forecasting, it should not be ignored that they usually fall into the local minimum because of the restriction on generalization ability which barely makes full use of information from selecting the sample (Cui et al., 2021). Fortunately, the support vector machine developed by Vapnik (1999), one of the outstanding data mining techniques, can overcome this problem and improve the accuracy of prediction. Because of the excellence of the characteristics, the support vector machine has become one of the popular methods in forecasting the short-term electric load. Stojanović et al. (2013) used least square support vector regression (LSSVR) based on historical daily load demands in combination with the calendar and climate features for forecasting the half-hourly load demand of the next day. Chen et al. (2017) established a new support vector regression (SVR) forecasting model with the ambient temperature of 2 hours before the demand response event as input variables, and the result showed the model offered a higher degree of prediction accuracy and stability in short-term load forecasting.

The SVR has been proved to be an excellent model for load demand forecasting. However, the SVR can be improved in many aspects actually; the parameters of the support vector machine play an important role in the accuracy of prediction and are a core part in improving the SVR (Kisi et al., 2015; Najafzadeh et al., 2016). Various optimization algorithms have been used for the selection of these parameters like the grid search algorithm and gradient descent algorithm (Kisi et al., 2015). Computational complexity seems to be the main disadvantage of the grid method, which restricts its applicability to simple cases. The grid search algorithm is also prone to local minima.

Among the methods of optimizing parameters by using data mining technology, a classic way of optimizing parameters of the SVR is meta-heuristic optimization algorithms. At present, with the development of optimizers, meta-heuristic optimization algorithms are increasingly popular in selecting the optimal parameter value because the algorithms can bypass local optima and are easy to implement (Mirjalili and Lewis, 2016).

The idea of meta-heuristic algorithms comes from the behavior of animal or physical phenomena. In addition, the algorithms can be grouped into three main categories (**Figure 1**). The process of searching for an optimal parameter can be divided into two phases: exploration and exploitation (Olorunda and Engelbrecht, 2008). More specifically, the exploration phase is targeted to investigate the search space globally, and the exploitation phase is employed to search for the best results by following the exploration phase. Therefore, meta-heuristic optimization algorithms are widely utilized to find the

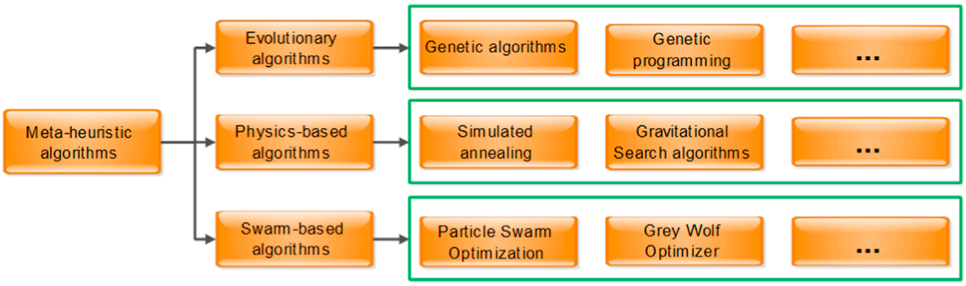

FIGURE 1
Classification of meta-heuristic algorithms.

parameters of support vector regression for short-term electric loads. Peng et al. (2016) presented a support vector regression model hybridized with the quantum particle swarm optimization algorithm for electric load forecasting, and the results showed the proposed model can simultaneously provide forecasting with good accuracy. Hong (2011) proposed an electric load forecasting model which combines the support vector regression model with the chaotic artificial bee colony algorithm to improve the forecasting performance, and the forecasting results indicated the hybrid model was a promising alternative for electric load forecasting. Xiao et al. (2017) employed the multi-objective flower pollination algorithm to optimize the parameters of support vector regression for short-term load forecasting, and the experimental results clearly showed that both the accuracy and stability of the proposed model were superior to those of the single models. Yan et al. (2012) proposed an innovative hybrid model comprising the least square support vector machine and chaos optimization, obtaining the optimal parameters for short-term electric load forecasting. For short-term load forecasting, Zhang and Guo (2019) proposed a hybrid method-based support vector regression (SVR) with meteorological factors and electricity price. This model is optimized by an improved adaptive genetic algorithm (IAGA), which is an improved method of the GA (Najafzadeh et al., 2018).

To prevent the optimization algorithm from falling into the local minimum and make it search parameters over a wide range to expand detection probability in the early period, the current study applies an optimization algorithm which is the firefly algorithm improved by a logarithmic spiral (LS-FA). This algorithm can increase the search efficiency in the late period. Hence, it shows good performance to prevent the operation from falling into local optima and to ensure convergence for searching the parameters of the SVR.

Considering the advantages of the LS-FA and SVR, we combined the LS-FA and SVR and then proposed a novel short-term electric load predictive model for the goal of generating accurate electric load predictions. In this model, better model parameters are obtained by the FA improved by a logarithmic spiral. We intend to apply the proposed approach in this study to real electric load forecasting tasks to verify the ability of the proposed model. Therefore, the proposed algorithm is compared to existing approaches which use the SVR improved by FA, LR-FA (Yang, 2010a), WOA (Mirjalili and Lewis, 2016), and DA (Mirjalili, 2016) to demonstrate the optimization performance of the LS-FA. The experimental results prove that the LS-FA-SVR can achieve better forecasting performance, which demonstrates that the LS-FA optimization algorithm can optimize better parameters for the SVR.

The main contributions of this study can be summarized as follows:

1) From the perspective of parameter optimization, we introduced the Lévy-flight firefly algorithm (LF-FA) and the logarithmic spiral firefly algorithm (LS-FA) to enhance the searching ability of exploring the global space and exploiting the local space. Specifically, the LS-FA can obtain a great trade-off between the exploration and exploitation ability of the FA.
2) Since the LS-FA can improve the poor convergence of the LF-FA, we combined the introduced LS-FA and SVR into a novel hybrid model which is denoted as LS-FA-SVR for the tasks of generating accurate electric load tasks. We applied the proposed model to five real electric load time series in Australia, and the experiments proved that the LS-FA can optimize better parameters for the SVR model, and the LS-FA-SVR can generate more accurate electric load predictions.

This study is organized as follows. In **Section 2**, the support vector regression (SVR), firefly algorithm (FA), Lévy-flight firefly algorithm (LF-FA), logarithmic spiral firefly algorithm (LS-FA), and the establishment of the new model are detailed; **Section 3** introduces the dataset of the experiment, the evaluation criteria of the model, the results of the proposed model, and the comparative performance of all the considered models. **Section 4** summarizes the proposed model and makes corresponding conclusions. Moreover, future work is also given in this section.

2 Methodology formulation

2.1 Support vector regression

Support vector regression (SVR), one of the greatest data learning tools, is developed by Boser et al. (1992). Compared with other data mining techniques, SVR obtains minimal upper bound generalization error by the principle of the statistical machine learning process and structural risk minimization (Che et al., 2012). According to the theory proposed by Vapnik, given a training dataset $v = \{(x_i, y_i) | i = 1, 2, \ldots, l; x_i \in R_n; y_i \in R\}$; here, x_t is the n dimensional input vector, y_t represents the target value, and l stands for the number of samples in the training dataset. SVR can be solved by estimating the linear regression as follows:

$$\text{Minimize } \frac{1}{2}\|w\|^2 + C\sum_{i=1}^{l}(\xi_i + \xi_i^*)$$
$$\text{Subject to } \begin{cases} y_i - \langle w, \phi(x_i)\rangle - b \le \varepsilon + \xi_i \\ \langle w, \phi(x_i)\rangle + b - y_i \le \varepsilon + \xi_i^* \\ \xi_i, \xi_i^* \ge 0, (i = 1, 2, \ldots, l), \end{cases} \tag{1}$$

where ω is the weight vector, b is a scale quantity, C represents the regularization constant, and ε is the insensitive loss function. Moreover, the slack variables ξ_i and ξ_i^* represent the upper and lower excess deviation, respectively (**Figure 2**).

Formula 1 can be solved by the Lagrangian multipliers, and the nonlinear regression can be obtained as follows:

$$f(x) = \sum_{i=1}^{l}(\beta_i^* - \beta_i) \cdot k(x_i, x) + b, \tag{2}$$

where β_i and β_i^* are the Lagrangian multipliers.

It must be noticed that $k(x_i, x)$ is called the kernel function which converts a nonlinear problem in input space to a linear problem in feature space. Moreover, the selection of kernel functions is discussed in **Section 3.4**.

2.2 Firefly algorithm

The firefly algorithm is proposed by Yang in 2008, and it is based on the idealized behavior of the flashing characteristics of fireflies (Yang, 2010b). For simplicity in describing the FA, the following three rules are idealized (Yang, 2009):

1) All fireflies are unisex so that one firefly will be attracted to other fireflies regardless of their sex.
2) Attractiveness is proportional to their brightness, so for any two flashing fireflies, the less bright one will move toward the brighter one. The attractiveness is proportional to the brightness, and they both decrease as their distance increases. If there is no brighter one than a particular firefly, it will fly randomly.
3) The brightness of a firefly is affected or determined by the landscape of the objective function to be optimized.

In general, the brightness can simply be proportional to the objective function when dealing with the maximum problem. In contrast, when dealing with the minimum problem, some techniques are employed to convert the minimum problem into a maximization problem. Based on what is mentioned previously, the pseudo-code of the FA is shown in **Figure 3**.

In the FA, there are two issues: the variation of light intensity and the formulation of attractiveness. Generally speaking, the attractiveness of a firefly is determined by its brightness or light intensity which is associated with the objective function. The brightness I of a firefly at location x can be shown as $I(x) \propto f(x)$. But the attractiveness β can be seen in the eyes of the beholder or judged by other fireflies (Kavousi-Fard et al., 2014). Moreover, the light intensity decreases with the distance from its source, and light is absorbed in the media. Hence, attractiveness is allowed to vary with the degree of absorption. Hence, the light intensity $I(r)$ can be obtained on the inverse square law and absorption as

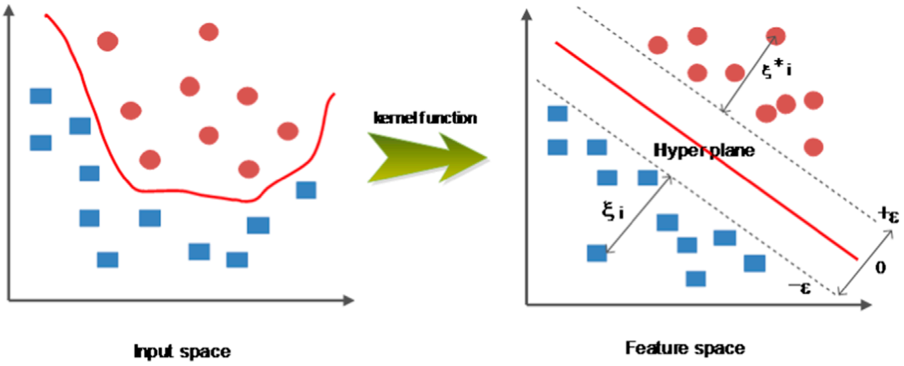

FIGURE 2
Transformation process illustration of the SVR.

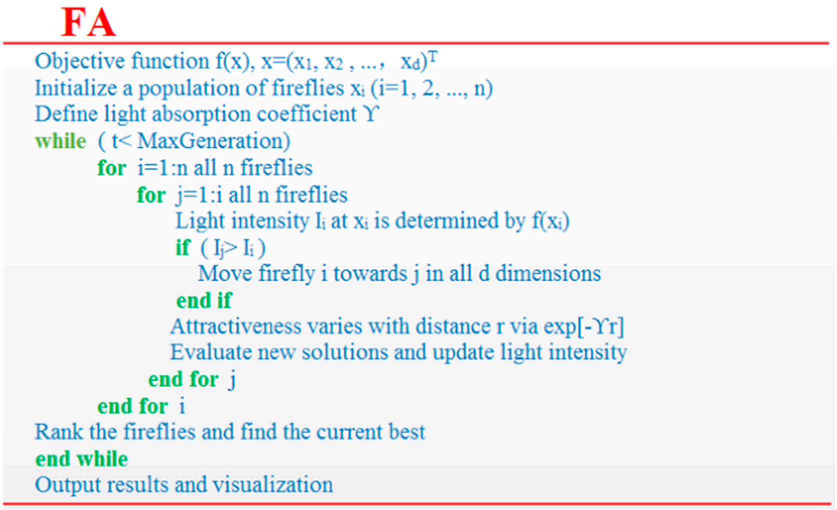

```
FA
Objective function f(x), x=(x1, x2 , ..., xd)^T
Initialize a population of fireflies xi (i=1, 2, ..., n)
Define light absorption coefficient ϒ
while ( t< MaxGeneration)
        for i=1:n all n fireflies
            for j=1:i all n fireflies
                Light intensity Ii at xi is determined by f(xi)
                if ( Ij> Ii )
                    Move firefly i towards j in all d dimensions
                end if
                Attractiveness varies with distance r via exp[-ϒr]
                Evaluate new solutions and update light intensity
            end for j
        end for i
Rank the fireflies and find the current best
end while
Output results and visualization
```

FIGURE 3
Pseudo-code of the FA.

follows:

$$I(r) = I_0 \cdot e^{-\gamma r^2}, \tag{3}$$

where I_0 and γ stand for the original light intensity and light absorption coefficient, respectively. Here, the definition of attractiveness β can be expressed by

$$\beta(r) = \beta_0 \cdot e^{-\gamma r^2}, \tag{4}$$

where β_0 is the attractiveness at $r = 0$.

Then, the Cartesian distance is employed to calculate the distance between any two fireflies i and j at x_i and x_j as follows:

$$r_{ij} = \sqrt{\sum_{p=1}^{d} \left(x_{i,p} - x_{j,p}\right)^2}, \tag{5}$$

where $x_{i,p}$ is the pth component of the spatial coordinate x_i of ith firefly.

Finally, the position of firefly i which is attracted to the brighter firefly j at $t+1$ time can be expressed by

$$x_{i,t+1} = x_{i,t} + \beta_0 \cdot e^{-\gamma r_{ij}^2}\left(x_j - x_i\right) + \alpha\left(rand - 0.5\right), \tag{6}$$

where $rand$ is a random number in [0,1], and α is the parameter in [0,1].

2.3 Lévy-flight firefly algorithm

The Lévy-flight firefly algorithm (LF-FA) is proposed by Yang (2010a) to enhance the ability of exploring the global space and exploiting the local space. Specifically, this algorithm can obtain a great trade-off between the exploration and exploitation ability of the FA. Hence, the LF-FA is utilized to update the position next time as follows (Yang and Deb, 2009; Kaveh and Khayatazad, 2012):

$$x_{i,t+1} = x_{i,t} + \beta_0 \cdot e^{-\gamma r_{ij}^2}\left(x_j - x_i\right) + \alpha \cdot sign\left[rand - 0.5\right] \oplus Levy, \tag{7}$$

where α is the randomization parameter, and $\oplus$ is the dot product. $rand$ is a random number in [0,1], and $sign[rand - 0.5]$ provides a random direction while the random step length is drawn from the Lévy flights. It is required to explain **formula 7** combining α and $sign[rand - 0.5] \oplus Levy$ which can make a firefly walk more randomly (Mirjalili et al., 2014). In other words, the LF-FA can jump out of the local optimum and enhance the global search capability of the FA.

The LF is one of the random walks, and its steps are decided by the step length. Furthermore, jumps conforming to the Lévy distribution can be shown as follows (Walster et al., 1985):

$$Levy(\eta) \sim \mu = t^{-1-\eta}\,(0 \le \eta \le 2), \tag{8}$$

and the Lévy random number is calculated by

$$Levy(\eta) \sim \frac{\phi \times \mu}{|\upsilon|^{1/\eta}}, \tag{9}$$

where υ and μ conform to the standard normal distributions. ϕ can be calculated as follows:

$$\phi = \left[\frac{\Gamma(1+\eta) \times \sin(\pi \times \eta/2)}{\Gamma((1+\eta)/2) \times \eta \times 2^{(\eta-1)/2}}\right]^{1/\eta}, \tag{10}$$

where Γ stands for the standard gamma function and $\eta = 1.5$.

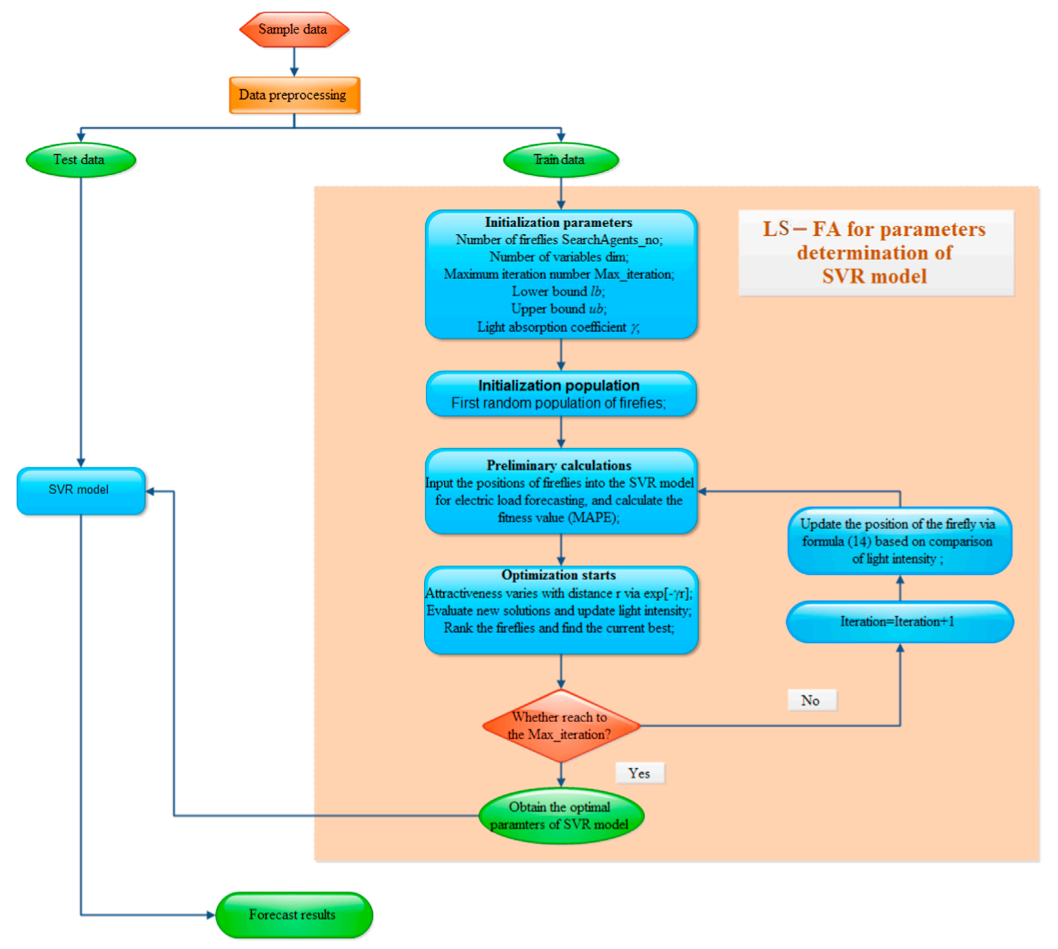

FIGURE 4
Flow of the LS-FA-SVR model for electric load forecasting.

2.4 Logarithmic spiral firefly algorithm

In the section, because of the poor convergence of the LF-FA, the logarithmic spiral is introduced in this study to balance the abilities of exploration and exploitation (Mirjalili and Lewis, 2016). The logarithmic spiral is selected to improve the performance of the FA. Considering **formula 6**, we propose a modified formula as follows:

$$x_{i,t+1} = x_{i,t} + \beta_0 \cdot e^{-\gamma r_{ij}^2}\left(x_j - x_i\right)\cos\left(2\pi t\right) + \alpha\left(rand - 0.5\right), \quad (11)$$

in which t is a random number from-1 to 1.

In **Section 3.1**, some experiments would be carried out to assess the performance of the LS-FA by comparing it with some optimizers based on the FA.

2.5 Hybrid model LS-FA-SVR

In this section, the proposed hybrid model LS-FA-SVR will be introduced in detail, and the flow of this proposed model is shown in **Figure 4**.

1) Input train data set;
2) initialization parameters;
3) initialization population;
4) preliminary calculations;
5) optimization starts;
6) update the position and calculate the fitness;
7) optimization stops;
8) SVR model obtained; and
9) output result of the test dataset.

Above all, the innovative hybrid model LS-FA-SVR can be obtained.

3 Empirical study

3.1 Performance of the LS-FA

This section aims to test the performance of the optimization by the proposed modified algorithm LS-FA through some classical unimodal benchmark functions. The structure of the four benchmarks considered in this experiment is as follows (Mirjalili and Lewis, 2016):

$$F1: f_1 = \sum_{i=1}^{l} x_i^2, \tag{12}$$

$$F2: f_2 = \max\left\{|x_i|, 1 \le i \le l\right\}, \tag{13}$$

$$F3: f_3 = \sum_{i=1}^{l} |x_i| + \prod_{i=1}^{l} |x_i|, \tag{14}$$

$$F4: f_4 = \sum_{i=1}^{l} i \cdot x_i^4 + random\,[0,1), \tag{15}$$

where the value of the dimension in this experiment is 20. To compare the LS-FA with the FA and LF-FA, all the numbers of fireflies are set at the same value (10), and the values of alpha and gamma are 0.25 and 1, respectively.

To perform the result of the proposed method LS-FA, minimum (Min), maximum (Max), and standard deviation (Std) are selected to measure the errors of the optimizer. After implementing the FA, LF-FA, and LS-FA using Matlab 2014(b), every algorithm has been run 30 times to get the average error for each method. Table 1 shows the results with the optimization.

Multiple studies have shown that the modified algorithm LS-FA has the best predictive results among the other two algorithms (FA and LF-FA) by searching the minimum of four benchmark functions. To be specific, the maximum of the LS-FA is smaller than that of the FA and LF-FA. The minimum of the LS-FA is relatively small among all the three methods. Moreover, the LS-FA has the smallest standard deviation, and it means the performance has the best stabilization. In addition, Figure 5 presents the trace of optimization by calculating the mean of errors for the four benchmark functions. The LS-FA has outstanding performance for searching the minimum of the

TABLE 1 Performance of FA, LF-FA, and LS-FA.

Criterion	**F1**			**F2**			**F3**			**F4**		
	FA	**LF-FA**	**LS-FA**	**FA**	**LF-FA**	**LS-FA**	**FA**	**LF-FA**	**LS-FA**	**FA**	**LF-FA**	**LS-FA**
Max[a]	5.34	6.65	4.87	1.24	1.26	1.10	8.82	8.52	8.05	59.87	41.35	35.41
Min[b]	1.50	2.16	1.68	0.80	0.70	0.68	4.58	4.66	3.69	4.73	5.90	3.49
Std[c]	1.10	1.17	0.72	0.12	0.16	0.10	1.32	0.99	0.81	13.91	9.75	8.40

[a] Min is the minimum.

[b] Max is the maximum.

[c] Std is the standard deviation.

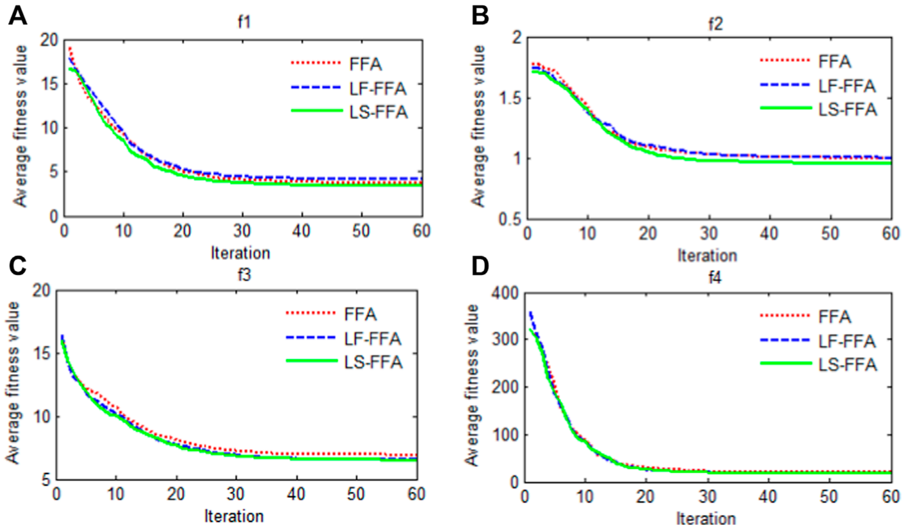

FIGURE 5
Trace of fitness for FA, LF-FA, and LS-FA.

four functions. Specifically, the speed of the LS-FA is faster than that of the FA and LF-FA. Moreover, the average error for all four models by the LS-FA is significantly smaller than that by other algorithms. In short, through these studies, it can be proved that the proposed algorithm LS-FA has a better performance of optimization. In other words, the logarithmic spiral can improve the performance of the FA by boosting the ability to balance exploration and exploitation. Hence, this modified optimizer is chosen to search for suitable parameters of SVR in the study.

3.2 Data description

To verify the effectiveness of the proposed model, the datasets of electric load from 1 January 2018 to 1 February 2018 in NSW, QLD, SA, TAS, and VIC are used as the experimental data (Table 2 and Figure 6). The datasets of the electric load (MW) are retrieved from the website of energy security for all Australians (http://www.aemo.com.au/). The sample data used in this study are half-hourly electric load, and the total number of these five regions is 1,488. In this study, each dataset was divided into two sets: the training dataset including 960 data points (from 2018/1/1 0:30 to 2018/1/21 0:00) and the remaining as the test dataset (from 2018/1/21 0:30 to 2018/2/1 0:00).

3.3 Evaluation criteria

Because there is no confirmed universal standard method, this study adapts multiple error criteria to evaluate the effectiveness of the proposed hybrid model: the mean absolute error (MAE), root mean square error (RMSE), and mean absolute percent error (MAPE). The MAE, RMSE, and MAPE are applied to quantify the forecast error, and the performance of the model is reliable when their value is close to zero.

These three criteria are calculated as follows:

$$\mathrm{MAE} = \frac{1}{N}\sum_{i=1}^{N}|y_i - \hat{y}_i|, \tag{16}$$

$$\mathrm{RMSE} = \sqrt{\frac{1}{N}\sum_{i=1}^{N}(y_i - \hat{y}_i)^2}, \tag{17}$$

$$\mathrm{MAPE} = \frac{1}{N}\sum_{i=1}^{N}|\frac{\hat{y}_i - y_i}{y_i}| \times 100\%, \tag{18}$$

where y_i is the observed value, $\hat{y}_i$ is the predicted value to y_i, and N is the number of samples.

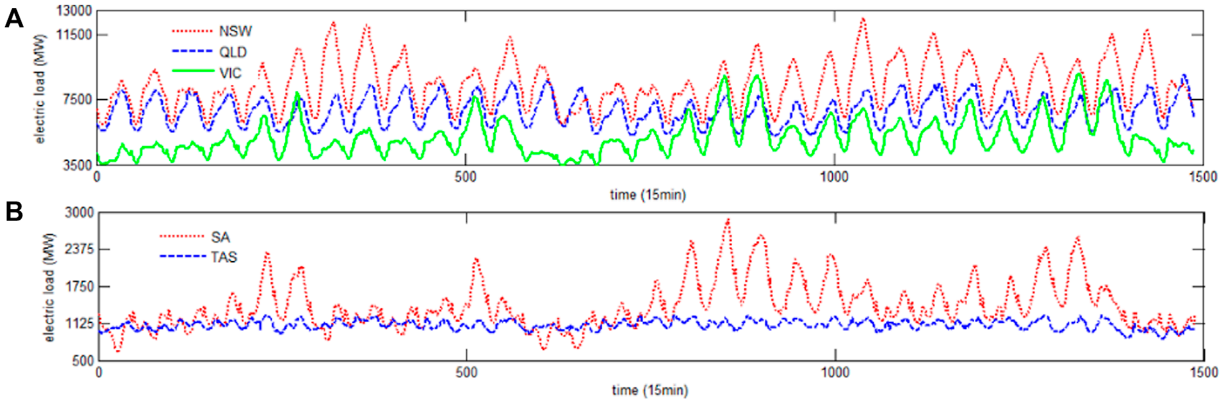

FIGURE 6
Datasets of all five regions.

TABLE 2 Statistical properties for each dataset.

Region	Training set					Test set				
	NSW	QLD	SA	TAS	VIC	NSW	QLD	SA	TAS	VIC
N	960	960	960	960	960	528	528	528	528	528
Mean	8115.3	6720.3	1375.8	1102.9	4987.3	8818.6	6937.8	1503.0	1085.7	5578.9
Std	1350.0	873.1	417.8	70.3	1095.6	1493.2	905.8	357.5	86.3	1156.5
Min	5910.1	5258.4	653.2	950.8	3449.8	6197.6	5359.5	894.2	865.2	3683.1
Max	12230.6	8670.0	2879.9	1263.8	8999.2	12494.6	9020.4	2609.9	1256.5	9085.2

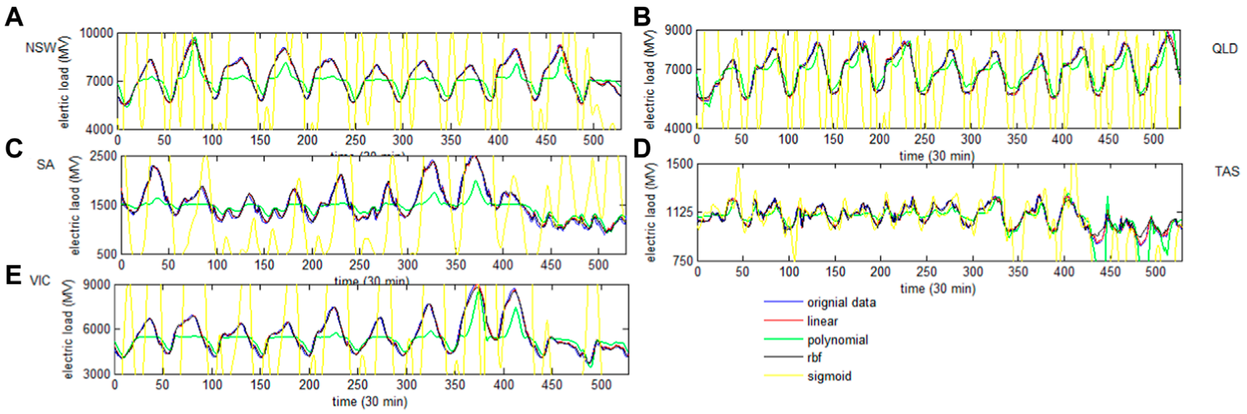

FIGURE 7
Predictive results of the SVR with different kernel functions.

TABLE 3 Performance of the SVR with different kernel functions based on MAPE, MAE, and RMSE.

Criterion	Linear			Polynomial			rbf			Sigmoid		
	MAPE	MAE	RMSE	MAPE	MAE	RMSE	MAPE	MAE	RMSE	MAPE	MAE	RMSE
NSW	1.13	99.08	123.22	8.58	786.68	964.58	1.38	122.32	155.59	61.88	5462.42	6533.04
QLD	1.04	73.10	91.57	4.41	312.24	401.27	1.27	88.97	113.14	38.79	2638.53	3916.17
SA	3.38	48.78	59.70	11.00	182.03	256.63	3.75	54.11	64.30	62.73	941.26	1154.82
TAS	1.38	14.85	20.99	5.04	51.30	99.96	1.70	17.78	25.19	24.34	242.74	612.28
VIC	2.07	112.63	137.15	9.28	565.44	763.20	2.28	124.07	151.53	91.87	5327.46	7083.36

3.4 Selection of the kernel function

In this section, the selection of the kernel function in the SVR for electric load forecasting is discussed, and the data of five regions in Australia are applied to search for the fittest choice of the kernel function. First, four main kernel functions are provided when the model is established by SVR, and they are shown as follows:

$$\begin{aligned} &Linear: K(x,x_i) = x^T x_i,\\ &Polynomial: K(x,x_i) = \left(\gamma x^T x_i + r\right)^p, \quad \gamma > 0\\ &Rbf: K(x,x_i) = \exp\left(-\gamma \|x - x_i\|^2\right), \quad \gamma > 0\\ &Sigmoid: K(x,x_i) = \tanh\left(\gamma x^T x_i + r\right). \end{aligned} \tag{19}$$

Second, in order to find the best kernel function for forecasting electric load, we selected the last twelve half-hour load data $(x_{n-12}, x_{n-11}, x_{n-10}, \ldots, x_{n-2}, x_{n-1})$ as the input variables of SVR with different kernel functions, and the output variable is x_n. At last, the best kernel function can be selected from the four kernel functions based on the performance of prediction. The experiment is performed, and the results of forecasting electric load based on different kernel functions are shown in Figure 7. It is obvious that the sigmoid kernel function has the worst performance, and the accuracy of the polynomial is just higher than it. In addition, the SVR based on the rbf kernel function and linear kernel function has better predictive results since it approaches the original data.

In order to show the performances clearly, the three criteria (MAPE, MAE, and RMSE) of errors are calculated, and the results are shown in Table 3. The MAPE, MAE, and RMSE of the liner kernel function have the smallest values in all five regions. It must be noted that the rbf kernel function is just slightly poorer than the linear one. Moreover, it can be found that the polynomial and sigmoid functions are not suitable for electric load forecasting with larger errors. Based on this research, the linear is chosen as the kernel function of SVR in the study.

3.5 Process of LS-FA-SVR

In Section 2.5, the hybrid model LS-FA-SVR is established for short-term load forecasting. Here, the bandwidth of liner

TABLE 4 Performance of the LS-FA-SVR in NSW, QLD, SA, TAS, and VIC.

Run No.	NSW			QLD			SA			TAS			VIC		
	MAPE	MAE	RMSE	MAPE	MAE	RMSE	MAPE	MAE	RMSE	MAPE	MAE	RMSE	MAPE	MAE	RMSE
1	0.866	91.237	112.178	0.819	59.613	75.405	2.777	42.653	51.459	1.116	11.390	10.356	1.363	89.422	109.661
2	0.933	91.397	112.035	0.753	59.866	75.402	2.689	42.857	51.378	1.131	11.338	10.424	1.346	89.354	109.649
3	1.048	91.211	112.124	0.582	59.756	75.571	2.832	42.701	51.371	1.138	11.487	10.402	1.438	89.289	109.463
4	0.892	91.307	112.078	0.673	59.861	75.288	2.718	42.624	51.360	1.043	11.440	10.318	1.243	89.362	109.710
5	0.804	91.467	112.038	0.793	59.838	75.523	2.716	42.704	51.385	1.048	11.424	10.430	1.281	89.365	109.837
6	0.951	91.380	112.071	0.699	59.726	75.462	2.693	42.554	51.402	1.061	11.424	10.408	1.367	89.426	109.517
7	0.830	91.363	112.133	0.666	59.853	75.420	2.767	42.724	51.458	1.218	11.381	10.263	1.390	89.280	109.722
8	0.905	91.442	112.044	0.652	59.831	75.308	2.811	42.737	51.387	1.069	11.567	10.371	1.294	89.279	109.558
9	0.905	91.460	112.077	0.686	59.718	75.474	2.652	42.752	51.291	1.086	11.256	10.444	1.364	89.299	109.648
10	0.965	91.416	112.118	0.824	59.745	75.365	2.754	42.686	51.469	1.092	11.335	10.389	1.404	89.321	109.570
11	1.031	91.331	112.079	0.682	59.636	75.429	2.732	42.728	51.281	1.202	11.441	10.276	1.394	89.307	109.647
12	0.970	91.253	111.879	0.784	59.727	75.369	2.791	42.647	51.452	1.108	11.323	10.468	1.347	89.454	109.552
13	0.880	91.348	112.161	0.807	59.755	75.398	2.809	42.859	51.469	1.103	11.356	10.441	1.270	89.373	109.685
14	1.026	91.370	112.218	0.889	59.602	75.275	2.683	42.542	51.369	1.069	11.422	10.424	1.254	89.289	109.686
15	0.921	91.213	112.109	0.757	59.721	75.470	2.775	42.685	51.394	1.133	11.367	10.317	1.297	89.364	109.664
16	0.950	91.286	112.156	0.732	59.819	75.410	2.756	42.695	51.324	1.022	11.325	10.544	1.293	89.429	109.651
17	1.101	91.397	112.010	0.715	59.825	75.440	2.938	42.698	51.274	1.132	11.329	10.405	1.395	89.379	109.647
18	0.936	91.311	112.100	0.517	59.785	75.496	2.653	42.580	51.448	0.975	11.268	10.464	1.257	89.454	109.520
19	0.903	91.342	112.152	0.778	59.769	75.399	2.711	42.740	51.367	1.130	11.489	10.221	1.453	89.303	109.728
20	1.076	91.205	112.122	1.018	59.737	75.456	2.783	42.803	51.485	1.020	11.367	10.428	1.304	89.557	109.658
21	0.987	91.256	112.003	0.805	59.738	75.469	2.690	42.774	51.253	1.221	11.470	10.410	1.216	89.322	109.643
22	1.049	91.240	112.212	0.962	59.714	75.455	2.704	42.565	51.516	1.152	11.361	10.410	1.291	89.237	109.392
23	0.948	91.286	112.062	0.673	59.609	75.375	2.770	42.617	51.434	1.074	11.394	10.287	1.248	89.387	109.560
24	0.965	91.481	112.172	0.824	59.943	75.511	2.789	42.858	51.326	1.041	11.563	10.437	1.306	89.391	109.602
25	0.929	91.292	112.064	0.666	59.749	75.371	2.872	42.721	51.480	1.085	11.395	10.502	1.426	89.357	109.758
26	0.990	91.352	112.283	0.864	59.827	75.449	2.714	42.693	51.544	0.934	11.351	10.386	1.321	89.211	109.665
27	1.010	91.248	112.087	0.644	59.884	75.447	2.737	42.628	51.406	1.231	11.424	10.429	1.213	89.367	109.685
28	0.841	91.413	112.305	0.616	59.589	75.411	2.818	42.695	51.385	1.097	11.317	10.269	1.436	89.377	109.528
29	1.038	91.219	112.098	0.800	59.687	75.389	2.759	42.858	51.435	1.064	11.384	10.379	1.414	89.331	109.560
30	0.971	91.315	112.171	0.818	59.841	75.469	2.808	42.854	51.305	1.068	11.266	10.475	1.311	89.330	109.485
MEAN	0.954	91.328	112.111	0.750	59.759	75.423	2.757	42.708	51.397	1.095	11.389	10.393	1.330	89.354	109.622

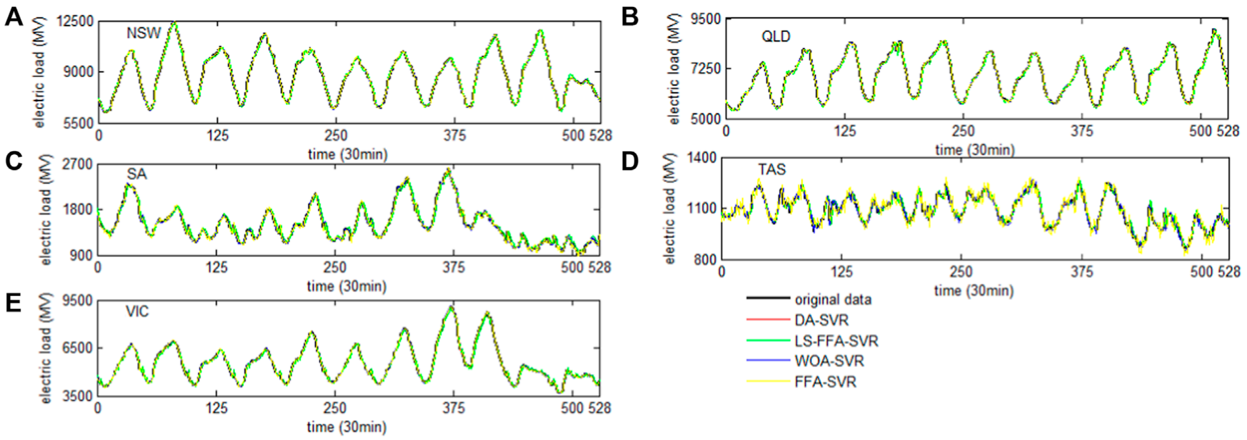

FIGURE 8
Results of the SVR with different optimizers.

TABLE 5 Performance of the LS-FA-SVR based on MAE, MAPE, and RMSE compared to other models.

Region	DA-SVR			WOA-SVR			LS-FA-SVR			FA-SVR		
	MAPE	MAE	RMSE	MAPE	MAE	RMSE	MAPE	MAE	RMSE	MAPE	MAE	RMSE
NSW	1.089	95.816	119.326	1.089	95.786	119.294	0.954	91.328	112.111	1.11	96.88	119.92
QLD	0.920	63.994	80.608	0.921	64.020	80.597	0.750	59.759	75.423	0.92	64.15	80.72
SA	3.379	48.791	59.686	3.376	48.763	59.656	2.757	42.708	51.397	3.41	49.12	60.13
TAS	1.376	20.961	14.797	1.376	14.796	20.964	1.095	11.389	10.393	1.38	13.93	14.49
VIC	1.702	116.478	94.186	1.701	94.169	116.498	1.330	89.354	109.622	1.70	94.26	116.60

To verify the proposed model LS-FA-SVR, we conducted a forecasting experiment with the same electric load in NSW, QLD, SA; TAS and VIC. The comparisons of electric load values forecast using WOA-SVR, DA-SVR; FA-SVR, and the new proposed LS-FA-SVR are shown in Table 5 (Mirjalili and Lewis,2016; Mirjalili, 2016). It is clear that the new model LS-FA-SVR has the lowest MAE, MAPE, and RMSE, among all four models.

kernel and the regularization parameter of SVR can be optimized by the LS-FA. In this study, the numbers of fireflies, absorption coefficient, and iteration of LS-FA are 15, 1, and 20, respectively. Based on these, the prediction of short-term load in NSW, QLD, VIC, SA and TAS can be obtained.

3.6 Empirical analysis

To avoid some accidental situations which would cause unreliable conclusions, we conducted 30 runs for experiments in five regions, and three error indicators are recorded in Table 4 in each run.

Comparing the LS-FA-SVR with FA-SVR, the difference between them is whether the logarithmic spiral has been improved. It can be found that after introducing the logarithmic spiral into the model, the MAE, MAPE, and RMSE in five regions all decrease, which indicates that the LS is necessary for forecasting the electric load. Moreover, this study compared LS-FA-SVR with two new optimizers which were developed in 2016. The two benchmark models are DA-SVR and WOA-SVR. Through the comparisons, the three error indicators have decreased significantly. For example, the RMSE of THE LS-FA-SVR in NSW is 112.111, yet the values of DA-SVR and WOA-SVR are 119.326 and 119.294, respectively. The smaller the values of MAE, MAPE, and RMSE, the better the model will be. According to the aforementioned results, it is clear that the proposed model LS-FA-SVR outperforms the three benchmark models for five regions, and they are shown in Figure 8.

We applied the LS-FA-SVR model to the forecasting experiments for the five experimental datasets and stated the results in Table 5. As the last row of this table shows, the mean values of MAE, MAPE, and RMSE in NSW are 91.328, 0.954, and 112.111, respectively. Meanwhile, the mean values of MAE, MAPE, and RMSE in QLD are 59.759, 0.750, and 75.423, respectively. Moreover, Figure 8 clearly shows that the model LS-FA-SVR interprets the curves of the original electric load in NSW, QLD, SA, SAT, and VIC, which indicates that the new model gets a satisfactory performance and a high forecasting accuracy. Comprehensively considering the results of MAE, MAPE, and RMSE in NSW, QLD, SA, TAS, and VIC, it can be concluded that the LS-FA-SVR model is the best overall, and its prediction is the best.

4 Conclusion and future work

Accurate forecasting of the electric load can provide valuable references for economic managers and electric power system operators. The study proposed a hybrid model LS-FA-SVR for improving the forecasting accuracy, where the parameters of SVR are optimally determined by the optimization algorithm LS-FA. This hybrid approach can search over a wide range to expand the detection probability in the early period. It can increase the search efficiency in the late period. Hence, the LS-FA has a good performance to prevent the operation from falling into local optima and to ensure the convergence for searching the parameters of SVR. In addition, the empirical results show that the MAE, MAPE, and RMSE values of LS-FA-SVR are all modestly smaller than those of WOA-SVR, DA-SVR, and FA-SVR. Compared with these other methods, the new method has a strong ability to find the optimal solution, and the run time is shorter. In other words, LS-FA-SVR is an attractive and effective model which combines a novel optimization algorithm to determine the parameters of SVR. In future work, several research directions can be tried. More related variables can be taken into consideration. One possibility is to apply other factors which may influence electrical demand, such as the population and GDP, to obtain more comprehensive results (Li et al., 2017).

Data availability statement

The original contributions presented in the study are included in the article/Supplementary Material; further inquiries can be directed to the corresponding author.

Author contributions

WZ: formal analysis and writing—original draft; LG: writing—review *and* editing; YS: writing—review *and* editing; XL: writing—review *and* editing; and HZ: supervision, investigation, and project administration.

Conflict of interest

WZ and LG were employed by Nari Technology Co., Ltd, and YS was employed by State Grid Xiong'an Integrated Energy Service Co, Ltd. The remaining authors declare that the research was conducted in the absence of any commercial or financial relationships that could be construed as a potential conflict of interest.

Publisher's note

References

Afrasiabi, M., Mohammadi, M., Rastegar, M., Stankovic, L., Afrasiabi, S., Khazaei, M., et al. (2020). Deep-based conditional probability density function forecasting of residential loads. *IEEE Trans. Smart Grid* 11, 3646–3657. doi:10.1109/tsg.2020.2972513

An, N., Zhao, W., Wang, J., Shang, D., and Zhao, E. (2013). Using multi-output feedforward neural network with empirical mode decomposition based signal filtering for electricity demand forecasting. *Energy* 49, 279–288. doi:10.1016/j.energy.2012.10.035

Boser, B. E., Guyon, I. M., and Vapnik, V. N. (1992). A training algorithm for optimal margin classifiers. *Proc. fifth Annu. workshop Comput. Learn. theory*, 144–152.

Che, J., Wang, J., and Tang, Y. (2012). Optimal training subset in a support vector regression electric load forecasting model. *Appl. Soft Comput.* 12, 1523–1531. doi:10.1016/j.asoc.2011.12.017

Chen, B., and Wang, Y. (2021). Short-term electric load forecasting of integrated energy system considering nonlinear synergy between different loads. *IEEE Access* 9, 43562–43573. doi:10.1109/access.2021.3066915

Chen, Y., Xu, P., Chu, Y., Li, W., Wu, Y., Ni, L., et al. (2017). Short-term electrical load forecasting using the support vector regression (svr) model to calculate the demand response baseline for office buildings. *Appl. Energy* 195, 659–670. doi:10.1016/j.apenergy.2017.03.034

Cui, Z., Wu, J., Ding, Z., Duan, Q., Lian, W., Yang, Y., et al. (2021). A hybrid rolling grey framework for short time series modelling. *Neural comput. Appl.*, 33, 11339–11353. doi:10.1007/s00521-020-05658-0

Feng, C., Sun, M., and Zhang, J. (2019). Reinforced deterministic and probabilistic load forecasting via *q*-learning dynamic model selection. *IEEE Trans. Smart Grid* 11, 1377–1386. doi:10.1109/tsg.2019.2937338

Hong, W.-C. (2011). Electric load forecasting by seasonal recurrent svr (support vector regression) with chaotic artificial bee colony algorithm. *Energy* 36, 5568–5578. doi:10.1016/j.energy.2011.07.015

Kaur, A., Nonnenmacher, L., and Coimbra, C. F. (2016). Net load forecasting for high renewable energy penetration grids. *Energy* 114, 1073–1084. doi:10.1016/j.energy.2016.08.067

Kaveh, A., and Khayatazad, M. (2012). A new meta-heuristic method: Ray optimization. *Comput. Struct.* 112, 283–294. doi:10.1016/j.compstruc.2012.09.003

Kavousi-Fard, A., Samet, H., and Marzbani, F. (2014). A new hybrid modified firefly algorithm and support vector regression model for accurate short term load forecasting. *Expert Syst. Appl.* 41, 6047–6056. doi:10.1016/j.eswa.2014.03.053

Kisi, O., Shiri, J., Karimi, S., Shamshirband, S., Motamedi, S., Petković, D., et al. (2015). A survey of water level fluctuation predicting in urmia lake using support vector machine with firefly algorithm. *Appl. Math. Comput.* 270, 731–743. doi:10.1016/j.amc.2015.08.085

Kong, W., Dong, Z. Y., Hill, D. J., Luo, F., and Xu, Y. (2017). Short-term residential load forecasting based on resident behaviour learning. *IEEE Trans. Power Syst.* 33, 1087–1088. doi:10.1109/tpwrs.2017.2688178

Li, W., Kong, D., and Wu, J. (2017). A new hybrid model fpa-svm considering cointegration for particular matter concentration forecasting: A case study of kunming and yuxi, China. *Comput. Intell. Neurosci.* 2017, 2843651. doi:10.1155/2017/2843651

Mirjalili, S. (2016). Dragonfly algorithm: A new meta-heuristic optimization technique for solving single-objective, discrete, and multi-objective problems. *Neural comput. Appl.* 27, 1053–1073. doi:10.1007/s00521-015-1920-1

Mirjalili, S., and Lewis, A. (2016). The whale optimization algorithm. *Adv. Eng. Softw.* 95, 51–67. doi:10.1016/j.advengsoft.2016.01.008

Mirjalili, S., Mirjalili, S. M., and Lewis, A. (2014). Grey wolf optimizer. *Adv. Eng. Softw.* 69, 46–61. doi:10.1016/j.advengsoft.2013.12.007

Najafzadeh, M., Etemad-Shahidi, A., and Lim, S. Y. (2016). Scour prediction in long contractions using anfis and svm. *Ocean. Eng.* 111, 128–135. doi:10.1016/j.oceaneng.2015.10.053

Najafzadeh, M., Saberi-Movahed, F., and Sarkamaryan, S. (2018). Nf-gmdh-based self-organized systems to predict bridge pier scour depth under debris flow effects. *Mar. Georesources Geotechnol.* 36, 589–602. doi:10.1080/1064119x.2017.1355944

Olorunda, O., and Engelbrecht, A. P. (2008). "Measuring exploration/exploitation in particle swarms using swarm diversity," in 2008 IEEE congress on evolutionary computation (IEEE world congress on computational intelligence), Hong Kong, China, 01-06 June 2008 (IEEE), 1128–1134.

Peng, L.-L., Fan, G.-F., Huang, M.-L., and Hong, W.-C. (2016). Hybridizing demd and quantum pso with svr in electric load forecasting. *Energies* 9, 221. doi:10.3390/en9030221

Stojanović, M., Božić, M., Stajić, Z., and Milošević, M. (2013). Ls-svm model for electrical load prediction based on incremental training set update. *Przeglad Elektrotechniczny* 89, 194–198.

Vapnik, V. (1999). *The nature of statistical learning theory*. Berlin/Heidelberg, Germany: Springer science & business media.

Walster, G., Hansen, E., and Sengupta, S. (1985). Test results for a global optimization algorithm. *Numer. Optim.* 1984, 272–287.

Wang, C., Hou, Y., Gao, Q., Hou, R., and Deng, T. (2016). Electric load simulator system control based on adaptive particle swarm optimization wavelet neural network with double sliding modes. *Adv. Mech. Eng.* 8, 168781401666426. doi:10.1177/1687814016664261

Wang, D., Liu, L., Jia, H., Wang, W., Zhi, Y., Meng, Z., et al. (2018). Review of key problems related to integrated energy distribution systems. *CSEE J. Power Energy Syst.* 4, 130–145. doi:10.17775/cseejpes.2018.00570

Wu, J., Wang, Y.-G., Tian, Y.-C., Burrage, K., and Cao, T. (2021). Support vector regression with asymmetric loss for optimal electric load forecasting. *Energy* 223, 119969. doi:10.1016/j.energy.2021.119969

Xiao, L., Shao, W., Yu, M., Ma, J., and Jin, C. (2017). Research and application of a combined model based on multi-objective optimization for electrical load forecasting. *Energy* 119, 1057–1074. doi:10.1016/j.energy.2016.11.035

Yan, G., Tang, G.-h., and Xiong, J.-m. (2012). "Electric load forecasting based on improved ls-svm algorithm," in Proceedings of the 10th World Congress on Intelligent Control and Automation, Beijing, China, 06-08 July 2012 (IEEE), 3064–3067.

Yang, X.-S., and Deb, S. (2009). "Cuckoo search via lévy flights," in 2009 World congress on nature & biologically inspired computing (NaBIC), Coimbatore, India, 09-11 December 2009 (IEEE), 210–214.

Yang, X.-S. (2010a). "Firefly algorithm, levy flights and global optimization," in *Research and development in intelligent systems XXVI* (New York, United States: Springer), 209–218.

Yang, X.-S. (2010b). Firefly algorithm, stochastic test functions and design optimisation. *Int. J. Bio-inspired Comput.* 2, 78. doi:10.1504/ijbic.2010.032124

Yang, X.-S. (2009). "Firefly algorithms for multimodal optimization," in *International symposium on stochastic algorithms* (New York, United States: Springer), 169–178.

Yang, Y., Liu, Q., Yue, D., and Han, Q.-L. (2021a). Predictor-based neural dynamic surface control for bipartite tracking of a class of nonlinear multiagent systems. *IEEE Trans. Neural Netw. Learn. Syst.* 33, 1791–1802. doi:10.1109/tnnls.2020.3045026

Yang, Y., Tao, Z., Qian, C., Gao, Y., Zhou, H., Ding, Z., et al. (2021b). A hybrid robust system considering outliers for electric load series forecasting. *Appl. Intell. (Dordr).* 1–23, 1630–1652. doi:10.1007/s10489-021-02473-5

Yang, Y., Wang, Z., Gao, Y., Wu, J., Zhao, S., Ding, Z., et al. (2022a). An effective dimensionality reduction approach for short-term load forecasting. *Electr. Power Syst. Res.* 210, 108150. doi:10.1016/j.epsr.2022.108150

Yang, Y., Zhou, H., Gao, Y., Wu, J., Wang, Y.-G., Fu, L., et al. (2022b). Robust penalized extreme learning machine regression with applications in wind speed forecasting. *Neural comput. Appl.* 34, 391–407. doi:10.1007/s00521-021-06370-3

Yang, Y., Zhou, H., Wu, J., Ding, Z., and Wang, Y.-G. (2022c). Robustified extreme learning machine regression with applications in outlier-blended wind-speed forecasting. *Appl. Soft Comput.* 122, 108814. doi:10.1016/j.asoc.2022.108814

Yang, Y., Zhou, H., Wu, J., Liu, C.-J., and Wang, Y.-G. (2022d). A novel decompose-cluster-feedback algorithm for load forecasting with hierarchical structure. *Int. J. Electr. Power & Energy Syst.* 142, 108249. doi:10.1016/j.ijepes.2022.108249

Zhang, G., and Guo, J. (2019). A novel method for hourly electricity demand forecasting. *IEEE Trans. Power Syst.* 35, 1351–1363. doi:10.1109/tpwrs.2019.2941277

Zhang, S., Wu, J., Jia, Y., Wang, Y.-G., Zhang, Y., Duan, Q., et al. (2021). A temporal lasso regression model for the emergency forecasting of the suspended sediment concentrations in coastal oceans: Accuracy and interpretability. *Eng. Appl. Artif. Intell.* 100, 104206. doi:10.1016/j.engappai.2021.104206

Zhang, S., Wu, J., Wang, Y.-G., Jeng, D.-S., and Li, G. (2022a). A physics-informed statistical learning framework for forecasting local suspended sediment concentrations in marine environment. *Water Res.* 218, 118518. doi:10.1016/j.watres.2022.118518

Zhang, Y., Wu, J., Zhang, S., Li, G., Jeng, D.-S., Xu, J., et al. (2022b). An optimal statistical regression model for predicting wave-induced equilibrium scour depth in sandy and silty seabeds beneath pipelines. *Ocean. Eng.* 258, 111709. doi:10.1016/j.oceaneng.2022.111709

frontiers | Frontiers in Energy Research

TYPE Original Research
PUBLISHED 26 September 2022
DOI 10.3389/fenrg.2022.953039

Check for updates

OPEN ACCESS

EDITED BY
Qiuye Sun,
Northeastern University, China

REVIEWED BY
Sanbo Ding,
Hebei University of Technology, China
Lei Liu,
Liaoning University of Technology, China

*CORRESPONDENCE
Hui Tian,
tianhui@cqupt.edu.cn
Ping Zhu,
100794@cqmu.edu.cn

SPECIALTY SECTION
This article was submitted to Smart Grids, a section of the journal Frontiers in Energy Research

RECEIVED 25 May 2022
ACCEPTED 05 August 2022
PUBLISHED 26 September 2022

CITATION
Zheng Z, Tian H, Zhu P, Chi Y, Liu Y and Jia X (2022), Research on strategy of green electricity acquisition transaction of park-level energy internet by using STP. *Front. Energy Res.* 10:953039.
doi: 10.3389/fenrg.2022.953039

Research on strategy of green electricity acquisition transaction of park-level energy internet by using STP

Zhe Zheng[1], Hui Tian[2]*, Ping Zhu[3]*, Yingying Chi[1], Yong Liu[1] and Xiaoguang Jia[1]

[1]Beijing Smartchip Microelectronics Technology Company Limited, Beijing, China, [2]Key Laboratory of Industrial Internet of Things & Networked Control, Ministry of Education, Chongqing University of Posts and Telecommunications, Chongqing, China, [3]Chongqing Medical University Center for Faculty Development, Chongqing Medical University, Chongqing, China

In order to save resources and reduce air pollution, human beings have begun to pay attention to the production and use of photovoltaic, wind power and other green power. Due to the difficulty of direct transaction between green power producers and power users, a park-level energy Internet has been proposed and used to connect all kinds of green electricity with power users. Then park users can effectively buy and use green electricity. Taking the park-level energy Internet as the scenario, this paper constructs a transaction model between green power operators and green power producers. The model is a dynamic game of complete and perfect information. The dynamic characteristics of this game model are analyzed by using semi-tensor product method, and corresponding strategies are provided for all players. From the results obtained, it is easy to find that in many cases, the strategy profile of all participants are constantly changing to obtain more profits, rather than stable at some traditional Nash equilibrium.

KEYWORDS

park-level energy internet, green electricity, green power operator, green power producer, game, semi-tensor product of matrices, Nash equilibrium

1 Introduction

Because of the limited resources and the increasingly serious environmental pollution, in recent years, many countries in the world have paid much attention to the production and consumption of renewable energy. For example, China has issued many policy documents on renewable resources, which promoted the rapid development of China's renewable resources. More and more households are trying to produce and use green power, such as photovoltaic and wind power. These households may sell their excess electricity to the grid company or directly to other customers. In the future, the power grid company may be more responsible for power grid operation, maintenance, power transmission, system upgrade and capacity expansion. For both sides of the direct transaction of green power, the power grid company charges an appropriate network fees to ensure sufficient communication capability between the power management system and scheduling agencies (Deng et al., 2019).

On the other hand, since green power transactions involve many technical issues in data processing, security and so on, a kind of energy Internet appears, called park-level energy Internet. Through interconnection of multiple types of distributed energy sources, multiple types of loads, energy storage and information flow, etc., park-level energy Internets can promote a large proportion of renewable energy access and green power market transaction (Huang et al., 2020). And in order to realize the continuous power supply to the users in the park, the park-level energy Internet is connected to the external power grid, which plays a unified role in the allocation of power resources and acts as a backup power source through the dual-main line configuration (Zhang and Tong, 2022).

However, there are various difficulties in the process of direct transaction between green power producers (GPPs) and power users. The current direct trade rules can not guarantee the interests of all parties directly related to the transaction. Therefore, there is usually a green power operator (GPO) in the park. The GPO purchases power from traditional energy generators, renewable energy generators and external grids. And it determines a price at which the GPO sells green electricity to users by referring to the traditional electricity price and the history of transactions.

Many excellent researchers have considered the transaction model between GPOs and park users and have given some results (Sun and Nie, 2015; Pineda and Bock, 2016; Tai et al., 2016; Zhang and Tong, 2022). But they all emphasize the application of block chain technology in energy trading. For example, Zhang used block chain technology to build a bargaining game model of power transaction between GPOs and power users (Zhang and Tong, 2022). However, there is little discussion on how to determine a price at which small-scale GPPs sell green power to GPOs. Taking the park as the application background, we try to model and analyze the transaction process of GPOs and GPPs.

2 Preliminaries

For the sake of simplicity, we introduce some notations.

- δ_n^i: the ith column of the $n \times n$ identity matrix;
- $\Delta_n := \{\delta_n^i \mid i = 1, 2, \ldots, n\}$, namely Δ_n denotes the set of all columns of $n \times n$ identity matrix;
- $\delta_n[i_1, i_2, \ldots, i_s] := [\delta_n^{i_1} \ \delta_n^{i_2} \cdots \delta_n^{i_s}]$, called logical matrix;
- $\mathbb{L}_{m\times n}$: the set of $m \times n$ logical matrices;
- $\mathbb{M}_{m\times n}$: the set of all $m \times n$ real matrices;
- $\mathbb{R}^n$: the set of all n-dimensional real vectors;
- $Col_i(M)(Row_i(M))$: the ith column (row) of a matrix M.

The green power trading model we will establish later is a game model, so we need to give a proper strategic updating rule and analyze its characteristics. The following are two basic concepts of game theory.

Definition 1 [(Cheng et al., 2015; Robert, 1999)]. *A normal game consists of three factors:*

1) *n players $N = \{1, 2, \ldots, n\}$;*
2) *Player i has the strategy set $S_i = \{1, 2, \ldots, k_i\}, i = 1, 2, \ldots, n$, and $S = \Pi_{i=1}^n S_i$ is the set of profiles;*
3) *Payoff functions $c_i : S \to \mathbb{R}, \quad i = 1, 2, \ldots, n$.*

Definition 2 [(Robert, 1999)]. *In the n-player normal game $G = \{S_1, \ldots, S_n; c_1, \ldots, c_n\}$, the strategies $\{s_1^*, \ldots, s_n^*\}$ are a Nash equilibrium if, for each player i, s_i^* is player i's best response to the strategies specified for the $n-1$ other players $\{s_1^*, \ldots, s_{i-1}^*, s_{i+1}^*, \ldots, s_n^*\}$:*

$$c_i\left(s_1^*, \ldots, s_{i-1}^*, s_i^*, s_{i+1}^*, \ldots, s_n^*\right) \geq c_i\left(s_1^*, \ldots, s_{i-1}^*, s_i, s_{i+1}^*, \ldots, s_n^*\right) \tag{1}$$

For a dynamical game, it has been proved in (Cheng et al., 2015) that the game can be determined as a logical dynamic system, as long as its strategy updating rule is assigned. By using a new mathematical tool, called semi-tensor product of matrices (STP), we are able to convert a logical system into its algebraic form (Cheng and Qi, 2009; Cheng and Qi, 2010). Then it is convenient to study logical system under an algebraic framework. In the following, we recall STP and some basic results.

Definition 3 [(Cheng and Qi, 2010)]. *Let $A \in \mathbb{M}_{m\times n}, B \in \mathbb{M}_{p\times q}$, and denote the least common multiplier of n and p by $l = l\,cm\,(n, p)$. Then the STP of A and B is defined as*

$$A \ltimes B := \left(A \otimes I_{\frac{l}{n}}\right)\left(B \otimes I_{\frac{l}{p}}\right), \tag{2}$$

where I_k is the $k \times k$ identity matrix, $\otimes$ is the Kronecker product of matrices.

Remark 1. *STP is a natural generalization of the traditional matrix product, since all fundamental properties of the traditional matrix product are retained. Especially, STP coincides with the traditional matrix product when $n = p$. So the matrix products used in this paper can be thought of as STP and the symbol $\ltimes$ is usually omitted. Some important properties of STP are listed in the following. We refer to (Cheng et al., 2011) for more details.*

1) A $mn \times mn$ matrix

$$\begin{aligned} W_{[m,n]} = \delta_{mn}\,[&1, m+1, 2m+1, \ldots, (n-1)m+1, 2, m \\ &+ 2, 2m+2, \ldots, (n-1)m \\ &+ 2, \ldots, m, 2m, 3m, \ldots, nm]. \end{aligned}$$

is called swap matrix. For any two column vectors $x \in \mathbb{R}^m$ and $y \in \mathbb{R}^n$, we have

$$W_{[m,n]}xy = yx.$$

2) A $2^{2n} \times 2^n$ logical matrix Φ_n is defined as

$$\Phi_n = \delta_{2^{2n}}\left[1, 2^n + 2, 2 \times 2^n + 3, \ldots, (2^n - 2)\,2^n + 2^n - 1, 2^{2n}\right].$$

For any $\delta_{2^n}^i \in \Delta_{2^n}$, we have $\delta_{2^n}^i \ltimes \delta_{2^n}^i = \Phi_n \delta_{2^n}^i$.

Example 1.

1) *Let* $A = \begin{bmatrix} 3 & 1 & 3 & 0 \\ 1 & 3 & 2 & 2 \end{bmatrix}$, $B = \begin{bmatrix} 1 & -2 \\ 2 & 0 \end{bmatrix}$. *According to Definition* 3*, we have*

$$\begin{aligned} &A \ltimes B \\ &= \begin{bmatrix} \begin{bmatrix} 3 & 1 \end{bmatrix} \times 1 + \begin{bmatrix} 3 & 0 \end{bmatrix} \times 2 & \begin{bmatrix} 3 & 1 \end{bmatrix} \times (-2) + \begin{bmatrix} 3 & 0 \end{bmatrix} \times 0 \\ \begin{bmatrix} 1 & 3 \end{bmatrix} \times 1 + \begin{bmatrix} 2 & 2 \end{bmatrix} \times 2 & \begin{bmatrix} 1 & 3 \end{bmatrix} \times (-2) + \begin{bmatrix} 2 & 2 \end{bmatrix} \times 0 \end{bmatrix} \\ &= \begin{bmatrix} 9 & 1 & -6 & -2 \\ 5 & 7 & -2 & -6 \end{bmatrix} \end{aligned}$$

2) *Let* $x = \begin{bmatrix} 2 & 3 & 8 & 1 \end{bmatrix}^T$, $y = \begin{bmatrix} -3 & 0.5 & 2 \end{bmatrix}^T$. *Then*

$$x \ltimes y = \begin{bmatrix} -6 & 1 & 4 & -9 & 1.5 & 6 & -24 & 4 & 16 & -3 & 0.5 & 2 \end{bmatrix}^T$$

3 Model

3.1 Problem analysis

Normally, a small-scale GPP can only sell its green electricity to GPOs, but a GPO may choose to buy traditional electricity outside the park when the electricity price of surrounding GPPs is too high. A GPO usually has multiple GPPs as its neighborhoods. Similarly, each GPP often has multiple GPOs nearby to trade with. Therefore, there is not only competition among operators, but also among nearby GPOs, and none of them can dominate the market alone. To sum up, when the traditional electricity price is lower than the green electricity price, the green power acquisition transaction is regarded as a game model, where the neighbors of a GPP are only GPOs, and the GPO's neighbor has only GPPs, too.

The GPO usually exists in the form of a company or enterprise, and the majority of GPPs are households. So GPPs have no opportunity to bargain directly with GPOs. The transaction process of GPOs and GPPs is roughly as follows:

- *Step1*. It is required by the third-party platform that all GPPs participating in trading activities, must give their quoted price before the official quotation of the GPO on the same day.
- *Step2*. The GPO quotes once a day based on the current market conditions.
- *Step3*. If a GPP agrees to the quotation, then a green electricity transaction between them takes place. Otherwise, the transaction fails and they look forward to next deal.

It is noted that in Step 1, no GPO knows these prices before its quotation. In other words, only after the GPO makes a quotation can it learn of the price of each GPP from the third-party platform, and use it as the reference data for its next quotation. GPOs will make appropriate strategic adjustments according to the previous historical transaction data. Roughly speaking, when the previous transaction price is low, the quotation is still not high and then many GPPs are reluctant to sell green electricity to GPOs. When the transaction volume decreases to a certain extent, or even threatens to be insufficient to maintain the green power supply of GPOs to park users, the quoted price is raised but still not higher than the traditional electricity price.

Similar to the study of general game problems, we assume that.

1) All players are rational and choose the appropriate decisions in order to make more profits every time;
2) GPOs cannot make profits in partnership and must quote independently, and the same to GPPs;
3) GPPs can only sell green power to GPOs nearby, and any one of GPOs has the ability to accept all the renewable electricity in the vicinity.

3.2 Strategy updating rule

As analyzed in **Section 3.1**, the transaction process of GPOs and GPPs is regarded as a game. We adopt Unconditional Imitation (Nowak and May 1992) as the strategy updating rule. Precisely speaking, if

$$j^* = \arg\max_{j \in U(i)} c_j(x(t)), \tag{3}$$

then

$$x_i(t+1) = x_{j^*}(t). \tag{4}$$

where $x(t) = (x_1(t), \ldots, x_i(t), \ldots, x_n(t))^T$, $x_i(t)$ is the strategy of player i at time t, $U(i)$ is the neighborhood of player i (here, meaning those players that can trade with player i).

When there are two different subscripts j_1^* and j_2^*, satisfying

$$c_{j_1^*}(x(t)) = c_{j_2^*}(x(t)) = \max_{j \in U(i)} c_j(x(t)), \tag{5}$$

We describe the strategy in two cases. One is that when the player i is GPP, we set

$$x_i(t+1) = \max\left\{x_{j_1^*}(t), x_{j_2^*}(t)\right\}. \tag{6}$$

Another is that when the player i is GPO, we choose

$$x_i(t+1) = \min\left\{x_{j_1^*}(t), x_{j_2^*}(t)\right\}. \tag{7}$$

3.3 Payoff Bi-matrix

The traditional electricity price of the external network is used as a reference of GPOs. The general cost C_g of a GPO includes two parts: the cost C_1 of purchasing green power from GPPs, the cost C_2 of operation and maintenance of the GPO, namely

$$C_g = C_1 + C_2. \tag{8}$$

According to Assumption 1, only when the green electricity price sold to park users is not higher than the traditional electricity price outside the park, these users are willing to buy green electricity instead of traditional electricity. Therefore, in order to retain these users, the price P_{users} at which GPO sells green power to users, should be less than the traditional electricity price $P_{traditional}$, namely

$$P_{users} \le P_{traditional}. \tag{9}$$

For any GPO, the following inequality holds to ensure the investment profit in green power

$$P_{quotation} + P_{operation} \le P_{users}, \tag{10}$$

where $P_{quotation}$ is GPO's quotation for green electricity from GPPs; $P_{operation}$ is the cost price of GPO′ operation and maintenance, i.e., the average operating cost of GPO.

Combing (**Eqs. 9**, **10**), we have

$$P_{quotation} + P_{operation} \le P_{users} \le P_{traditional}. \tag{11}$$

Hence we get

$$P_{quotation} \le P_{traditional} - P_{operation} \tag{12}$$

That is, when purchasing green power from GPPs, GPO's quotation should not be higher than the difference between the traditional electricity price and the cost price of GPO′ operation and maintenance.

For any GPP, it is also necessary to ensure its profit, so that the GPP is willing to make a green electricity deal with a GPO. Therefore, $P_{quotation}$ should not be lower than the cost price $P_{produce}$ of the GPP.

$$P_{produce} \le P_{quotation} \tag{13}$$

From (**Eqs. 11–13**), we have

$$P_{produce} \le P_{traditional} - P_{operation} \tag{14}$$

Let $P_{produce} = A$ and $P_{traditional} - P_{operation} = B$. We divide interval $[A, B]$ into $n+2$ grades: A, $A + \frac{B-A}{n+1}, A + \frac{2(B-A)}{n+1}, \ldots, A + \frac{n(B-A)}{n+1}$ and B. From Assumption 1, no player (i.e. GPO and GPP) wants to choose extreme strategy A or strategy B. Assume that there are m GPPs and GPOs. We set

$$\begin{aligned} S_1 &= S_2 = \cdots = S_m \\ &= \left\{ A + \frac{B-A}{n+1}, A + \frac{2(B-A)}{n+1}, \ldots, A + \frac{n(B-A)}{n+1} \right\} \end{aligned}$$

We simply denote $A + \frac{i(B-A)}{n+1}$ as $i, i = 1, 2, \ldots, n$. Using Unconditional Imitation as the strategy updating rule, we get the payoff bi-matrix as in **Table 1**.

TABLE 1 Payoff bi-matrix.

GPP ∖ GPO	**1**	**2**	**⋯**	**$n-1$**	**n**
1	$(1, n)$	$(2, n-1)$	⋯	$(n-1, 2)$	$(n, 1)$
2	$(0, 0)$	$(2, n-1)$	⋯	$(n-1, 2)$	$(n, 1)$
⋯	⋯	⋯	⋯	⋯	⋯
$n-1$	$(0, 0)$	$(0, 0)$	⋯	$(n-1, 2)$	$(n, 1)$
n	$(0, 0)$	$(0, 0)$	⋯	$(0, 0)$	$(n, 1)$

Remark 2.

1) *The profit of green power is divided into $n+1$ shares on average. The number of shares to win, except for extreme strategies, is considered as a strategy for each player to act in our model.*
2) *From **Table 1**, it is easy to find that the payoff bi-matrix is an asymmetry and upper triangular matrix. This characteristic is determined by the transaction process of GPOs and GPPs, which is shown in **Section 3.1**.*

According to Theorem 3.1 of (Cheng et al., 2015), the strategy dynamics of each player can be expressed as a n-valued logical dynamic system. Now we identify δ_n^k with $k, k = 1, 2, \ldots, m$, then each strategy profile $(k_1, k_2, \ldots, k_m)^T$ is equivalent to $\delta_{n^m}^r$, where

$$\begin{aligned} \delta_{n^m}^r &= \delta_n^{k_1} \ltimes \delta_n^{k_2} \ltimes \cdots \ltimes \delta_n^{k_m} \\ &= \delta_{n^m}^{(k_1-1)n^{m-1}+(k_2-1)n^{m-2}+\cdots+(k_{m-1}-1)n+k_m} \end{aligned}$$

Namely,

$$r = (k_1 - 1)\, n^{m-1} + (k_2 - 1)\, n^{m-2} + \cdots + \left(k_{m-1} - 1\right) n + k_m.$$

We use $x_i(t)$ to express the strategy of player i at time step t. Define $x(t) = \ltimes_{i=1}^m x_i(t) \in \triangle_{n^m}$. Then based on STP (Cheng and Qi, 2010), enable us to equivalently transform the above green power transaction model into a linear form as in (**Eq. 15**).

$$x(t+1) = Mx(t), \tag{15}$$

where $M \in \mathbb{L}_{n^m \times n^m}$ is called the structure matrix of system.

Theorem 1. *Assume that there are m_1 GPOs and m_2 GPPs nearby, and denote $m = m_1 + m_2$. For the green power transaction model provided above, a strategy profile $(s_1^*, s_2^*, \ldots, s_m^*)$ is a*

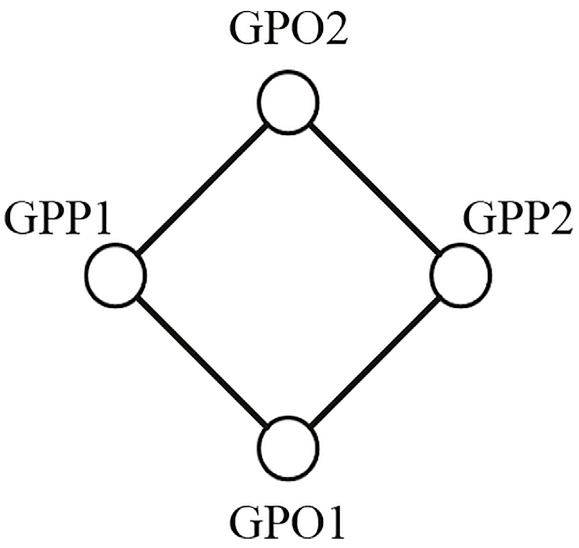

FIGURE1
The topology diagram of two GPOs and two GPPs.

Nash equilibrium, if and only if $Row_r(Col_r(M)) = 1$, *where* $r = (s_1^* - 1)n^{m-1} + (s_2^* - 1)n^{m-2} + \cdots + (s_{m-1}^* - 1)n + s_m^*$.

Froof. *For a strategy profile* $(s_1^*, s_2^*, \ldots, s_m^*)$, *if* $Row_r(Col_r(M)) = 1$, *where* $r = (s_1^* - 1)n^{m-1} + (s_2^* - 1)n^{m-2} + \cdots + (s_{m-1}^* - 1)n + s_m^*$, *then* $x = \delta_{n^m}^r$ *is a fixed point of system* (15), *since it satisfies* $\delta_{n^m}^r = M\delta_{n^m}^r$. *According to the strategy updating rule, each player adopt the best strategy from his neighborhoods. So the fixed point shows that player i still choose the same strategy as before, as long as the strategies of all other players remain unchanged. From Definition 2,* $(s_1^*, s_2^*, \ldots, s_m^*)$ *is a Nash equilibrium. The above analysis process can be deduced backwards. Therefore, the proof is completed.*

4 Illustrative example

For the convenience of showing the method itself, we assume that there are two GPOs and two GPPs nearby. The topology diagram is given as in Figure 1.

Set $n = 2$ and divide interval $[A, B]$ into 4 grades: $A, A + (B - A)/3, A + 2(B - A)/3$ and B. According to the above analysis, four players consisting of two GPPs and two GPOs, definitely not choose extreme strategies A or B. We denote $A + (B - A)/3$ and $A + 2(B - A)/3$ by 1 and 2, respectively. From Table 1, the payoff bi-matrix is given as in Table 2.

TABLE 2 Payoff bi-matrix for the case of $n = 2$.

GPP ∖ GPO	1	2
1	$(1,2)$	$(2,1)$
2	$(0,0)$	$(2,1)$

In the following, we illustrate how to use the payoff bi-matrix and the strategy updating rule, introduced above, to establish the dynamic characteristics for each player. For example, let $x_1(t) = x_4(t) = 2, x_2(t) = x_3(t) = 1$. For GPP1, it has two neighborhoods: GPO 1 and GPO 2. Then we get

$$\begin{aligned}
&c_{1,2}(x_1(t), x_2(t)) = 0, c_{1,4}(x_1(t), x_4(t)) \\
&\quad = 2 \Rightarrow c_1(t) = \max(c_{1,2}, c_{1,4}) = 2 \Rightarrow x_1(t+1) = x_4(t) = 2; \\
&c_{2,1}(x_2(t), x_1(t)) = 0, c_{2,3}(x_2(t), x_3(t)) \\
&\quad = 2 \Rightarrow c_2(t) = \max(c_{2,1}, c_{2,3}) = 2 \Rightarrow x_2(t+1) = x_3(t) = 1; \\
&c_{3,2}(x_3(t), x_2(t)) = 1, c_{3,4}(x_3(t), x_4(t)) \\
&\quad = 2 \Rightarrow c_3(t) = \max(c_{3,2}, c_{3,4}) = 2 \Rightarrow x_3(t+1) = x_4(t) = 2; \\
&c_{4,1}(x_4(t), x_1(t)) = 1, c_{4,3}(x_4(t), x_3(t)) \\
&\quad = 1 \Rightarrow c_4(t) = \max(c_{4,1}, c_{4,3}) = 1 \Rightarrow x_4(t+1) = x_3(t) = 1.
\end{aligned}$$

We use the same argument for each profile $(x_1(t), x_2(t), x_3(t), x_4(t))^T$, and can compute next action for each player as in Table 3.

Identify action k with δ_2^k, $k = 1, 2$. From Table 3, it is verified for each player' strategy that its dynamic characteristics is

$$x_i(t+1) = M_i x(t), \quad i = 1, 2, 3, 4, \tag{16}$$

where $x_i(t) \in \triangle_2, x(t) = \ltimes_{i=1}^4 x_i(t)$, and

$$\begin{aligned}
M_1 &= \delta_2[1,2,1,2,2,2,2,2,1,2,1,2,2,2,2,2], \\
M_2 &= \delta_2[1,1,1,1,1,1,1,1,1,1,2,2,1,1,2,2], \\
M_3 &= \delta_2[1,2,1,2,2,2,2,2,1,2,1,2,2,2,2,2], \\
M_4 &= \delta_2[1,1,1,1,1,1,1,1,1,1,2,2,1,1,2,2].
\end{aligned}$$

By using properties of STP, we obtain

$$\begin{aligned}
x(t+1) &= x_1(t+1)\, x_2(t+1)\, x_3(t+1)\, x_4(t+1) \\
&= M_1 x(t)\, M_2 x(t)\, M_3 x(t)\, M_4 x(t) \\
&= M_1 W_{[2,16]} M_2 x(t)\, x(t)\, M_3 x(t)\, M_4 x(t) \\
&= M_1 W_{[2,16]} M_2 \Phi_4 x(t)\, M_3 x(t)\, M_4 x(t) \\
&= M_1 W_{[2,16]} M_2 \Phi_4 W_{[2,16]} M_3 x(t)\, x(t)\, M_4 x(t) \\
&= M_1 W_{[2,16]} M_2 \Phi_4 W_{[2,16]} M_3 \Phi_4 x(t)\, M_4 x(t) \\
&= M_1 W_{[2,16]} M_2 \Phi_4 W_{[2,16]} M_3 \Phi_4 W_{[2,16]} M_4 x(t)\, x(t) \\
&= M_1 W_{[2,16]} M_2 \Phi_4 W_{[2,16]} M_3 \Phi_4 W_{[2,16]} M_4 \Phi_4 x(t) \\
&= M x(t)
\end{aligned}$$

where

$$\begin{aligned}
M &= M_1 W_{[2,16]} M_2 \Phi_4 W_{[2,16]} M_3 \Phi_4 W_{[2,16]} M_4 \Phi_4 \\
&= \delta_{16}[1,11,1,11,11,11,11,11,1,11,6,16,11,11,16,16].
\end{aligned}$$

TABLE 3 Strategy updating for the case of two GPOs and two GPPs.

Profile	**1111**	**1112**	**1121**	**1122**	**1211**	**1212**	**1221**	**1222**
$c_1(t)$	1	2	1	2	2	2	2	2
$c_2(t)$	2	2	2	2	1	1	1	1
$c_3(t)$	1	2	0	2	2	2	2	2
$c_4(t)$	2	1	2	1	2	1	2	1
$x_1(t+1)$	1	2	1	2	2	2	2	2
$x_2(t+1)$	1	1	1	1	1	1	1	1
$x_3(t+1)$	1	2	1	2	2	2	2	2
$x_4(t+1)$	1	1	1	1	1	1	1	1
Profile	2111	2112	2121	2122	2211	2212	2221	2222
$c_1(t)$	0	2	0	2	2	2	2	2
$c_2(t)$	2	2	0	0	1	1	1	1
$c_3(t)$	1	2	0	2	2	2	2	2
$c_4(t)$	2	1	0	1	2	1	0	1
$x_1(t+1)$	1	2	1	2	2	2	2	2
$x_2(t+1)$	1	1	2	2	1	1	2	2
$x_3(t+1)$	1	2	1	2	2	2	2	2
$x_4(t+1)$	1	1	2	2	1	1	2	2

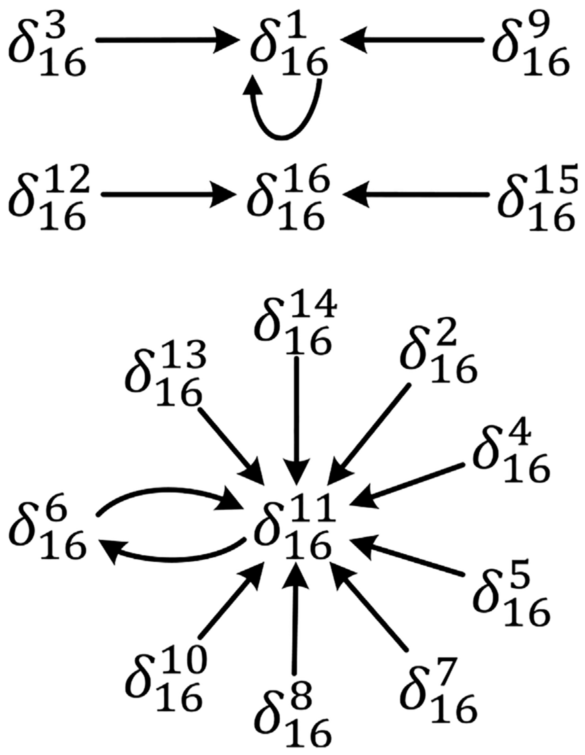

FIGURE 2
The state transition diagram of system (16).

It is easy to find two elements on the diagonal of matrix M. So there are only two equilibrium points in this game: δ_{16}^{1} and δ_{16}^{16}, namely Nash equilibriums. In addition, by a simple computation we get a limit cycle $C: \delta_{16}^{6} \rightarrow \delta_{16}^{11} \rightarrow \delta_{16}^{6}$. And their attraction domains are

$$
\begin{aligned}
D(\delta_{16}^{1}) &= \left\{\delta_{16}^{1}, \delta_{16}^{3}, \delta_{16}^{9}\right\} \sim \{(1,1,1,1),(1,1,2,1),(2,1,1,1)\} \\
D\left(\delta_{16}^{16}\right) &= \left\{\delta_{16}^{12}, \delta_{16}^{15}, \delta_{16}^{16}\right\} \sim \{(2,1,2,2),(2,2,2,1),(2,2,2,2)\} \\
D(C) &= \left\{\delta_{16}^{2}, \delta_{16}^{4}, \delta_{16}^{5}, \delta_{16}^{6}, \delta_{16}^{7}, \delta_{16}^{8}, \delta_{16}^{10}, \delta_{16}^{11}, \delta_{16}^{13}, \delta_{16}^{14}\right\} \\
&\sim \{(1,1,1,2),(1,1,2,2),(1,2,1,1),(1,2,1,2), \\
&\quad (1,2,2,1),(1,2,2,2),(2,1,1,2),(2,1,2,1), \\
&\quad (2,2,1,1),\ (2,2,1,2)\}
\end{aligned}
$$

The state transition diagram of system 16) is given in Figure 2. From Figure 2 and Theorem 1, we know that only when the initial state is taken from $D(\delta_{16}^{1})$ and $D(\delta_{16}^{16})$, system (16) will be stable at the Nash equilibrium δ_{16}^{1} (meaning strategy profile (1, 1, 1, 1)) and δ_{16}^{16} (meaning strategy profile (2, 2, 2, 2)), respectively.

Remark 3. The results obtained above show that the strategy profile depends on its initial state, and finally be stable at one of three attractors. We explain it in three cases.

- *If player i chooses an initial strategy profile from* $\{(1,1,1,1),(1,1,2,1),(2,1,1,1)\}$, *then the strategy profile will reach* (1, 1, 1, 1) *and be stable at this point in order to make as much profit as possible.*
- *If the player adopts an initial strategy profile from* $\{(2,1,2,2),(2,2,2,1),(2,2,2,2)\}$, *then the strategy profile will be stable at* (2, 2, 2, 2).
- *For other initial strategy profiles, they change every time. That is, they are unstable.*

Data availability statement

The original contributions presented in the study are included in the article/Supplementary Material, further inquiries can be directed to the corresponding authors.

Author contributions

All authors listed have made a substantial, direct, and intellectual contribution to the work and approved it for publication.

Funding

This work is supported by the Chongqing Nature Science Foundation (cstc2020jcyj-msxmX0708), Chongqing Project of Technology Innovation and Application Demonstration (cstc2018jszx-cyzdX0152), National Key R&D Program of China (2020YFB1708803, 2021YFB 3203200).

Conflict of interest

Authors ZZ, YC, YL and XJ were employed by Beijing Smartchip Microelectronics Technology Company Limited.

The remaining authors declare that the research was conducted in the absence of any commercial or financial relationships that could be construed as a potential conflict of interest.

The authors declare that this study received funding from company Beijing Smartchip Microelectronics Technology Company Limited. The funder had the following involvement in the study: ZZ has conducted simulation verification and technical summary. YC was responsible for model analysis and improvement. YL has carried out data sorting and modeling. XJ was in charge of data collection and modeling.

Publisher's note

References

Cheng, D., He, F., Qi, H., and Xu, T. (2015). Modeling, analysis and control of networked evolutionary games. *IEEE Trans. Autom. Contr.* 60 (9), 2402–2415. doi:10.1109/tac.2015.2404471

Cheng, D., and Qi, H. (2010). A linear representation of dynamics of boolean networks. *IEEE Transaction Automatic Control* 55, 2251–2258. doi:10.1109/TAC.2010.2043294

Cheng, D., and Qi, H. (2009). Controllability and observability of boolean control networks. *Automatica* 45, 1659–1667. doi:10.1016/j.automatica.2009.03.006

Cheng, D., Qi, H., and Li, Z. (2011). *Analysis and control of boolean networks: A semi-tensor product approach*. London: Springer-Verlag.

Deng, M., Qu, B., and Xing, G. (2019). Business model exploration of customer energy service under the back-ground of energy Internet. *Power Demand Side Manag.* 21 (3), 59–62+68.

Huang, Y., Shao, C., Hao, J., Cai, M., Gao, C., and Chen, T., (2020). Multi-energy demand response technology in energy Internet environment. *Power Demand Side Manag.* 22 (05), 2–6+18.

Nowak, M., and May, R. (1992). Evolutionary games and spatial chaos. *Nature* 359, 826–829. doi:10.1038/359826a0

Pineda, S., and Bock, A. (2016). Renewable-based generation expansion under a green certificate market. *Renew. Energy* 93, 53–63. doi:10.1016/j.renene.2015.12.061

Robert, G. (1999). *A primer in game theory*. New Jersey, United States: Prentice-Hall.

Sun, P., and Nie, P. (2015). A comparative study of feed in tariff and renewable portfolio standard policy in renewable energy industry. *Renew. Energy* 74, 255–262. doi:10.1016/j.renene.2014.08.027

Tai, X., Sun, H., and Guo, Q. (2016). Electricity trans-actions and congestion management based on blockchain in energy Internet. *Power Syst. Technol.* 40 (12), 3630–3638.

Zhang, L., and Tong, L. (2022). Consortium blockchain power trading strategy of par-level energy Internet under RPS. , *Control Theory & Appl.* 12, 570–580.

frontiers | Frontiers in Energy Research

TYPE Original Research
PUBLISHED 10 January 2023
DOI 10.3389/fenrg.2022.919041

The classification model for identifying single-phase earth ground faults in the distribution network jointly driven by physical model and machine learning

Su Xueneng[1*†], Zhang Hua[1†], Gao Yiwen[1†], Huang Yan[2†], Long Cheng[1†], Li Shilong[1†], Zhang Weiwei[2†] and Zheng Qin[2†]

[1]State Grid Sichuan Electric Power Research Institute, Chengdu, Sichuan, China, [2]Nari Technology Nanjing Control Systems Co., Ltd., Jiangning, Jiangsu, China

Check for updates

OPEN ACCESS

EDITED BY
Qiuye Sun,
Northeastern University, China

REVIEWED BY
Lipeng Zhu,
Hunan University, China
Kenneth E. Okedu,
National University of Science and Technology (Muscat), Oman
Srete Nikolovski,
Josip Juraj Strossmayer University of Osijek, Croatia

*CORRESPONDENCE
Su Xueneng,
suxueneng_sgcc@163.com

†These authors have contributed equally to this work and share first authorship

SPECIALTY SECTION
This article was submitted to Smart Grids,
a section of the journal
Frontiers in Energy Research

RECEIVED 13 April 2022
ACCEPTED 30 August 2022
PUBLISHED 10 January 2023

CITATION
Xueneng S, Hua Z, Yiwen G, Yan H, Cheng L, Shilong L, Weiwei Z and Qin Z (2023), The classification model for identifying single-phase earth ground faults in the distribution network jointly driven by physical model and machine learning.
Front. Energy Res. 10:919041.
doi: 10.3389/fenrg.2022.919041

Single-phase earth ground faults are the most frequent faults likely to occur but hard to identify in a distribution system, especially in a neutral ineffectively grounded system. Targeting on this goal, a novel AdaBoost-based single-phase earth ground fault identification model is put forward. First, after depicting the zero-sequence circuit of the distribution system, a feature engineering that can reflect local and global evolutionary processes in the fault period is constructed in detail. Second, to overcome two problems, namely, different number problems between fault and non-fault samples and curse of dimension, principal component analysis is used for feature extraction, in which only a small number of low-dimension mapped features are extracted, and then transmitted into the AdaBoost-based ground fault identification model. Subsequently, this work borrows from machine learning and applies its learning curve and receiver operating characteristic curve to guide the optimization of the proposed identification model. Numerical studies verify the effectiveness and adaptability of the proposed model toward solving single-phase earth ground faults.

KEYWORDS

distribution network, machine learning, single-phase ground fault, principal component analysis, ROC, classification model

1 Introduction

In extreme short-circuit situations, designing feeder relays would be simple in general. However, the single-phase earth ground fault is out of this category, especially in low- and medium-voltage distribution networks (3~66 kV) with ineffectively grounded neutral points (Cui et al., 2011; Xue et al., 2015). In this regard, it is also referred to as a small-current grounded system. In contrast with other short-circuit faults, single-phase earth ground faults are mostly to happen, and by incomplete statistics, they account for around 60%~80%. Interestingly, most interphase faults are the deteriorated outcomes of single-

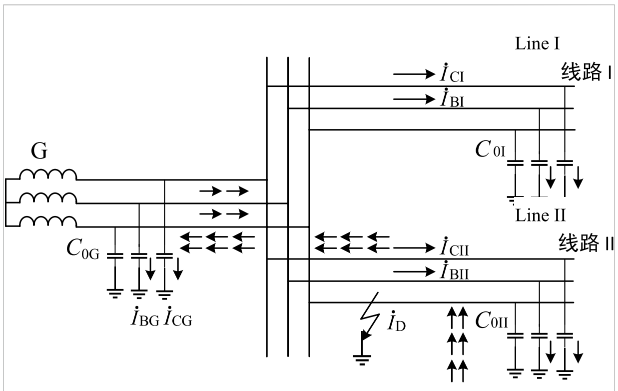

FIGURE 1
Capacitance current distribution represented by the three-phase system during single-phase grounding.

phase earth ground faults. Therefore, detecting this "weak" earth fault is very important for protection engineers in order to prevent more severe hazards and to ensure the safety and reliability of power delivery.

Most scholars have conducted many studies in this field. So far, some staged and conclusive achievements have been made. Specifically, the approach in identification single-phase earth ground fault can be normally categorized into two mainstream branches: steady-state method and transient method. As for the former, it includes six sub-approaches (Xu et al., 2005; Ai et al, 2009; Gautam and Brahma, 2012; Li, 2017): zero-sequence current amplitude comparison method, zero-sequence current phase comparison method, fifth harmonic component method, zero-sequence active power component method, zero-sequence reactive power method, and zero-sequence admittance method. The main principal of these methods is that zero-sequence current of the fault line is the summation of all non-fault lines, and it shall be larger than any of other lines. Considering the line-to-ground conductance and the resistance loss of an arc suppression coil, a new protection criterion is established *via* recognizing the direction difference of active power (Xu et al., 2005; Li, 2017). Although not limited to the arc suppression coil, its active component is generally small, especially when the three-phase imbalance degree is relatively large, it will be easier to misjudge faults due to the false active current component. With respect to the transient method, it includes three parts: first half-wave polarity method, transient power direction method, and transient parameter identification method (Yao and Cao, 2009; Zeng et al., 2012). Compared with the former, this method is relatively less influenced by the form that the neutral point is grounded or noneffective. From this perspective, it possesses better adaptability (Zhu, 2011). Hence, it has been gradually becoming more important and popular in this single-phase earth ground fault identification field, especially as the function of transient-recording-type devices is becoming a mainstream product (Jiale et al., 2007; Zhang and Yin, 2011; Ghaderi et al., 2017).

Moreover, revolving around this target, there are several novel techniques, such as three-phase current method and transient frequency band method. Specifically, Song et al. (2011) propose the three-phase current method, which collects the sudden change of three-phase current in a transient process, calculates the relevant coefficients between each pair of phases, and subsequently discriminates the ground fault according to the fault phase that has the smallest relevance degree. As for the latter, some scholars have proposed a method of extracting information of specific frequency in transient zero-sequence current and then identifying single-phase earth ground faults by comparing the difference between the amplitude and polarity (Xue et al., 2003; Liu et al., 2018). An et al. (2020) propose the grounding protection principle based on half-wave Fourier algorithm and establish an action criterion algorithm model based on half-wave Fourier algorithm. Shu et al. (2019) propose the wavelet transform method to realize the extraction of transient zero-sequence information. Lishan et al. (2020) propose a fault line identification scheme with admittance asymmetry parameters as the criterion and utilize the fifth harmonic principle to solve the issue regarding the disappearance of fault differences between the fault lines and non-fault lines of the neutral point after passing through the extinction coil grounding system. He et al. (2017) identify grounding faults by using relative entropy of the generalized S-transform energy of zero-sequence current. Zhou (2016) establishes a dynamic grounding fault sensing criterion based on the features of injection current variables after fault occurrence and identifies fault lines by comparing the effective value of zero-sequence current variables of different feeders. Although these transient signal methods produce ideal effects in handling faults with a large zero-sequence current, they are likely to be affected by systematic influences in multiple processes (e.g., constant startup value, sampling noise, and electromagnetic interference, etc.) during actual operation when fault zero-sequence current is low, leading to low algorithmic sensitivity. They are too easily affected by operating conditions of the distribution network and rely excessively on the differential configuration of various configuration parameters.

In fact, the issue of identifying faults can be viewed as the scope of classification, for which it is highly relevant to machine learning (e.g., clustering, classification, and regression under the semi-supervised/supervised mode). Recently, machine learning technology has developed rapidly. With reference to the 2016 International Summit on Application of Machine Learning Industry jointly held by IBM and CDA Data Analysis and Research Institute, this has been applied in many fields, for e.g., finance, IT, computers, and transportation, and has proven to be extraordinarily valuable. In view of this, some researchers are working on building an intelligent fault identification model *via* machine learning

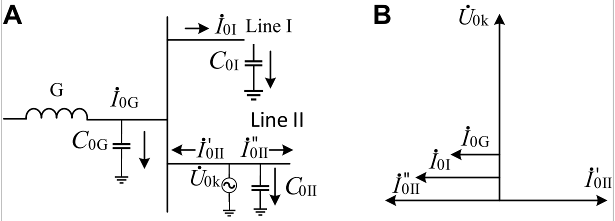

FIGURE 2
Zero-sequence equivalent network and phasor network during single-phase grounding.

technology (Wang et al., 2021). Although relatively reliable identification results have been elementarily achieved, the lack of hyperparameter adjustment, over/underfitting judgment, and feature extraction in optimizing the identification model is its critical defect. In general, exploring the application of machine learning in the fault identification field requires more systematic and theoretical discussions in depth.

In light of the aforementioned background, this article borrows from machine learning and puts forward a novel single-phase earth ground fault identification method jointly driven by practical fault data and Simulink model.

Major contributions of this article include:

1) In reflecting the local and global evolutional process of fault features and forms, this article chooses two major fault features (including their amplitudes, delta variations and phase degrees), which could form an entire feature engineering taking the stable/transient state of the faulty network into account.
2) In combination with machine learning, a mainstream feature reduction method of principal component analysis (PCA) is applied into which feature reduction of high-dimension fault features can in validity select only a small number of but key mapped features of potential values and further elevate model identification efficiency in engineering practice.
3) AdaBoost-based single-phase earth fault identification model is designed in this work into which the features of high priority are fed, where several manners of learning curve, validation curve, and receiver operating characteristic curve (ROC) are all brought out into guiding model optimization, and thus an entire fault identification technology based on machine learning is gradually formed. Additionally, model performance is quantitively analyzed from the perspective of accuracy and area under the curve (AUC) indicators.

The remainder of this article is organized as follows: in Section 2 depicts the equivalent circuit diagram of a distribution system when a single-phase earth ground fault occurs in this system and constructs the ground fault feature engineering. Next, a machine-learning-based ground fault identification model is built. To overcome its underfitting/overfitting possibilities, some hyperparameter optimization techniques have been applied, such as up-sampling technology, feature reduction, learning/validation curve, and receiver operating characteristic curve (ROC). Finally, the practical dataset and the Simulink dataset are both used as learning samples in the Numerical studies part, and in this section, it demonstrates the validity and adaptability of the proposed ground fault identification model under multiple scenarios.

2 Feature engineering of single-phase earth ground faults

2.1 Physical model of single-phase grounding faults

To construct reasonable and complete fault features, this section will analyze the change features of system parameters in single-phase earth ground faults, like the capacitance current distribution in the system, from the perspective of the circuit of the distribution network. The distribution of capacitance current during single-phase grounding is shown in Figure 1. In Figure 1: C_{OG}, C_{OI}, and $\mathrm{C_{OII}}$ are the capacitive parameters over the ground of each generator, line I, and line II, respectively; $\dot{I}_{BG}$ and $\dot{I}_{CG}$ are, respectively, the capacitive parameters over the ground of phase B and phase C on generator G; $\dot{I}_{BI}$ and $\dot{\mathrm{I}}_{\mathrm{CI}}$ are, respectively, the capacitive parameters over the ground of phase B and phase C on line I; and $\dot{I}_{BII}$ and $\dot{\mathrm{I}}_{\mathrm{CII}}$ are, respectively, the capacitive parameters over the ground of phase B and phase C on line I.

In combination with information from Figure 1, it can be seen that the voltage drop of load current and capacitance current on line impedance can be ignored after phase A of line II is grounded. It can be inferred that capacitance current over the ground of phase A of all element equipment also equals zero when phase A of the entire system is grounded, and voltage and capacitance current over the ground of phase B and phase C are increased by 1.732 times. The distribution of the capacitance current under such circumstances is as shown in "→" of Figure 1. The zero-sequence equivalent network and phasor network of single-phase grounding are, respectively, depicted in Figures 2A,B.

2.2 Feature engineering of single-phase grounding faults

According to the zero-sequence equivalent network model of single-phase grounding faults in Figure 2, the fault features of fault lines, non-fault lines, and non-fault elements are totally different. Given this understanding, we could construct the features of single-phase grounding faults. In addition, as we also take into account the needs of wildfire prevention, it is necessary to give further consideration to integration with transient recording data when constructing the features. The engineering constructed in this article puts focus on and includes the amplitude, phase position, and variables of the zero-sequence voltage and zero-sequence current of the same cycle.

2.2.1 Features of zero-sequence voltage

There are three features of zero-sequence voltage: amplitude cycle sequence, variable amplitude cycle sequence, and phase position cycle sequence. The cycle sequence that they belong to refers to the sampling dataset of a cycle. The definitions of the three features, namely, zero-sequence voltage amplitude cycle U_p^{amp}, zero-sequence voltage variable amplitude cycle ΔU_p^{amp}, and zero-sequence voltage phase position cycle U_p^{theta}, are, respectively, shown in Eqs 1–3.

$$\begin{gathered}\dot{U}_p = \left[\dot{U}_P^1, \dot{U}_p^2, \cdots, \dot{U}_p^k, \cdots \dot{U}_p^T\right], \forall k \in T,\\ \dot{U}_p^k = fft\left(\left[\dot{U}_p^{t-T}, \cdots, \dot{U}_p^{t-1}, \dot{U}_p^t\right], base\right),\\ U_p^{amp,k} = func\_ext\left(\dot{U}_p^k, amp\right),\\ U_p^{theta,k} = func\_ext\left(\dot{U}_p^k, theta\right),\\ U_p^{amp} = \left[U_p^{amp,1}, U_p^{amp,2}, \cdots, U_p^{amp,k}, \cdots U_p^{amp,T}\right],\end{gathered} \tag{1}$$

$$\begin{cases}\Delta U_p^{amp} = \left[\Delta U_p^{amp,1}, \Delta U_p^{amp,2}, \cdots, \Delta U_p^{amp,k}, \cdots, \Delta U_p^{amp,T}\right],\\ \Delta U_p^{amp,k} = U_p^{k,t} - U_p^{k,t-1},\\ U_p^{k,t} = func\_ext\left(\dot{U}_p^k\right),\end{cases}, \tag{2}$$

$$U_p^{theta} = \left[U_p^{theta,1}, U_p^{theta,2}, \cdots, U_p^{theta,k}, \cdots, U_p^{theta,T}\right]. \tag{3}$$

Here, *Up* is the zero-sequence voltage cycle vector sequence; $\dot{U}_p^k$is the *k*th zero-sequence voltage phasor in the zero-sequence voltage vector, which can be obtained by extracting the fundamental wave phasor with Fourier decomposition after the corresponding moment *t* moves forward by a cycle and constructs a sequence; T is the cycle sequence scale related to equipment sampling frequency (in this article, sampling frequency = 12,800 Hz, $T = 256$); $U_p^{amp,k}$ and $U_p^{theta,k}$, respectively, correspond to the amplitude and phase mass of the *k*th zero-sequence voltage; $fft(\cdot)$ and $func\_ext(\cdot)$, respectively, correspond to Fourier decomposition function and amplitude/phase position extraction function; and $\Delta U_p^{amp,k}$ is the *k*th zero-sequence voltage variable amplitude.

2.2.2 Features of zero-sequence current

Similarly, there are also three features of zero-sequence current: amplitude cycle sequence, variable amplitude cycle sequence, and phase position cycle sequence. The definitions of the three features, zero-sequence current amplitude cycle I_p^{amp}, zero-sequence current variable amplitude cycle ΔI_p^{amp}, and zero-sequence current phase position cycle I_p^{theta}, are shown in Eqs 4–6, respectively.

$$\begin{cases}\dot{I}_p = \left[\dot{I}_p^1, \dot{I}_p^2, \cdots, \dot{I}_p^k, \cdots, \dot{I}_p^T\right], \forall k \in T,\\ \dot{I}_p^k = fft\left(\left[\dot{I}_p^{t-T}, \cdots, \dot{I}_p^{t-1}, \dot{I}_p^t\right], base\right),\\ I_p^{amp,k} = func\_ext\left(\dot{I}_p^k, amp\right),\\ I_p^{theta,k} = func\_ext\left(\dot{I}_p^k, theta\right),\\ I_p^{amp} = \left[I_p^{amp,1}, I_p^{amp,2}, \cdots, I_p^{amp,k}, \cdots, I_p^{amp,T}\right],\end{cases}, \tag{4}$$

$$\begin{cases}\Delta I_p^{amp} = \left[\Delta I_p^{amp,1}, \Delta I_p^{amp,2}, \cdots, \Delta I_p^{amp,k}, \cdots, \Delta I_p^{amp,T}\right],\\ \Delta I_p^{amp,k} = I_p^{k,t} - I_p^{k,t-1},\\ I_p^{k,t} = func\_ext\left(\dot{I}_p^k\right),\end{cases}, \tag{5}$$

$$I_p^{theta} = \left[I_p^{theta,1}, I_p^{theta,2}, \cdots, I_p^{theta,k}, \cdots, I_p^{theta,T}\right]. \tag{6}$$

Here, $\dot{I}_p$is the zero-sequence current cycle vector sequence; $\dot{I}_p^k s$ is the *k*th zero-sequence current phasor in zero-sequence current vector, which can be obtained by extracting the fundamental wave phasor with Fourier decomposition after the corresponding moment t moves forward by a cycle and constructs a sequence; $I_p^{amp,k}$ and $I_p^{theta,k}$, respectively, correspond to the amplitude and phase mass of the *k*th zero-sequence current; $fft(\cdot)$ and $func\_ext(\cdot)$, respectively, correspond to Fourier decomposition function and amplitude/phase position extraction function; and $\Delta I_p^{amp,k}$ is the k^{th} zero-sequence current variable amplitude.

By using the zero-sequence voltage amplitude U_p^{amp}, zero-sequence voltage variable amplitude ΔU_p^{amp}, zero-sequence voltage phase position U_p^{theta}, zero-sequence current amplitude I_p^{amp}, zero-sequence current variable amplitude ΔI_p^{amp}, and zero-sequence current phase position I_p^{theta} in Eqs 1–6, the feature engineering of single-phase grounding faults can be constructed as $\mathcal{M} = [U_p^{amp}, \Delta U_p^{amp}, U_p^{theta}, I_p^{amp}, \Delta I_p^{amp}, I_p^{theta}]$.

3 Single-phase grounding fault classification model driven by machine learning

Combined with the feature-target key value sequence of single-phase grounding faults acquired from the true-type test and simulation model, this model is categorized as supervised learning in the field of machine learning and, to be more precise, belongs to the classification category. In theory, supervised learning is often oriented and signifies better training effects. However, directly lifting machine learning to the classification of single-phase grounding faults may lead to a result that falls short of expectation. There are three reasons behind this possibility. The first reason is that the present studies lack a complete and sufficient database of single-phase grounding faults, which will result in good training effects but will not lead to ideal practical generalization ability. The second reason is that the present database of single-phase grounding faults mainly contains grounding faults and does not have the database of waveforms related to the interfered system during normal operation. The third reason is that, combined with the fault feature vector

TABLE 1 PCA algorithm principle and pseudo-code.

```
Input: Sample set
$D = \{x_1, x_2, \cdots, x_m\}$

Dimensional index of
low-dimensional space $d_{index}$

Process:

1: Neutralize all grounding fault feature samples: $x_i \leftarrow x_i - \frac{1}{m}\sum_{i=1}^{m} x_i$
2: Calculate the covariance matrix of the sample $XX^T$
3: Conduct eigenvalue decomposition for the covariance matrix $XX^T$
4: Take $w_1, w_2, \cdots, w_{d_{index}}$ eigenvector corresponding to $d_{index}$ the largest eigenvalue
Output: Projection matrix $W = \{w_1, w_2, \cdots, w_{d_{index}}\}$
```

The bold term of $\{x_m, y_m\}$ represents the m^{th} feacture vector and its fault label. The **SVM** is the abbreviation of supporting vector machine.

constructed in Section 2.2, there could be 1,536 dimensions. When considering the vertical expansion of sample database dimensions, the model classification effects would not be as good as expected, even when high-performance machine learning classification models are adopted.

Concerning the aforementioned three problems, this section will introduce the sampling method, feature dimension reduction, and classification algorithm in the machine learning technique in the hope of constructing a single-phase grounding fault classification model with great robustness.

3.1 Sampling technique

The sampling technique is mainly used to solve problems in class-imbalance, namely, situations where training samples of different types vary significantly from each other in the classification task. Normally, the classifier decision rule is: $y/(1-y) > 1$, where y is the probability threshold predicted to be a positive sample. The threshold $y/(1-y)$ is set at 0.5, indicating that possibility of true-positive and -negative samples is the same. However, when the number of positive samples and the number of negative samples are not the same, having m^+ and m^-, respectively, representing the number of positive and negative samples, then the observation probability is m^+/m^-. Since the general hypothetical training set is the overall unbiased sampling of authentic samples, the observation probability represents the true probability. Therefore, as long as the prediction of the classifier is higher than the observation probability, as in $y/(1-y) > m^+/m^-$, the result should be deemed as a positive sample.

Based on the aforementioned details, there are three methods to solve class-imbalance (Shu et al., 2019): the first method is to directly carry out under-sampling for the negative samples in the training set, as in removing some negative samples to make sure the number of positive samples and the number of negative samples are close. The second method is to implement oversampling for the positive samples in the training set, as in adding some positive samples to make sure the number of positive samples and the number of negative samples are close. The third method, also referred to as "threshold movement," is to directly implement learning based on the primary training set, but it is necessary to embed $m^- y/(m^+ - ym^+)$ in the decision-making process when using the trained classifier for prediction.

In comparison, the under-sampling method is prone to losing negative samples and some important information. At the same time, threshold movement should be based on the premise that "the training set is the overall unbiased sampling of true samples," which is usually false. In other words, it is often unable to effectively infer the real probability based on the training set observation probability in real practice. Therefore, this section will focus on the up-sampling method to resolve class-imbalance.

3.2 Feature dimension reduction

Among the feature dimensionality reduction methods, the mainstream and mature option is the principal component analysis method (PCA). The idea central to the PCA method is the reduction of dimensionality. In the analysis process, multiple variables are transformed into a small number of comprehensive variables (principal components). The transformed principal components are not related to each other and are in the form of a linear combination of original variables. Therefore, a great deal of information can be displayed in the form of a linear combination and without repetitions. The PCA algorithm principle and pseudo code are shown in Table 1.

In combination with the principal component analysis method, the dimensionality reduction engineering construction of grounding fault features in Section 1.2 is carried out. There is an independent and unrelated eigenvalue distribution in the new space after construction. After considering the principle of the "90%" value space, Figure 3 depicts the selection of the top 10 eigenvalues, and the cumulative ratio of features accounts for 91.37%. Therefore, the initial structure with 1,536-dimension load feature engineering can be optimized and reduced to 12 dimensions, and the space compression rate can reach as high as 99.21%.

3.3 AdaBoost classification model

Since for every set of feature vectors, its classification result is provided; obviously, this issue belongs to the supervised learning field. In machine learning, logistic regression,

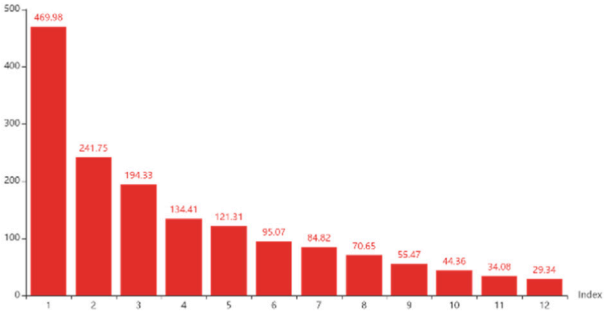

FIGURE 3
Distribution of eigenvalues of single-phase grounding faults after dimensionality reduction using the PCA method.

support vector machine, K-neighbor proximity, and decision tree, as well as integration-based learners, such as AdaBoost, XGBoost, and LightGBM, are typical technologies used (Wu and Hiroshi, 2014; Dahlan, 2018; Pan et al., 2020). Compared with a single classifier (also known as a “weak learner”), integrated learning combined with multiple learners can often obtain significantly better generalization performance than a single learner. As demonstrated by many practical applications, however, AdaBoost presents better convergence performance, consumes less time, and occupies lower memory resources. As such, this section will mainly focus on extending this algorithm to the online model in identifying single-phase earth faults.

Bagging and boosting methods focus on sample sampling and parallel learning, and error sample relearning and reinforcement of the base learner, respectively. It is obvious that the latter has more advantages. In view of this, based on optimization of the fault feature set by dimensionality reduction of the PCA method, this section will build a single-phase grounding fault classification model combined with Boosting’s AdaBoost method. Of which, the base learner of the AdaBoost method primarily utilizes SVM in order to enhance the robustness of the classification effect of the model.

Furthermore, the pseudo-code of the principle of constructing the grounding fault classification model combined with the AdaBoost method is shown in Figure 2.

3.4 The flowchart of the proposed identification model

Combined with Sections 2–3, the proposed single-phase earth fault identification model based on AdaBoost is detailed in Figure 4. As seen from Figure 4, it mainly includes five key steps: data preprocessing, construct feature, feature engineering, build AdaBoost-based identification model, and optimize hyperparameter. Particularly, data preprocessing used for extracting zero-sequence voltage and zero-sequence current is first conducted. Second, Step B constructs fault features *via* current mainstream algorithms in addition to the proposed angle-conversion model. Next, feature engineering is explored according to PCA-based algorithm to select the best and most sensitive features. Subsequently, a custom-designed single-phase earth ground fault identification model is put forward, where an AdaBoost-based model is conducted as an example and numerically compared in detail.

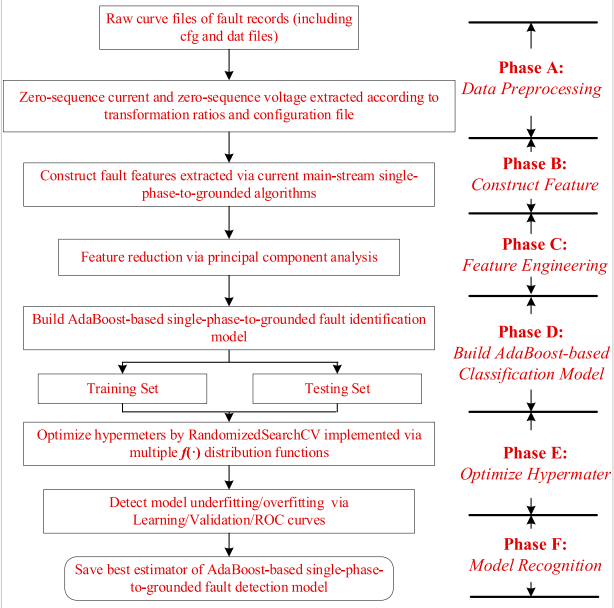

FIGURE 4
AdaBoost-based single-phase earth ground fault identification model.

4 Numerical studies

In order to verify the effectiveness of the method proposed in this article, a single-phase grounding fault feature set is constructed by combining the two dimensions of true waveform and simulation modeling. Of these, the distribution network model based on PSCAD, as shown in Figure A1, and the selected Mianyang true test waveform are established. The single-phase grounding fault with variable parameters such as arc suppression coil grounding system and ungrounded system under different load levels, fault initial phase angle, and transitional resistance, along with normal operation tests of the system, such as non-synchronization closing, magnetizing inrush current, and non-synchronization load commissioning and decommissioning, has been taken into consideration.

The result is that the number of single-phase grounding fault samples and anti-interference samples is, respectively, 108 and 27, equating to a ratio of nearly 6:1. In combination with up-

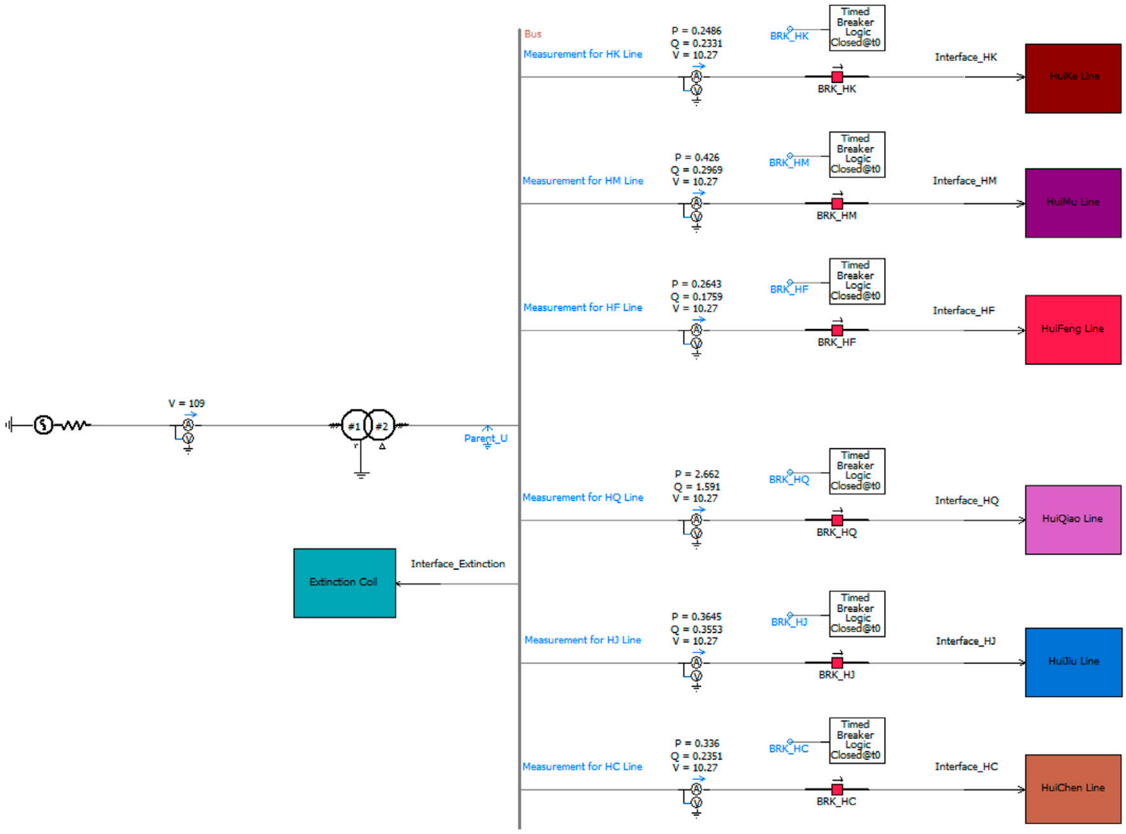

FIGURE A1
Single-phase grounding fault simulation system of a distribution network based on PSCAD.

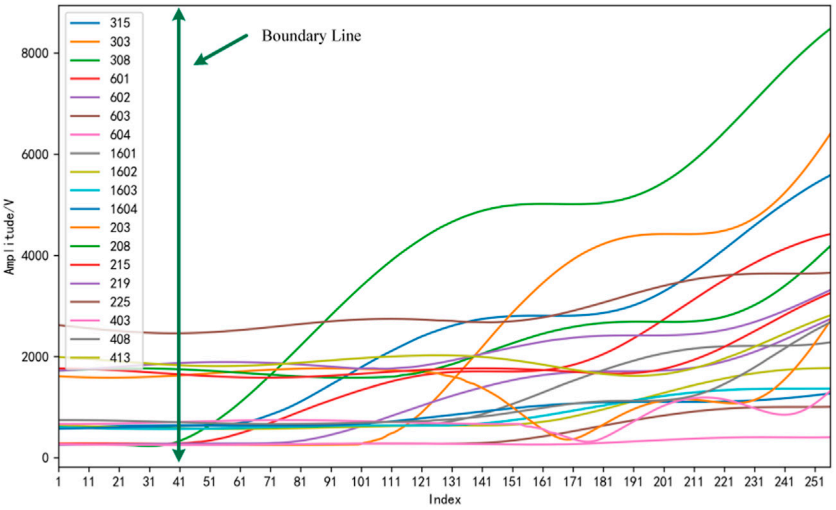

FIGURE 5
$3U_0$ amplitude change curve when a single-phase grounding fault occurs in arc suppression coil grounded and ungrounded systems.

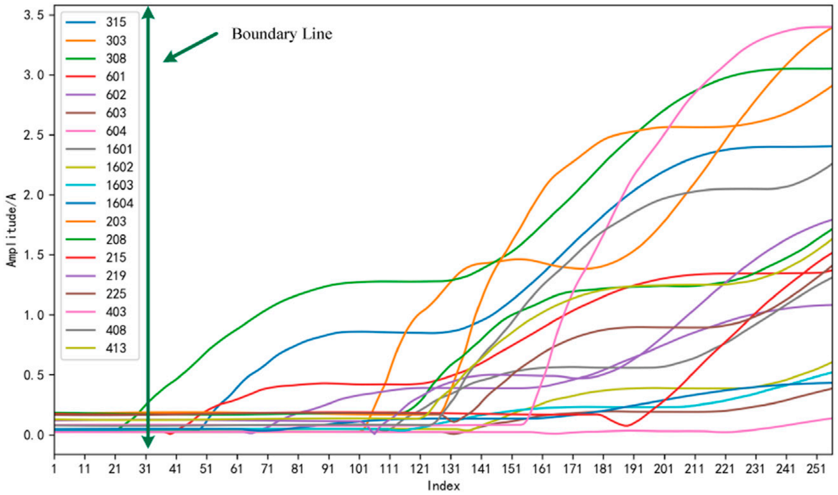

FIGURE 6
3I0 amplitude change curve when a single-phase grounding fault occurs in arc suppression coil grounded and ungrounded systems.

TABLE 2 Pseudo-code of the ground fault classification learning model based on AdaBoost proposed by Shu et al. (2019).

Input: grounding fault feature sample set $D = \{\{x_1, y_1\}, \{x_2, y_2\}, \cdots, \{x_m, y_m\}\}$

Base learning algorithm $\mathfrak{I} = SVM$

Number of training rounds T

Process:

```
1: $D_1(t) = 1/m$. Neutralize all samples: $x_i \leftarrow x_i - \frac{1}{m}\sum_{i=1}^{m} x_i$
2: $for\ t = 1, 2, \cdots, T\ do$
3: $h_t = \mathfrak{I}(D, D_t)$
4: $\epsilon_t = P_{x \sim D_t}(h_t(x) \neq f(x))$
5: $if\ \epsilon_t > 0.5\ then\ break$
6: $\alpha_t = \frac{1}{2} ln\ (\frac{1-\epsilon_t}{\epsilon_t})$
7: $D_{t+1}(x) = \frac{D_t(x)}{Z_t} \times \begin{cases} exp(-\alpha_t), & if\ h_t(x) = f(x) \\ exp(\alpha_t), & if\ h_t(x) \neq f(x) \end{cases} = \frac{D_t(x)\, exp\ (-\alpha_t f(x) h_t(x))}{Z_t}$
8: end for
Output: $H(x) = sign(\sum_{t=1}^{T} \alpha_t h_t(x))$
```

sampling technology, the ratio of the number of fault samples and non-fault samples will be adjusted to 1:1, and the total number of samples will be 216. In addition, the initial fault feature dimension is 1,536 dimensions. After dimensionality reduction by the PCA method in Section 2.2, the dimension of the eigenvector will be adjusted to 12 dimensions, with a compression rate as high as 99.21%.

4.1 Statistical analysis of single-phase grounding fault features

In combination with Section 1.2, the $\mathcal{M} = [U_p^{amp}, \Delta U_p^{amp}, U_p^{theta}, I_p^{amp}, \Delta I_p^{amp}, I_p^{theta}]$ of single-phase grounding fault feature engineering can be constructed directly, but there is a lack of the boost method to learn the process mechanism between feature engineering and target. In this regard, the following will take $3U_0$ of zero-sequence voltage amplitude and $3I_0$ of zero-sequence current amplitude of single-phase grounding fault under systems of arc suppression coils being grounded and ungrounded as examples to provide their distribution statistical curves, as shown in Figures 5, 6, respectively.

It can be seen from Figures 5, 6 that no matter whether the system is grounded or not, there are obvious demarcations for the zero-sequence voltage and zero-sequence current of the system, which correspond to before and after the fault. In addition, after demarcation, $\boldsymbol{3U_0}$ and $\boldsymbol{3I_0}$ show a trend of gradual increase and deterioration. The two features clearly illustrate the necessity and importance of adopting $\boldsymbol{3U_0}$ and $\boldsymbol{3I_0}$ to build feature engineering for grounding faults, and they can provide favorable learning features for the AdaBoost method, thus guiding it to build a reasonable single-phase grounding fault classification learning model.

4.2 AdaBoost accuracy rate of the AdaBoost grounding fault classification model

For the simulation test and true waveform fault set, after adopting the single-phase grounding fault classification model

TABLE 3 AdaBoost confusion matrix.

	Predicted fault sample	Predicted non-fault sample
Actual fault samples	101/TPR	7/TFR
Actual non-fault samples	0/FPR	108/FFR

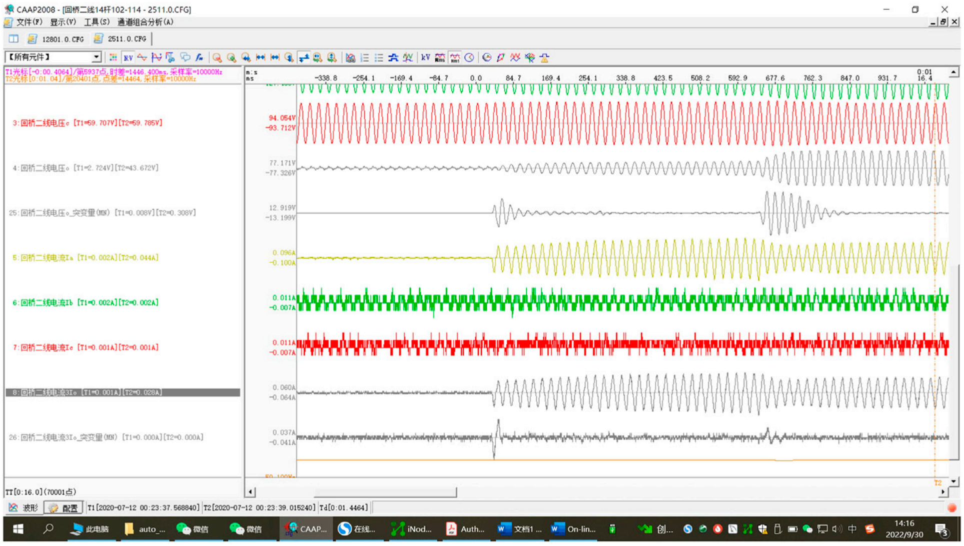

FIGURE 7
Single-phase grounding fault under the mixed medium of branches and leaves on the cement ground through a 50-cm conductor.

constructed using AdaBoost algorithm in Table 2, the confusion matrix (Shu et al., 2019) of fault and non-fault samples, including the training set and test set, can be obtained, as shown in Table 3.

In Table 3, indicators TPR, TFR, FPR, and FFR represent the true-positive rate, true-false rate, false-positive rate, and false rate, respectively (Shu et al., 2019). According to the confusion matrix in Table 3, there are 101 correct predictions of fault cases, up to 93.52% of the total, while the prediction accuracy of non-fault examples is 100%, with all predictions divided correctly. After analyzing the seven waveforms being incorrectly divided for fault examples, the errors are all attributed to one type of reason, namely, the grounding fault of ultra-high resistance Rd. Data from a real test in Mianyang is taken as an example: single-phase grounding fault under the mixed medium of branches and leaves on the cement ground through 50 cm conductor; line voltages U_{ab}, U_{bc}, U_0, I_a, I_b, I_c, and I_0 of corresponding line are shown in Figure 7.

According to Figure 6, when the system is in normal operation, the voltage imbalance is nearly 3%. As far as the zero-sequence voltage change curve is concerned, the fault belongs to a long-term gradual fault, and the change of zero-sequence voltage is also a process of gradual deterioration and increase. At the first fault moment, the transitional resistance reaches as high as 27k, and $3U_0$ and $3I_0$ change slightly. Most algorithms are likely to include this into the category of zero-sequence voltage fluctuation caused by non-synchronization load of system commissioning and decommissioning. However, in the second fault after 612 ms, the sudden trend changing of zero-sequence voltage and the obvious characteristics of opposite polarity of $3U_0$ and $3I_0$ can obviously be judged as a single-phase grounding fault for most algorithms. In terms of the latter, the single-phase grounding fault classification model based on AdaBoost constructed in this article can also study and judge the grounding fault.

In addition, after further analyzing the waveform, it is found that the reasons for the poor effect of most algorithms also relate to two aspects. The first aspect is the algorithm level. Looking at the waveform, even 100 ms after the fault has occurred, in combination with the obvious opposite direction characteristics of zero-sequence voltage and zero-sequence current, the head half-wave method and

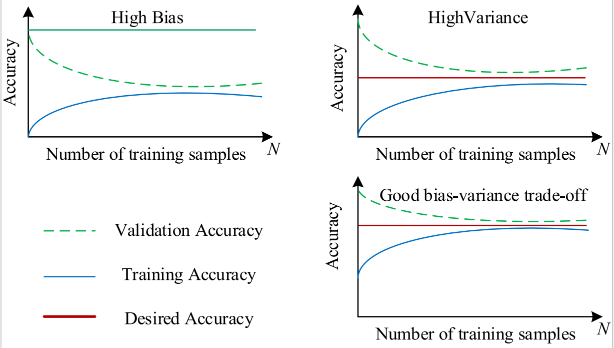

FIGURE 8
Learning curve used for assessing model overfitting/underfitting.

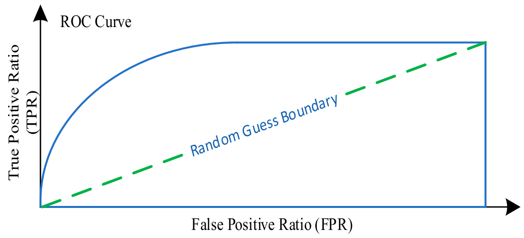

FIGURE 9
ROC curve to measure the pros and cons of model classification performance.

steady-state method can still identify the fault. For the parameter method, the zero voltage change trend is not obvious in the middle of the fault, which can easily lead to the failure of the parameter method. The second aspect is the response speed. From the perspective of fault form, this is a long-time gradual fault, and the interval between the salient features of the two faults is 618 ms. If the fault can be identified only in the second salient feature, it is likely that the hidden danger of mountain fire will occur due to the burning of dry leaves caused by the previous fault, and the best rescue opportunity will be missed.

4.3 Performance of the AdaBoost single-phase grounding fault classification model

In order to help build the algorithm and give full play to its practical application, the performance of the proposed AdaBoost single-phase grounding fault classification model will be verified from the dimensions of the learning curve and ROC curve. In order to understand the intuitive evaluation of the performance of the classification model from the perspective of the two types of curves, the definitions of the two types of curves will be described first.

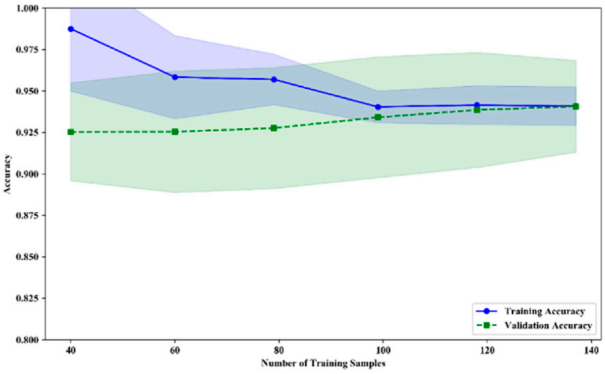

FIGURE 10
Application of the AdaBoost ground fault classification model learning curve.

4.3.1 Learning curve

The learning curve is the score change curve of sizes and models of different training sets on the training set and verification set, that is, the number of samples is taken as the abscissa, and the scores on the training and cross-validation sets (such as accuracy) are taken as the ordinate. A learning curve can help us judge the current state of the model: overfitting/high variance or underfitting/high-bias. Figure 8 shows the learning curve for measuring the degree of overfitting or underfitting of the model. The high variance emphasizes that the generalization ability of the model is not ideal when applied to the test set, while the high-bias characterization model lacks the deep mining of feature engineering.

4.3.2 Receiver operating characteristic curve

The receiver operating characteristic curve (ROC curve in short) is also known as the sensitivity curve. The reason for such a name is that the points on the curve reflect the same sensitivity. They are all responses to the same signal stimulus, but the results have been obtained under several different criteria. The general outline of the ROC curve is shown in Figure 9.

In Figure 9, the receiver operating characteristic curve is a coordinate diagram composed of false alarm probability as the horizontal axis and hit probability as the vertical axis. The curve drawn reflects the different results obtained by the subjects under specific stimulus conditions due to different judgment criteria. The ROC curve emphasizes the balance between TPR and FPR, which can effectively avoid the influence of differentiation of different judgment criteria.

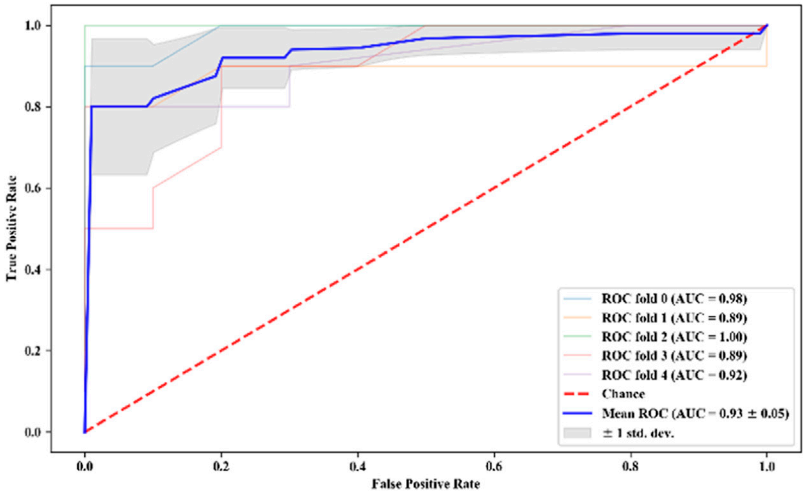

FIGURE 11
ROC curve of the AdaBoost ground fault classification model.

TABLE 4 Identification effects of six models based on machine learning under PCA-based feature engineering.

	Indicator	LR	KN	AdaBoost
PCA	Accuracy/%	88.58	83.74	93.52
	AUC	0.92	0.87	0.93

Combined with the classification characteristics of single-phase grounding faults, the higher the proportion TPR of the samples predicted to be positive and actually positive in Figure 8 in all positive samples, the lower the proportion FPR of the samples predicted to be positive but actually negative in all negative samples; or the higher the area of the blue closed area constructed by points (FPR and TPR) (random guess: the area of the closed graph is 0.5), the better the performance of the fault classification model.

Furthermore, the learning curve and ROC curve based on the AdaBoost single-phase grounding fault classification model are given in Figures 10, 11, respectively.

It can be seen from Figure 10 that with the increase of the number of training samples, the classification accuracy of the training set and the verification set gradually trend toward sameness, and the classification accuracy of the verification set gradually increases. The generalization ability of the characterization model applied to the unknown fault set is strong, but the improvement of this ability comes at the expense of a certain level of weakening of the training effect of the training set. Therefore, the performance of the classification model constructed by the machine learning method represented by AdaBoost depends on the compromise of training and verification effects, and it is also the balance between high-bias and high variance of the classification model.

With regard to Figure 10, it can be seen that under the premise of cross validation of five copies for the training set, the AUC of each corresponding ROC curve is 0.98, 0.89, 1.00, 0.89, and 0.92, respectively, which are far higher than 0.5 of random guess, and the overall average AUC /standard deviation of AUC is 0.93 and ±0.05. A small standard deviation indicates that the training effect of the model is relatively stable. Moreover, comparative studies between the proposed and the other two methods are also conducted, namely, logistic regression (LR) and K-neighbor (KN), as shown in Table 4. As seen from Table 4, both the accuracy and AUC indicators of the model constructed in this work are superior, which fully demonstrates the validity and the high value in engineering practice.

In general, the AdaBoost single-phase grounding fault classification model established in this article can better adapt to the differential selection of different judgment criteria under specific stimulus conditions, the overall performance is more stable, and the robust performance is better.

5 Conclusion

This article discusses the classification research of machine learning algorithm jointly driven by both physical model and fault data in single-phase earth ground fault identification and constructs a single-phase grounding fault classification model based on AdaBoost. For PSCAD simulation model and fault and non-fault examples under the true waveform test, the classification accuracy of the model is 93.52%. Second, in conjunction with up-sampling technology, PCA dimensionality reduction technology, learning curve, and ROC curve, the construction of feature engineering, dimensionality reduction optimization, and model performance evaluation are achieved, respectively. Among them, after PCA dimensionality reduction technology is adopted, feature engineering can be transformed into the feature space represented by a 12-dimension vector with a space compression rate as high as 99.21%. The training effect of the training set and verification set in the learning curve tends to be 0.93 as a whole, and the average AUC under cross verification also reaches nearly 0.93, which mutually confirms the highly accurate training effect of the proposed AdaBoost model and the identification and generalization ability of grounding faults under strong interference and bad working conditions.

Data availability statement

The raw data supporting the conclusion of this article will be made available by the authors, without undue reservation.

Author contributions

All authors listed have made a substantial, direct, and intellectual contribution to the work and approved it for publication.

Funding

This work was supported by the State Grid Sichuan Supply Company Science Project under grant no. 52199720002T.

Conflict of interest

HY, ZW, and ZQ were employed by Nari Technology Nanjing Control Systems Co., Ltd.

The remaining authors declare that the research was conducted in the absence of any commercial or financial relationships that could be construed as a potential conflict of interest.

The authors declare that this study received funding from State Grid Sichuan Supply Company Science Project. The funder had the following involvement in the study: collection, analysis, interpretation of data.

Publisher's note

References

An, D., Chen, T., Li, J., Yao, K., Zhang, H., and Wang, H. (2020). Design of a small current grounding line selection device based on a half-wave Fourier algorithm. *[J], Power Syst. Prot. Control* 48 (09), 157–163.

Ai, B., Zhang, R., and Li, Y. (2009). *Overview of line selection technology for small current earth fault*. North China Electric Power, Beijing.

Cui, T., Dong, X., Zhiqian, B., and Juszczyk, A. (2011). Hilbert-transform-based transient/intermittent earth fault detection in noneffectively grounded distribution systems. *IEEE Trans. Power Deliv.* 26 (1), 143–151. doi:10.1109/tpwrd.2010.2068578

Dahlan, R. (2018). "AdaBoost noise estimator for subspace based speech enhancement[C]," in *2018 international conference on computer, Control, informatics and its applications (IC3INA)*, 110–113.

Gautam, S., and Brahma, S. M. (2012). Detection of high impedance fault in power distribution systems using mathematical morphology. *IEEE Trans. Power Syst.* 28 (2), 1226–1234 Aug. doi:10.1109/tpwrs.2012.2215630

Ghaderi, A., Ginn, H. L., and Mohammadpour, H. A. (2017). High impedance fault detection: A review. *Electr. Power Syst. Res.* 143, 376–388. doi:10.1016/j.epsr.2016.10.021

He, L., Shi, C., Yan, Z., Cui, J., and Zhang, B. (2017). A fault location method for small current grounded systems based on the relative entropy of generalized S-transform energy[J]. *Trans. Chin. Soc. Electr. Eng.* 32 (08), 274–280.

Jiale, S., Kang, X., and Song, G. (2007). etc. A preliminary study on the principle of relay protection based on parameter identification[J]. *J. Electr. Power Syst. Automation* 19 (1), 14–20.

Li, X. (2017). Line selection method of small current Earth fault based on three lines display. *Electr. Eng.* 4, 6–7.

Lishan, W., Jia, W., and Jiao, Y. (2020). Single-phase fault line selection scheme of a distribution system based on fifth harmonic and admittance asymmertry[J]. *Power Syst. Prot. control* 48 (15), 77–83.

Liu, W., Xu, B., Liu, Y., Wang, A., and Chen, H. (2018). Small current grounding fault demarcation method based on transient current[J]. *Automation Electr. Power Syst.* 42 (24), 157–162+202.

Pan, Z., Fang, S., and Wang, H. (2020). LightGBM technique and differential evolution algorithm-based multi-objective optimization design of DS-APMM. *IEEE Trans. Energy Convers.* 36 (1), 441–455. doi:10.1109/tec.2020.3009480

Shu, H., Li, Y., Tian, X., and Yi, F. (2019). Distribution network fault line selection based on correlation analysis of cross-overlap differential transformation[J]. *Automation Electr. Power Syst.* 43 (06), 137–144+ 176.

Song, G., Guang, L., and Yu, Y. (2011). Location of single-phase grounding fault section in distribution network based on sudden changes in phase current [J]. *Automation Electr. Power Syst.* 35 (21), 84–90.

Wang, W., Cheng, L., and Fan, Y. (2021). Earth fault identification method for distribution station independent of zero sequence voltage. *Automation Electr. Power Syst.* 45 (9), 122–129.

Wu, S., and Hiroshi, N. (2014). Parameterized AdaBoost: Introducing a parameter to speed up the training of real AdaBoost. *IEEE Signal Process. Lett.* 21. (6), 687–691. doi:10.1109/lsp.2014.2313570

Xu, B., Xue, Y., and Li, T. (2005). Overview of line selection technology for small current Earth fault. *Electr. Equip.* 4, 1–7.

Xue, Y., Li, J., and Xu, B. (2015). The transient equivalent circuit and transient analysis of the small current grounding fault of the neutral point through the arc suppression coil grounding system[J]. *Proc. Chin. Soc. Electr. Eng.* 35 (22), 5703–5714.

Xue, Y., Zuren, F., Xu, B., Chen, Y., and Jing, L. (2003). Research on low current grounding line selection based on transient zero sequence current comparison [J]. *Automation Electr. Power Syst.* 4 (09), 48–53.

Yao, H., and Cao, M. (2009). *Resonant grounding of power system [M]*. Beijing: China Electric Power Press.

Zeng, X., Wang, Y., Jian, L., and Xiong, T. (2012). New principles of fault arc suppression and feeder protection based on flexible grounding control of distribution network[J]. *Proc. Chin. Soc. Electr. Eng.* 32 (16), 137–143.

Zhang, B., and Yin, X. (2011). *Power system relay protection [M]*. Background: China Electric Power Press.

Zhou, Z. (2016). *Machine learning [M]*. Beijing: Tsinghua University Press.

Zhu, L. (2011). *Research on single-phase short-circuit fault and its protection of low resistance grounding system in 10kV distribution network [D]*. Changsha: Hunan University.

Frontiers in
Energy Research

Advances and innovation in sustainable, reliable and affordable energy Explores sustainable and environmental developments in energy. It focuses on technological advances supporting Sustainable Development Goal 7: access to affordable, reliable, sustainable and modern energy for all.

Discover the latest Research Topics

See more →

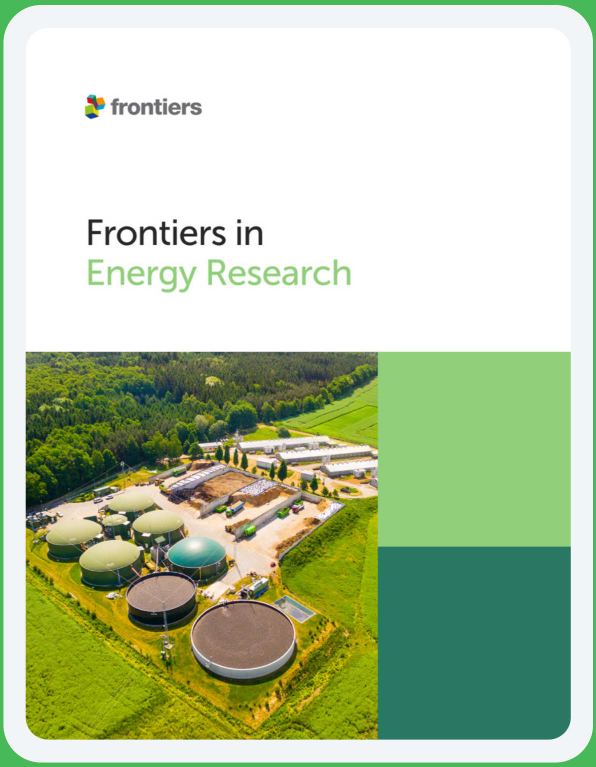

Frontiers

Avenue du Tribunal-Fédéral 34
1005 Lausanne, Switzerland
frontiersin.org

Contact us

+41 (0)21 510 17 00
frontiersin.org/about/contact